UNIVERSITÉ DE STRASBOURG

ÉCOLE DOCTORALE Physique et Chimie-Physique (ED182)

IPHC/UMR7178

THÈSE présentée par :

Léna MOUAWAD

soutenue le : **16 Décembre 2017**

pour obtenir le grade de : **Docteur de l'université de Strasbourg**

Discipline/ Spécialité : Physique

Monte Carlo simulations and a theoretical study of the damage induced by ionizing particles at the macroscopic scale as well as the molecular scale

THÈSE dirigée par :

Dr. EL BITAR Ziad	Chargé de recherche CNRS, université de Strasbourg
Pr. KHALIL Mohamad	Directeur de recherche, université Libanaise

RAPPORTEURS :

Dr. BORDAGE Marie-Claude	Chargée de recherche, université Paul Sabatier
Dr. ROUMIE Mohamad	Directeur de recherche, commissariat Libanais à l'énergie atomique

---

AUTRES MEMBRES DU JURY :

Pr. NAJA Adnan	Professeur, université Libanaise
Dr. FRANCIS Ziad	Maître de conférences, université Saint Joseph

Université Libanaise
École Doctorale
Sciences et Technologies

UNIVERSITÉ DE STRASBOURG

Doctorat Université Libanaise

THESE de doctorat

Pour obtenir le grade de Docteur délivré par

L'Ecole Doctorale des Sciences et Technologie

(Université Libanaise)

Spécialité : Physique

Présentée et soutenue publiquement par

Mouawad Léna

Le 16 Décembre 2017

Monte Carlo simulations and a theoretical study of the damage induced by ionizing particles at the macroscopic scale as well as the molecular scale

Directeur de thèse **: Khalil Mohamad**

Co-encadrement de la thèse **: El Bitar Ziad**

Membre du Jury

M.Mohamad Khalil,Professeur,CRSI,Université Libanaise	Directeur de thèse
M.Ziad El Bitar,Chargé de recherche CNRS,IPHC-CNRS,Université de Strasbourg	Directeur de thèse
Mme.Marie-Claude Bordage,Chargée de recherche,CRCT,Université Paul Sabatier Toulouse	Rapporteur
M.Mohamad Roumie,Professeur,CNRS,Comissariat Libanais à l'energie atomique	Rapporteur
M.Adnan Naja,Professeur,Faculté des sciences III,Université Libanaise	Examinateur
M.Ziad Francis,Maitre de conférences,Faculté des sciences,Université Saint Joseph	Examinateur
M.Ahmad Osman,Maitre de conférences,Faculté des sciences III,Université Libanaise	Invité

Résumé

Le travail effectué au cours de cette thèse se place dans le cadre des simulations des dommages biologiques induits par les rayonnements ionisants pour les traitements de cancer en radiothérapie. La radiothérapie commence par l'imagerie, qui permet de déceler la forme et l'emplacement de la tumeur, et comprends plusieurs étapes qui précèdent l'exécution de l'irradiation. Cette série d'étapes visent à optimiser l'irradiation de façon à cibler les cellules cancéreuses et constitue la planification de traitement. A ce niveau, les simulations Monte Carlo ont été largement utilisées et permettent de prévoir le résultat de l'irradiation avant son exécution. Ainsi, il est possible d'ajuster les paramètres de l'irradiation afin d'avoir l'effet biologique demandé. Les interactions des particules avec les constituants du milieu biologique sont simulées grâce à des modèles physiques et des processus physiques définis dans les codes de simulations et sélectionnés selon l'application. Des simulations aux échelles macroscopiques et moléculaires sont ainsi possibles. Ces modèles se basent sur des sections efficaces pour déterminer les probabilités des interactions. En raison de la complexité et la diversité du milieu biologique, il est difficile de déterminer les sections efficaces d'interaction avec les vraies composantes de ce milieu et ces sections efficaces sont souvent approximées par des sections efficaces d'interaction avec l'eau. Evidemment, l'eau est la composante principale du milieu biologique, mais pour des simulations plus exactes il est impératif d'avoir les sections efficaces d'interaction avec les molécules biologiques plus complexes. D'où l'importance des études fondamentales qui sont menées en parallèle, pour fournir ces sections efficaces et optimiser les modèles physiques sur lesquels sont basés ces simulations. Les sections efficaces d'interaction des particules avec les molécules biologiques ne sont toujours pas disponibles due à la difficulté de les calculer et la difficulté de mener des expériences précises pour ces molécules complexes. Ainsi, le but principal de cette thèse est de proposer un formalisme qui permet de déterminer les sections efficaces d'interaction avec des molécules biologiques complexes pour améliorer les simulations des dommages biologiques induits par les rayonnements ionisants et par la suite établir des plans de traitements plus efficaces.

D'abord nous abordons une étude macroscopique qui vise à développer un plan de traitement en protonthérapie petit-animal, puis une étude de micro-dosimétrie où on quantifie les dégâts biologiques induits par le nombre de cassures double-brin de l'ADN, et finalement une étude fondamentale où on propose un algorithme pour déterminer les sections efficaces d'ionisation des molécules biologiques. Chaque étude adresse une problématique différente et propose une approche pour des simulations plus exactes. En effet, plusieurs considérations adoptées et

approximations faites en radiothérapie ont été mise en question au cours des années. Par exemple, plusieurs études ont montré que la dose absorbée, qui est considérée comme indicateur des dommages induits, doit être remplacée par des paramètres biologiques. Les plans de traitements se basent souvent sur la dose physique prédite par des simulations macroscopiques. Dans ce cadre, nous effectuons des simulations macroscopiques dans le but d'ajuster les différents paramètres de l'irradiation de façon à avoir un dépôt de dose homogène dans la tumeur. Nous montrons que le choix de l'incertitude de la dose physique qui permet d'avoir un traitement efficace ne peux pas être fait sans prendre en compte l'effet biologique réalisé. Alors nous passons à des simulations microscopiques, grâce aux interactions Geant4-DNA qui permettent des simulations micro-dosimétriques, et nous étudions les dégâts induits à l'échelle de l'ADN. On calcule ainsi le nombre de cassures simple et double-brin de l'ADN, induits par le faisceau de protons et on compare la distribution biologique de dégât à la distribution physique de dose pour mettre en relief l'insuffisance de la dose physique pour décrire les dommages biologiques réalisés. Dans ces simulations, la cible biologique est modélisée par des volumes simples remplis d'eau. Plusieurs études ont proposé des modèles géométriques sophistiqués pour décrire l'ADN et le milieu biologique, mais de telles études ferons toujours défaut si les modèles physiques qui décrivent les interactions des particules se basent sur les sections efficaces de l'eau. Alors nous nous intéressons à fournir ces sections efficaces pour les molécules biologiques diverses en proposant un cadre théorique adapté aux molécules complexes.

En première partie, une approche macroscopique est abordée où la dose absorbée est utilisée pour quantifier les dommages induits en considérant une application particulière : la protonthérapie petit animal. Les simulations Monte Carlo ont été largement utilisées dans ce cadre pour simuler les interactions des particules avec le milieu biologique et prédire la distribution de dose dans la cible [1]. Pour modéliser l'environnement biologique que les particules parcourent, des structures en eau sont souvent utilisées, l'eau étant la composante majoritaire de la matière biologique [2]. La planification de traitement porte sur plusieurs étapes en commençant par l'obtention d'une image de la tumeur pour déterminer sa position, sa taille et son contourage jusqu'à l'irradiation pendant laquelle la dose nécessaire est livrée à la tumeur. Le but principal de la planification du traitement est d'assurer une répartition de dose homogène dans la cible en sauvegardant autant que possible les tissus sains voisins. Les paramètres du faisceau ainsi que les conditions d'irradiation peuvent être déterminés avant l'irradiation et ajustés de façon à assurer la dose prescrite à la tumeur, grâce aux simulations Monte Carlo.

La méthode Monte Carlo est une méthode statistique qui utilise des générateurs de nombres aléatoires, des distributions de probabilités et des sections efficaces d'interaction pour déterminer la probabilité d'interaction de chaque particule avec le milieu considéré. Plusieurs codes de simulations ont été développés et utilisés pour des applications diverses [3–6]. Le calcul de dose précis dans des structures hétérogènes, la possibilité de prédire et suivre les particules secondaires émises, ainsi que la description stochastique des interactions physiques, sont des atouts des simulations Monte Carlo qui les rendent particulièrement intéressantes dans le

domaine médical surtout en radiothérapie, radioprotection et médecine nucléaire. L'idée principale est de créer un modèle représentatif du système considéré et de simuler les interactions d'un faisceau de particules avec ce système en se basant sur l'échantillonnage aléatoire des fonctions de densité de probabilité. Ces simulations offrent la possibilité de changer des paramètres et tester l'effet de ces modifications ce qui n'est pas possible dans l'approche expérimentale. Le code Geant4 (GEometry ANd Tracking) [7] est un code source ouvert qui a été conçu pour simuler les interactions des particules avec la matière en se basant sur plusieurs modèles physiques pour déterminer les sections efficaces des processus électromagnétiques standards. GATE (Geant4 Application for Emission Tomography) [8] est un simulateur Monte Carlo basé sur Geant4 qui profite alors de la validation des composantes physiques de Geant4. L'utilisateur peut sélectionner les interactions à considérer dans la simulation ainsi que les matériaux des différentes structures modélisant le système.

L'optimisation des conditions d'irradiation pour l'application considérée dans ce travail a été faite avec la version 2.9 de GATE. La plateforme petit-animal disponible à l'équipe ImaBio, dont je faisais partie pendant ma première année de thèse, ainsi que l'installation du cyclotron Cyrcé [9] à l'Institut Pluridisciplinaire Hubert Curien (IPHC), capable de livrer un faisceau de protons jusqu'à 24 MeV d'énergie, a encouragé plusieurs projets de recherche parmi lesquels la conception d'un plan de traitement en proton thérapie petit animal qui était le but de ma thèse. Nous nous sommes particulièrement intéressés à la conception d'un outil de collimation qui permettra de déposer la dose dans une sphère de 5 millimètres de diamètre, structure équivalente à une tumeur de forme sphérique chez une souris [10]. Nous avons proposé différents modèles de compensateurs qui pourront être placés entre le faisceau et la cible pour contrôler la forme spatiale du dépôt de dose en 3 dimensions. Deux géométries possibles sont représentées dans la figure 1.

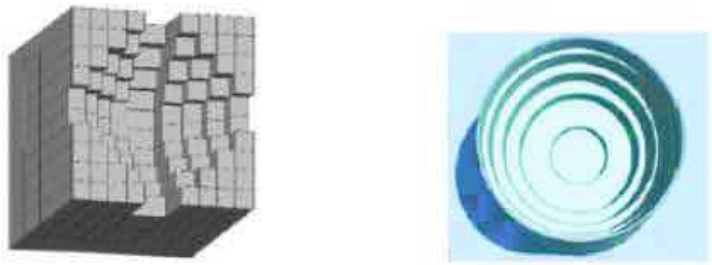

Figure 1: Modèles de compensateurs utilisés pour créer des pertes différentes en énergie selon la position du proton en 3 dimensions.

Une des configurations proposées consiste à rassembler des cylindres de dimensions différentes de façon à créer une perte en énergie qui conduit à l'arrêt des protons correspondants à la périphérie de la sphère. Un code Matlab a été développé pour déterminer les positions des constituants élémentaires du compensateur ainsi que leurs dimensions et générer la partie correspondante qui concerne la description de ce compensateur dans GATE. Il apparait alors qu'en augmentant le nombre de

cylindres constituants le compensateur, le profil de dose se rapproche d'un profil sphérique. Néanmoins, la diffusion des électrons et la déviation de leur trajectoire initiale à la suite des collisions avec le compensateur mènent à des dépôts de dose en dehors du profil prévu. De plus, ce profil ne peut pas être respecté dans la moitié proximale de la cible. Due à la complexité de la réalisation d'une telle technique en pratique, une approche plus simple, qui consiste à insérer des atténuateurs d'épaisseurs différentes entre la source et la cible pour moduler l'énergie du faisceau, a été considérée.

En effet, l'atout de la proton thérapie [11] par rapport à la radiothérapie conventionnelle est bien illustré par le pic de Bragg : les protons déposent leur énergie juste avant de s'arrêter. La distance à laquelle cette énergie est déposée peut être contrôlée en faisant varier l'énergie des protons. Ainsi, en changeant l'épaisseur de l'atténuateur, l'énergie des protons est modifiée et la dose est déposée à des profondeurs différentes de la cible. Le nombre d'atténuateurs nécessaires pour avoir une dose homogène ainsi que la durée d'irradiation à travers chaque atténuateur ont été optimisés à travers un code Matlab que nous avons développé pour cette approche plus simple. Deux matériaux ont été utilisés pour les atténuateurs, l'Aluminium et le Poly méthacrylate de méthyle et l'incertitude sur l'homogénéité de la dose de 10 Gy a été calculée en fonction du nombre d'atténuateurs ainsi que l'incertitude sur l'énergie du faisceau. Les expériences n'ont pas été faites dans le cadre de cette thèse qui s'est orientée vers les simulations et les approches théoriques pour modéliser les interactions particules-matière biologique et par la suite les dommages biologiques à l'échelle de l'ADN. Dans la figure 2, on montre le profil de dose déposée obtenu en utilisant 21 atténuateurs en Poly méthacrylate de méthyle.

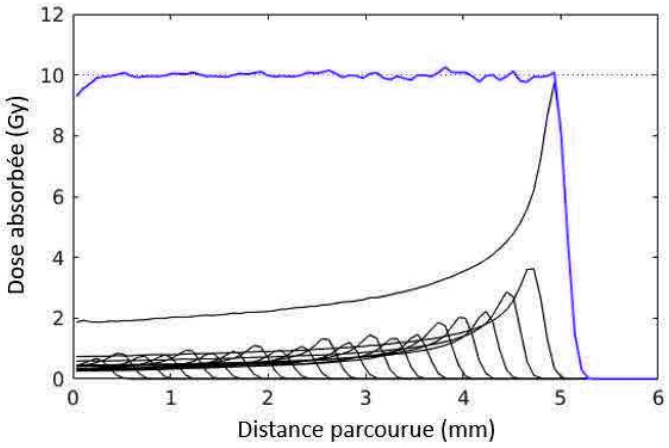

Figure 2: Dose déposée par le faisceau de protons de 24 MeV dans un volume en eau à la suite du passage à travers 21 atténuateurs en Poly méthacrylate de méthyle de longueurs différentes.

L'incertitude de la dose, qui est le paramètre utilisé pour juger efficacité du traitement ne constitue pas un véritable indice du dommage biologique effectué. Bien que la dose absorbée permette d'avoir une idée macroscopique sur la répartition de ces dégâts dans la cible, une approche basée sur la dose absorbée ne prend pas en compte les différentes interactions élémentaires qui ont lieu à l'échelle moléculaire et cellulaire. L'intensité des dégâts induits ne dépend pas uniquement de la dose déposée. Il existe également des codes Monte Carlo qui permettent de simuler les dégâts biologiques

au niveau des cellules et des molécules [12–14]. L'extension Geant4-DNA [15] au code Geant4 a permis de telles simulations en ajoutant des interactions physiques pour simuler la production des particules secondaires jusqu'à des énergies de quelques électron volts dans des volumes sub-nanométriques. Ces processus comme l'excitation, l'ionisation et l'échange de charge, sont décrits dans des modèles théoriques utilisés pour calculer les sections efficaces des interactions analytiquement ou par interpolation de bases de données. Les sections efficaces actuellement utilisées pour les interactions Geant4-DNA ont été validées par comparaison à des sections efficaces expérimentales et en comparant les parcours des différentes particules ainsi que les pouvoirs d'arrêts à des résultats publiés.

Nous nous sommes alors intéressés à évaluer les dégâts induits par le faisceau de protons à l'échelle de l'ADN dans une étude micro dosimétrique. Nous avons alors considéré les conditions de la simulation macroscopique dans une simulation microscopique où le volume macroscopique en eau a été divisé en plusieurs volumes de dimension de l'ordre du micromètre. Les dépôts de dose ont été identifiés dans ces petits volumes grâce aux simulations Geant4 avec l'extension Geant4-DNA. Les informations sur ces évènements (position spatiale et énergie déposée) ont été ensuite introduites dans un fichier qui est utilisé pour calculer les cassures simple et double-brin de l'ADN.

Les dommages induits par les rayonnements ionisants visent plusieurs composantes de la cellule. Les dommages à l'ADN sont considérés comme la cause principale de la mort cellulaire comme l'ADN contient toute l'information génétique [16, 17]. Les cassures double-brin, qui peuvent résulter des cassures simple-brin non réparées ou mal réparées, sont les plus létales et leur processus de réparation est très complexe [18, 19]. Les cassures des brins de l'ADN peuvent être identifiées en fonctions de la dose absorbée. Plusieurs modèles ont été proposés pour ce but : Le modèle constant, le modèle seuil et le modèle linéaire. En général, les cassures simple-brin situés à une distance inférieure à la distance entre 10 paires de bases de l'ADN, et réparties sur les deux brins opposés de l'ADN, sont considérées comme une cassure double-brin [20–22]. Dans le modèle constant, la probabilité d'induction de cassures simple-brin est supposée invariante en fonction de l'énergie déposée [23]. Selon le modèle seuil, cette probabilité est nulle si l'énergie déposée est inférieure à une énergie seuil, notée E_{th}, et elle est égale à 1 si l'énergie déposée est supérieure à E_{th} [22]. Dans le modèle linéaire, la probabilité d'induction de cassure simple-brin de l'ADN augmente linéairement de 0 à 1 entre deux énergies E_{min} et E_{max} [24]. Les études utilisant ces modèles les appliquent en général dans une région sensible dehors laquelle d'autres considérations sont prises en compte pour évaluer les dommages induits par les effets indirects.

Les algorithmes de partitionnement de données sont très utiles pour de telles études parce qu'ils permettent de regrouper les dépôts d'énergies en grappes (ou clusters) de cassures de brins de l'ADN. Nous avons alors utilisé une version de l'algorithme DBSCAN (Density Based Spatial Clustering for Applications with Noise algorithm) [25], développée pour regrouper les évènements de dépôt d'énergie, selon leur distribution spatiale et leur énergie, en grappes de dommages à l'ADN [26]. Cette version de DBSCAN nous permet de prédire le nombre de cassures simple-brin et double-brin

de l'ADN à partir des structures de traces issues de Geant4. Elle permet aussi de différentier les cassures double-brin simples, qui résultent de deux cassures simple-brin, et les cassures double-brin complexes qui consistent de 3 cassures simple-brin ou plus. Le modèle linéaire est adopté pour classifier les dépôts d'énergie en cassures simple-brin, avec une énergie minimale E_{min} = 5 eV et une énergie maximale E_{max} = 37.5 eV [24]. Cinq paramètres d'entrée sont demandés : Le nombre minimal d'évènements constituants une grappe de dégât (*MinPts*), le rayon délimitant le voisinage d'un évènement (*eps*), la probabilité qu'un évènement se situe dans une région sensible (*SPointsProb*) ainsi que l'énergie minimale et l'énergie maximale qui définissent la probabilité d'induction des cassures de brins de l'ADN. Nous considérons que *MinPts = 2* comme il suffit d'avoir deux cassures simple-brin pour constituer une cassure double-brin, *eps = 3.2 nm* équivaut à la distance entre 10 paires de bases de l'ADN, et *SPointsProb = 15%* comme définie dans [26]. Tous les évènements identifiés par la simulation Geant4 dans chaque volume élémentaire passent par une fonction de probabilité qui décide si l'évènement considéré se situe dans une région sensible et est donc capable d'induire une cassure à un brin de l'ADN. Les évènements qui se situent dans cette région sensible sont ainsi considérés comme des cassures simple-brin. Ensuite, les cassures simple-brin identifiées sont groupées en grappes de dommage selon leurs localisations. Finalement, les cassures double-brin sont identifiées parmi les grappes de cassures en considérant qu'il suffit d'avoir deux cassures simple-brin avec une cassure située sur le brin opposé pour qu'une grappe de cassure soit classifiée comme cassure double-brin.

Les résultats de ces simulations, représentés dans la figure 3, montrent que le nombre de cassures simple-brin est presque invariant en fonction de la distance parcourue dans la cible. Au bout de 6 millimètres, distance correspondante au parcours des protons de 24 MeV dans l'eau, une chute est observée dans la distribution des cassures simple-brin qui s'annule au-delà de 6 millimètres. D'autre part, la distribution des cassures double-brin en fonction de la distance parcourue ressemble davantage à la distribution de la dose absorbée. Le nombre de cassures double-brin est presque constant à l'entrée du faisceau dans le volume en eau et puis augmente vers 6 millimètres en présentant un pic étroit qui ressemble au pic de Bragg de la dose absorbée. Dans une comparaison entre les deux distributions, on montre qu'il y a effectivement des différences entre ces deux profils. Mais la comparaison des cassures de brins de l'ADN avec la dose absorbée ne permet pas vraiment de faire des conclusions quantitatives sur l'efficacité de la dose absorbée pour décrire les dommages à l'ADN. L'évaluation de la dose biologique à partir d'une efficacité biologique relative des cassures doubles brins de l'ADN est nécessaire pour une meilleure comparaison. De telles études sont très importantes mais aussi très délicates et les résultats obtenus dépendent fortement des approximations et des considérations employées comme par exemple la modélisation du milieu biologique, les sections efficaces utilisées pour les interactions avec les molécules biologiques et le modèle utilisé pour quantifier les cassures des brins de l'ADN.

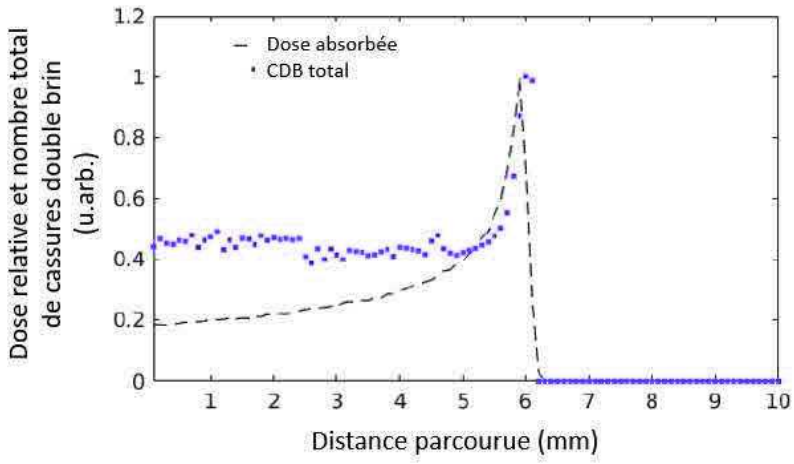

Figure 3: Distribution de cassures double-brin de l'ADN comparée au profil de dose déposée par le faisceau de protons de 24 MeV.

La recherche fondamentale qui accompagne les développements des codes de simulations est importante pour résoudre ces problématiques et pouvoir avancer correctement et profiter pleinement des simulations Monte Carlo. Nous passons alors à une étude fondamentale dans le but de calculer les sections efficaces de l'ionisation des molécules biologiques qui sont actuellement remplacées par les sections efficaces de l'eau dans ces simulations. Les interactions des particules sont souvent modélisées par les sections efficaces d'interactions dans l'eau, étant la principale composante de la matière biologique. Des études récentes ont cependant montré que cette approximation n'est valide qu'à très hautes énergies incidentes. En dessous de 250 eV, les sections efficaces des molécules de l'ADN sont clairement différentes de celles de l'eau [27, 28]. Néanmoins, une description détaillée de ces interactions à très basse énergie est très difficile surtout pour les molécules complexes comme l'ADN et n'est toujours pas disponible dans les codes de simulations. Des études fondamentales qui cherchent à développer des modèles théoriques pour une description exacte des processus particules-matière biologique qui couvrent la totalité des régions énergétiques avec les énergies intermédiaires et les basses énergies sont essentielles pour des simulations correctes des dommages induits par les rayonnements ionisants. Nous avons choisi d'étudier l'ionisation par impact d'un électron des molécules complexes qui joue un rôle important dans l'induction des dommages biologiques. Pendant longtemps, il était considéré que les particules primaires de plus haute énergie étaient responsables pour la plus grande partie des dommages induits. Le travail du groupe de Sanche [29] a montré que les électrons de faible énergie sont aussi capables de causer des dommages à l'ADN. Plusieurs études ont suivi pour étudier les interactions des électrons de basse énergie [30–32]. Fournir les sections efficaces pour l'ionisation par impact d'électrons des molécules biologiques est une nécessité pour avoir une description correcte de cette interaction dans les simulations.

Nous avons alors abordé une étude fondamentale qui vise à développer un algorithme pour déterminer les sections efficaces d'ionisation des molécules d'intérêt biologique par impact d'un électron. Nous nous sommes intéressés au calcul des sections

efficaces triplement différentielles qui permettent d'avoir la probabilité d'interaction en fonction de plusieurs paramètres comme par exemple, l'angle suivant lequel l'électron est éjecté après l'ionisation. On s'est basé sur un ancien programme écrit par le professeur Paul-Antoine Hervieux en fortran 90. Nous avons effectué plusieurs tests sur les fonctions et les routines utilisées dans le code et nous les avons utilisées dans le nouveau programme. En première étape, nous avons considéré un modèle simple, basé sur la première approximation de Born selon laquelle l'électron incident et l'électron diffusé sont décrits par des ondes planes et l'électron éjecté est décrit par une onde coulombienne. Pour calculer les fonctions d'ondes des électrons liés la molécule, nous avons utilisé le programme de chimie quantique Gaussian 09 [33] qui fournit les informations nécessaires pour développer des fonctions d'ondes moléculaires multicentriques sur une base de fonctions gaussiennes. La présence de plusieurs centres constitue un défi quand on considère une molécule complexe avec un grand nombre d'atomes et d'électrons et impose des difficultés de calcul. Ces fonctions d'ondes sont alors réduites à des fonctions monocentriques, toutes centrées sur le même origine, grâce à une méthode décrite en détails dans [34] et utilisée dans plusieurs études [35–38]. De plus, les développements en ondes partielles de toutes les fonctions d'ondes sont utilisés, ce qui permet une structure du cadre théorique qui peut être facilement traduite en un programme parallèle. Ces deux outils permettent de réduire le temps de calcul et ainsi d'utiliser ce programme pour générer les sections efficaces d'interaction avec des molécules complexes. Effectivement, un plus grand nombre d'ondes partielles sont nécessaires pour des molécules plus complexes mais la parallélisation du programme permet de faire ces calculs avec le même temps nécessaire pour calculer les sections efficaces d'une molécule simple.

Nous présentons dans un premier temps les résultats pour des molécules simples : l'eau et l'ammoniac. Pour les deux cibles, ainsi que pour l'atome hydrogène, les sections efficaces calculées dans le programme ont été comparées à des sections efficaces calculées par le professeur Claude Dal Cappello pour valider l'algorithme développé. L'approche théorique adoptée dans cet algorithme a été utilisée auparavant pour des molécules simples comme l'eau [39] et des molécules plus complexes comme la thymine [38]. L'originalité de ce travail est que le programme développé possède une structure qui permet à l'utilisateur de l'appliquer facilement à n'importe quelle molécule en indiquant seulement les conditions cinématiques et le modèle théorique à utiliser. En effet, nous sommes en cours d'ajouter la possibilité d'utiliser une onde distordue pour décrire l'électron éjecté au lieu d'une onde coulombienne. Les résultats préliminaires pour l'eau et l'ammoniac avec ce deuxième modèle sont aussi présentés dans cette thèse. Nous pouvons facilement implémenter d'autres méthodes dans le programme afin d'avoir une description complète des interactions dans les régimes d'énergie intermédiaire et basse.

En parallélisant le code avec la méthode *message passing interface* (mpi) [40], nous avons pu calculer les sections efficaces triplement différentielles de quelques molécules plus complexes. Nous avons aussi utilisé la grille de calcul de l'IPHC pour accélérer les calculs et le temps de calcul a été ainsi réduit de plusieurs jours à quelques heures. Nous présentons dans cette thèse les résultats obtenus pour l'acide formique et le tétrahydrofurane. Nos résultats pour l'acide formique ont été publiés

dans *Journal of Physics B: Atomic, Molecular and Optical Physics* [41]. Pour les deux cibles considérées, les seules études théoriques qui ont été faites utilisent l'approximation OAMO (Orientation Averaged Molecular Orbital) [42] qui consiste à faire la moyenne sur les fonctions d'ondes de la molécule et puis calculer une section efficace triplement différentielle unique au lieu de calculer les sections efficaces pour toutes les orientations possibles de la molécule et puis déduire une section efficace moyenne. Cette approximation réduit le temps et la complexité du calcul et permet alors d'appliquer un modèle sophistiqué, comme le modèle M3DW (Molecular 3-body Distorted Wave) [43] qui consiste à décrire tous les électrons par des ondes distordues, pour l'étude des molécules complexes. La méthode OAMO a été utilisée pour déterminer les sections efficaces triplement différentielles de l'ionisation de plusieurs cibles et les études ont montrées que cette approximation n'est pas toujours fiable, et ne réussit que pour certaines symétries [44, 45]. Nos résultats pour les deux cibles sont en meilleur accord avec les mesures expérimentales et mettent en relief l'importance de notre approche qui permet de bien reproduire les sections efficaces même avec un modèle aussi simple que la première approximation de Born.

L'acide formique est l'acide organique le plus simple et il est souvent utilisé comme un modèle pour représenter des molécules biologiques plus complexes comme les protéines et les acides aminés. Il est également considéré comme le catalyseur principal de l'activité enzymatique. On identifie 12 orbitales moléculaires occupées pour l'acide formique ; l'orbitale la plus haute occupée est l'orbitale 10a' et la deuxième orbitale la plus haute occupée est l'orbitale 2a''. Ces deux orbitales sont séparées par environ 1.07 eV ce qui les rends difficilement discriminables. En effet, pour distinguer deux électrons qui proviennent chacun de l'ionisation d'une de ces deux orbitales, la résolution de l'appareil de coïncidence, utilisé dans l'expérience, doit être supérieure à 1.07 eV.

L'expérience qui a été réalisée pour l'acide formique dans le régime d'énergie intermédiaire a été faite avec une résolution de 1.2 eV, supérieure à 1.07 eV [46]. Il en résulte que les sections efficaces présentées dans cette étude pour l'ionisation de l'orbitale 10a' de l'acide formique, contiennent aussi des contributions de l'orbitale 2a''. Des résultats théoriques ont été présentés dans cette même étude avec le modèle M3DW-OAMO [46]. Dans ce modèle, l'électron projectile ainsi que l'électron éjecté sont décrits par des ondes distordues et deux considérations différentes du potentiel d'interaction ont été adoptées. La première consiste à prendre en compte des effets d'échange, de polarisation et de corrélation et il en résulte le modèle M3DW-CPE. La deuxième consiste à considérer uniquement le potentiel statique et le modèle correspondant est noté M3DW. Dans ces deux approches, la moyenne en orientation est effectuée au niveau des fonctions d'ondes moléculaires et donc l'approximation OAMO est utilisée. L'utilisation de cette approximation fait que le modèle n'est applicable qu'à l'orbitale 10a'. La moyenne de la fonction d'onde de 2a'' est nulle à cause de la symétrie de cette orbitale. Par conséquent, les résultats expérimentaux, comprenant la contribution des orbitales 10a' et 2a'' ont été comparés aux sections efficaces calculées pour l'orbitale 10a' seulement.

Avec notre approche basée sur la méthode PA (Proper Average) qui consiste à faire la moyenne des orientations au niveau de la section efficace, on peut obtenir des

résultats pour les deux orbitales 10a’ et 2a’’. Et ainsi on compare la somme des sections efficaces triplement différentielles des deux orbitales calculées selon notre modèle aux résultats expérimentaux comprenant des contributions des deux orbitales. On voit clairement que notre modèle réussit à décrire les résultats expérimentaux. En comparaison avec les résultats M3DW et M3DW-CPE, nous remarquons que notre modèle simple décrit mieux la région binaire ainsi que l’intensité relative de la région de recul. Ceci montre l’importance de faire la moyenne des orientations sur la section efficace et non pas sur la fonction d’onde, et met en question l’utilité et la fiabilité de l’approximation OAMO.

Un autre groupe a récemment calculé ces sections efficaces aussi avec le méthode PA mais en utilisant une onde distordant pour l’électron éjecté [47]. Ce modèle a été noté MCDW pour Multi-Center Distorted Wave et consiste à calculer la fonction distordue à partir d’un potentiel de distorsion isotropique. Ils appuient dans leur étude sur l’intérêt de préserver la nature multicentrique de la molécule et ils obtiennent aussi un bon accord avec l’expérience. Il sera alors intéressant de calculer les sections efficaces triplement différentielles avec notre second modèle (1DW) pour voir plus clairement l’influence de préserver cet aspect. Ils distinguent aussi deux approches pour le potentiel d’interaction et présentent les résultats avec et sans la contribution du noyau. Les modèles correspondants sont notés MCDW-NT et MCDW respectivement. On compare dans la figure 4 nos résultats (en rouge) aux données expérimentales ainsi qu’aux résultats M3DW et MCDW pour l’ionisation des deux couches 2a’’ et 10a’ de l’acide formique.

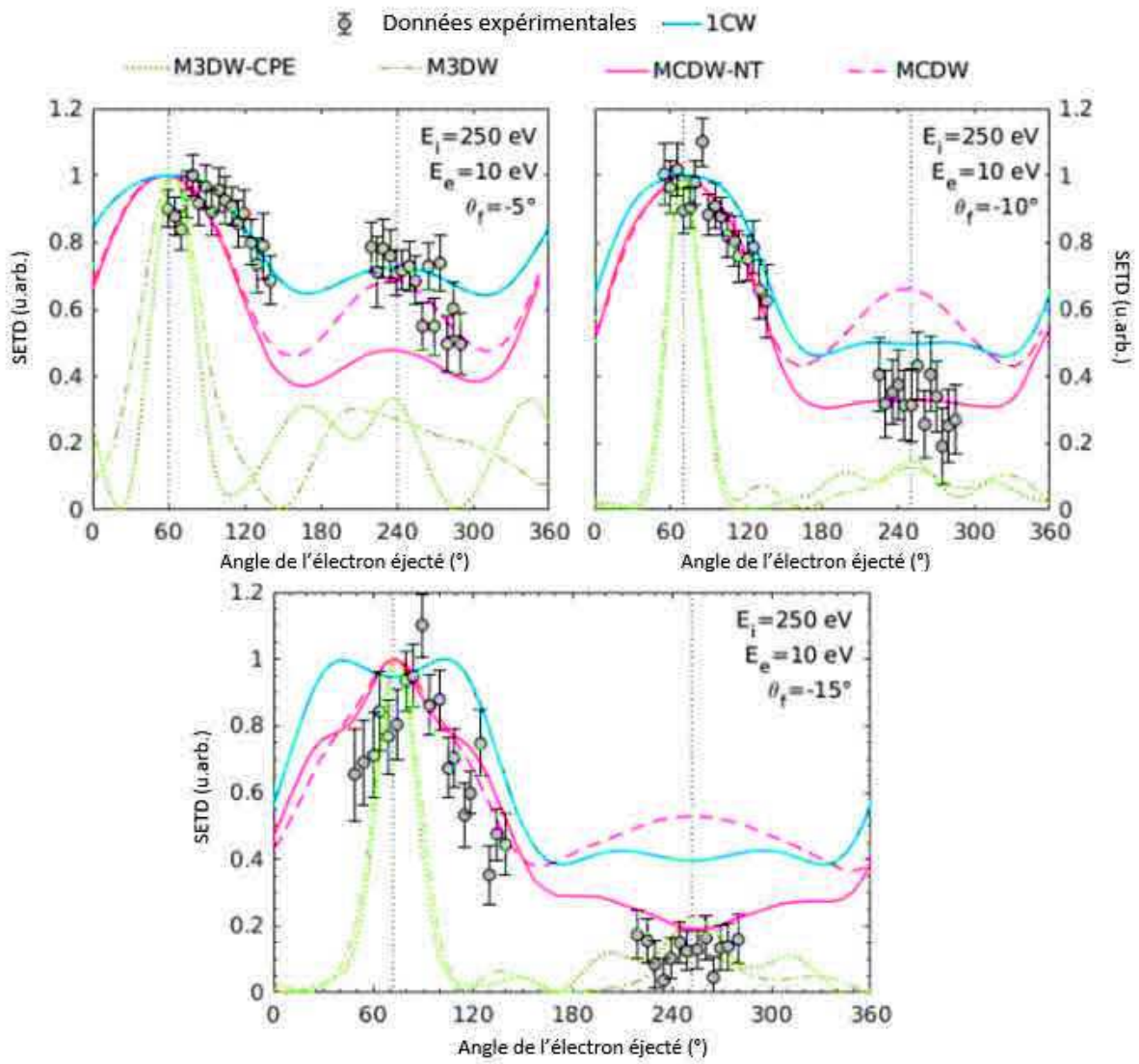

Figure 4: Sections efficaces triplement différentielles de l'ionisation de l'acide formique par impact d'un électron en fonction de l'angle de l'électron éjecté. Les résultats M3DW [46] sont représentés en vert avec deux descriptions différentes du potentiel d'interaction, les résultats MCDW [47] en rouge avec et sans le terme du noyau dans l'amplitude de transition, et nos résultats [41] sont représentés en bleu.

Le tétrahydrofurane est aussi une molécule intéressante pour modéliser des molécules biologiques. En effet, sa structure ressemble à une unité de l'épine dorsale de phosphate-sucre de l'ADN et ce dernier est souvent considéré comme une série de tétrahydrofurane et d'autre éthers cycliques liés aux bases de l'ADN et à des unités de phosphate. Ainsi, déterminer les sections efficaces d'interaction des particules avec le tétrahydrofurane est une étape importante pour pouvoir comprendre les dommages induits par les rayonnements ionisants à l'ADN. Le tétrahydrofurane existe dans trois géométries différentes donc trois isomères du tétrahydrofurane peuvent être identifiés : C_1, C_2, et C_s. Ces isomères sont caractérisés par des symétries différentes comme présenté dans la figure 5.

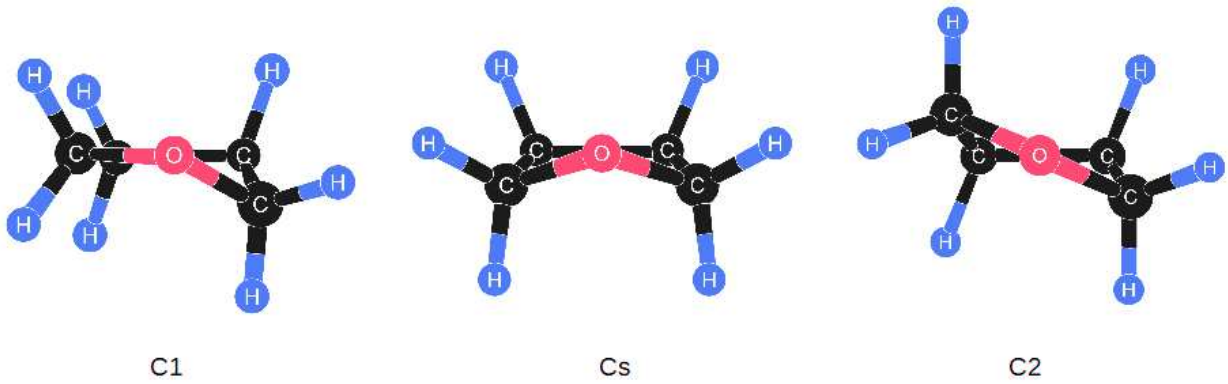

Figure 5: Les trois isomères du tétrahydrofurane: C1 (à droite), Cs (au milieu) et C2 (à gauche).

Plusieurs études ont été faites pour déterminer laquelle de ces géométries est la plus stable et les études expérimentales de très haute résolution et théoriques très précises ont montré que l'isomère C_1 est le moins stable et est un état de transition avec une fréquence imaginaire. De plus, il a été conclu que les deux isomères C_2 et C_s sont également peuplés et coexistent à température ambiante. Les sections efficaces triplement différentielles pour l'ionisation du tétrahydrofurane ont été données dans la littérature pour l'ionisation des orbitales les plus hautes occupées des deux isomères C_2 et C_s : 9b et 12a' respectivement. En effet, les énergies d'ionisation de ces deux orbitales sont très proches : 9.94 eV pour 9b et 9.91 eV pour 12a', et il est impossible de distinguer les électrons provenant de l'ionisation de ces deux orbitales.

Les études expérimentales et théoriques qui visent à déterminer les sections efficaces triplement différentielles ont été aussi effectuées par le groupe qui a appliqué le modèle M3DW pour calculer les sections efficaces triplement différentielles de l'acide formique. Dans cette étude [48], la moyenne des fonctions d'ondes moléculaires est nulle pour les deux orbitales 9b et 12a' et donc ils ont calculé la moyenne de la valeur absolue des fonctions d'ondes moléculaires au lieu de calculer directement la moyenne de ces fonctions d'onde. Le potentiel d'interaction comprend trois parties : un terme statique, un terme d'échange et un terme de corrélation-polarisation. Les sections efficaces obtenues avec ce modèle pour les deux orbitales montrent un pic binaire étroit alors qu'une région binaire plus large et formée par deux pics binaires est identifiée par les données expérimentales. Ceci a été justifié par l'emploi de la méthode OAMO qui produit toujours une distribution en fonction de l'angle qui est du type 's' d'où un pic binaire unique. Dans une autre étude [49], ils ont considéré d'autres conditions cinématiques pour mieux comprendre l'influence de ces conditions sur les sections efficaces obtenues et ont conclu que la distribution du moment en fonction de l'angle éjecté explique bien l'intensité relative entre le pic binaire et le pic de recul. Ils ont également considéré l'influence de la structure de la cible sur la forme des distributions de sections efficaces triplement différentielles et ont présenté dans une autre étude, ces sections efficaces pour deux autres éthers cycliques [50].

Avec notre modèle, on a un meilleur accord avec les données expérimentales dans la région binaire où on a clairement deux pics binaires, et dans la région de recul où l'intensité relative de la section efficace est bien décrite par notre modèle. Ces

résultats sont montrés dans la figure 6 et sont comparés aux résultats M3DW et aux données expérimentales.

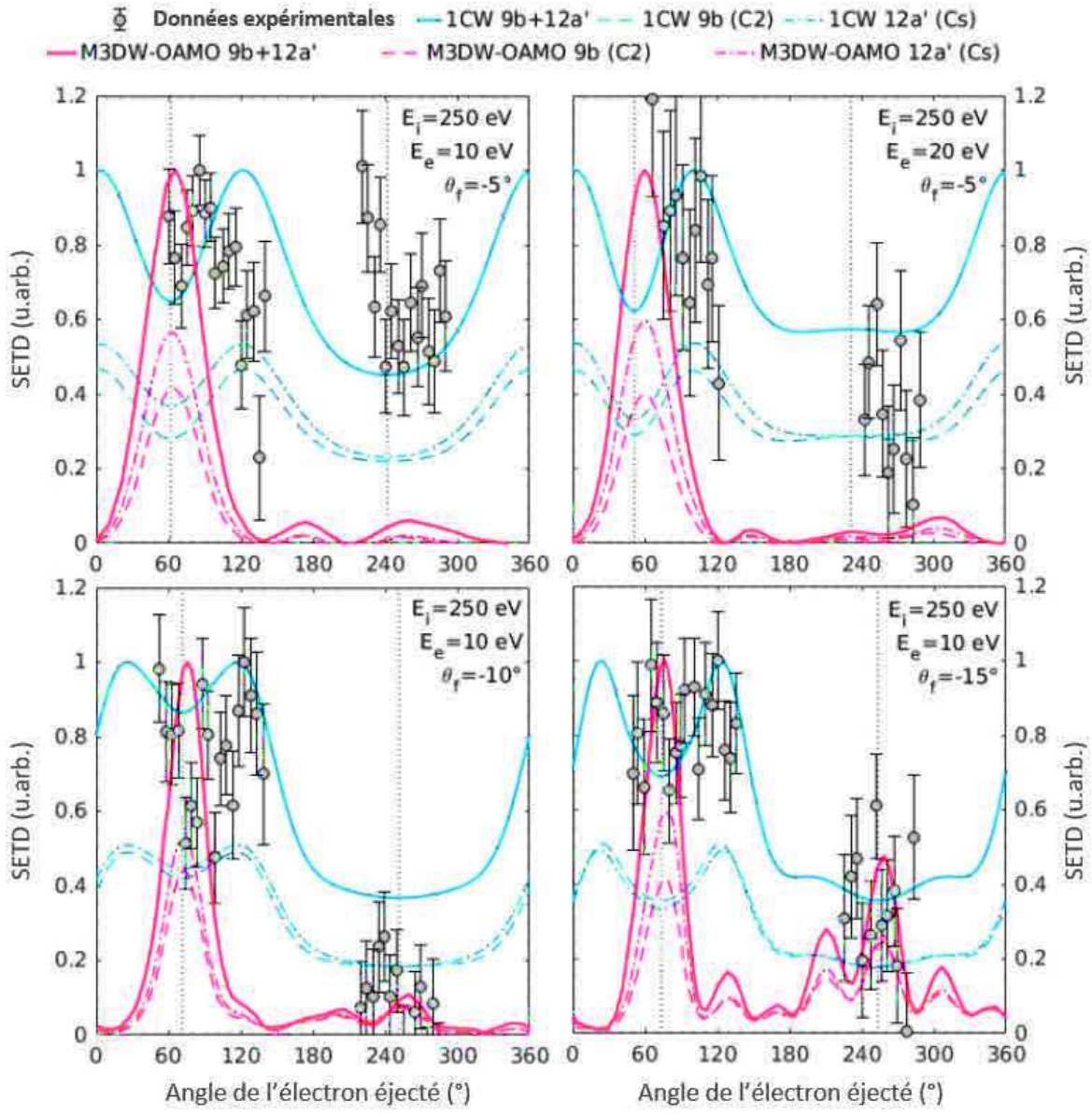

Figure 6: Sections efficaces triplement différentielles de l'ionisation des orbitales les plus hautes occupées des deux isomères C_2 et C_s du tétrahydrofurane. Nos résultats obtenus avec le modèle 1CW sont représentés par les courbes bleues.

Nous avons ainsi montré que notre formalisme réussit à bien décrire l'ionisation par impact d'un électron des molécules simples ainsi que complexes. Ce travail ne constitue que la première étape de développement et validation du programme dans un formalisme simple, et présente plusieurs perspectives parmi lesquels l'implémentation des modèles théoriques plus sophistiqués. Nous avons considéré des conditions d'énergie qui conviennent au modèle 1CW, basé sur la première approximation de Born. Pour pouvoir bien décrire l'ionisation dans des régimes d'énergies plus basses, un modèle plus sophistiqué doit être adopté. Nous avons alors pour but de développer des modèles théoriques convenables pour d'autres régimes énergétiques tels que le modèle 1DW que nous avons déjà ajouté au programme.

Une autre perspective de ce travail est d'appliquer les modèles 1CW et 1DW pour l'étude de molécule complexes comme les bases de l'ADN et les protéines. Les applications de ce programme sont nombreuses surtout parce qu'il permet de calculer les sections efficaces de n'importe quelle molécule. On cite par exemple des applications possibles en dosimétrie moléculaire [51].

Les sections efficaces simplement et doublement différentielles ainsi que les sections efficaces totales pourrons aussi être déterminées par intégration. Et ces sections efficaces pourront être implémenté dans les codes de simulation et permettrons d'avoir des simulations plus correctes des interactions des particules dans le milieu biologique et alors des résultats plus exacts.

Plus généralement, le but ultime de ce travail sera de créer une base de données en accès libre où les sections efficaces d'ionisation par impact d'un électron sont générées pour plusieurs molécules et dans des conditions cinématiques choisies par l'utilisateur.

Références:

[1] H. Nikjoo, S. Uehara, D. Emfietzoglou, and F. A. Cucinotta, "Track-structure codes in radiation research," Radiation Measurements, vol. 41, no. 9, pp. 1052–1074, 2006.

[2] B. Alberts, D. Bray, A. Johnson, J. Lewis, M. Ra, K. Roberts, P. Walter, and D. S. Latchman, "Essential Cell Biology: An Introduction to the Molecular Biology of the Cell," Trends in Biochemical Sciences, vol. 23, no. 7, pp. 268–268, 1998.

[3] I. El Naqa, P. Pater, and J. Seuntjens, "Monte Carlo role in radiobiological modelling of radiotherapy outcomes," Physics in Medicine and Biology, vol. 57, no. 11, p. R75, 2012.

[4] G. Battistoni, F. Cerutti, A. Fassò, A. Ferrari, S. Muraro, J. Ranft, S. Roesler, and P. R. Sala, "The FLUKA code: description and benchmarking," AIP Conference Proceedings, vol. 896, no. 1, pp. 31–49, 2007.

[5] S. Agostinelli, J. Allison, K. a. Amako, J. Apostolakis, H. Araujo, P. Arce, M. Asai, D. Axen, S. Banerjee, G. Barrand, et al., "GEANT4—a simulation toolkit," Nuclear instruments and methods in physics research section A: Accelerators, Spectrometers, Detectors and Associated Equipment, vol. 506, no. 3, pp. 250–303, 2003.

[6] W. Friedland, M. Dingfelder, P. Kundrát, and P. Jacob, "Track structures, DNA targets and radiation effects in the biophysical Monte Carlo simulation code PARTRAC," Mutation Research/Fundamental and Molecular Mechanisms of Mutagenesis, vol. 711, no. 1, pp. 28–40, 2011.

[7] J. Allison, K. Amako, J. Apostolakis, H. Araujo, P. A. Dubois, M. Asai, G. Barrand, R. Capra, S. Chauvie, R. Chytracek, et al., "Geant4 developments and applications," IEEE Transactions on Nuclear Science, vol. 53, no. 1, pp. 270–278, 2006.

[8] D. Strulab, G. Santin, D. Lazaro, V. Breton, and C. Morel, “Gate (geant4 Application for Tomographic Emission): a PET/SPECT general-purpose simulation platform,” Nuclear Physics B-Proceedings Supplements, vol. 125, pp. 75–79, 2003.

[9] P. Marchand, A. Ouadi, M. Pellicioli, and D. Brasse, “Cyrcé, un cyclotron pour la recherche et l’enseignement en alsace,” L’Actualité Chimique, vol. 386, pp. 9–14, 2014.

[10] L. Mouawad, M. Rousseau, D. Brasse, Z. El Bitar, A. Osman, M. Khalil, and Z. Francis, “Beam shaping systems for small animal proton therapy,” in Advances in Biomedical Engineering (ICABME), 2015 International Conference on, pp. 174–177, IEEE, 2015.

[11] H. Paganetti, Proton therapy physics. CRC Press, 2016.

[12] H. Nikjoo, C. E. Bolton, R. Watanabe, M. Terrissol, P. O’Neill, and D. T. Goodhead, “Modelling of DNA damage induced by energetic electrons (100 eV to 100 KeV),” Radiation protection dosimetry, vol. 99, no. 1-4, pp. 77–80, 2002.

[13] L. Zhang and Z. Tan, “A new calculation on spectrum of direct DNA damage induced by low-energy electrons,” Radiation and environmental biophysics, vol. 49, no. 1, pp. 15–26, 2010.

[14] W. Friedland, P. Jacob, P. Bernhardt, H. G. Paretzke, and M. Dingfelder, “Simulation of DNA damage after proton irradiation,” Radiation research, vol. 159, no. 3, pp. 401–410, 2003.

[15] S. Incerti, G. Baldacchino, M. Bernal, R. Capra, C. Champion, Z. Francis, P. Guèye, A. Mantero, B. Mascialino, P. Moretto, et al., “The geant4-DNA project,” International Journal of Modeling, Simulation, and Scientific Computing, vol. 1, no. 02, pp. 157–178, 2010.

[16] D. T. Goodhead, “Initial events in the cellular effects of ionizing radiations: clustered damage in DNA,” International journal of radiation biology, vol. 65, no. 1, pp. 7–17, 1994.

[17] P. O’Neill, “The chemical basis of radiation biology,” International Journal of Radiation Biology and Related Studies in Physics, Chemistry and Medicine, vol. 52, no. 6, pp. 976–976, 1987.

[18] D. Frankenberg, M. Frankenberg-Schwager, D. Blöcher, and R. Harbich, “Evidence for DNA Double-Strand Breaks as the Critical Lesions in Yeast Cells Irradiated with Sparsely or Densely Ionizing Radiation under Oxic or Anoxic Conditions,” Radiation Research, vol. 88, no. 3, pp. 524–532, 1981.

[19] P. Bryant, “Enzymatic restriction of mammalian cell DNA: evidence for double-strand breaks as potentially lethal lesions,” International Journal of Radiation Biology and Related Studies in Physics, Chemistry and Medicine, vol. 48, no. 1, pp. 55–60, 1985.

[20] M. Dos Santos, C. Villagrasa, I. Clairand, and S. Incerti, “Influence of the DNA density on the number of clustered damages created by protons of different energies,”

Nuclear Instruments and Methods in Physics Research Section B: Beam Interactions with Materials and Atoms, vol. 298, pp. 47–54, 2013.

[21] M. Tajik, A. S. H. Rozatian, and F. Semsarha, “Simulation of ultrasoft x-rays induced DNA damage using the Geant4 Monte Carlo toolkit,” Nuclear Instruments and Methods in Physics Research Section B: Beam Interactions with Materials and Atoms, vol. 342, pp. 258–265, 2015.

[22] S. Incerti, C. Champion, H. N. Tran, M. Karamitros, M. Bernal, Z. Francis, V. Ivanchenko, A. Mantero, et al., “Energy deposition in small-scale targets of liquid water using the very low energy electromagnetic physics processes of the Geant4 toolkit,” Nuclear Instruments and Methods in Physics Research Section B: Beam Interactions with Materials and Atoms, vol. 306, pp. 158–164, 2013.

[23] P. Bernhardt, W. Friedland, P. Jacob, and H. Paretzke, “Modeling of ultrasoft x-ray induced DNA damage using structured higher order DNA targets,” International Journal of Mass Spectrometry, vol. 223, pp. 579–597, 2003.

[24] W. Friedland, M. Dingfelder, P. Jacob, and H. G. Paretzke, “Calculated DNA double- strand break and fragmentation yields after irradiation with He ions,” Radiation Physics and Chemistry, vol. 72, no. 2, pp. 279–286, 2005.

[25] M. Ester, H.-P. Kriegel, J. Sander, X. Xu, et al., “A density-based algorithm for discovering clusters in large spatial databases with noise.,” in Kdd, vol. 96, pp. 226–231, 1996.

[26] Z. Francis, C. Villagrasa, and I. Clairand, “Simulation of DNA damage clustering after proton irradiation using an adapted DBSCAN algorithm,” Computer methods and programs in biomedicine, vol. 101, no. 3, pp. 265–270, 2011.

[27] P. Bernhardt and H. G. Paretzke, “Calculation of electron impact ionization cross sections of DNA using the Deutsch–Märk and Binary-Encounter-Bethe formalisms,” International Journal of Mass Spectrometry, vol. 223, pp. 599–611, 2003.

[28] I. Plante and F. A. Cucinotta, “Binary-Encounter-Bethe ionisation cross sections for simulation of DNA damage by the direct effect of ionising radiation,” Radiation protection dosimetry, vol. 166, no. 1-4, pp. 19–23, 2015.

[29] B. Boudaifa, P. Cloutier, D. Hunting, M. A. Huels, and L. Sanche, “Resonant formation of DNA strand breaks by low-energy (3 to 20 eV) electrons,” Science, vol. 287, no. 5458, pp. 1658–1660, 2000.

[30] R. Barrios, P. Skurski, and J. Simons, “Mechanism for damage to DNA by low-energy electrons,” The Journal of Physical Chemistry B, vol. 106, no. 33, pp. 7991–7994, 2002.

[31] X. Pan and L. Sanche, “Mechanism and site of attack for direct damage to DNA by low-energy electrons,” Physical review letters, vol. 94, no. 19, p. 198104, 2005.

[32] J. Berdys, I. Anusiewicz, P. Skurski, and J. Simons, “Damage to model DNA fragments from very low-energy (< 1 eV) electrons,” Journal of the American Chemical Society, vol. 126, no. 20, pp. 6441–6447, 2004.

[33] M. Frisch, G. Trucks, H. Schlegel, G. Scuseria, M. Robb, J. Cheeseman, G. Scalmani, V. Barone, B. Mennucci, G. Petersson, et al., “Gaussian 09, revision a, gaussian,” Inc., Wallingford CT, 2009.

[34] K. Kaufmann and W. Baumeister, “Single-centre expansion of gaussian basis functions and the angular decomposition of their overlap integrals,” Journal of Physics B: Atomic, Molecular and Optical Physics, vol. 22, no. 1, p. 1, 1989.

[35] H. Hafied, A. Eschenbrenner, C. Champion, M. F. Ruiz-Lopez, C. Dal Cappello, I. Charpentier, and P. A. Hervieux, “Electron momentum spectroscopy of the valence orbitals of the water molecule in gas and liquid phase: A comparative study,” Chemical physics letters, vol. 439, no. 1, pp. 55–59, 2007.

[36] C. Dal Cappello, P. A. Hervieux, I. Charpentier, and M. F. Ruiz-Lopez, “Ionization of the cytosine molecule by protons: Ab initio calculation of differential and total cross sections,” Physical Review A, vol. 78, no. 4, p. 042702, 2008.

[37] C. Dal Cappello, I. Charpentier, S. Houamer, P. A. Hervieux, M. F. Ruiz-Lopez, A. Mansouri, and A. C. Roy, “Triple-differential cross sections for the ionization of thymine by electrons and positrons,” Journal of Physics B: Atomic, Molecular and Optical Physics, vol. 45, no. 17, p. 175205, 2012.

[38] C. Dal Cappello, Z. Rezkallah, S. Houamer, I. Charpentier, A. C. Roy, P. A. Hervieux, and M. F. Ruiz-Lopez, “Ionization of thymine by electron impact: investigation of inner shell orbitals,” European Physics Journal D, vol. 67, no. 6, p. 117, 2013.

[39] H. D. Hafied, Etude théorique de l’ionisation par impact électronique des molécules d’eau en phase gazeuse et liquide. PhD thesis, Université de Metz, 2007.

[40] W. Gropp, E. Lusk, and A. Skjellum, Using MPI: portable parallel programming with the message-passing interface, vol. 1. MIT press, 1999.

[41] L. Mouawad, P. A. Hervieux, C. Dal Cappello, J. Pansanel, A. Osman, M. Khalil, and Z. El Bitar, “Triple differential cross sections for the ionization of formic acid by electron impact,” Journal of Physics B: Atomic, Molecular and Optical Physics, 2017.

[42] J. Gao, J. L. Peacher, and D. H. Madison, “An elementary method for calculating orientation-averaged fully differential electron-impact ionization cross sections for molecules,” The Journal of chemical physics, vol. 123, no. 20, p. 204302, 2005.

[43] J. Gao, D. H. Madison, and J. L. Peacher, “Distorted wave Born and three-body distorted wave Born approximation calculations of the fully differential cross section for electron-impact ionization of nitrogen molecules,” The Journal of Chemical Physics, vol. 123, no. 20, p. 204314, 2005.

[44] H. Chaluvadi, C. G. Ning, and D. H. Madison, “Theoretical triple-differential cross sections of a methane molecule by a proper-average method,” Physical Review A, vol. 89, no. 6, p. 062712, 2014.

[45] E. Ali, K. L. Nixon, A. Murray, C. G. Ning, J. Colgan, and D. H. Madison, “Comparison of experimental and theoretical electron-impact-ionization triple-differential cross sections for ethane,” Physical Review A, vol. 92, p. 042711, 2015.

[46] C. J. Colyer, M. A. Stevenson, O. Al-Hagan, D. H. Madison, C. G. Ning, and B. Lohmann, “Dynamical (e, 2e) studies of formic acid,” *Journal of Physics B: Atomic, Molecular and Optical Physics*, vol. 42, no. 23, p. 235207, 2009.

[47] X. Li, M. Gong, L. Liu, Y.Wu, J.Wang, Y. Qu, and X. Chen, “Calculation of (e, 2e) triple-differential cross sections of formic acid: An application of the multicenter distorted-wave method,” *Phys. Rev. A*, vol. 95, p. 012703, Jan 2017.

[48] C. J. Colyer, S. M. Bellm, B. Lohmann, G. F. Hanne, O. Al-Hagan, D. H. Madison, and C. G. Ning, “Dynamical (e, 2e) studies using tetrahydrofuran as a DNA analog,” *The Journal of chemical physics*, vol. 133, no. 12, p. 124302, 2010.

[49] D. B. Jones, J. D. Builth-Williams, S. M. Bellm, L. Chiari, H. Chaluvadi, D. H. Madison, C. G. Ning, B. Lohmann, O. Ingólfsson, and M. J. Brunger, “Dynamical (e, 2e) investigations of tetrahydrofuran and tetrahydrofurfuryl alcohol as DNA analogues,” *Chemical Physics Letters*, vol. 572, pp. 32–37, 2013.

[50] J. D. Builth-Williams, S. M. Bellm, L. Chiari, P. A. Thorn, D. B. Jones, H. Chaluvadi, D. H. Madison, C. G. Ning, B. Lohmann, G. B. Da Silva, *et al.*, “A dynamical (e, 2e) investigation of the structurally related cyclic ethers tetrahydrofuran, tetrahydropyran, and 1,4-dioxane,” *The Journal of chemical physics*, vol. 139, no. 3, p. 034306, 2013.

[51] V. E. Walker, T. R. Fennell, P. B. Upton, J. P. MacNeela, and J. A. Swenberg, “Molecular dosimetry of DNA and hemoglobin adducts in mice and rats exposed to ethylene oxide.,” Environmental health perspectives, vol. 99, p. 11, 1993.

Table of Contents

Introduction

The biological effects of ionizing radiation are still not well understood due to the complexity of the involved damage and repair mechanisms and the diversity of the traversed biological medium. Monte Carlo simulations, based on the generation of random numbers to reproduce the stochastic nature of particle interactions, have been proven to be the best tool to investigate the damage induced by ionizing radiation [1]. According to the application, only selected processes are explicitly simulated in order to achieve an acceptable compromise between execution time and the acquired precision. Accurate modeling of low energy secondary particle interactions is of great importance in studies of biological damage. For a long time, it was thought that the primary particles carrying the most energy are the main actors in the damage process. However, the work of *Sanche and coworkers* [2] showed that secondary species and particles with energy even below the ionization threshold can induce important damage to the DNA. Low energy electrons produced through the ionization of biological molecules are responsible for almost two third of the induced damage [3]. These findings initiated much work to investigate the interactions of low energy electrons [4–6], with a focus on the electron ionization process through which they are produced [7]. In some Monte Carlo codes, the interactions of secondary particles are simulated after every step by calculating the energy loss distribution of primary particles [8, 9]. In others, a more detailed view of these interactions is offered and secondary particle interactions are explicitly simulated [10]. Biological matter is often modeled by water volumes in Monte Carlo simulations and the cross sections for particle interactions with biological molecules are approximated by interaction cross sections with water, since water is the main constituent of the biological medium. These cross sections are obtained through experimental and theoretical studies and are implemented in Monte Carlo codes either through analytical models that are applicable in particular energy ranges or in the form of extrapolated data tables.

The fundamental research that is being carried out in parallel to provide these cross sections allows to continuously update and improve Monte Carlo codes. According to some studies, there is a non-negligible difference between the cross sections of water and those of DNA bases especially in the low energy range [11–13]. Providing interaction cross sections for molecules of biological interest has become an urgent requirement for valid simulations of biological damage. Evaluating triple differential cross sections is particularly interesting because this quantity involves all kinematical parameters and therefore provides the most details about the ionization dynamics. Many experimental and theoretical challenges make it a hard task to determine these cross sections especially for complex molecules such as DNA bases. It is also important to note that the biological medium is composed of various species and using the different interaction cross sections for each elementary entity instead

of using water cross sections for the entire targeted volume could significantly improve the accuracy of the simulations. Providing the cross sections for the components of the biological medium is essential to keep up with the developments of Monte Carlo codes and allow further improvements.

The main purpose of this thesis is to develop an algorithm that can determine the triple differential cross sections for the electron ionization of any molecule, including biological molecules, in any chosen kinematical setting. Specific tools are used to overcome the analytical and computing difficulties that are posed by the complex nature of bio-molecules. Another asset of this algorithm is that it is "user friendly" and can be easily adapted for low, intermediate and high energy regimes. This work presents interests for many fields since the developed algorithm can be used for any molecule. Providing cross sections for the electron ionization of biological molecules for Monte Carlo codes is only one of its many possible applications.

Monte Carlo codes offer the possibility to simulate particle interactions with biological matter at different levels of accuracy according to the desired application. These interactions can be simulated down to the DNA scale by using a detailed description of the low energy processes and identifying track structures in small volumes. In some codes, sophisticated models of the DNA [14–17] as well as descriptions of complex repair processes [18] have been implemented to have the best modeling of the biological effects at the sub-cellular level. On the other end of the spectrum, Monte Carlo simulations have been extensively used in macroscopic applications where the absorbed dose in a volume of the size of an organ or a tumor can be predicted for radiotherapy treatment planning [19]. Treatment planning precedes any radiotherapy treatment and relies on dose calculation engines to set up the beam properties and irradiation conditions in a way to deliver a high dose to the tumor while protecting neighboring structures. The scope of this thesis was initially oriented towards optimizing a radiotherapy treatment plan using Monte Carlo simulations and we only briefly discuss the initial work that was done in this respect in the following chapters. The work presented here is focused on a micro-dosimetry study of the subsequent biological damage by performing Monte Carlo simulations at the sub-cellular level, and deals in more details with a fundamental approach to study particle interactions with biological matter considering the electron ionization process.

The aim of this thesis was originally to develop a proton therapy treatment plan for small animals. The motivation for this work was the installation of the Cyrcé cyclotron at IPHC (Institut Pluridisciplinaire Hubert Curien) [20] which is able to deliver a proton beam up to 24 MeV energy, convenient for small animal applications, as well as the availability of a small animal facility at the Imabio group of IPHC. Proton therapy offers very precise ballistics allowing to deliver a high dose to the tumor while little dose is deposited in neighboring structures [21]. As the protons travel through a medium, they slowly transfer their energy to its constituents and deposit most of their energy right before they stop. The absorbed dose distribution in function of the traveled distance presents a low entrance dose with a narrow peak, known as the Bragg peak, at a certain distance from the surface and followed by a sharp fall off at the end of which the protons stop having lost all of their energy. To cover the entire tumor depth, a Spread Out Bragg Peak (SOBP) is formed from multiple narrow Bragg peaks created at different depths along the direction of the beam as presented in figure 1. The depth at which the peak occurs, known as the range, is directly related to the energy of the beam [22].

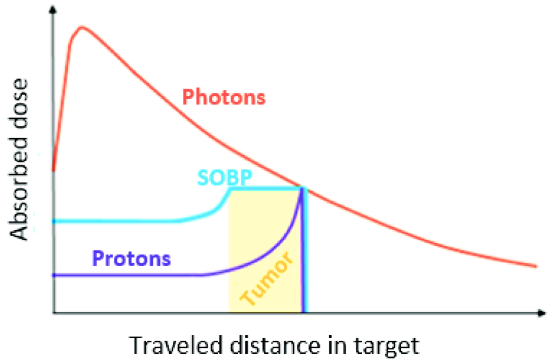

Figure 1: The dose deposited in the target as a function of the traveled distance by a beam of protons, represented by the Bragg peak (purple), and by photons (orange). The spread out Bragg peak (SOBP) is formed to cover the entire tumor depth (blue) with protons of different energies.

Preclinical research utilizing small animal models is of great importance in cancer research bridging the gap between cell experiments and clinical implementation. Small animal studies are a useful tool to evaluate treatment plans and test novel techniques before their use for human radiotherapy. A higher precision is required for small animal subjects and additional challenges are imposed for the irradiation technique [23], beam shaping system [24, 25], as well as the imaging systems that are used [26]. Many small animal radiotherapy platforms are currently available worldwide, providing small animal models to accelerate the development and evaluation of new radiotherapy techniques [27], and small animal treatment plans are designed to optimize dose delivery [28]. The optimization of the beam shaping system and of the beam characteristics and irradiation settings were studied but are only briefly presented hereafter.

Particular focus was concerned with the choice of a beam shaping system that enables a dose deposit within a spherical shape of 5 millimeters diameter representing a small animal tumor. Different models of range compensators made out of individual layers of varying thicknesses were proposed and the resultant dose profile was simulated with the Geant4 Application for Tomographic Emission (GATE) [29] Monte Carlo code. Examples of these models are given in figure 2.

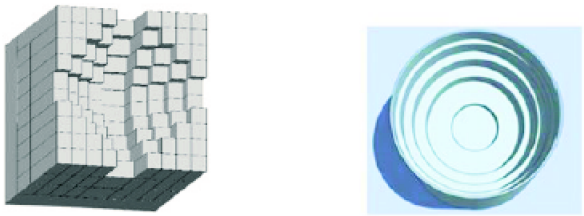

Figure 2: Range compensator models that can be used to create energy loss in the incoming beam of protons in a way to deposit dose along a spherical distal shape.

Indeed, the intended passive scattering irradiation technique is not adequate for achieving a spherical dose profile. The relevance of designing a beam shaping system dedicated for spherical tumors with such a simple irradiation technique was questioned since tumors are very unlikely to be perfectly spherical. Consequently, a simpler approach was chosen and consists in inserting attenuators of different thicknesses between the source and the target to control the dose deposit in a way to cover a 5 millimeters depth. The three dimensional study was reduced to a one dimensional optimization of the dose profile [30]. Different materials were proposed and an algorithm was developed to optimize the number of individual slabs and their thicknesses in function of the desired accuracy on the prescribed dose. A homogeneous dose was ensured along the direction of the beam by controlling the irradiation duration through each attenuator. An example is given in figure 3 illustrating the obtained dose profile through the irradiation of a water volume with the 24 MeV proton beam using 21 Plexiglas attenuators.

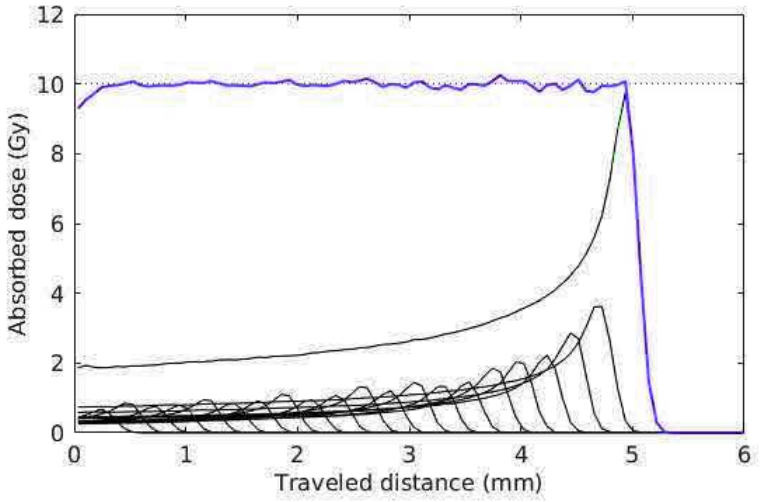

Figure 3: Spread out Bragg peak (purple) created after 21 irradiations through Plexiglass attenuators of different thicknesses in a way to have a deposited dose of 10 ±0.08 Gy along a 5 millimeters distance within a water volume. The horizontal dotted line indicates a deposited dose of 10 Gy.

The corresponding experimental work was not performed in the framework of this thesis which objectives deviated towards an investigation of the induced damage at the DNA level and the underlying fundamental considerations allowing simulations of biological damage.

The absorbed dose homogeneity along the tumor depth is often used to characterize the efficiency of the treatment and optimize the irradiation conditions which are adjusted in a way to deliver a prescribed dose to the targeted volume. A more biologically relevant parameter would certainly give a more truthful estimation of the induced biological damage. The response of the irradiated medium depends not only on the absorbed dose but also on other factors, such as radiation quality and the nature of the target. The required dose is different for different radiation types producing the same biological response. The relative biological effectiveness (RBE) was introduced as a measure of the relative effectiveness of a specific type of ionizing radiation in producing a biological effect, in comparison to

an arbitrary chosen other type of ionizing radiation [31–33]. It was initially proposed to make use of the available experience in photon treatments to determine the prescribed dose for other particle and ion treatments [34, 35]. For example, the RBE for a particular proton beam is calculated as the ratio of the required doses from a photon beam and from this proton beam, to reach the same biological effect [36, 37]. This concept of the RBE in function of the absorbed dose assumes a homogenous energy deposition in the considered volume. At the microscopic level, this approximation is fortuitous since the energy is transferred to a non-homogenous medium and hence the energy deposition is distributed in a non-homogenous pattern. The absorbed dose does not indicate the exact distribution of the energy deposition events. The localization of the energy deposits can only be well identified at the microscopic scale by examining clusters of energy deposits. The biological endpoint that was most studied is cell survival [38–40]. Other biological endpoints were also investigated such as chromosome aberrations [41, 42] and DNA strand breaks [43, 44].

In order to investigate the damage induced by ionizing radiation at the cellular and molecular level, a new research field emerged: micro-dosimetry [45], proposing alternative approaches to absorbed-dose based treatment planning. Micro-dosimetry provides a microscopic view of the energy deposition events taking place in the macroscopic biological volume. The absorbed dose describes the mean energy transferred to a macroscopic volume. Nonetheless, each particle interacts with the medium individually, creating clusters of deposited energy in microscopic volumes making up the target. The dosimetry parameters are thus replaced by new parameters that allow the investigation of the biological damage patterns at the microscopic scale rather than describing the damage process from a macroscopic viewpoint. Instead of determining the amount of energy transferred to the medium per unit length (LET) to quantify radiation quality, the lineal energy (y) [46] is calculated as the energy imparted to a given volume of the medium by a single energy deposition event, divided by the mean chord length of the volume $\bar{l}$. The mean chord length for a convex surface is given by $4\frac{V}{s}$ where V is the considered volume and S its surface [47]. Owing to the stochastic nature of the interactions leading to energy loss, the lineal energy is indeed more relevant to characterize track structures on molecular and sub-cellular scales. The probability density distributions of the lineal energy were compared to LET values for different particle types as a function of the target dimensions [48] and it was concluded that while the LET is invariant with volume size, the lineal energy has clearly more relevance when the volume dimensions decrease. In such volumes, the interactions of secondary particles are important but missing from the LET calculations since the LET is centered on the primary particle track. Moreover, the specific energy, which is the sum of all energies imparted to the considered volume by unit of mass, replaces the absorbed dose in micro-dosimetry [45] and the average specific energy is equal to the absorbed dose when the radiation field and the medium are both uniform. Monte Carlo codes can provide the track structure and energy deposition patterns that are essential for micro-dosimetry studies of DNA damage. In micro-dosimetry simulations, the macroscopic volume is split into microscopic structures where the dose deposition events are mapped to identify the damage clusters. Appropriate physics processes down to a few electron volts allow to track primary and secondary particles along their path and simulate all their interactions.

In **chapter 1**, we consider a micro-dosimetry application where we investigate the bio-

logical damage induced by the 24 MeV proton beam in a liquid water volume and that by calculating the DNA strand break yields. In **chapter 2**, we discuss the fundamental considerations for simulations of biological damage and the theoretical and experimental approaches to determine the cross sections of electron ionization. The theoretical framework used to calculate triple differential cross sections, providing the most detailed view of the ionization dynamics, is presented in **chapter 3**. The first results obtained with the developed algorithm for simple targets (the hydrogen atom, water and ammonia molecules) are given in **chapter 4**. More complex molecules are considered in **chapter 5** where we provide the calculated cross sections for formic acid and tetrahydrofuran. We finally conclude on our work and also discuss the improvements that will be done and the perspectives that this work offers. One of these applications is to calculate the cross sections for the DNA bases and implement them in Geant4 for more precise simulations of biological damage.

References

[1] I. El Naqa, P. Pater, and J. Seuntjens, "Monte Carlo role in radiobiological modelling of radiotherapy outcomes," *Physics in Medicine and Biology*, vol. 57, no. 11, p. R75, 2012.

[2] B. Boudaiffa, P. Cloutier, D. Hunting, M. A. Huels, and L. Sanche, "Resonant formation of DNA strand breaks by low-energy (3 to 20 eV) electrons," *Science*, vol. 287, no. 5458, pp. 1658–1660, 2000.

[3] B. D. Michael and P. O'neill, "A sting in the tail of electron tracks," *Science*, vol. 287, no. 5458, pp. 1603–1604, 2000.

[4] R. Barrios, P. Skurski, and J. Simons, "Mechanism for damage to DNA by low-energy electrons," *The Journal of Physical Chemistry B*, vol. 106, no. 33, pp. 7991–7994, 2002.

[5] X. Pan and L. Sanche, "Mechanism and site of attack for direct damage to DNA by low-energy electrons," *Physical review letters*, vol. 94, no. 19, p. 198104, 2005.

[6] J. Berdys, I. Anusiewicz, P. Skurski, and J. Simons, "Damage to model DNA fragments from very low-energy (< 1 eV) electrons," *Journal of the American Chemical Society*, vol. 126, no. 20, pp. 6441–6447, 2004.

[7] T. D. Märk and G. H. Dunn, *Electron impact ionization*. Springer Science & Business Media, 2013.

[8] J. F. Briesmeister *et al.*, "MCNPTM-A general Monte Carlo N-particle transport code," *Version 4C, LA-13709-M, Los Alamos National Laboratory*, p. 2, 2000.

[9] M. J. Berger and S. M. Seltzer, "Etran," *Monte Carlo code system for electron and photon transport through extended media Documentation for RSIC Computer Package CCC-107*, 1973.

[10] J. Allison, K. Amako, J. Apostolakis, H. Araujo, P. A. Dubois, M. Asai, G. Barrand, R. Capra, S. Chauvie, R. Chytracek, *et al.*, "Geant4 developments and applications," *IEEE Transactions on Nuclear Science*, vol. 53, no. 1, pp. 270–278, 2006.

[11] P. Bernhardt and H. G. Paretzke, "Calculation of electron impact ionization cross sections of DNA using the Deutsch–Märk and Binary-Encounter-Bethe formalisms," *International Journal of Mass Spectrometry*, vol. 223, pp. 599–611, 2003.

[12] I. Plante and F. A. Cucinotta, "Binary-Encounter-Bethe ionisation cross sections for simulation of DNA damage by the direct effect of ionising radiation," *Radiation protection dosimetry*, vol. 166, no. 1-4, pp. 19–23, 2015.

[13] Z. Francis, Z. El Bitar, S. Incerti, M. A. Bernal, M. Karamitros, and H. N. Tran, "Calculation of lineal energies for water and DNA bases using the Rudd model cross sections integrated within the Geant4-DNA processes," *Journal of Applied Physics*, vol. 122, no. 1, p. 014701, 2017.

[14] V. Michalik and M. Běgusova, "Target model of nucleosome particle for track structure calculations and DNA damage modelling," *International journal of radiation biology*, vol. 66, no. 3, pp. 267–277, 1994.

[15] H. Nikjoo and P. Girard, "A model of the cell nucleus for DNA damage calculations," *International journal of radiation biology*, vol. 88, no. 1-2, pp. 87–97, 2012.

[16] W. Friedland, M. Dingfelder, P. Kundrát, and P. Jacob, "Track structures, DNA targets and radiation effects in the biophysical Monte Carlo simulation code PARTRAC," *Mutation Research/Fundamental and Molecular Mechanisms of Mutagenesis*, vol. 711, no. 1, pp. 28–40, 2011.

[17] M. A. Bernal and J. A. Liendo, "An investigation on the capabilities of the penelope mc code in nanodosimetry," *Medical physics*, vol. 36, no. 2, pp. 620–625, 2009.

[18] W. Friedland, P. Jacob, and P. Kundrat, "Mechanistic simulation of radiation damage to DNA and its repair: on the track towards systems radiation biology modelling," *Radiation protection dosimetry*, vol. 143, no. 2-4, pp. 542–548, 2010.

[19] J. Seco and F. Verhaegen, *Monte Carlo techniques in radiation therapy*. CRC press, 2013.

[20] P. Marchand, A. Ouadi, M. Pellicioli, and D. Brasse, "Cyrcé, un cyclotron pour la recherche et l'enseignement en alsace," *L'Actualité Chimique*, vol. 386, pp. 9–14, 2014.

[21] H. Paganetti, *Proton therapy physics*. CRC Press, 2016.

[22] T. Bortfeld and W. Schlegel, "An analytical approximation of depth-dose distributions for therapeutic proton beams," *Physics in medicine and biology*, vol. 41, no. 8, p. 1331, 1996.

[23] F. Tillner, P. Thute, R. Buetof, M. Krause, and W. Enghardt, "Pre-clinical research in small animals using radiotherapy technology–a bidirectional translational approach," *Zeitschrift für Medizinische Physik*, vol. 24, no. 4, pp. 335–351, 2014.

[24] N. B. Cho, J. Wong, P. Kazanzides, R. Beare, A. C. Senra Filho, J. Woehr, R. Grothausmann, A. Choudhary, N. Moretto, F. Pizzorni Ferrarese, *et al.*, "Dose painting with a variable collimator for the small animal radiation research platform (SARRP)," *Retrieved online from MIDAS Journal*, 2014.

[25] E. E. Graves, H. Zhou, R. Chatterjee, P. J. Keall, S. S. Gambhir, C. H. Contag, and A. L. Boyer, "Design and evaluation of a variable aperture collimator for conformal radiotherapy of small animals using a microCT scanner," *Medical physics*, vol. 34, no. 11, pp. 4359–4367, 2007.

[26] S. Branco, "Small animal PET imaging using GATE Monte Carlo simulations: Implementation of physiological and metabolic information," 2010.

[27] F. Verhaegen, P. Granton, and E. Tryggestad, "Small animal radiotherapy research platforms," *Physics in medicine and biology*, vol. 56, no. 12, p. R55, 2011.

[28] F. Verhaegen, S. van Hoof, P. V. Granton, and D. Trani, "A review of treatment planning for precision image-guided photon beam pre-clinical animal radiation studies," *Zeitschrift für Medizinische Physik*, vol. 24, no. 4, pp. 323–334, 2014.

[29] D. Sarrut, M. Bardiès, N. Boussion, N. Freud, S. Jan, J.-M. Létang, G. Loudos, L. Maigne, S. Marcatili, T. Mauxion, *et al.*, "A review of the use and potential of the GATE Monte Carlo simulation code for radiation therapy and dosimetry applications," *Medical physics*, vol. 41, no. 6, 2014.

[30] L. Mouawad, M. Rousseau, D. Brasse, Z. El Bitar, A. Osman, M. Khalil, and Z. Francis, "Beam shaping systems for small animal proton therapy," in *Advances in Biomedical Engineering (ICABME), 2015 International Conference on*, pp. 174–177, IEEE, 2015.

[31] J. B. Storer, P. S. Harris, J. E. Furchner, and W. H. Langham, "The relative biological effectiveness of various ionizing radiations in mammalian systems," *Radiation Research*, vol. 6, no. 2, pp. 188–288, 1957.

[32] H. Paganetti, A. Niemierko, M. Ancukiewicz, L. E. Gerweck, M. Goitein, J. S. Loeffler, and H. D. Suit, "Relative biological effectiveness (RBE) values for proton beam therapy," *International Journal of Radiation Oncology Biology Physics*, vol. 53, no. 2, pp. 407–421, 2002.

[33] R. Grün, T. Friedrich, M. Krämer, and M. Scholz, "Systematics of relative biological effectiveness measurements for proton radiation along the spread out bragg peak: experimental validation of the local effect model," *Physics in medicine and biology*, vol. 62, no. 3, p. 890, 2017.

[34] T. Elsässer, W. K. Weyrather, T. Friedrich, M. Durante, G. Iancu, M. Krämer, G. Kragl, S. Brons, M. Winter, K.-J. Weber, *et al.*, "Quantification of the relative biological effectiveness for ion beam radiotherapy: direct experimental comparison of proton and carbon ion beams and a novel approach for treatment planning," *International Journal of Radiation Oncology Biology Physics*, vol. 78, no. 4, pp. 1177–1183, 2010.

[35] H. Paganetti, "Relating proton treatments to photon treatments via the relative biological effectiveness—should we revise current clinical practice?," *International Journal of Radiation Oncology Biology Physics*, vol. 91, no. 5, pp. 892–894, 2015.

[36] P. Chaudhary, T. I. Marshall, F. M. Perozziello, L. Manti, F. J. Currell, F. Hanton, S. J. McMahon, J. N. Kavanagh, G. A. P. Cirrone, F. Romano, *et al.*, "Relative biological effectiveness variation along monoenergetic and modulated bragg peaks of a 62-MeV therapeutic proton beam: A preclinical assessment," *International Journal of Radiation Oncology Biology Physics*, vol. 90, no. 1, pp. 27–35, 2014.

[37] H. Paganetti, "Relative biological effectiveness (RBE) values for proton beam therapy. Variations as a function of biological endpoint, dose, and linear energy transfer," *Physics in medicine and biology*, vol. 59, no. 22, p. R419, 2014.

[38] A. Yogo, T. Maeda, T. Hori, H. Sakaki, K. Ogura, M. Nishiuchi, A. Sagisaka, H. Kiriyama, H. Okada, S. Kanazawa, T. Shimomura, Y. Nakai, M. Tanoue, F. Sasao, P. R. Bolton, M. Murakami, T. Nomura, S. Kawanishi, and K. Kondo, "Measurement of relative biological effectiveness of protons in human cancer cells using a laser-driven quasimonoenergetic proton beamline," *Applied Physics Letters*, vol. 98, no. 5, p. 053701, 2011.

[39] D. Słonina, B. Biesaga, J. Swakoń, D. Kabat, L. Grzanka, M. Ptaszkiewicz, and U. Sowa, "Relative biological effectiveness of the 60-MeV therapeutic proton beam at the Institute of Nuclear Physics (IFJ PAN) in Kraków, Poland," *Radiation and Environmental Biophysics*, vol. 53, pp. 745–754, Nov 2014.

[40] O. Keta, D. Todorović, N. Popović, L. Korićanac, G. Cuttone, I. Petrović, and A. Ristić-Fira, "Radiosensitivity of human ovarian carcinoma and melanoma cells to γ-rays and protons," *Archives of medical science: AMS*, vol. 10, no. 3, p. 578, 2014.

[41] M. Mognato, E. Bortoletto, P. Ferraro, L. Baggio, R. Cherubini, S. Canova, A. Russo, and L. Celotti, "Genetic Damage Induced by In Vitro Irradiation of Human G0 Lymphocytes with Low-Energy Protons (28 keV/μm): HPRT Mutations and Chromosome Aberrations," *Radiation research*, vol. 160, no. 1, pp. 52–60, 2003.

[42] R. D. Govorun, M. Deperas-Kaminska, E. M. Zaitseva, E. A. Krasavin, G. V. Mitsyn, and A. G. Molokanov, "Investigation of chromosome damage in human cells irradiated by beam for proton therapy produced by phasotron at the joint institute for nuclear research," *Physics of Particles and Nuclei Letters*, vol. 3, no. 1, pp. 54–58, 2006.

[43] R. Belli, M. Cherubini, V. Dalla Vecchia, G. Dini, C. Moschini, G. Signoretti, M. A. Simone, P. Tabocchini, and M. Tiveron, "DNA DSB induction and rejoining in V79 cells irradiated with light ions: a constant field gel electrophoresis study," *International journal of radiation biology*, vol. 76, no. 8, pp. 1095–1104, 2000.

[44] L. M. Green, D. K. Murray, D. T. Tran, A. M. Bant, G. Kazarians, M. F. Moyers, and G. A. Nelson, "Response of thyroid follicular cells to gamma irradiation compared to proton irradiation. I. initial characterization of DNA damage, micronucleus formation, apoptosis, cell survival, and cell cycle phase redistribution," *Radiation research*, vol. 155, no. 1, pp. 32–42, 2001.

[45] A. M. Kellerer *et al.*, "Fundamentals of microdosimetry," *The dosimetry of ionizing radiation*, vol. 1, pp. 77–162, 1985.

[46] L. Lindborg and H. Nikjoo, "Microdosimetry and radiation quality determinations in radiation protection and radiation therapy," *Radiation protection dosimetry*, vol. 143, no. 2-4, pp. 402–408, 2011.

[47] A. M. Kellerer, "Considerations on the random traversal of convex bodies and solutions for general cylinders," *Radiation Research*, vol. 47, no. 2, pp. 359–376, 1971.

[48] L. Lindborg, M. Hultqvist, Å. C. Tedgren, and H. Nikjoo, "Lineal energy and radiation quality in radiation therapy: model calculations and comparison with experiment," *Physics in medicine and biology*, vol. 58, no. 10, p. 3089, 2013.

Chapter 1

A microscopic simulation of DNA damage

As the ionizing particles travel through the target, they transfer their energy to the constituents of the medium in the form of localized clusters that are responsible for the biological damage which can take various forms. The absorbed dose, the mean transfered energy, is therefore used as an indicator for the induced damage and treatment plans are often based on the prescribed dose. It is however essential to investigate the interactions of individual particles if the complex process through which the biological damage is induced by ionizing radiation, leading to cell death, is to be well understood. Indeed, biological damage is induced through different stages and by various actors. DNA damage is considered the main indicator of the induced damage and therefore many studies were focused on identifying DNA damage following irradiation. Monte Carlo track structure codes allow such studies by quantifying parameters describing particle interactions that are difficult to measure experimentally.

Just as the particles enter the medium, the energy transfer begins through collisions with the electrons of the molecules in the traversed medium within a few femtoseconds. The damages caused by this direct interaction of the incident particles with the medium are classified as direct damages. If the energy transferred is sufficiently high, the molecules are ionized and secondary electrons are liberated. These electrons can themselves interact with other molecules inducing further ionizations. At a chemical level, the composition of the medium is changed as the chemical bonds between its constituents are altered and new species are formed. These species can interact with one another and modify the structure of the cells. Free radicals such as the hydroxyl radical, which comes from the ionization and subsequent dissociation of water molecules, are produced in large quantities and can induce severe modifications to the DNA. The damages induced by secondary species are classified as indirect effects. A biological reparation process is then launched and the damages are repaired through enzymatic reactions at the DNA. Unrepaired damages, or alterations caused by failed repairs, can eventually lead to cell death.

In this chapter, we explore the induced DNA damage by the 24 MeV proton beam provided by the Cyrcé cyclotron which will be used for small animal proton therapy applications, as presented in the introduction. We particularly evaluate DNA strand breaks through Geant4

simulations with the Geant4-DNA extension describing the interactions at the DNA scale. The biological material is modeled by water and the strand breaks are calculated using the Density Based Spatial Clustering for Applications with Noise algorithm (DBSCAN) [1] adapted for DNA damage calculations. We begin by presenting the different approaches used to identify single and double strand breaks before we move on to briefly presenting the Geant4-DNA extension and the version of the DBSCAN algorithm which we use in our work. We then compare the computed strand break yields to the absorbed dose profile to further put into light the necessity for more biologically relevant parameters to indicate the induced damage in treatment planning.

1.1 Characterizing DNA strand breaks

Although important damage is induced by ionizing radiation at cellular membranes, cytoplasm and proteins, DNA damage is considered the main biological effect since the DNA contains all the genetic information [2, 3]. Indeed, the DNA is the most vital part of the cell. It consists of a double helix with two strands linked together through hydrogen bonds between DNA bases on opposite strands, in a way that purine bases (Adenine and Guanine) are linked to pyrimidines (Thymine and Cytosine). These bases are attached to the DNA backbone consisting of phosphate and sugar units. DNA damage is any modification of the DNA, such as base alterations, creation of cross-links with proteins surrounding the DNA and strand breaks, that can eventually lead to cell death if unrepaired or falsely repaired [4, 5]. Figure 1.1 illustrates the main types of DNA lesions caused by ionization radiation.

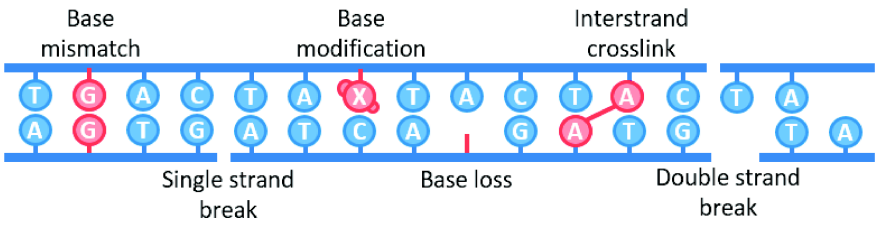

Figure 1.1: Main types of DNA lesions.

Double strand breaks (DSBs) are thought to be the most critical because their repair process is the most complex [6–8]. They can result from unsuccessful attempts to repair clustered DNA damage [9–11]. The energy deposition patterns obtained from Monte Carlo track structures have been widely used to determine DNA damage with a greater focus on single and double strand breaks (SSBs and DSBs) [6, 12]. In such studies, DSB yields are often deduced from the spatial distribution of energy deposition events by considering that two or more SSBs occurring within a delimiting distance with at least one of them located on an opposite strand form a DSB. The maximum distance between energy deposition events potentially leading to a DSB is usually taken as the equivalent of 10 base pairs which is about 3.2 nm. While most studies use this concept of a DSB [13–15], some studies argue that an additional probability of 1% should be added to take into account DSBs resulting from the replication of a DNA with an unrepaired SSB [16].

To characterize SSBs as a function of the deposited energy, three models can be used: the constant model, the threshold model and the linear model. The probability of SSB formation is described by a constant function in the constant model and the SSB yields are therefore considered independent of the deposited energy. In most studies, this probability is assumed equal to about 12% [17]. On the other hand, the linear model describes the SSB probability with a probability density function that is equal to zero below a minimal energy, and equal to one above a maximum energy. Between these two limits, the SSB probability increases linearly from zero to one. The minimum energy is chosen around 5 eV in order to take into account the non-negligible participation of low energy electrons in DNA strand breaking. For the upper energy limit, a value of 37.5 eV is used according to a ramp function proposed by *Friedland et al.* [16]. In their work, *Friedland et al.* applied this linear model in a sensitive region consisting of a shell of 10 water molecules around a nucleotide where the energy deposition events are considered as a source of potential DNA damage. In other studies, this energy was determined by assuming a number of SSBs per deposited energy and cell nucleus as well as a ratio between direct and indirect effects. In [17], a slope of 1.9% by eV was obtained by considering that 1000 SSBs are created per Gray of deposited energy and cell nucleus [18] and that the ratio between direct and indirect effects is of 35:65 [19]. In the threshold model, SSBs are created when the deposited energy is greater than a certain threshold which is usually taken as the first excitation level or the first ionization level of water: 8.22 eV or 10.79 eV. *Incerti et al.* [14] used a threshold energy of 8.22 eV to calculate strand break yields induced by 2 MeV protons and compared the results to those obtained from other models showing that the used method to determine SSBs highly influences the resultant yields. A more sophisticated approach was used by *Liang et al.* [20] setting the threshold energy to 10.79 eV but applying it to events falling in a sensitive target volume of 0.15 nm^3 while using a probability of 11% to account for indirect effects outside this region. The different models used to characterize SSBs are illustrated in figure 1.2.

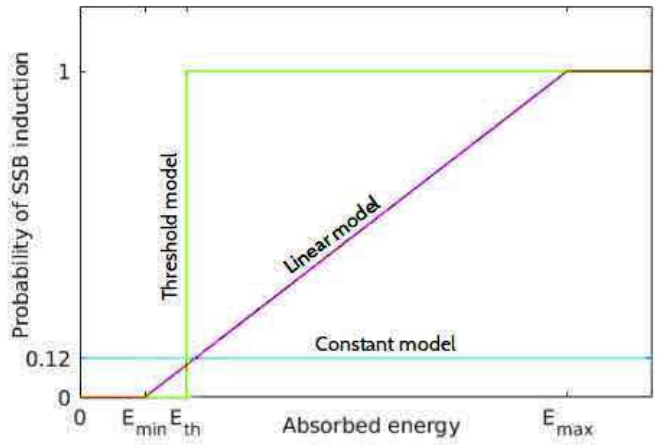

Figure 1.2: Models used to determine the probability of DNA single strand break induction by ionizing radiation in function of the absorbed energy.

1.2 Track structure simulation of biological damage

Monte Carlo track structure codes allow microscopic simulations of biological damage by considering all the possible physics interactions taking place in small volumes over a wide energy range. Different particle types are considered, and appropriate physics interactions at low and intermediate energies are included enabling a detailed view of the ionizing radiation tracks at the cellular, subcellular and molecular scales. A list of Monte Carlo codes used for microscopic simulations is given in figure 1.3 taken from [21].

Code	Particle	Energy range	Cross-section database[a]	Reference
CPA100[b,c]	e^-	$\geqslant$ 10 eV–100 eV e^-	Wat. (l)	Terrissol and Beaudre, 1990
DELTA[c]	e^-	$\geqslant$ 10 eV–10 keV e^-	Wat. (v)	Zaider et al. (1983)
ETRACK[c]	e^-, p, α	$\geqslant$ 10 eV–10 keV e^-	Wat. (v)	Ito (1987)
KURBUC[c]	e^-	$\geqslant$ 10 eV–10 MeV e^-	Wat. (v)	Uehara et al. (1993)
LEEPS	e^-, e^+	0.1–100 keV	Many materials	Fernandez-Varea et al. (1996)
LEPHIST[c]	p	$\geqslant$ 1 keV–1 MeV	Wat. (v)	Uehara et al. (1993)
LEAHIST[c]	α	$\geqslant$ 1 keV/u–2 MeV/u	Wat. (v)	Uehara and Nikjoo (2002a)
MC4	e^-, ions	$\geqslant$ 10 eV e^-, ions $\geqslant$ 0.3 MeV/u	Wat. (v,l)	Emfietzoglou et al. (2003)
NOTRE DAME[c]	e^-, ions	$\geqslant$ 10 eV e^-, ions $\geqslant$ 0.3 MeV/u	Wat. (v,l)	Pimblott et al. (1990)
OREC[c]	e^-, ions	$\geqslant$ 10 eV e^-, ions $\geqslant$ 0.3 MeV/u	Wat. (v,l)	Turner et al. (1983)
PARTRAC[b,c]	e^-, ions	$\geqslant$ 10 eV e^-, ions $\geqslant$ 0.3 MeV/u	Wat. (v,l)	Friedland et al. (2003)
PITS04[b]	e^-, ions	$\geqslant$ 10 eV e^-, ions $\geqslant$ 0.3 MeV/u	Wat. (l)	Wilson et al. (2004)
PITS99[c]	e^-, ions	$\geqslant$ 10 eV e^-, ions $\geqslant$ 0.3 MeV/u	Wat. (v)	Wilson and Nikjoo (1999)
SHERBROOKE[c]	e^-, ions	$\geqslant$ 10 eV e^-, ions $\geqslant$ 0.3 MeV/u	Wat. (v,l)	Cobut et al. (2004)
STBRGEN[c]	e^-, ions	$\geqslant$ 10 eV e^-, ions $\geqslant$ 0.3 MeV/u	Wat. (v,l)	Chatterjee and Holley (1993)
TRION	e^-, ions	$\geqslant$ 10 eV e^-, ions $\geqslant$ 0.3 MeV/u	Wat. (v,l)	Lappa et al. (1993)
TRACEL[c]	e^-, ions	$\geqslant$ 10 eV e^-, ions $\geqslant$ 0.3 MeV/u	Wat. (v,l)	Tomita et al. (1997)

[a]Nomenclatures 'l' and 'v' have been used for liquid and vapor. In reality it is not easy to distinguish between these modes as experimental cross-sections for water have been measured only in water vapor or ice phase (see Section 7).
[b]These codes have implemented the theoretical model of liquid water by Dingfelder et al. (1998).
[c]These codes have extension for generating distribution of radicals at 10^{-12} s and later times.

Figure 1.3: A list of Monte Carlo track structure codes for micro-dosimetry simulations, taken from [21].

These codes are conceived in a way to provide the most truthful modeling of cellular response to ionizing radiation. Evidently, such microscopic simulations are very convenient to investigate biological damage. Various models of the DNA are included in these simulations allowing the identification of single and double strand breaks and extensive research has been conducted using Monte Carlo track structure codes to explain the mechanisms of DNA damage [22–24]. These codes rely on a cross section database describing particle interactions with water, since water is the main constituent of biological material. Liquid water cross sections were used in some studies [24, 25] while in others, vapor water cross sections were used instead [26, 27].

Adding the Geant4-DNA physics models [28] to the electromagnetic processes in the open source Geant4 [29] Monte Carlo code, incited many studies using Geant4 for micro-dosimetry simulations of the biological damage induced by ionizing radiation. Physics interactions that were not taken into account in the Geant4 toolkit were added within the Geant4-DNA extension making it possible to simulate the interactions of electrons, hydrogen (H^0, H^+) and helium (He^0, He^+, He^{2+}) with liquid water, at the submicrometer scale and down to the electron volt. All collisions are explicitly simulated on an event-by-event basis allowing the tracking of secondary particles within a few nanometers and providing an accurate description of the energy deposits at the cellular and molecular scales. Each physical interaction is described by a physics process that can be defined

by different available and validated models [30] that apply to a particular energy range. These models are implemented in Geant4 classes that determine the total interaction cross sections and the final state products according to the chosen model. The cross sections are determined either analytically or based on interpolated data tables and the different implemented models are validated by comparing the cross sections, particle range and stopping powers to published experimental data. A list of the models and corresponding classes for the added physical interactions is given in table 1.1.

Details about the used models to determine the cross sections can be found in [30, 31]. The ionization cross sections of liquid water by electrons are for example obtained by interpolation of the data from [32] based on the First Born Approximation. These cross sections were compared to experimental data provided by many studies for vapor water and good agreement was found between the different experimental cross section trends and the Geant4-DNA cross sections.

As noted in the introduction, we performed macroscopic simulations of the irradiation of a targeted tumor by the 24 MeV proton beam where we evaluated the deposited dose along the depth of the tumor considering that the higher the absorbed dose is, the greater the induced damage. It is now clear that the absorbed dose is not sufficient to characterize biological effects. We examine the microscopic mechanisms taking place in order to have a more clear view of the induced biological damage.

In Geant4 simulations using the Geant4-DNA processes, we probe the DNA strand breaks induced by this proton beam by tracking the particles in small elementary volumes of the macroscopic volume. To identify strand breaks, the spatial distribution of the energy deposition events is required. We hence attach a small volume of 1 mm width, 1 mm thickness, and 0.5 μm length to the macroscopic water box of 1 mm width, 1 mm thickness, and 10 mm length, and we move it along the depth of this macroscopic volume. By doing so, the interaction coordinates and deposited energy for each event from the proton beam are obtained at a microscopic level over the entire macroscopic volume. Figure 1.4, taken from [33], illustrates the details provided by such a simulation in comparison to the macroscopic simulation without the Geant4-DNA extension for a 1 keV electron incident on slab of liquid water using. It is clear that with the standard processes the electron is killed after one interaction while every interaction of this electron is simulated within the Geant4-DNA processes.

Particle	Physics process	Geant4 process class	Geant4 model class	Energy range	Model type
Electron	Elastic scattering	G4DNAElastic	G4DNAScreenRutherfordElasticModel	9 eV - 1 MeV	Analytical
			G4DNAChampionElasticModel	9 eV - 1 MeV	Interplated
	Excitation	G4DNAExcitation	G4DNABornExcitationModel	9 eV - 1 MeV	Interpolated
	Ionization	G4DNAIonisation	G4DNABornIonisationModel	11 eV - 1 MeV	Interpolated
Proton	Excitation	G4DNAExcitation	G4DNAMillerGreenExcitationModel	10 eV - 500 keV	Analytical
			G4DNABornExcitationModel	500 keV - 100 MeV	Interpolated
	Ionization	G4DNAIonisation	G4DNARuddIonisationModel	100 eV - 500 keV	Interpolated
			G4DNABornIonisationModel	500 keV - 100 MeV	Interpolated
	Charge decrease	G4DNAChargeDecrease	G4DNADingfelderChargeDecreaseModel	100 eV - 10 MeV	Analytical
^{1}H	Ionization	G4DNAIonisation	G4DNARuddIonisationModel	100 eV - 100 MeV	Interpolated
	Charge increase	G4DNAChargeDecrease	G4DNADingfelderChargeIncreaseModel	100 eV - 10 MeV	Analytical
$^{4}He^{2+}$	Excitation	G4DNAExcitation	G4DNAMillerGreenExcitationModel	1 keV - 400 MeV	Analytical
	Ionization	G4DNAIonisation	G4DNARuddIonisationModel	1 keV - 400 MeV	Interpolated
	Charge decrease	G4DNAChargeDecrease	G4DNADingfelderChargeDecreaseModel	1 keV - 400 MeV	Analytical
$^{4}He^{+}$	Excitation	G4DNAExcitation	G4DNAMillerGreenExcitationModel	1 keV - 400 MeV	Analytical
	Ionization	G4DNAIonisation	G4DNARuddIonisationModel	1 keV - 400 MeV	Interpolated
	Charge decrease	G4DNAChargeDecrease	G4DNADingfelderChargeDecreaseModel	1 keV - 10 MeV	Analytical
	Charge increase	G4DNAChargeIncrease	G4DNADingfelderChargeIncreaseModel	1 keV - 10 MeV	Analytical
^{4}H	Excitation	G4DNAExcitation	G4DNAMillerGreenExcitationModel	1 keV - 400 MeV	Analytical
	Ionization	G4DNAIonisation	G4DNARuddIonisationModel	1 keV - 400 MeV	Interpolated
	Charge increase	G4DNAChargeIncrease	G4DNADingfelderChargeIncreaseModel	1 keV - 10 MeV	Analytical

Table 1.1: A list of the Geant4-DNA physics processes for liquid water for the different particle types with the classes and models that are used in the indicated energy ranges. The model type given in the last column indicates wether the cross sections of the process was obtained analytically or by interpolated data tables.

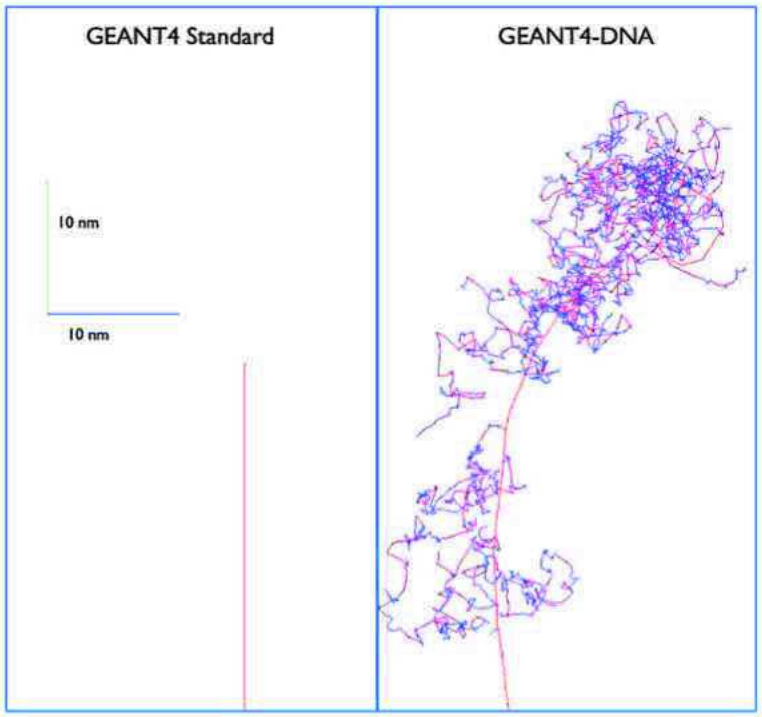

Figure 1.4: Comparison of the simulated interactions with and without the Geant4-DNA processes in Geant4 for a 1 keV electron incident on a slab of liquid water. In the representation to the left, only the electromagnetic process in Geant4 are simulated while in the representation to the right includes the Geant4-DNA processes.

The energy deposition events are grouped into damage clusters according to their spatial distribution and their energy. This is done using the Density Based Spatial Clustering for Applications with Noise algorithm (DBSCAN) [1].

1.3 Simulating DNA damage clustering

DBSCAN is a density based clustering algorithm developed by *Ester et al.* [1] and capable of identifying clustering formation in a region of events from simply two input parameters: the minimum number of points to form a cluster ($MinPts$) and the radius of the cluster (eps). In addition to that, DBSCAN has the ability to identify clusters of arbitrary shapes and a fast computational time compared to other data clustering algorithm. A modified version of DBSCAN created by *Francis et al.* [34] and particularly dedicated to determining DNA cluster damage is used in this work. In this version of DBSCAN, five input parameters are needed: the minimum number of points to form a cluster ($MinPts$), the radius delimiting the neighborhood of a point (eps), the probability that a point is in a sensitive region ($SPointsProb$), and the minimum and maximum energies ($EMinDamage$ and $EMaxDamage$) defining the damage probability function. Since at least two SSBs separated by less than 10 base pairs are required to form a DSB, $MinPts$ is set to 2 and eps is set to the distance corresponding to 10 base pairs which is approximately 3.2 nm. $SPointsProb$ is defined as the uniform probability that an interaction point is

located in a sensitive region where it can reach the DNA, it is an adjustable parameter that represents the ratio of the considered sensitive region to the total medium volume and a value of 15% was found to give good results [34]. Since not all events that reach the DNA actually lead to DNA damage, a probability damage function is used to decide whether a point falling in the sensitive region causes DNA damage or not. A linear probability function was considered; the lower energy limit is taken equal to 5 eV and the upper energy limit is 37.5 eV [16]. An input data file containing the spatial coordinates of energy deposition events and the deposited energy values is required for DBSCAN. This information is obtained from the Geant4-DNA simulations of the proton beam interactions with the microscopic volumes making up the target. For each event detected by the track structure simulation, DBSCAN determines, using $SPointsProb$, if this event is inside a sensitive region and is therefore capable of causing DNA damage. Then, using the linear damage probability, DBSCAN determines if this event, located in the sensitive region, did actually cause a DNA damage. If the event is in the sensitive region and causes DNA damage, it is considered as a SSB and positioned arbitrarily on one of the DNA strands. After all events are sampled through these probability functions, each SSB is studied individually. For a given SSB, if the number of neighboring SSBs within a radius eps is greater than $MinPts$, it is considered the center of a cluster. If a cluster contains a number of SSBs equal to or greater than 2 with one of them at least located on an opposite strand, it is considered a DSB. If two clusters have centers separated by a distance less than the radius eps, the two clusters are merged into one cluster. This version of DBSCAN also allows the distinction between double strand breaks consisting of two SSBs located on opposite strands and complex or clustered DSBs with 3 or more SSBs. The flowchart of this program is given in figure 1.5.

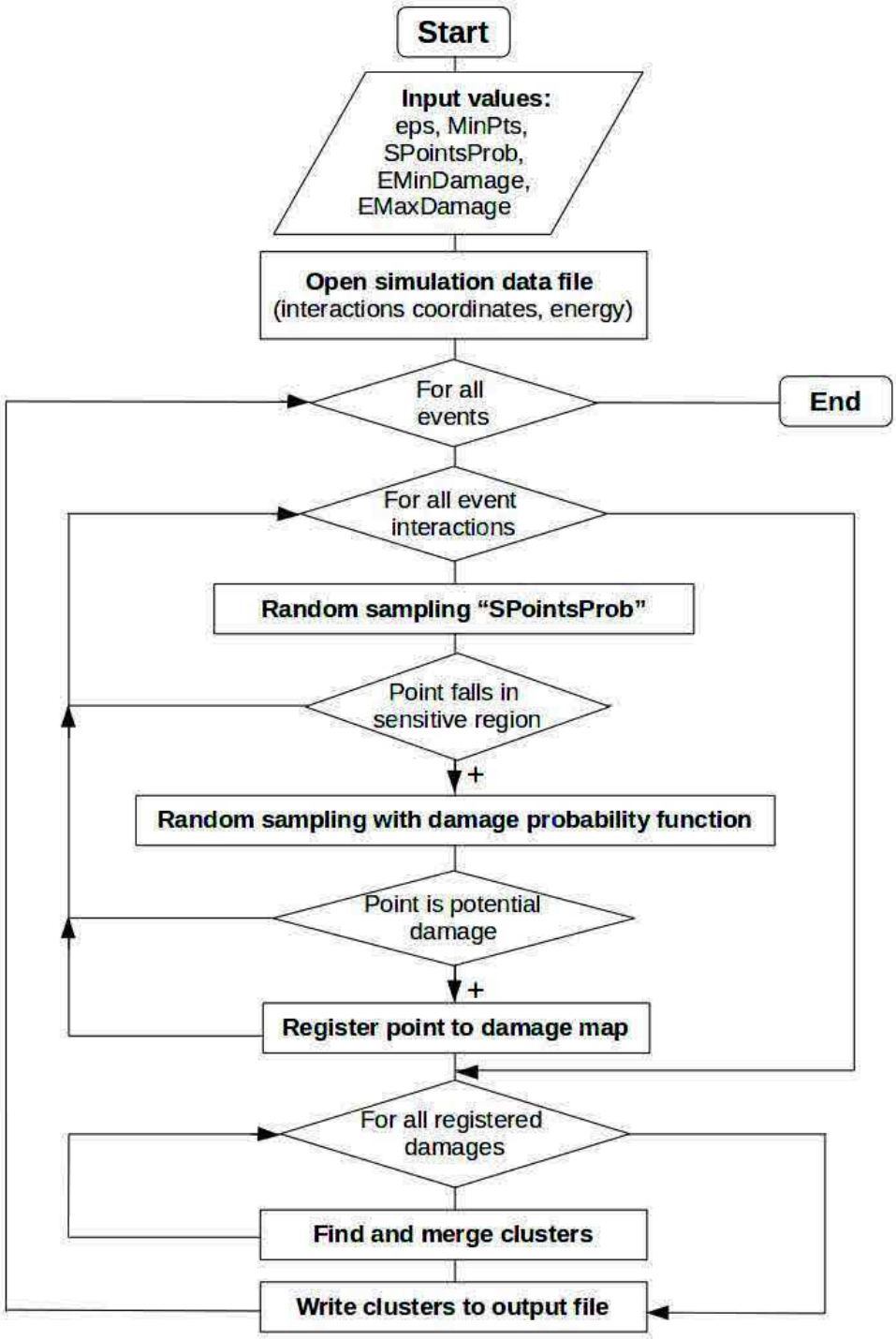

Figure 1.5: Flowchart of the DBSCAN algorithm adapted to DNA damage clustering [34].

The single and double strand break yields are obtained at each position of the microscopic volume which is shifted of 0.1 mm along the macroscopic box. The resultant SSB and DSB yields along the depth of the macroscopic volume are given in figure 1.6. The DSB yields are also given in the graph to the left of figure 1.6 where the simple and complex DSBs are represented. Complex DSB yields are considered the most lethal of strand breaks and are formed by more than two strand breaks.

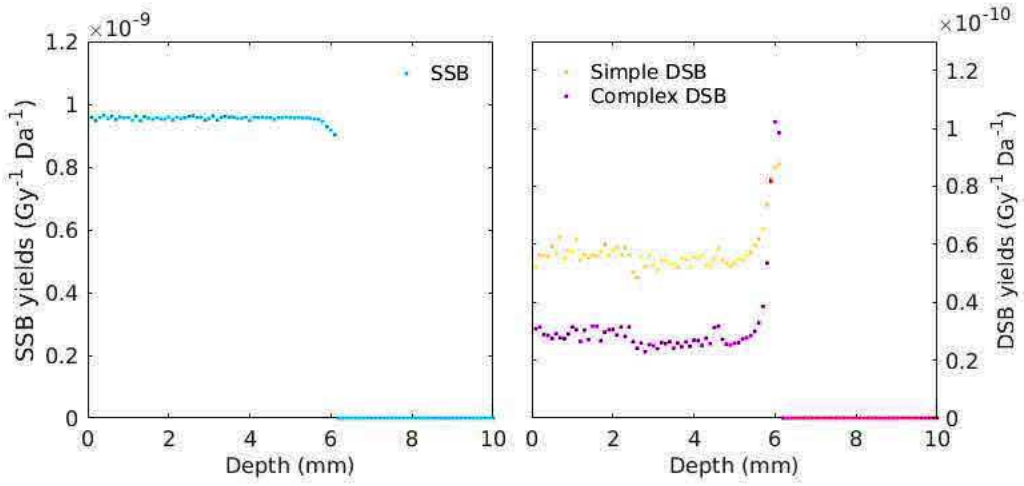

Figure 1.6: Single strand break yields (to the right) and double strand break yields (to the left) induced by a beam of 24 MeV protons incident on a liquid water box of 1 mm width, 1 mm thickness, and 10 mm length in function of the traveled distance from the entrance plane of the volume.

The SSB yield is invariant until about 5.7 mm where it slowly begins to decrease. This decrease is due to the increase of the deposited dose at this depth, which corresponds to the Bragg peak position, and hence more dense clusters of damage are expected leading to these energy depositions being considered as DSBs instead of SSBs. The order of magnitude and the general trend of the SSB and DSB yields are in agreement with the results of a previous study [34] done for a much larger range of proton energies (up to 10^8 eV). The strand break yields are steady in function of depth until approximately 5.7 mm where the DSB yield rapidly increases as the SSB yield decreases. The complex DSB yield increase is more apparent at this point implying that more damage is induced at the Bragg peak. At about 6 mm, all strand break yields become abruptly null. The total DSB yield evolution along the target depth reminds the shape of the macroscopic Bragg peak. We compare the two in figure 1.7.

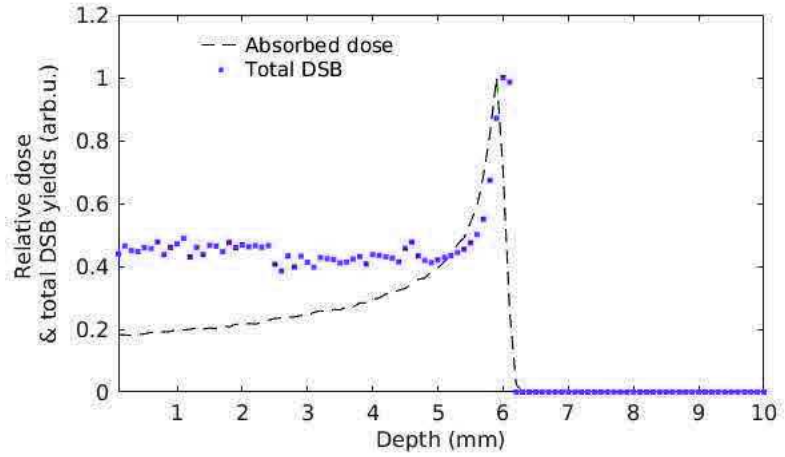

Figure 1.7: Total double strand break yield induced by a proton beam of 24 MeV energy compared to the absorbed dose in a liquid water volume of 1 mm width, 1 mm thickness, and 10 mm length.

The occurrence of the Bragg peak in the absorbed dose distribution is in accordance with the increase of DSB yields justifying that the most important DNA strand breaking occurs just before the protons stop depositing all their energy. The shape of the DSB distribution is more constant at the entrance with a faster increase near the Bragg peak than the dose distribution which presents a slow gradual increase of the dose as the protons enter the macroscopic volume until a dose increase at the Bragg peak starting almost a millimeter before the DSB peak.

1.4 Implications for treatment planning

The differences between the two distributions could be due to biological effects other than DNA strand breaks that are not included in this study. Indeed, DNA strand breaks are only one form of biological damage induced by ionizing radiation. Moreover, comparing the DNA strand breaks to absorbed dose only provides qualitative information about the validity of absorbed dose based treatment planning. A more complete approach would be to calculate the RBE of DNA strand breaks and compare the biological dose to the absorbed physical dose.

Many studies have been performed in the last decade to quantify DNA strand break yields induced by different types of ionizing radiation, in function of deposited energy [34], linear energy transfer [20, 35] and depth [36]. The RBE for DSB induction has also gained particular interest. A recent study performed by *Lin et al.* [37] provided RBE for DSB induction as a function of depth near the Bragg peak for 100 MeV protons and for helium and carbon ions. FLUKA [38] and the Monte Carlo Damage Structure (MCDS) code [39] were used. The target was modeled by a cylindrical water phantom of 3 cm diameter and 30 cm length divided into thin slabs of about 1 mm thickness. The aim of this study [37] was to compare the RBE for the considered radiation types. They concluded that the carbon beam has the highest RBE and that helium beams could be as beneficial as proton beams in cancer treatment. In another work [36], the physical absorbed dose was

directly compared to the biological dose which was obtained by multiplying the former with the RBE for DSB induction. FLUKA and MCDS were also used to simulate the track structure of a carbon ion beam of 300 MeV μ^{-1} and its fragments and to evaluate double strand breaks. The width of the Bragg peak as well as the entrance dose were increased in the biological dose compared to the physical dose. The influence of considering an RBE weighted biological dose instead of the absorbed dose was also examined in [40] where the proton RBE for DSB induction, as a function of depth near the Bragg peak, was determined in an experimental work using γ-H2AX, a component of the histone octomer in nucleosomes, as a precursor for DNA strand breaks [41]. The physical dose was also measured and they compared the corrected dose with the constant RBE of 1.1 to the corrected dose using the measured RBE for DSB induction. They found that the range and the effective biological dose were both greater in the Bragg peak region when the RBE for DSB induction is used. The RBE for DSB induction was also calculated in function of LET in other studies. *Pater et al.* [35] developed a Monte Carlo algorithm to calculate DNA strand breaks. The SSBs were identified according to a threshold model and the DSBs were calculated from the SSBs based on their number and localization. Only direct effects were taken into account and the RBE for DSB induction was given as a function of LET. Protons and light ions were considered and a sophisticated model of the cell nucleus [42, 43] was used. The obtained results were in agreement with experimental measurements [44], and simulation results using PARTRAC [24] and the MCDS code [45].

These studies of biological damage are indeed difficult studies that rely on many approximations and parameters that differ from one approach to another. For example, the classification of lesions and the model of DNA that are used influence the resulting strand break yields and consequently the RBE for DSB induction. An exact description of the physics interactions in the used codes is also difficult to obtain. As the energy of the particles decreases, the uncertainties on position and momentum increases. Many processes below the ionization threshold are sometimes not taken into account or are not correctly simulated although they play an important role in inducing strand breaks. Moreover, the cross sections of particle interactions with biological constituents of the DNA have only been recently investigated and are still not used in most track structure codes that still rely on water cross sections instead. New research fields arose attempting at providing a more complete understanding of the physical and biological mechanisms that are involved in the cellular response to ionizing radiation.

In the remaining part of this thesis we chose to focus on determining the interaction cross sections for biological molecules. If these cross sections are not available to date, it is because they are difficult to determine both experimentally and theoretically. In the next chapter we discuss these challenges and present the main fundamental and experimental concepts in determining these cross sections. We focus on the ionization by electron impact process which is responsible for the production of low energy electrons that have been proven to be the major contributors to DNA strand breaks.

References

[1] M. Ester, H.-P. Kriegel, J. Sander, X. Xu, *et al.*, "A density-based algorithm for discovering clusters in large spatial databases with noise.," in *Kdd*, vol. 96, pp. 226–231, 1996.

[2] D. T. Goodhead, "Initial events in the cellular effects of ionizing radiations: clustered damage in DNA," *International journal of radiation biology*, vol. 65, no. 1, pp. 7–17, 1994.

[3] P. O'Neill, "The chemical basis of radiation biology," *International Journal of Radiation Biology and Related Studies in Physics, Chemistry and Medicine*, vol. 52, no. 6, pp. 976–976, 1987.

[4] J.-P. Pouget and S. J. Mather, "General aspects of the cellular response to low- and high-LET radiation," *European Journal of Nuclear Medicine and Molecular Imaging*, vol. 28, no. 4, pp. 541–561, 2001.

[5] R. Painter, "The role of DNA damage and repair in cell killing induced by ionizing radiation," *Radiation biology in cancer research*, pp. 59–68, 1980.

[6] D. Frankenberg, M. Frankenberg-Schwager, D. Blöcher, and R. Harbich, "Evidence for DNA Double-Strand Breaks as the Critical Lesions in Yeast Cells Irradiated with Sparsely or Densely Ionizing Radiation under Oxic or Anoxic Conditions," *Radiation Research*, vol. 88, no. 3, pp. 524–532, 1981.

[7] P. Bryant, "Enzymatic restriction of mammalian cell DNA: evidence for double-strand breaks as potentially lethal lesions," *International Journal of Radiation Biology and Related Studies in Physics, Chemistry and Medicine*, vol. 48, no. 1, pp. 55–60, 1985.

[8] P. Pfeiffer, W. Goedecke, and G. Obe, "Mechanisms of DNA double-strand break repair and their potential to induce chromosomal aberrations," *Mutagenesis*, vol. 15, no. 4, pp. 289–302, 2000.

[9] B. M. Sutherland, P. V. Bennett, J. C. Sutherland, and J. Laval, "Clustered DNA damages induced by x rays in human cells," *Radiation research*, vol. 157, no. 6, pp. 611–616, 2002.

[10] Z. Francis, S. Incerti, V. Ivanchenko, C. Champion, M. Karamitros, M. Bernal, and Z. El Bitar, "Monte Carlo simulation of energy-deposit clustering for ions of the same LET in liquid water," *Physics in medicine and biology*, vol. 57, no. 1, p. 209, 2011.

[11] G. Garty, R. Schulte, S. Shchemelinin, C. Leloup, G. Assaf, A. Breskin, R. Chechik, V. Bashkirov, J. Milligan, and B. Grosswendt, "A nanodosimetric model of radiation-induced clustered DNA damage yields," *Physics in medicine and biology*, vol. 55, no. 3, p. 761, 2010.

[12] V. Michalik and D. Frankenberg, "Simple and complex double-strand breaks induced by electrons," *International journal of radiation biology*, vol. 66, no. 5, pp. 467–470, 1994.

[13] M. Dos Santos, C. Villagrasa, I. Clairand, and S. Incerti, "Influence of the DNA density on the number of clustered damages created by protons of different energies," *Nuclear Instruments and Methods in Physics Research Section B: Beam Interactions with Materials and Atoms*, vol. 298, pp. 47–54, 2013.

[14] S. Incerti, C. Champion, H. N. Tran, M. Karamitros, M. Bernal, Z. Francis, V. Ivanchenko, A. Mantero, *et al.*, "Energy deposition in small-scale targets of liquid water using the very low energy electromagnetic physics processes of the Geant4 toolkit," *Nuclear Instruments and Methods in Physics Research Section B: Beam Interactions with Materials and Atoms*, vol. 306, pp. 158–164, 2013.

[15] M. Tajik, A. S. H. Rozatian, and F. Semsarha, "Simulation of ultrasoft x-rays induced DNA damage using the Geant4 Monte Carlo toolkit," *Nuclear Instruments and Methods in Physics Research Section B: Beam Interactions with Materials and Atoms*, vol. 342, pp. 258–265, 2015.

[16] W. Friedland, M. Dingfelder, P. Jacob, and H. G. Paretzke, "Calculated DNA double-strand break and fragmentation yields after irradiation with he ions," *Radiation Physics and Chemistry*, vol. 72, no. 2, pp. 279–286, 2005.

[17] P. Bernhardt, W. Friedland, P. Jacob, and H. Paretzke, "Modeling of ultrasoft x-ray induced DNA damage using structured higher order DNA targets," *International Journal of Mass Spectrometry*, vol. 223, pp. 579–597, 2003.

[18] P. J. Tofilon and D. F. Deen, "BCNU-induced sister chromatid exchanges are increased by X irradiation," *Radiation research*, vol. 97, no. 1, pp. 171–177, 1984.

[19] J. F. Ward, "Biochemistry of DNA lesions," *Radiation research*, vol. 104, no. 2s, pp. S103–S111, 1985.

[20] Y. Liang, G. Yang, F. Liu, and Y. Wang, "Monte Carlo simulation of ionizing radiation induced DNA strand breaks utilizing coarse grained high-order chromatin structures," *Physics in medicine and biology*, vol. 61, no. 1, p. 445, 2015.

[21] H. Nikjoo, S. Uehara, D. Emfietzoglou, and F. Cucinotta, "Track-structure codes in radiation research," *Radiation Measurements*, vol. 41, no. 9, pp. 1052–1074, 2006.

[22] H. Nikjoo, C. E. Bolton, R. Watanabe, M. Terrissol, P. O'Neill, and D. T. Goodhead, "Modelling of DNA damage induced by energetic electrons (100 eV to 100 kev)," *Radiation protection dosimetry*, vol. 99, no. 1-4, pp. 77–80, 2002.

[23] L. Zhang and Z. Tan, "A new calculation on spectrum of direct DNA damage induced by low-energy electrons," *Radiation and environmental biophysics*, vol. 49, no. 1, pp. 15–26, 2010.

[24] W. Friedland, P. Jacob, P. Bernhardt, H. G. Paretzke, and M. Dingfelder, "Simulation of DNA damage after proton irradiation," *Radiation research*, vol. 159, no. 3, pp. 401–410, 2003.

[25] W. E. Wilson, J. H. Miller, D. J. Lynch, R. R. Lewis, and M. Batdorf, "Analysis of low-energy electron track structure in liquid water," *Radiation research*, vol. 161, no. 5, pp. 591–596, 2004.

[26] M. Zaider, D. J. Brenner, and W. E. Wilson, "The applications of track calculations to radiobiology I. Monte Carlo simulation of proton tracks," *Radiation research*, vol. 95, no. 2, pp. 231–247, 1983.

[27] S. Uehara and H. Nikjoo, "Track structure for low energy ions including charge exchange processes," *Radiation protection dosimetry*, vol. 99, no. 1-4, pp. 53–55, 2002.

[28] S. Incerti, G. Baldacchino, M. Bernal, R. Capra, C. Champion, Z. Francis, P. Guèye, A. Mantero, B. Mascialino, P. Moretto, *et al.*, "The geant4-DNA project," *International Journal of Modeling, Simulation, and Scientific Computing*, vol. 1, no. 02, pp. 157–178, 2010.

[29] S. Agostinelli, J. Allison, K. a. Amako, J. Apostolakis, H. Araujo, P. Arce, M. Asai, D. Axen, S. Banerjee, G. Barrand, *et al.*, "GEANT4—a simulation toolkit," *Nuclear instruments and methods in physics research section A: Accelerators, Spectrometers, Detectors and Associated Equipment*, vol. 506, no. 3, pp. 250–303, 2003.

[30] Z. Francis, S. Incerti, R. Capra, B. Mascialino, G. Montarou, V. Stepan, and C. Villagrasa, "Molecular scale track structure simulations in liquid water using the Geant4-DNA Monte-Carlo processes," *Applied radiation and isotopes*, vol. 69, no. 1, pp. 220–226, 2011.

[31] S. Incerti, A. Ivanchenko, M. Karamitros, A. Mantero, P. Moretto, H. Tran, B. Mascialino, C. Champion, V. Ivanchenko, M. Bernal, *et al.*, "Comparison of GEANT4 very low energy cross section models with experimental data in water," *Medical physics*, vol. 37, no. 9, pp. 4692–4708, 2010.

[32] J. M. Heller Jr, R. N. Hamm, R. D. Birkhoff, and L. R. Painter, "Collective oscillation in liquid water," *The Journal of Chemical Physics*, vol. 60, no. 9, pp. 3483–3486, 1974.

[33] I. El Naqa, P. Pater, and J. Seuntjens, "Monte Carlo role in radiobiological modelling of radiotherapy outcomes," *Physics in Medicine and Biology*, vol. 57, no. 11, p. R75, 2012.

[34] Z. Francis, C. Villagrasa, and I. Clairand, "Simulation of DNA damage clustering after proton irradiation using an adapted DBSCAN algorithm," *Computer methods and programs in biomedicine*, vol. 101, no. 3, pp. 265–270, 2011.

[35] P. Pater, G. Bäckström, F. Villegas, A. Ahnesjö, S. A. Enger, J. Seuntjens, and I. El Naqa, "Proton and light ion RBE for the induction of direct DNA double strand breaks," *Medical Physics*, vol. 43, no. 5, pp. 2131–2140, 2016.

[36] Y. W. Huang, C. Y. Pan, Y. Y. Hsiao, T. C. Chao, C. C. Lee, and C. J. Tung, "Monte Carlo simulations of the relative biological effectiveness for DNA double strand breaks from 300 MeV u-1 carbon-ion beams," *Physics in medicine and biology*, vol. 60, no. 15, p. 5995, 2015.

[37] Y.-S. Lin, T.-C. Chao, J.-H. Hong, and C.-J. Tung, "Comparisons of longitudinal and lateral dose profiles and relative biological effectiveness for DNA double strand breaks among ^{1}H, ^{4}He and ^{1}2C beams," *Radiation Physics and Chemistry*, vol. 137,

no. Supplement C, pp. 169 – 172, 2017. Proceedings of the 13th International Symposium on Radiation Physics.

[38] G. Battistoni, F. Cerutti, A. Fassò, A. Ferrari, S. Muraro, J. Ranft, S. Roesler, and P. R. Sala, "The FLUKA code: description and benchmarking," *AIP Conference Proceedings*, vol. 896, no. 1, pp. 31–49, 2007.

[39] V. A. Semenenko and R. D. Stewart, "A fast Monte Carlo algorithm to simulate the spectrum of DNA damages formed by ionizing radiation," *Radiation research*, vol. 161, no. 4, pp. 451–457, 2004.

[40] J. J. Cuaron, C. Chang, M. Lovelock, D. S. Higginson, D. Mah, O. Cahlon, and S. Powell, "Exponential increase in relative biological effectiveness along distal edge of a proton bragg peak as measured by deoxyribonucleic acid double-strand breaks," *International Journal of Radiation Oncology Biology Physics*, vol. 95, no. 1, pp. 62–69, 2016.

[41] L. J. Kuo and L.-X. Yang, "γ-H2AX-a novel biomarker for DNA double-strand breaks," *In vivo*, vol. 22, no. 3, pp. 305–309, 2008.

[42] M. A. Bernal and J. A. Liendo, "An investigation on the capabilities of the PENELOPE MC code in nanodosimetry," *Medical physics*, vol. 36, no. 2, pp. 620–625, 2009.

[43] M. A. Bernal, C. Dealmeida, C. Sampaio, S. Incerti, C. Champion, and P. Nieminen, "The invariance of the total direct DNA strand break yield," *Medical Physics*, vol. 38, no. 7, pp. 4147–4153, 2011.

[44] D. Frankenberg, H. J. Brede, U. J. Schrewe, C. Steinmetz, M. Frankenberg-Schwager, G. Kasten, and E. Pralle, "Induction of DNA double-strand breaks by ^{1}H and ^{4}He ions in primary human skin fibroblasts in the LET range of 8 to 124 keV/μm," *Radiation research*, vol. 151, no. 5, pp. 540–549, 1999.

[45] R. D. Stewart, V. K. Yu, A. G. Georgakilas, C. Koumenis, J. H. Park, and D. J. Carlson, "Effects of radiation quality and oxygen on clustered DNA lesions and cell death," *Radiation research*, vol. 176, no. 5, pp. 587–602, 2011.

Chapter 2

Fundamental considerations for simulations of biological damage

Developing macroscopic and microdosimetric considerations remains insufficient while the fundamental basis is still lacking. For truthful simulations of particle interactions with biological structures, accurate modeling of these structures and of the physical interactions is essential. For instance, it was shown that the simulated configuration of DNA has a great impact on the DNA strand break yields [1, 2]. For that reason, many geometries of varying complexity were proposed to model the biological medium. In some studies, the DNA was represented by simple cylinders and spheres [3]. In others, elementary structures for the DNA bases and for the backbone were considered [4]. More sophisticated models, for example describing the nucleosome and the chromatin fiber [2], were implemented in Monte Carlo codes, such as PARTRAC [5–7], TRION [8], PENELOPE [9, 10], KURBUC [11] and Geant4 [2, 12], enabling more truthful simulations of DNA damage. Nevertheless, the material used for these structures is water and the interactions of particles with these structures are described by the interaction cross sections with water.

Although biological structures are mainly made out of water, it has been shown in various studies that the cross sections of particle interactions with water differ significantly from particle interaction cross sections with DNA molecules, especially in the low incident electron energy range. These findings lead to many other studies attempting at determining the cross sections of particle interactions with DNA molecules and other biomolecules to improve the accuracy of the simulations. Despite the progress in computing and the tremendous research that has been done, this remains a difficult task due to the complexity of such molecules which comes from their large number of atoms as well as the many intermolecular interactions that determine their structure and their function [13, 14].

Among the interactions leading to DNA damage, the ionization by single electron impact has gained particular interest in the past decade and many studies aimed at measuring and calculating this interaction's cross sections for various atomic and molecular targets. A good description of this interaction is essential to have truthful simulations of biological damage since the low energy electrons produced through the ionization of biological molecules are greatly responsible for DNA damage. In this chapter, we recall the funda-

mental basics that are essential to understand this interaction on a theoretical level and we explain how the cross sections are determined theoretically and experimentally, highlighting the difficulty of such studies. We begin by bringing into light the importance of this fundamental approach by discussing the need to provide DNA electron ionization cross sections in the framework of Monte Carlo simulations of DNA damage.

2.1 Modeling electron interactions with DNA

As the primary ionizing particles travel through the biological medium, colliding with various biomolecules, secondary electrons and species are produced in large quantities. Low energy electrons produced from the ionization of biomolecules were proven to be greatly responsible for DNA damage and particularly DNA strand breaking [15]. These damages are created through excitation, ionization and dissociation processes caused by low energy electrons which cause DNA damage even when their energies are below the ionization threshold through dissociative electron attachment [16–18]. These findings attracted significant attention to further investigating the role of low energy electrons in DNA damage [19–23] resulting from the interactions of secondary electrons with different biomolecules such as water, sugars and DNA bases. An accurate description of these interactions is therefore necessary for simulations of biological damage.

In such simulations, cellular damage can be predicted by modeling the trajectories of the primary and secondary events as the particles travel through the biological medium. For this purpose, determining the differential interaction cross sections is essential as they provide a multi-dimensional description of the energy deposition and hence identify the spatial distribution of events. However, determining these cross sections for complex structures faces many difficulties experimentally and theoretically and so water cross sections are used in most track structure simulations instead; water being the main constituent of biological entities. The water molecule is indeed a simple molecule (H_2O) when compared to other biomolecules such as DNA bases ($C_5H_6N_2O_2$, $C_5H_5N_5O$, $C_4H_5N_3O$, $C_5H_5N_5$) and it makes up about 80% of biological structures. Nevertheless, recent studies comparing DNA cross sections with water cross sections show significant differences especially in the low incident energy range [24, 25].

In the work of *Bernhardt and Paretzke* [24], the total ionization cross sections per valence electron of DNA were calculated by dividing the sum of the cross sections for randomly chosen deoxynucleotide pairs by the number of valence electrons. They compared the resultant DNA cross sections to water total cross sections taken from [26]. As shown in figure 2.1, there is a more significant difference in DNA and water cross sections at lower energies.

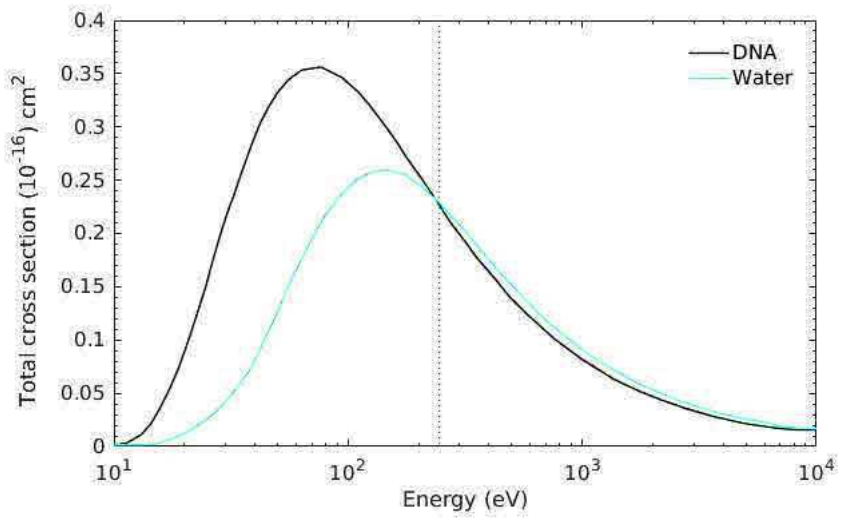

Figure 2.1: Total cross sections for the ionization by electron impact of DNA [24] and water [26] per valence electron. The vertical dotted line indicates an energy of 250 eV.

Below an incident electron energy of 250 eV, the total cross sections of DNA are significantly higher than water cross sections. Beyond this limit, little difference is observed. This work justifies the approximation of DNA material as water in simulations of DNA damage for high incident electron energies above 250 eV. On the other hand, it shows the failure of this approximation for low energy electrons and hence the falseness of using water cross sections for DNA electron ionization especially that low energy electrons are the ones who participate the most in DNA damage.

These observations pressed the need for understanding the complex dynamics of electron collisions with DNA molecules or smaller components of DNA, such as isolated DNA bases, since the biological damage was shown to take place in the elementary constituents of DNA and not in its bulk structure [27]. The molecular components of DNA are represented in figure 2.2.

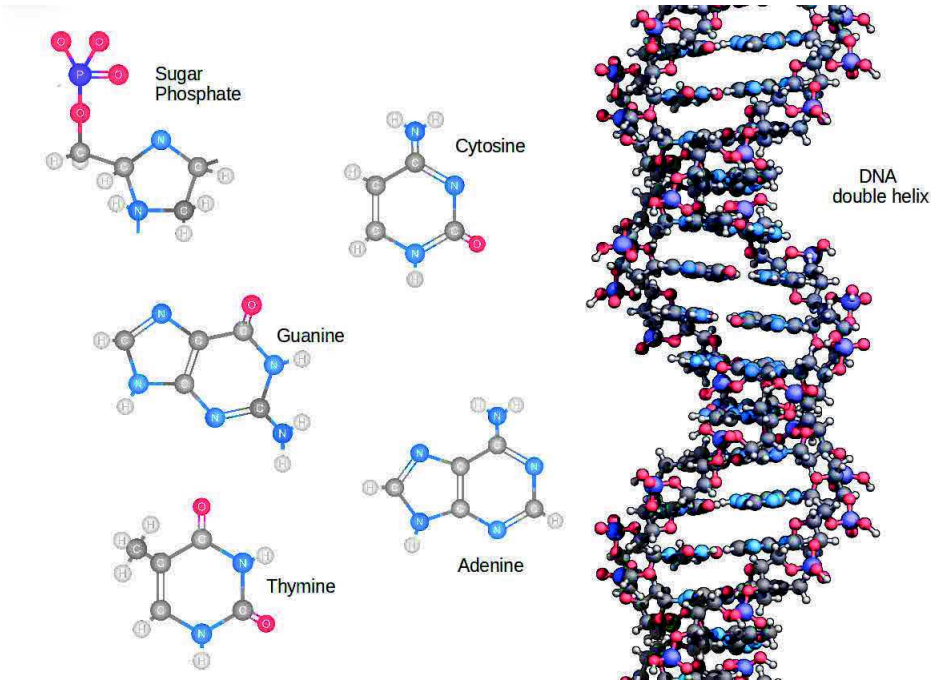

Figure 2.2: The DNA double helix and its molecular components.

Plante and Cucinotta [25] calculated the total electron ionization cross sections of the DNA bases as well as the sugar and phosphate moieties of DNA and compared them to water cross sections. This was also done in [24] but with different theoretical approaches. In figure 2.3 we present the calculated total cross sections in [25] for the electron ionization of DNA bases, the sugar and phosphate molecules, and for water. Water cross sections in figure fig:DNAmolecules are the same as those given in figure 2.3 but divided by 10 which is the number of water's valence electrons. It is clear from figure 2.3 that there is a non negligible difference between the total cross sections of DNA components and those of water.

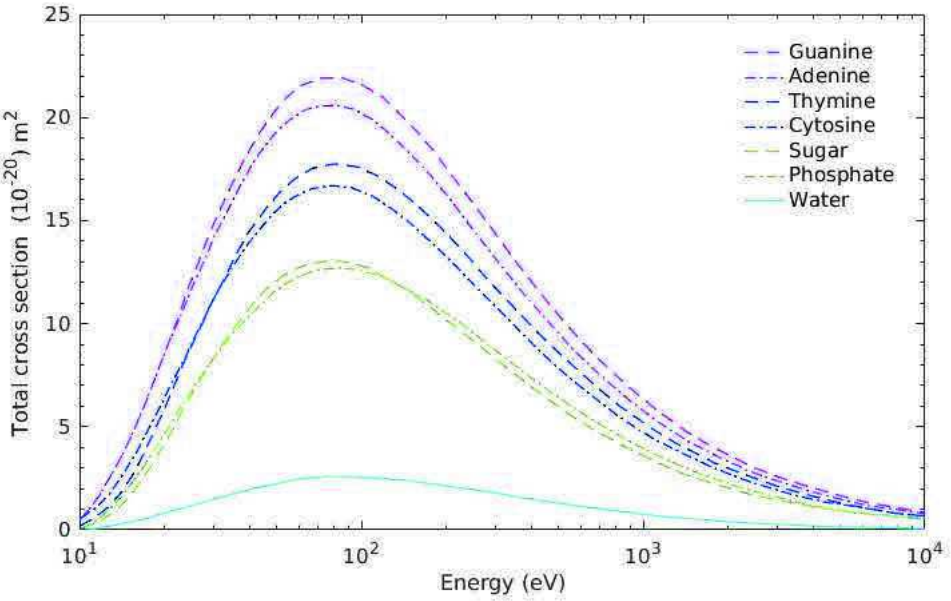

Figure 2.3: Total electron ionization cross sections of the DNA bases Guanine, Adenine, Thymine and Cytosine, sugar and phosphate entities of the DNA backbone compared to the total cross sections of water taken from [25].

It was hence suggested that the DNA should be modeled as a non-homogeneous structure using different interaction cross sections with its components to determine the probability of interaction as the electron travels through the DNA. Many studies followed using different theoretical approaches to calculate the total cross sections for the electron ionization of DNA bases and the sugar phosphate backbone [24, 28–34]. Analogues of DNA structures [29] can also serve as a probe to investigate DNA interactions since experiments providing the interaction cross sections are carried out on gaseous targets and it is difficult to prepare well-characterized pure gas from the solid components of DNA and determine their densities [35]. Theoretical studies are therefore much needed for such targets and allow to have a cross section data base to improve the description of electron collisions with DNA material. Providing the differential cross sections for DNA electron ionization is essential to have a more complete understanding of DNA electron ionization.

Although necessary, theoretical approaches have their share of difficulties. The theoretical and experimental challenges in determining the interaction cross sections are discussed in the last section of this chapter. The purpose of this work is to provide a theoretical framework that simplifies these problems and enables us to calculate the differential cross sections for the electron ionization of complex biomolecules. The theoretical approach is developed in the following chapter and we provide here the fundamental basics that are necessary for the understanding of the analytical calculations that provide the cross sections. We begin by explaining the dynamics of the ionization of molecules by electron impact before briefly presenting the theoretical and experimental methodologies to determine the cross sections of this interaction.

2.2 The process of ionization by electron impact

The ionization by single electron impact is the process through which an electron with energy E_i and momentum $\overrightarrow{k}_i$ collides with an atomic or molecular target A and extracts an electron that is ejected from A with energy E_e and momentum $\overrightarrow{k}_e$. The incident electron is scattered in a direction $\overrightarrow{k}_f$ and carries an energy E_f. The initial state of the system consists of the target A and the incoming electron e_i while the final state consists of the diffused electron e_f and the ejected electron e_e. The ionization by single electron impact can be represented as follows; A^+ being the residual ion:

$$A + e_i \rightarrow A^+ + e_f + e_e \ . \tag{2.1}$$

The kinematic constraints are the conservation of energy and momentum. The energy conservation law is:

$$E_i = E_f + E_e + IE \ , \tag{2.2}$$

where IE denotes the ionization energy of the orbital from which the e_e is ejected. The energy of the residual ion is not taken into account since it is very small compared to the energies of the other particles. The momentum conservation law reads:

$$\overrightarrow{k} = \overrightarrow{k}_i - \overrightarrow{k}_f = \overrightarrow{k}_e + \overrightarrow{q}_r \ , \tag{2.3}$$

where $\overrightarrow{k}$ is the momentum transferred from the projectile electron to the target and $\overrightarrow{q_r}$ is the recoil momentum of the residual ion. The higher the energy transferred to the target is, the more likely the electron is to be ejected following the direction of $\overrightarrow{k}$. In contrast, if the energy transfer to the target is small, the electron is ejected with two preferential directions: $\overrightarrow{k}$ and - $\overrightarrow{k}$. The probability of the -$\overrightarrow{k}$ ejection direction is directly related to the interaction between the ejected electron and the target after collision: the ejected electron is attracted by the residual ion and deflects from its path in the direction opposed to the momentum transfer.

The ionization by single electron impact was studied theoretically by calculating the triple differential cross sections (TDCS) of this interaction for many targets. The TDCS is a valuable quantity because it allows to have the probability of this interaction in function of the angular and energetic distributions of both outgoing electrons. It includes all the kinematic parameters and therefore provides a detailed description of the interaction dynamics:

$$\sigma^{(3)}(\Omega_f, \Omega_e, E_e) = \frac{2}{(2\pi)^5} \frac{k_f k_e}{k_i} \left| f_{\mathrm{B}_1} \right|^2 \ , \tag{2.4}$$

where f_{B_1} is the transition amplitude from the initial state to the final state. An exact calculation of this term is a very complex process that it sometimes becomes impossible. For this reason approximations are used to determine the matrix elements of the transition amplitude. In the Born approximation [36], the transition operator is given in the following development allowing to calculate the transition amplitude by iteration:

$$f_{\mathrm{B}_1} = V + VGV + VGVGV + \dots \ , \tag{2.5}$$

where V is the interaction potential between the projectile electron and the target and G is Green's operator [37]. In this approximation, the incident electron is considered to interact

with the target for only a short time and the two are treated independently. The interaction potential of the projectile electron with the electrons of the target is considered very small in comparison with its energy and the total target energy. The first Born approximation (FBA), consists in considering only the first term in equation 2.5 so that only one interaction of the incident electron with the target is taken into account. This approximation was widely used to calculate interaction cross sections and is particularly valid for fast projectile electron kinematics meaning that the incident and scattered electrons have a high enough energy to consider that they rapidly escape the influence of the target's particles. In general, this corresponds to incident electron energies of 250 eV as a lower limit. The TDCS calculated in the FBA is therefore given by:

$$\sigma^{(3)}(\Omega_f, \Omega_e, E_e) = \frac{d^3\sigma}{dE_e d\Omega_e d\Omega_f} = \frac{2}{(2\pi)^5}\frac{k_f k_e}{k_i}\left|\langle \Psi_f \left| V \right| \Psi_i \rangle\right|^2 , \tag{2.6}$$

where Ψ_i and Ψ_f are the initial and final states of the system respectively. Hence, to determine the TDCS we need to calculate the incident electron and the bound molecular electron wave functions making up the initial state wave function as well as the wave functions of scattered and ejected electrons making up the final state wave function. The probability of detecting the scattered electron, with energy E_f, within a solid angle Ω_f independently of the ejected electron's solid angle is given by the double differential cross section (DDCS) which can be calculated from the TDCS by integrating it over the solid angle of the ejected electron:

$$\sigma^{(2)}(\Omega_f, E_e) = \int \sigma^{(3)}(\Omega_f, \Omega_e, E_e) d\Omega_e = \frac{d^2\sigma}{d\Omega_f dE_e} . \tag{2.7}$$

Integrating the DDCS over the scattered electron solid angle yields the simple differential cross section (SDCS):

$$\sigma^{(1)}(E_e) = \int \sigma^{(2)}(\Omega_f, E_e) d\Omega_f = \frac{d\sigma}{dE_e} . \tag{2.8}$$

A total cross section can also be determined by integrating the SDCS over the ejected electron energy:

$$\sigma = \int_0^{E_i - IE} \frac{d\sigma}{dE_e} dE_e . \tag{2.9}$$

The TDCS is directly provided in experiments known as (e,2e) experiments where the two emerging electrons are detected in double coincidence.

2.3 Ionization by single electron impact (e,2e) experiments

These experiments are denoted to by the acronym (e,2e) which refers to an experiment through which a projectile electron collides with an atomic or molecular target and extracts one of its electrons. The initial and final state therefore consist of one electron (e) and two electrons (2e) respectively. In (e,2e) experiments, an incident electron beam interacts with

the particles of the target in gaseous phase and the outgoing electrons are detected through analyzers that determine the ones that result from the same ionization event. A weak target density and a slow incoming particle flux are ensured to have a particle-particle collision. The cross section is a measure of the rate of particles that undergo ionization from the total number of incident particles. It is proportional to the probability of transition P_{if} from the initial state i to a final state f and to the number of diffused particles N by unit of time. Knowing the flux F of the incoming beam and measuring the number of diffused particles per unit time N as well as the total number N_t of particles of the target, the cross section can be deduced:

$$\sigma = \frac{N}{FN_t} = \frac{P_{if}}{F} \ . \tag{2.10}$$

The total cross section takes into account all the particles that are emitted within a solid angle Ω integrated in space. In fact, not all emitted particles are detected by the analyzers and the spatial and energetic frames of detection are limited to $\Delta\Omega$ and ΔE. The differential cross sections in energy and angle provide more information since they are calculated for particular energies and directions of the incoming and outgoing electrons. The triple differential cross section is completely differential and gives the most information about the interaction dynamics since it includes all the kinematical parameters. In (e,2e) experiments, the TDCS is determined by analyzing the energy and direction of the two outgoing electrons.

Different geometries can be considered in experimental setups. In a coplanar geometry, the projectile and outgoing electrons are all detected in the scattering plane. If the two outgoing electrons are detected with the same energy or angle or both, the geometry is said to be symmetric in energy or angle or both. Since the ejected and scattered electrons are indiscernible in experiments, the faster electron is identified as the ejected electron. The theoretical framework given in the next chapter is applied to coplanar asymmetric geometries where the TDCS is given over the 0°-360° angular range. The three momentum vectors $\overrightarrow{k_i}$, $\overrightarrow{k_f}$ and $\overrightarrow{k_e}$ are in the same plane and the ejected and scattered electrons have unequal energies. The momentum vectors of the incident, scattered and ejected electrons as well as the polar angles θ_f, θ_e (θ_i=0°) are represented in the following figure. The azimuthal angles ϕ_i, ϕ_f, ϕ_e are all equal to zero in the presented geometry.

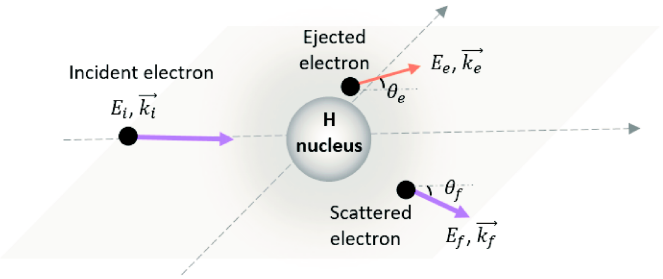

Figure 2.4: The ionization by single electron impact of the hydrogen atom in a coplanar asymmetric geometry.

These experiments not only improve our understanding of the ionization dynamics but also provide valuable information about the structure of the target. In general, when the

kinematical conditions correspond to a high energy transfer to the target, the ionization process becomes similar to a simple electron-electron interaction where the ionized target is only a spectator. In these conditions, most of the energy is transferred to the ejected electron and the interaction dynamics are greatly simplified. Such experiments serve as a probe for particular characteristics of the target's structure. For example, to determine the ionization potentials of the target's orbitals [38, 39] or the momentum distributions [40].

2.4 Electron Momentum Spectroscopy experiments

Particular kinematics of this kind of experiments are electron momentum spectroscopy (EMS) kinematics which provide the TDCSs in function of the momentum transferred to the ejected electron q_r. These experiments are usually done in non coplanar symmetric kinematics with E_i=1200 eV plus the ionization energy of the ionized orbital, $E_f = E_e$=600 eV and $\theta_f = \theta_e$ =45° [41, 42]. Since the electrons are very fast compared to the valence electrons of the target, they are described by plane waves in most theoretical studies under these conditions. The TDCSs are calculated in function of the recoil momentum q_r which is determined for each direction ϕ_e of the ejected electron.

$$q_r = \sqrt{\begin{array}{l}(-k_f sin\theta_f cos\phi_f - k_e sin\theta_e cos\phi_e)^2 \\ + (-k_f sin\theta_f sin\phi_f - k_e sin\theta_e sin\phi_e)^2 \\ + (k_i - k_f cos\theta_f - k_e cos\theta_e)^2\end{array}} . \tag{2.11}$$

In these conditions, ϕ_i=ϕ_f=0°, ϕ_e=180°-ϕ, with ϕ varied in a way to have q_r between 0 a.u. and 3 a.u. approximately. Since the incident energy is very high, we can neglect the ionization energy. Equation 2.11 becomes:

$$q_r = \sqrt{k_e^2(1 - cos\phi)} . \tag{2.12}$$

Some EMS studies were also carried out in coplanar asymmetric kinematics [43] with E_i=820 eV plus the ionization energy, E_e=105 eV, E_f=715 eV and θ_f=-20.5°. The recoil momentum is calculated as follows:

$$q_r = 2\sqrt{(E_i - \tfrac{IE}{2}) + \sqrt{E_f E_e}(cos\theta_f cos\theta_e - sin\theta_f sin\theta_e) - \sqrt{E_i}(\sqrt{E_f} cos\theta_f + \sqrt{E_e} cos\theta_e)} . \tag{2.13}$$

In this case, the momenta of the incident, scattered and ejected electrons are in the same plane and the ejected electron angle is varied so that q_r is between 0 a.u. and 3 a.u. approximately. The TDCSs are then presented as function of q_r or θ_e.

2.5 Experimental and theoretical challenges

These experiments can be very difficult depending on the considered target. For example, it is very difficult to experimentally discriminate the contributions from orbitals that are very closely separated in energy. Consequently, comparing the resultant data to theoretical calculations becomes also critical. Such studies require a high resolution experimental

apparatus, capable of identifying the individual contributions of the orbitals, and on the other hand high level calculations to accurately describe the molecular orbital wave functions. Moreover, some molecules exist under different forms that cannot be experimentally distinguished. Hence, theoretical studies should also include the added contributions from these conformers. However, the population rates of each conformer remain problematic hence limiting the sameness of the theoretical and experimental considerations.

Despite these difficulties, many theoretical models were developed and used to determine the cross sections for the ionization by single electron impact of atomic and molecular targets. As seen in the previous chapter, the interaction cross sections of particles with biological matter that are used in monte carlo codes are essential to simulate particle transport and predict the damage induced by ionizing radiation at the molecular level. Defining biological structures as water volumes in such simulations has been necessary due to the complexity of the analytical calculations that are required to determine these cross sections for the much more complex biological molecules. As the number of atoms in the molecule increases, the multiple centers render the calculations very difficult and sometimes impossible. For this reason, many more studies were performed on atomic targets or simple molecules, such as the water molecule. However, new tools that simplify these calculations are being developed and tested. Reducing the multicenter molecular wave function to a single center wave function is one of these tools that has proven to simplify the calculations without compromising the accuracy of the theoretical model [44–48]. Another theoretical challenge is to accurately describe the post collision interactions (PCI) of the ejected electron with the residual ion, with the other bound electrons and with the scattered electron. While these interactions can be neglected at high energy kinematics, they play an important role at low energy kinematics and must be taken into account in the theoretical model for a good estimation of the cross sections. In such cases, the ejected and scattered electron travel at almost the same speeds and interact one with another along their path. The repulsion between them hence needs to be included as a PCI in the theoretical model. Moreover, at very low incident energies ($<$100 eV), the ionized target's role is more and more important as the ejected electron remains close to the residual ion for a longer time. This increases the probability of multiple collisions and enhances the interaction of the ejected electron with the ionized target. The polarization of the target by the projectile electron and the distortion of the ejected electron are examples of the effects that need to be taken into account in theoretical models describing low energy interactions.

Determining the orientation of the molecule before collision is also a difficult task. Although research is being conducted to make this possible, this advancement is still in its early stage [49] and most experimental data were provided for unknown molecular alignment and orientation. The theoretical TDCSs must therefore be calculated for an average molecular orientation, which requires determining the TDCSs for all possible orientations and then deducing an average TDCS by integrating over Euler angles which define the molecular orientation. Although this method provides good agreement between experimental and theoretical results, it imposes heavy computing for sophisticated theoretical models and complex targets. Another approach was proposed to simplify these calculations, known as the orientation averaged molecular orbital (OAMO) [50]. In the OAMO, the averaging is performed on the molecular wave functions before calculating the TDCS hence eliminating the need to calculate multiple TDCSs and greatly reducing the

computing time. However this method worked for some molecules and some highly symmetric states and in particular kinematics [51–53] while it failed in other cases [54–60]. The need for a theoretical approach that allows to overcome the computing challenges without compromising the quality of the results has become urgent to profit from the experimental data that are being provided for the advancement of our understanding of particle interactions with complex molecular targets.

In this work, we address these difficulties by proposing a theoretical model to calculate the TDCS of the ionization by single electron impact of molecular targets using particular tools that enable us to simplify the complex calculations and the heavy computing without compromising the validity of the results. We begin with one of the simple theoretical models, the First Born approximation, which is used to provide the cross sections for the electron ionization process in Geant4 starting from electron energies of 11 eV up to 1 MeV. Indeed, this theoretical approach is not sufficient to describe the complexity of the interaction along the entire 11 eV- 1 MeV incident energy range. We present some of the extensive research that has been done recently to calculate the triple differential cross sections of this process for some targets mainly of biological interest. Although we focus on molecules of biological interest with the main application for this fundamental research being the integration of these advancements to support biological damage simulation in treatment planning, we develop a program that is easily applied to any molecule and hence can be used for many other purposes. We begin by presenting our theoretical framework in chapter 3, then we apply it for simple targets for which many studies were conducted allowing us to compare our results with those of similar studies and hence validate our program, and finally we present some results for more complex molecules. In fact, the framework we propose is particularly interesting for complex molecules such as the DNA bases because it allows to overcome the computing difficulties for such targets.

References

[1] M. A. Bernal, C. DeAlmeida, S. Incerti, C. Champion, V. Ivanchenko, and Z. Francis, "The influence of dna configuration on the direct strand break yield," *Computational and mathematical methods in medicine*, vol. 2015, 2015.

[2] M. Dos Santos, C. Villagrasa, I. Clairand, and S. Incerti, "Influence of the dna density on the number of clustered damages created by protons of different energies," *Nuclear Instruments and Methods in Physics Research Section B: Beam Interactions with Materials and Atoms*, vol. 298, pp. 47–54, 2013.

[3] D. T. Goodhead and H. Nikjoo, "Track structure analysis of ultrasoft x-rays compared to high-and low-let radiations," *International journal of radiation biology*, vol. 55, no. 4, pp. 513–529, 1989.

[4] D. Charlton, H. Nikjoo, and J. Humm, "Calculation of initial yields of single-and double-strand breaks in cell nuclei from electrons, protons and alpha particles," *International journal of radiation biology*, vol. 56, no. 1, pp. 1–19, 1989.

[5] W. Friedland, P. Jacob, H. G. Paretzke, and T. Stork, "Monte carlo simulation of the production of short dna fragments by low-linear energy transfer radiation using higher-order dna models," *Radiation research*, vol. 150, no. 2, pp. 170–182, 1998.

[6] W. Friedland, P. Jacob, P. Bernhardt, H. G. Paretzke, and M. Dingfelder, "Simulation of dna damage after proton irradiation," *Radiation research*, vol. 159, no. 3, pp. 401–410, 2003.

[7] W. Friedland, M. Dingfelder, P. Kundrát, and P. Jacob, "Track structures, dna targets and radiation effects in the biophysical monte carlo simulation code partrac," *Mutation Research/Fundamental and Molecular Mechanisms of Mutagenesis*, vol. 711, no. 1, pp. 28–40, 2011.

[8] V. Michalik and M. Běgusova, "Target model of nucleosome particle for track structure calculations and dna damage modelling," *International journal of radiation biology*, vol. 66, no. 3, pp. 267–277, 1994.

[9] M. Bernal and J. Liendo, "An investigation on the capabilities of the penelope mc code in nanodosimetry," *Medical physics*, vol. 36, no. 2, pp. 620–625, 2009.

[10] F. Salvat, X. Llovet, J. M. Fernández-Varea, and J. Sempau, "Monte carlo simulation in electron probe microanalysis. comparison of different simulation algorithms," *Microchimica Acta*, vol. 155, no. 1, pp. 67–74, 2006.

[11] H. Nikjoo and P. Girard, "A model of the cell nucleus for dna damage calculations," *International journal of radiation biology*, vol. 88, no. 1-2, pp. 87–97, 2012.

[12] M. A. Bernal, C. Dealmeida, C. Sampaio, S. Incerti, C. Champion, and P. Nieminen, "The invariance of the total direct dna strand break yield," *Medical Physics*, vol. 38, no. 7, pp. 4147–4153, 2011.

[13] N. Huang and A. D. MacKerell, "An ab initio quantum mechanical study of hydrogen-bonded complexes of biological interest," *The Journal of Physical Chemistry A*, vol. 106, no. 34, pp. 7820–7827, 2002.

[14] W. Qian and S. Krimm, "C- h... o and o- h... o hydrogen bonding in formic acid dimer structures: A qm/mm study confirms the common origin of their different spectroscopic behavior," *The Journal of Physical Chemistry A*, vol. 106, no. 47, pp. 11663–11671, 2002.

[15] B. Boudaïffa, P. Cloutier, D. Hunting, M. A. Huels, and L. Sanche, "Resonant formation of dna strand breaks by low-energy (3 to 20 ev) electrons," *Science*, vol. 287, no. 5458, pp. 1658–1660, 2000.

[16] R. Abouaf and H. Dunet, "Structures in dissociative electron attachment cross-sections in thymine, uracil and halouracils," *The European Physical Journal D-Atomic, Molecular, Optical and Plasma Physics*, vol. 35, no. 2, pp. 405–410, 2005.

[17] A. Kumar and M. D. Sevilla, "Low-energy electron attachment to 5 '-thymidine monophosphate: Modeling single strand breaks through dissociative electron attachment," *The Journal of Physical Chemistry B*, vol. 111, no. 19, pp. 5464–5474, 2007.

[18] J. Berdys, I. Anusiewicz, P. Skurski, and J. Simons, "Theoretical study of damage to dna by 0.2- 1.5 ev electrons attached to cytosine," *The Journal of Physical Chemistry A*, vol. 108, no. 15, pp. 2999–3005, 2004.

[19] J. Kohanoff, M. McAllister, G. Tribello, and B. Gu, "Interactions between low energy electrons and dna: A perspective from first-principles simulations.," *Journal of physics. Condensed matter: an Institute of Physics journal*, 2017.

[20] E. Alizadeh, T. M. Orlando, and L. Sanche, "Biomolecular damage induced by ionizing radiation: the direct and indirect effects of low-energy electrons on dna," *Annual review of physical chemistry*, vol. 66, pp. 379–398, 2015.

[21] S. M. Pimblott and J. A. LaVerne, "Production of low-energy electrons by ionizing radiation," *Radiation Physics and Chemistry*, vol. 76, no. 8, pp. 1244–1247, 2007.

[22] B. C. Garrett, D. A. Dixon, D. M. Camaioni, D. M. Chipman, M. A. Johnson, C. D. Jonah, G. A. Kimmel, J. H. Miller, T. N. Rescigno, P. J. Rossky, *et al.*, "Role of water in electron-initiated processes and radical chemistry: Issues and scientific advances," *Chemical Reviews*, vol. 105, no. 1, pp. 355–390, 2005.

[23] M. A. Huels, B. Boudaïffa, P. Cloutier, D. Hunting, and L. Sanche, "Single, double, and multiple double strand breaks induced in dna by 3- 100 ev electrons," *Journal of the American Chemical Society*, vol. 125, no. 15, pp. 4467–4477, 2003.

[24] P. Bernhardt and H. Paretzke, "Calculation of electron impact ionization cross sections of dna using the deutsch–märk and binary–encounter–bethe formalisms," *International Journal of Mass Spectrometry*, vol. 223, pp. 599–611, 2003.

[25] I. Plante and F. A. Cucinotta, "Binary-encounter-bethe ionisation cross sections for simulation of dna damage by the direct effect of ionising radiation," *Radiation Protection Dosimetry*, vol. 166, no. 1-4, pp. 19–23, 2015.

[26] M. Dingfelder, D. Hantke, M. Inokuti, and H. G. Paretzke, "Electron inelastic-scattering cross sections in liquid water," *Radiation Physics and Chemistry*, vol. 53, no. 1, pp. 1 – 18, 1999.

[27] P. Swiderek, "Fundamental processes in radiation damage of dna," *Angewandte Chemie International Edition*, vol. 45, no. 25, pp. 4056–4059, 2006.

[28] P. Możejko and L. Sanche, "Cross section calculations for electron scattering from dna and rna bases," *Radiation and environmental biophysics*, vol. 42, no. 3, pp. 201–211, 2003.

[29] P. Możejko and L. Sanche, "Cross sections for electron scattering from selected components of dna and rna," *Radiation Physics and Chemistry*, vol. 73, no. 2, pp. 77–84, 2005.

[30] P. Możejko, A. Domaracka, E. Ptasińska-Denga, and C. Szmytkowski, "Total cross-section measurements for electron collisions with α-tetrahydrofurfuryl alcohol (c 5 h 10 o 2)," *Chemical Physics Letters*, vol. 429, no. 4, pp. 378–381, 2006.

[31] A. Peudon, S. Edel, and M. Terrissol, "Molecular basic data calculation for radiation transport in chromatin," *Radiation protection dosimetry*, vol. 122, no. 1-4, pp. 128–135, 2006.

[32] F. Blanco and G. García, "Calculated cross sections for electron elastic and inelastic scattering from dna and rna bases," *Physics Letters A*, vol. 360, no. 6, pp. 707–712, 2007.

[33] M. Vinodkumar, C. Limbachiya, M. Barot, M. Swadia, and A. Barot, "Electron impact total ionization cross sections for all the components of dna and rna molecule," *International Journal of Mass Spectrometry*, vol. 339, pp. 16–23, 2013.

[34] M. Vinodkumar, C. Limbachiya, M. Barot, A. Barot, and M. Swadia, "Electron impact total cross sections for components of dna and rna molecules," *International Journal of Mass Spectrometry*, vol. 360, pp. 1–7, 2014.

[35] R. Ritchie, R. Hamm, J. Turner, H. Wright, and W. Bolch, "Radiation interactions and energy transport in the condensed phase," in *Physical and Chemical Mechanisms in Molecular Radiation Biology*, pp. 99–135, Springer, 1991.

[36] M. Born, "Quantum mechanics of collision processes," *Zeit fur Phys*, vol. 38, p. 803, 1926.

[37] A. Messiah, *Mécanique quantique, Tome 2*. Dunod, Paris, 1964.

[38] A. Trofimov, J. Schirmer, V. Kobychev, A. Potts, D. Holland, and L. Karlsson, "Photoelectron spectra of the nucleobases cytosine, thymine and adenine," *Journal of Physics B: Atomic, Molecular and Optical Physics*, vol. 39, no. 2, p. 305, 2005.

[39] O. Dolgounitcheva, V. Zakrzewski, and J. Ortiz, "Ionization energies and dyson orbitals of thymine and other methylated uracils," *The Journal of Physical Chemistry A*, vol. 106, no. 36, pp. 8411–8416, 2002.

[40] E. Weigold and I. McCarthy, *Electron momentum spectroscopy*. Springer Science & Business Media, 2012.

[41] A. Bawagan and C. Brion, "Studies of the electron density in the outermost orbitals of nh2ch3, nh (ch3) 2, n (ch3) 3 and nf3 by electron momentum spectroscopy: evidence for charge delocalization," *Chemical physics*, vol. 123, no. 1, pp. 51–63, 1988.

[42] C. Ning, K. Liu, Z. Luo, S. Zhang, and J. Deng, "Electron momentum spectroscopy study on valence electronic structures of pyrimidine," *Chemical Physics Letters*, vol. 476, no. 4–6, pp. 157 – 162, 2009.

[43] K. Nixon, W. Lawrance, and M. Brunger, "Electron momentum spectroscopy of formic acid," *Chemical Physics Letters*, vol. 474, no. 1, pp. 23 – 27, 2009.

[44] H. Hafied, A. Eschenbrenner, C. Champion, M. Ruiz-Lopez, C. Dal Cappello, I. Charpentier, and P.-A. Hervieux, "Electron momentum spectroscopy of the valence orbitals of the water molecule in gas and liquid phase: A comparative study," *Chemical physics letters*, vol. 439, no. 1, pp. 55–59, 2007.

[45] C. Dal Cappello, P. Hervieux, I. Charpentier, and F. Ruiz-Lopez, "Ionization of the cytosine molecule by protons: Ab initio calculation of differential and total cross sections," *Phys. Rev. A*, vol. 78, no. 4, p. 042702, 2008.

[46] C. Dal Cappello, I. Charpentier, S. Houamer, P. Hervieux, M. Ruiz-Lopez, A. Mansouri, and A. Roy, "Triple-differential cross sections for the ionization of thymine by electrons and positrons," *J. Phys. B: At. Mol. Opt. Phys.*, vol. 45, no. 17, p. 175205, 2012.

[47] C. Dal Cappello, Z. Rezkallah, S. Houamer, I. Charpentier, A. Roy, P. Hervieux, and M. Ruiz-Lopez, "Ionization of thymine by electron impact: investigation of inner shell orbitals," *Eur. Phys. J. D*, vol. 67, no. 6, p. 117, 2013.

[48] M. F. Khelladi, A. Mansouri, C. Dal Cappello, I. Charpentier, P. A. Hervieux, M. F. Ruiz-Lopez, and A. C. Roy, "Angular distributions in the double ionization of dna bases by electron impact," *J. Phys. B: At. Mol. Opt. Phys.*, vol. 49, no. 22, p. 225201, 2016.

[49] M. Mayle, R. González-Férez, and P. Schmelcher, "Controlling molecular orientation through radiative rotational transitions in strong static electric fields," *Physical Review A*, vol. 75, no. 1, p. 013421, 2007.

[50] J. Gao, J. Peacher, and D. H. Madison, "An elementary method for calculating orientation-averaged fully differential electron-impact ionization cross sections for molecules," *The Journal of chemical physics*, vol. 123, no. 20, p. 204302, 2005.

[51] J. Gao, D. H. Madison, and J. Peacher, "Theoretical calculation of fully differential cross sections for electron-impact ionization of hydrogen molecules," *Journal of Physics B: Atomic, Molecular and Optical Physics*, vol. 39, no. 6, p. 1275, 2006.

[52] J. Gao, D. H. Madison, and J. Peacher, "Fully differential cross sections for low-energy electron-impact ionization of nitrogen molecules," *Physical Review A*, vol. 72, no. 2, p. 020701, 2005.

[53] J. Gao, D. H. Madison, and J. Peacher, "Distorted wave born and three-body distorted wave born approximation calculations of the fully differential cross section for electron-impact ionization of nitrogen molecules," *The Journal of chemical physics*, vol. 123, no. 20, p. 204314, 2005.

[54] K. L. Nixon, A. J. Murray, H. Chaluvadi, C. Ning, J. Colgan, and D. H. Madison, "Low energy (e, 2 e) coincidence studies of nh3: Results from experiment and theory," *The Journal of chemical physics*, vol. 138, no. 17, p. 174304, 2013.

[55] K. Nixon, A. J. Murray, H. Chaluvadi, C. Ning, and D. H. Madison, "Low energy (e, 2e) studies from ch4: Results from symmetric coplanar experiments and molecular three-body distorted wave theory," *The Journal of chemical physics*, vol. 134, no. 17, p. 174304, 2011.

[56] K. L. Nixon, A. J. Murray, H. Chaluvadi, S. Amami, D. H. Madison, and C. Ning, "Low energy (e, 2e) measurements of ch4 and neon in the perpendicular plane," *The Journal of chemical physics*, vol. 136, no. 9, p. 094302, 2012.

[57] G. da Silva, R. Neves, L. Chiari, D. Jones, E. Ali, D. H. Madison, C. Ning, K. Nixon, M. Lopes, and M. Brunger, "Triply differential (e, 2e) studies of phenol," *The Journal of chemical physics*, vol. 141, no. 12, p. 124307, 2014.

[58] D. Jones, E. Ali, K. Nixon, P. Limão-Vieira, M.-J. Hubin-Franskin, J. Delwiche, C. Ning, J. Colgan, A. J. Murray, D. H. Madison, *et al.*, "Electron-and photon-impact ionization of furfural," *The Journal of chemical physics*, vol. 143, no. 18, p. 184310, 2015.

[59] C. J. Colyer, S. M. Bellm, B. Lohmann, G. F. Hanne, O. Al-Hagan, D. H. Madison, and C. Ning, "Dynamical (e, 2e) studies using tetrahydrofuran as a dna analog," *The Journal of chemical physics*, vol. 133, no. 12, p. 124302, 2010.

[60] D. Jones, E. Ali, C. Ning, J. Colgan, O. Ingólfsson, D. H. Madison, and M. Brunger, "Electron impact ionization dynamics of para-benzoquinone," *J. Chem. Phys.*, vol. 145, no. 16, p. 164306, 2016.

Chapter 3

A theoretical framework to calculate the TDCS for the electron impact ionization of molecules

In this chapter, we present the formalism used to calculate triple differential cross sections for the ionization by single electron impact of some molecules of different orders of complexity: water, ammonia, formic acid and tetrahydrofuran. This is done in the framework of the First Born Approximation (FBA) using two approaches. In the first one, the interaction between the ejected electron and the residual ion is described by a Coulomb interaction and hence the ejected electron is represented by a Coulomb wave function. We denote this approach by 1CW for one Coulomb Wave model. In the second approach, denoted as 1DW for one Distorted wave model, the ejected electron is described by a distorted wave derived from an averaged potential which can be considered as a Coulomb potential modified by a short range interaction. The 1DW model provides a more detailed description of the ionization process when the ejected electron is near the ionized target.

3.1 Description of the system

The triple differential cross section $\sigma^{(3)}_{\alpha,\beta,\gamma}$, for a particular molecular orientation defined by Euler angles α, β, and γ, is given in function of the transition amplitude f_{B_1} in the FBA by:

$$\sigma^{(3)}_{\alpha,\beta,\gamma} = \frac{d^3\sigma}{dE_e \mathrm{d}\Omega_e d\Omega_f} = \frac{2}{(2\pi)^5}\frac{k_f k_e}{k_i}\left|f_{\mathrm{B}_1}\right|^2 \ . \tag{3.1}$$

The transition amplitude from the initial state of the system Ψ_i to its final state Ψ_f is given by:

$$f_{\mathrm{B}_1} = \left\langle \Psi_f \left| V \right| \Psi_i \right\rangle \ . \tag{3.2}$$

The interaction potential V can be written as the sum of two main terms; $V_{e_i,k}$ and V_{e_i,e_j} which represent the interaction of the incident electron e_i with respectively the k^{th} nucleus of the target and the j^{th} bound molecular electron. We consider a purely Coulomb potential that is given by:

$$\begin{aligned} V = & \quad V_{e_i,k} \quad + \quad V_{e_i,e_j} \\ = & \sum_{k=1}^{N_{\text{atoms}}} \frac{Z_k Z_{e_i}}{\left|\overrightarrow{R} - \overrightarrow{R}_k\right|} + \sum_{j=1}^{N_{\text{electrons}}} \frac{Z_{e_j} Z_{e_i}}{\left|\overrightarrow{R} - \overrightarrow{r}_j\right|} \, . \end{aligned} \tag{3.3}$$

In the above equation, $N_{\text{electrons}}$ and N_{atoms} are respectively the number of bound electrons and the number of atoms in the molecule. Z_{e_j}, Z_{e_i}, and Z_k are the atomic numbers of respectively the j^{th} molecular electron, the incident electron and the k^{th} atom. $\overrightarrow{R}$, $\overrightarrow{r}_j$, $\overrightarrow{R}_k$ are the position vectors of respectively the origin with respect to the incident electron, the j^{th} electron with respect to the origin and the k^{th} atom with respect to the origin.

As an example, let's consider the water molecule with the Oxygen atom as the origin. In this case, $N_{\text{atoms}} = 3$, $N_{\text{electrons}} = 10$, $Z_1 = Z_2 = +1$ and $Z_3 = +8$ assuming that $k = 1, 2$ indicate the two hydrogen atoms and that $k = 3$ indicates the Oxygen atom. The position vectors used in the description of the interaction potential are illustrated in the figure 3.1.

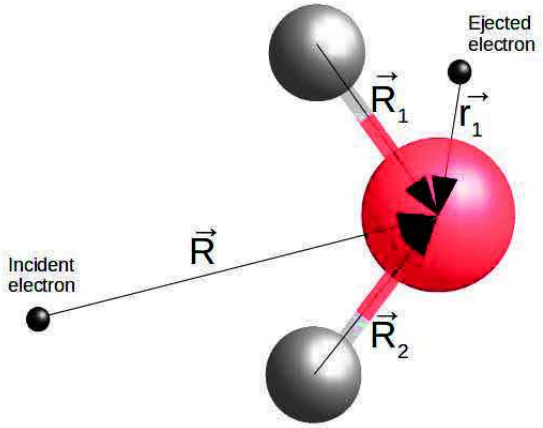

Figure 3.1: Position vectors used in the description of the interactions between the incident electron and the H_2O molecule. The ejected electron's position vector with respect to the Oxygen atom is the only molecular electron position vector that is represented. We suppose that the electron e_1 is the ejected electron.

It is clear that the interaction potential for this molecule includes 3 components for the interaction of the incident electron with the three nuclei and 10 components for the interaction of the incident electron with the 10 bound electrons:

$$V = -\frac{1}{\left|\overrightarrow{R} - \overrightarrow{R}_1\right|} - \frac{1}{\left|\overrightarrow{R} - \overrightarrow{R}_2\right|} - \frac{8}{\left|\overrightarrow{R}\right|} + \sum_{j=1}^{10} \frac{1}{\left|\overrightarrow{R} - \overrightarrow{r}_j\right|} \quad ; \quad \overrightarrow{r}_j = \overrightarrow{r}(e_j, \text{Oxygen atom}) \, . \tag{3.4}$$

The initial state wave function can therefore be written as the product of the incident electron plane wave $e^{i\vec{k}_i\cdot\vec{R}}$ and the molecular wave functions $\phi(\vec{r}_j)$ of the bound molecular electrons:

$$\begin{aligned}\psi_i &= e^{i\vec{k}_i\cdot\vec{R}}\ \phi(\vec{r}_1)\ \phi(\vec{r}_2)\ \phi(\vec{r}_3)\ \ldots\ \phi(\vec{r}_{10}) \\ &= e^{i\vec{k}_i\cdot\vec{R}}\ \phi_{\text{in}}(\vec{r}_1,\vec{r}_2,\vec{r}_3,..,\vec{r}_{10})\ ,\end{aligned} \tag{3.5}$$

$$\text{with } \phi_{\text{in}}(\vec{r}_1,\vec{r}_2,\vec{r}_3,..,\vec{r}_{10}) = \phi(\vec{r}_1)\phi(\vec{r}_2)\phi(\vec{r}_3)\ \ldots\ \phi(\vec{r}_{10})\ . \tag{3.6}$$

We suppose that e_1 is the ejected electron with position vector $\vec{r}_1 = \vec{r}$ with respect to the Oxygen atom. This electron's wave function is denoted by $\mathscr{F}^{(-)}_{\vec{k}_e}(\vec{r}_1)$ and refers to either a Coulomb wave function or a distorted wave function. We also suppose that all the other molecular electrons are passive electrons; their wave functions remain unchanged from the initial to the final state.

The final state wave function can therefore be written as follows:

$$\begin{aligned}\psi_f &= e^{i\vec{k}_f\cdot\vec{R}}\ \mathscr{F}^{(-)}_{\vec{k}_e}(\vec{r}_1)\ \phi(\vec{r}_2)\phi(\vec{r}_3)\ \ldots\ \phi(\vec{r}_{10}) \\ &= e^{i\vec{k}_f\cdot\vec{R}}\ \phi_f(\vec{r}_1,\vec{r}_2,\vec{r}_3,\ldots,\vec{r}_{10})\ ,\end{aligned} \tag{3.7}$$

$$\text{with } \phi_f(\vec{r}_1,\vec{r}_2,\vec{r}_3,\ldots,\vec{r}_{10}) = \mathscr{F}^{(-)}_{\vec{k}_e}(\vec{r}_1)\ \phi(\vec{r}_2)\phi(\vec{r}_3)\ \ldots\ \phi(\vec{r}_{10})\ . \tag{3.8}$$

3.2 The transition amplitude in the FBA

Also considering the water molecule, by replacing (3.4), (3.5) and (3.7) in (3.2) we get the following expressions of the transition amplitude:

$$
\begin{aligned}
f_{B_1} = \Big\langle e^{i\vec{k}_f\cdot\vec{R}}\phi_f(\vec{r}_1,...,\vec{r}_{10})\Big| -\frac{8}{\left|\vec{R}\right|} - \frac{1}{\left|\vec{R}-\vec{R}_1\right|} - \frac{1}{\left|\vec{R}-\vec{R}_2\right|} \\
+ \sum_{j=1}^{10}\frac{1}{\left|\vec{R}-\vec{r}_j\right|}\Big| e^{i\vec{k}_i\cdot\vec{R}}\phi_{\text{in}}(\vec{r}_1,...,\vec{r}_{10})\Big\rangle \\
= \Big\langle e^{i\vec{k}_f\cdot\vec{R}}\,\phi_f(\vec{r}_1,...,\vec{r}_{10})\Big|\sum_{j=1}^{10}\frac{1}{\left|\vec{R}-\vec{r}_j\right|}\Big|\, e^{i\vec{k}_i\cdot\vec{R}}\,\phi_{\text{in}}(\vec{r}_1,...,\vec{r}_{10})\Big\rangle \qquad (3.9) \\
- \Big\langle e^{i\vec{k}_f\cdot\vec{R}}\,\phi_f(\vec{r}_1,...,\vec{r}_{10})\Big|\frac{8}{\left|\vec{R}\right|} + \frac{1}{\left|\vec{R}-\vec{R}_1\right|} \\
+ \frac{1}{\left|\vec{R}-\vec{R}_2\right|}\Big| e^{i\vec{k}_i\cdot\vec{R}}\,\phi_{\text{in}}(\vec{r}_1,...,\vec{r}_{10})\Big\rangle\ .
\end{aligned}
$$

f_{B_1} can hence be written as the sum of two contributions E and N; E represents the interaction of the incident electron with the molecular electrons:

$$
E = \Big\langle e^{i\vec{k}_f\cdot\vec{R}}\,\phi_f(\vec{r}_1,..,\vec{r}_{10})\Big|\sum_{j=1}^{10}\frac{1}{\left|\vec{R}-\vec{r}_j\right|}\Big|\, e^{i\vec{k}_i\cdot\vec{R}}\,\phi_{\text{in}}(\vec{r}_1,...,\vec{r}_{10})\Big\rangle\ , \qquad (3.10)
$$

and N is the nuclear term due to the interaction of the incident electron with the hydrogen and Oxygen nuclei:

$$
N = -\Big\langle e^{i\vec{k}_f\cdot\vec{R}}\phi_f(\vec{r}_1,..,\vec{r}_{10})\Big|\frac{8}{\left|\vec{R}\right|} + \frac{1}{\left|\vec{R}-\vec{R}_1\right|} + \frac{1}{\left|\vec{R}-\vec{R}_2\right|}\Big| e^{i\vec{k}_i\cdot\vec{R}}\phi_{\text{in}}(\vec{r}_1,...,\vec{r}_{10})\Big\rangle\ . \qquad (3.11)
$$

Denoting $\vec{k}$ as the momentum transfer from the incident electron to the target, $\vec{k} = \vec{k}_i - \vec{k}_f$, equation (3.9) becomes:

$$
\begin{aligned}
f_{B_1} = \int \mathscr{F}^{(-)*}_{\vec{k}_e}(\vec{r}_1)\phi^*(\vec{r}_2)...\phi^*(\vec{r}_{10})\ \phi(\vec{r}_1)\phi(\vec{r}_2)...\phi(\vec{r}_{10}) \Bigg[\sum_{j=1}^{10} \int \frac{e^{i\vec{k}\cdot\vec{R}}}{\left|\vec{R}-\vec{r}_j\right|} d\vec{R} \\
- \int 8\frac{e^{i\vec{k}\cdot\vec{R}}}{\left|\vec{R}\right|} d\vec{R} - \int \frac{e^{i\vec{k}\cdot\vec{R}}}{\left|\vec{R}-\vec{R}_1\right|} d\vec{R} - \int \frac{e^{i\vec{k}\cdot\vec{R}}}{\left|\vec{R}-\vec{R}_2\right|} d\vec{R} \Bigg] d\vec{r}_1 d\vec{r}_2 .. d\vec{r}_{10} \\
= \int \mathscr{F}^{(-)*}_{\vec{k}_e}(\vec{r}_1)\phi(\vec{r}_1)\phi^*(\vec{r}_2)\phi(\vec{r}_2)...\phi^*(\vec{r}_{10})\phi(\vec{r}_{10}) \Bigg[\sum_{j=1}^{10} \int \frac{e^{i\vec{k}\cdot\vec{R}}}{\left|\vec{R}-\vec{r}_j\right|} d\vec{R} \\
- \int 8\frac{e^{i\vec{k}\cdot\vec{R}}}{\left|\vec{R}\right|} d\vec{R} - \int \frac{e^{i\vec{k}\cdot\vec{R}}}{\left|\vec{R}-\vec{R}_1\right|} d\vec{R} - \int \frac{e^{i\vec{k}\cdot\vec{R}}}{\left|\vec{R}-\vec{R}_2\right|} d\vec{R} \Bigg] d\vec{r}_1 d\vec{r}_2 .. d\vec{r}_{10} \ .
\end{aligned}
\tag{3.12}
$$

Using Bethe equality we can make the following replacements:

$$
\int \frac{e^{i\vec{k}\cdot\vec{R}}}{\left|\vec{R}-\vec{r}_j\right|} d\vec{R} = \frac{4\pi}{q^2} e^{i\vec{k}\cdot\vec{r}_j} \ , \ \int \frac{e^{i\vec{k}\cdot\vec{R}}}{\left|\vec{R}\right|} d\vec{R} = \frac{4\pi}{q^2} e^{i\vec{k}\cdot\vec{R}} \ , \ \int \frac{e^{i\vec{k}\cdot\vec{R}}}{\left|\vec{R}-\vec{R}_{1,2}\right|} d\vec{R} = \frac{4\pi}{q^2} e^{i\vec{k}\cdot\vec{R}_{1,2}} \ . \tag{3.13}
$$

Assuming a small transfer of momentum $|\vec{q}|$, $e^{i\vec{k}\cdot\vec{R}}$ and $e^{i\vec{k}\cdot\vec{R}_{1,2}}$ tend to 1 and hence:

$$
\int \phi^*(\vec{r}_j)\phi(\vec{r}_j)e^{i\vec{k}\cdot\vec{r}_j} d\vec{r}_j \to 1 \ , \ \int \phi^*(\vec{r}_j)\phi(\vec{r}_j)e^{i\vec{k}\cdot\vec{R}} d\vec{r}_j \to 1 \ , \ \int \phi^*(\vec{r}_j)\phi(\vec{r}_j)e^{i\vec{k}\cdot\vec{R}_{1,2}} d\vec{r}_j \to 1 \ . \tag{3.14}
$$

Equation (3.12) becomes:

$$
\begin{aligned}
f_{B_1} &= \int \mathscr{F}^{(-)^*}_{\vec{k}_e}(\vec{r}_1)\ \phi(\vec{r}_1)\ \frac{4\pi}{q^2} \left[e^{i\vec{k}\cdot\vec{r}_1} + 9 - 8 - 1 - 1 \right] d\vec{r}_1 \\
&= \frac{4\pi}{q^2} \int \mathscr{F}^{(-)^*}_{\vec{k}_e}(\vec{r}_1)\ \phi(\vec{r}_1)\ \left[e^{i\vec{k}\cdot\vec{r}_1} - 1 \right] d\vec{r}_1 \ .
\end{aligned}
\tag{3.15}
$$

This expression for the transition amplitude is valid for all molecules and not only the water molecule. In fact, substituting the potential in equation (3.12) with its general form, given in equation (3.3), leads to:

$$
\begin{aligned}
f_{B_1} = \int \mathscr{F}^{(-)*}_{\vec{k}_e}(\vec{r}_1)\phi(\vec{r}_1)\phi^*(\vec{r}_2)\phi(\vec{r}_2)...\phi^*(\vec{r}_{N_{electrons}})\phi(\vec{r}_{N_{electrons}}) \\
\left[\sum_{k=1}^{N_{atoms}} \int e^{i\vec{k}\cdot\vec{R}} \frac{Z_k Z_{e_i}}{\left|\vec{R}-\vec{R}_k\right|} d\vec{R} + \sum_{j=1}^{N_{electrons}} \int e^{i\vec{k}\cdot\vec{R}} \frac{Z_{e_j} Z_{e_i}}{\left|\vec{R}-\vec{r}_j\right|} d\vec{R} \right] d\vec{r}_1 \ ... \ d\vec{r}_{N_{electrons}} \ .
\end{aligned}
\tag{3.16}
$$

Using Bethe equality this becomes:

$$f_{\mathrm{B}_1} = \int \mathscr{F}^{(-)*}_{\vec{k}_e}(\vec{r}_1)\phi(\vec{r}_1)\phi^*(\vec{r}_2)\phi(\vec{r}_2)...\phi^*(\vec{r}_{N_{electrons}})\phi(\vec{r}_{N_{electrons}}) \left[-\frac{4\pi}{q^2} \sum_{k=1}^{N_{\mathrm{atoms}}} Z_k e^{i\vec{k}\cdot\vec{R_k}} + \frac{4\pi}{q^2} \sum_{j=1}^{N_{\mathrm{electrons}}} e^{i\vec{k}\cdot\vec{r}_j} \right] d\vec{r}_1 d\vec{r}_2 \ldots d\vec{r}_{N_{electrons}} . \tag{3.17}$$

For small $|\vec{q}|$ the transition amplitude reads:

$$\begin{aligned} f_{\mathrm{B}_1} &= \frac{4\pi}{q^2} \int \mathscr{F}^{(-)*}_{\vec{k}_e}(\vec{r}_1)\ \phi(\vec{r}_1) \left[-\sum_{k=1}^{N_{\mathrm{atoms}}} Z_k + e^{i\vec{k}\cdot\vec{r}_1} + \sum_{j=1}^{N_{\mathrm{electrons}}-1} 1 \right] d\vec{r}_1 \\ &= \frac{4\pi}{q^2} \int \mathscr{F}^{(-)*}_{\vec{k}_e}(\vec{r}_1)\ \phi(\vec{r}_1) \left[-\sum_{k=1}^{N_{\mathrm{atoms}}} Z_k + e^{i\vec{k}\cdot\vec{r}_1} + N_{\mathrm{electrons}} - 1 \right] d\vec{r}_1 \\ &= \frac{4\pi}{q^2} \int \mathscr{F}^{(-)*}_{\vec{k}_e}(\vec{r}_1)\ \phi(\vec{r}_1) \left[e^{i\vec{k}\cdot\vec{r}_1} - 1 \right] d\vec{r}_1 . \end{aligned} \tag{3.18}$$

Substituting the final expression of the transition amplitude in (3.1), we get:

$$\sigma^{(3)}_{\alpha,\beta,\gamma} = \frac{2}{(2\pi)^5} \frac{k_f k_e}{k_i} \left| \frac{4\pi}{q^2} \int d\vec{r}_1\ \mathscr{F}^{(-)^*}_{k_e}(\vec{r}_1)\ \phi(\vec{r}_1) \left[e^{i\vec{k}\cdot\vec{r}_1} - 1 \right] \right|^2 . \tag{3.19}$$

To solve the integral over $\vec{r_1}$ we use $\int d\vec{r}_1 = \int r_1^2 dr_1 \int d\hat{r}_1$, where r_1 and $\hat{r}_1$ are respectively the radial and angular components of $\vec{r}_1$. In order to separate the radial and angular components of the wave functions, we develop their expressions in partial wave expansion.

3.3 Partial wave expansion

Writing the wave functions in partial wave expansion simplifies the calculations and allows the translation of the theoretical framework into a parallel code. An optimization of the number of partial waves that ensures convergence of the results is important to ascertain the validity of the computed cross sections while minimizing the computing time as much as possible. This step is done automatically in our program, for each ejected electron angle, and the presented results in the next chapter are calculated considering a relative precision of 10^{-5} a.u. on the TDCSs. Hence, the number of partial waves in the series development of the projectile electron wave function is optimized and that of the ejected electron wave function is deduced from relations imposed by the triangle inequality within the Wigner-3j symbols as will be seen later in this chapter. The number of partial waves for the bound electron wave function is optimized by verifying the orthonormalization of the developed wave functions for all occupied orbitals at a chosen precision on the scalar products. In this section, we give the expressions of the wave functions of the projectile, ejected and bound electrons in partial wave expansion starting with the projectile electron.

3.3.1 The projectile electron wave function

In spherical coordinates, the partial wave expansion of the plane wave $e^{i\vec{k}\cdot\vec{r}_1}$ of the projectile electron is given by:

$$e^{i\vec{k}\cdot\vec{r}_1} = \sum_{l=0}^{\infty}\sum_{m=-l}^{+l}(4\pi)i^l j_l(kr_1)Y^*_{l,m}(\hat{k})Y_{l,m}(\hat{r}_1)\ . \tag{3.20}$$

$j_l(kr_1)$ is the spherical Bessel function and $Y^*_{l,m}(\hat{k}), Y_{l,m}(\hat{r}_1)$ are complex spherical harmonics $Y_{l,m}(\theta,\phi)$. They are calculated in terms of the associated Legendre polynomials $P_{l,m}(cos\theta)$ as follows:

$$Y_{l,m}(\theta,\phi) = (-1)^{\frac{1}{2}(m+|m|)}\sqrt{\frac{(2l+1)(l-|m|)!}{4\pi(l+|m|)!}}\,P_{l,|m|}(cos\theta)\,e^{im\phi}\ , \tag{3.21}$$

$$\text{and}: Y^*_{l,m}(\theta,\phi) = (-1)^m\,Y_{l,-m}(\theta,\phi)\ . \tag{3.22}$$

The associated Legendre polynomials $P_{l,|m|}(cos\theta)$ are calculated using the plgndr(l,m,x) fortran function using their recurrence properties.

3.3.2 The ejected electron wave function

For the ejected electron we give the wave functions in the two considered approaches: a Coulomb ejected electron wave function and a distorted ejected electron wave function.

One Coulomb wave model

In the 1CW model, the partial wave expansion of the ejected electron's Coulomb wave function $\mathscr{F}^{(-)*}_{\vec{k}_e}(\vec{r}_1)$ is:

$$\mathscr{F}^{(-)*}_{\vec{k}_e}(\vec{r}_1) = \sum_{l_e=0}^{\infty}\sum_{m_e=-l_e}^{l_e}(4\pi)(-i)^{l_e}e^{i\delta_{l_e}}\frac{F^*_{l_e}(k_e r_1)}{k_e r_1}Y_{l_e,m_e}(\hat{k}_e)Y^*_{l_e,m_e}(\hat{r}_1)\ . \tag{3.23}$$

$Y_{l_e,m_e}(\hat{k}_e), Y^*_{l_e,m_e}(\hat{r}_1)$ are complex spherical harmonics and $\delta_{l_e} = \delta^c_{l_e}$ is the Coulomb phase shift given by:

$$\delta^c_{l_e} = arg\Gamma(l_e+1+i\eta_e)\ , \tag{3.24}$$

where Γ denotes the gamma function, $\eta_e = \frac{Z}{k_e} = \frac{-1}{k_e}$ is the Sommerfeld parameter for a purely Coulomb potential, and $F_{l_e}(k_e r_1)$ is the radial hypergeometric function, solution of the Schrôdinger equation with a Coulomb potential V:

$$\left[\frac{1}{2}\frac{\mathrm{d}^2}{\mathrm{d}r_1^2} + E_e - \frac{l_e(l_e+1)}{2r_1^2} - V\right] F_{l_e}(k_e r_1) = 0 \ . \tag{3.25}$$

This function exhibits an asymptotic behavior given by:

$$F_{l_e}(k_e r_1) \sim sin(k_e r_1 - l_e\frac{\pi}{2} - \eta_e ln(2k_e r_1) + \delta_{l_e}^c) \ . \tag{3.26}$$

It can also be calculated from the confluent hypergeometric function ${}_1F_1(l_e+1-i\eta_e, 2l_e+2, 2ik_e r_1)$ as follows:

$$F_{l_e}(k_e r_1) = C_1 \ (k_e r_1)^{l_e+1} \ e_1^{-ik_e r_1} \ {}_1F_1(l_e+1-i\eta_e, 2l_e+2, 2ik_e r_1) \ , \tag{3.27}$$

with:

$$C_1 = \frac{2^{l_e} e^{-\frac{\pi\eta_e}{2}} \ |\Gamma(l_e+1+i\eta_e)|}{(2l_e+1)!} \tag{3.28}$$

The confluent hypergeometric function is calculated using Kummer's equation as a Kummer's function of the first kind:

$${}_1F_1(a,b,z) = \sum_{n=0}^{\infty} \frac{a^{(n)} z^n}{b^{(n)} n!} \quad , \quad a^{(n)} = a(a+1)(a+2)...(a+n-1) \ . \tag{3.29}$$

In our program, the radial hypergeometric function is calculated in function of the confluent hypergeometric function as explained in the above equations, with the *coulfg* fortran subroutine, by taking $\eta = -\frac{1}{k_e}$ [1]. The spherical Bessel functions $j_l(kr_1)$ in the series development of the plane wave (equation 3.20) are also calculated with this same subroutine by taking $\eta = 0$ and dividing the result by qr_1. In fact, for $\eta = 0$, the series development of the Coulomb wave function given in equation (3.23) becomes that of a plane wave with the spherical Bessel function $j_l(kr_1)$ replacing $\frac{F_{l_e}(k_e r_1)}{k_e r_1}$:

$$\mathscr{F}_{\overrightarrow{k}_e}^{(-)*}(\overrightarrow{r}_1) = \sum_{l_e,m_e} (4\pi)(-i)^{l_e} j_{l_e}^*(k_e r_1) Y_{l_e,m_e}(\hat{k}_e) Y_{l_e,m_e}^*(\hat{r}_1) \quad , \quad \text{for } \eta_e = 0 \ . \tag{3.30}$$

One distorted wave model

The partial wave expansion of the distorted wave function of the ejected electron in the 1DW model also reads:

$$\mathscr{F}^{(-)*}_{\vec{k}_e}(\vec{r}_1) = \sum_{l_e=0}^{\infty} \sum_{m_e=-l_e}^{l_e} (4\pi)(-i)^{l_e} e^{i\delta_{l_e}} \frac{F^*_{l_e}(k_e r_1)}{k_e r_1} Y_{l_e,m_e}(\hat{k}_e) Y^*_{l_e,m_e}(\hat{r}_1) \,, \tag{3.31}$$

where a short range phase shift $\delta^{sr}_{l_e}$, associated with the distortion potential, is added to the Coulomb phase shift $\delta^{c}_{l_e}$:

$$\delta_{l_e} = \delta^{c}_{l_e} + \delta^{sr}_{l_e} \,, \tag{3.32}$$

and the radial function $F_{l_e}(k_e r_1)$ is now the solution of the differential equation (3.25) with an averaged distortion potential $U = V + V_{sr}$:

$$\left[\frac{1}{2} \frac{\mathrm{d}^2}{\mathrm{d}r_1^2} + E_e - \frac{l_e(l_e+1)}{2r_1^2} - (V + V_{sr}) \right] F_{l_e}(k_e r_1) = 0 \,, \tag{3.33}$$

where V_{sr} is a short-range potential added to the Coulomb potential V and resulting from the short-range interaction of the ejected electron with the residual ion with $(N_{electrons} - 1)$ electrons.

This radial function also exhibits an asymptotic behavior as follows:

$$F_{l_e}(k_e r_1) \sim sin(k_e r_1 - l_e \frac{\pi}{2} - \eta_e ln(2k_e r_1) + \delta^{c}_{l_e} + \delta^{sr}_{l_e}) \,. \tag{3.34}$$

We calculate $F_{l_e}(k_e r_1)$ by numerically integrating the differential equation (3.33) using the Fox-Goodwin method [2] after calculating the potential U. Far from the origin, $F_{l_e}(k_e r_1)$ can be written as the comination of regular and irregular Coulomb functions $X^{(\pm)}_{l_e}$:

$$F_{l_e}(k_e r_1) \rightarrow_{r\to\infty} X^{(-)}_{l_e}(k_e, r) + e^{2i\delta_{l_e}} X^{(+)}_{l_e}(k_e, r) \,, \tag{3.35}$$

with:

$$X^{(\pm)}_{l_e}(k_e, r) = e^{(\pm i\delta^{c}_{l_e})} \{H_{l_e}(k_e r) + iG_{l_e}(k_e r)\} \tag{3.36}$$

Using the asymptotic behavior of $F_{l_e}(k_e r_1)$ in function of the regular and irregular Coulomb functions, H_{l_e} and G_{l_e} respectively, we can numerically determine the short range phase shift $\delta^{sr}_{l_e}$ generated with the *coulfg* subroutine:

$$tg(\delta^{sr}_{l_e}) = \frac{H_{l_e}(k_e, b-h)F_{l_e}(b) - H_{l_e}(k_e, b)F_{l_e}(b-h)}{G_{l_e}(k_e, b-h)F_{l_e}(b) - G_{l_e}(k_e, b)F_{l_e}(b-h)} \,, \tag{3.37}$$

where b and h are determined by the radial grid that is used; b being the maximum distance considered from the origin and $h = r_{limit}/ngrid$, $ngrid$ being the number of

points in the radial grid and r_{limit} a limit distance beyond which the effect of the short range potential becomes negligible. In fact, as the ejected electron moves away from the ion, it is the Coulomb potential that becomes more and more dominant. Far from the nucleus, at infinity, the charge seen by the fleeing electron is equal to unity: the nucleus charge minus the charge of the ion's remaining electrons. The variable charge seen by the ejected electron reads:

$$Z(r) = -r\ U(r)\ . \tag{3.38}$$

$U(r)$ is calculated as an averaged potential as follows:

$$U(r) = \frac{1}{4\pi}\int V_d(\overrightarrow{r})\mathrm{d}\hat{r}\ , \tag{3.39}$$

where $V_d(\overrightarrow{R})$ is the distortion potential given by:

$$V_d(\overrightarrow{r}) = \sum_{i=1}^{N_{atoms}} \frac{Z_{elec}Z_i}{|\overrightarrow{r} - \overrightarrow{R}_i|} + \sum_{j=1}^{N_{orbitals}} (2 - \delta_{j,j*}) \int \frac{|\phi_j(\overrightarrow{r})|^2}{|\overrightarrow{r} - \overrightarrow{r}_j|}\mathrm{d}\overrightarrow{r}\ . \tag{3.40}$$

Considering that the electron is ejected from the orbital j^*, the term $(2 - \delta_{j,j*})$ indicates the occupancy of the j^{th} orbital. $Z_{elec} = -1$ is the electron charge and Z_i is the atomic number of the i^{th} atom, $\overrightarrow{R}_i$ is the position vector of the i^{th} atom with respect to the origin, $\phi_j(\overrightarrow{r})$ is the molecular wave function of the j^{th} orbital. The integral in the second term is calculated as a Hartree Y-function. The distortion potential is in fact the sum of the contribution of ions and of the bound electrons:

$$V_d(\overrightarrow{r}) = V_{ion}(\overrightarrow{r}) + V_{elec}^{j^*}(\overrightarrow{r})\ , \tag{3.41}$$

the electronic contribution $V_{elec}^{j^*}(\overrightarrow{r})$ depends on the orbital from which the electron is ejected.

To determine the ionic contribution to the distortion potential, we use the multipole series:

$$\frac{1}{|\overrightarrow{R} - \overrightarrow{r}|} = \sum_{l,m} \frac{4\pi}{\hat{l}} \frac{r_<^l}{r_>^{l+1}} Y_{l,m}^*(\hat{R})Y_{l,m}(\hat{r}) \tag{3.42}$$

where $r_< = min(R, r)$ and $r_> = max(R, r)$.

The calculated distortion potential is then replaced in the differential equation (3.33) to calculate the distorted wave function of the ejected electron and deduce the short range phase shift $\delta_{l_e}^{sr}$.

3.3.3 The bound electron wave function

In a later section, we explain in details how the molecular wave functions are derived. We focus here only on the partial wave expansion form of these wave functions. Our theoretical formalism should provide us with molecular wave functions that can be written in partial wave expansion under this form:

$$\phi(\hat{r}_1) = \sum_{\lambda,m_\lambda} \tilde{R}^i_{\lambda,m_\lambda}(r_1) Y_{\lambda,m_\lambda}(\hat{r}_1) \ , \quad \text{for a particular orbital } i. \tag{3.43}$$

It is essential to transform the molecular wave functions from the molecule's frame to the laboratory reference frame. In order to do that, we use the rotation operator $\mathscr{R}^\lambda_{\mu,m_\lambda}(\alpha\beta\gamma)$ where α, β, γ are Euler angles providing the link between the two frames. The spherical harmonic $Y_{\lambda,m_\lambda}(\hat{r}_1)$ is transformed by this rotation operator to the spherical harmonic in the laboratory frame $Y_{\lambda,\mu}(\hat{r}_1)$:

$$Y_{\lambda,m_\lambda}(\hat{r_1}) = \sum_{\mu=-\lambda}^{\lambda} \mathscr{R}^\lambda_{\mu,m_\lambda}(\alpha\beta\gamma) Y_{\lambda,\mu}(\hat{r}_1) \ . \tag{3.44}$$

The rotation operator $\mathscr{R}^\lambda_{\mu,m_\lambda}(\alpha\beta\gamma)$ is given by:

$$\mathscr{R}^\lambda_{\mu,m_\lambda}(\alpha\beta\gamma) = e^{-i\alpha m_\lambda} \ D^\lambda_{\mu,m_\lambda}(\beta) \ e^{-i\gamma\mu} \ . \tag{3.45}$$

The coefficients associated to the operator matrix D are calculated according to the following equation where t is an integer taking all allowed values for the factorial components:

$$D^\lambda_{\mu,m_\lambda}(\beta) = \sum_t (-1)^t \frac{\sqrt{(\lambda+m_\lambda)!\,(\lambda-m_\lambda)!\,(\lambda+\mu)!\,(\lambda-\mu)!}}{(\lambda+m_\lambda-t)!(\lambda-\mu-t)!\,t!\,(t-m_\lambda+\mu)!} \left(cos\left(\frac{\beta}{2}\right)\right)^{2\lambda+m_\lambda-\mu-2t} \left(sin\left(\frac{\beta}{2}\right)\right)^{2t-m} \ . \tag{3.46}$$

The partial wave expansion of the molecular wave function therefore reads:

$$\phi(\overrightarrow{r}_1) = \sum_{\lambda,m_\lambda} \tilde{R}^i_{\lambda,m_\lambda}(r_1) \sum_{\mu=-\lambda}^{\mu=+\lambda} \mathscr{R}^\lambda_{\mu,m_\lambda}(\alpha\beta\gamma) Y_{\lambda,\mu}(\hat{r}_1) \ . \tag{3.47}$$

We can now use the developed partial wave expansions of the plane, Coulomb and molecular wave functions and replace equations (3.20), (3.23), (3.47) in equation (3.19) to calculate the TDCSs.

3.4 The triple differential cross section

Having separated the radial and angular components of the wave functions, we can now write (3.19) as follows by replacing the wave functions with their partial wave expansions:

$$\sigma^{(3)} = \frac{2}{(2\pi)^5}\,\frac{k_f k_e}{k_i}\left|\frac{4\pi}{q^2}\int_0^\infty r_1^2 \mathrm{d}r_1 \int \mathrm{d}\hat{r}_1 \sum_{l_e=0}^{\infty}\sum_{m_e=-l_e}^{l_e}(4\pi)(-i)^{l_e}e^{i\delta_{l_e}}\frac{F^*_{l_e}(k_e r_1)}{k_e r_1}Y_{l_e,m_e}(\hat{k}_e)Y^*_{l_e,m_e}(\hat{r}_1)\right.$$
$$\sum_{\lambda,m_\lambda}\tilde{R}^i_{\lambda,m_\lambda}(r_1)\sum_{\mu=-\lambda}^{\mu=+\lambda}\mathscr{R}^\lambda_{\mu,m_\lambda}(\alpha\beta\gamma)Y_{\lambda,\mu}(\hat{r}_1)$$
$$\left.\left[\sum_{l=0}^{\infty}\sum_{m=-l}^{+l}(4\pi)i^l j_l(kr_1)Y^*_{l,m}(\hat{k})Y_{l,m}(\hat{r}_1)-1\right]\right|^2 . \tag{3.48}$$

Since $Y_{0,0}(x) = \frac{1}{\sqrt{4\pi}}$ for all x we can write:

$$\sum_{l=0}^{\infty}\sum_{m=-l}^{+l}(4\pi)i^l j_l(kr_1)Y^*_{l,m}(\hat{k})Y_{l,m}(\hat{r}_1)-1 = \sum_{l=0}^{\infty}\sum_{m=-l}^{+l}(4\pi)i^l\left(j_l(kr_1)-\delta_{l,0}\right)Y^*_{l,m}(\hat{k})Y_{l,m}(\hat{r}_1)\,, \tag{3.49}$$

where $\delta_{l,0}$ is Kronecker's symbol: if $l = 0$ $\delta_{l,0} = 1$ and if $l \neq 0$ $\delta_{l,0} = 0$.

Grouping the radial terms together and the angular terms together we can rewrite the TDCS as follows:

$$\sigma^{(3)}_{\alpha,\beta,\gamma} = \frac{2}{(2\pi)^5}\,\frac{k_f}{k_i k_e}\left|\frac{4\pi}{q^2}(4\pi)^2\sum_{l_e,m_e}\sum_{\lambda,m_\lambda}\sum_{\mu}\sum_{l,m}(-i)^{l_e}i^l e^{i\delta_{l_e}}Y_{l_e,m_e}(\hat{k}_e)Y^*_{l,m}(\hat{k})\mathscr{R}^\lambda_{\mu,m_\lambda}(\alpha\beta\gamma)\right.$$
$$\int_0^\infty r_1^2\,\frac{F^*_{l_e}(k_e r_1)}{r_1}\tilde{R}^i_{\lambda,m_\lambda}(r_1)\left(j_l(kr_1)-1\right)dr_1$$
$$\left.\int Y^*_{l_e,m_e}(\hat{r}_1)Y_{\lambda,\mu}(\hat{r}_1)Y_{l,m}(\hat{r}_1)d\hat{r}_1\right|^2 . \tag{3.50}$$

Now we use the following property of the spherical harmonics:

$$\begin{aligned}\int_0^\infty d\hat{r}\,Y^*_{l_e,m_e}(\hat{r})Y_{\lambda,\mu}(\hat{r})Y_{l,m}(\hat{r}) &= (-1)^{m_e}\int Y_{l_e,-m_e}(\hat{r})Y_{\lambda,\mu}(\hat{r})Y_{l,m}(\hat{r})d\hat{r}\\ &= (-1)^{m_e}\left(\frac{\hat{l}_e\hat{\lambda}\hat{l}}{4\pi}\right)^{\frac{1}{2}}\begin{pmatrix} l_e & \lambda & l\\ 0 & 0 & 0\end{pmatrix}\begin{pmatrix} l_e & \lambda & l\\ -m_e & \mu & m\end{pmatrix}\\ &= (-1)^{m_e}\left(\frac{\hat{l}_e\hat{\lambda}\hat{l}}{4\pi}\right)^{\frac{1}{2}}\begin{pmatrix} l_e & \lambda & l\\ 0 & 0 & 0\end{pmatrix}\begin{pmatrix} l_e & \lambda & l\\ -m_e & \mu & m_e-\mu\end{pmatrix}.\end{aligned} \tag{3.51}$$

And we let:

$$\mathcal{R}^i_{l_e,l,\lambda,m_\lambda} = \int_0^\infty r_1^2\,\frac{F^*_{l_e}(k_e r_1)}{r_1}\tilde{R}^i_{\lambda,m_\lambda}(r_1)\left(j_l(kr_1)-1\right)dr_1\,, \tag{3.52}$$

$$\mathcal{A}^{\lambda,\mu}_{l_e,m_e,l} = \left(\hat{l}_e\hat{\lambda}\hat{l}\right)^{\frac{1}{2}}\begin{pmatrix} l_e & \lambda & l\\ 0 & 0 & 0\end{pmatrix}\begin{pmatrix} l_e & \lambda & l\\ -m_e & \mu & m_e-\mu\end{pmatrix}. \tag{3.53}$$

And we replace in (3.50) which becomes:

$$\sigma^{(3)} = \frac{2}{(2\pi)^5}\frac{k_f}{k_i k_e}\left|\frac{2^5\pi^{\frac{5}{2}}}{q^2}\sum_{l_e,m_e}\sum_{\lambda,m_\lambda}\sum_{\mu}\sum_{l,m}(-1)^{m_e}\, i^{l-l_e}e^{i\delta_{l_e}}Y_{l_e,m_e}(\hat{k}_e)Y^*_{l,m}(\hat{k})\mathscr{R}^{\lambda}_{\mu,m_\lambda}(\alpha\beta\gamma)\mathcal{R}^{i}_{l_e,l,\lambda,m_\lambda}\mathcal{A}^{\lambda,\mu}_{l_e,m_e,l}\right|^2 . \quad (3.54)$$

Developing the square of the norm we get:

$$\begin{aligned}\sigma^{(3)}_{\alpha,\beta,\gamma} = \frac{2^6}{q^4}\frac{k_f}{k_i k_e}&\sum_{l_e,m_e}\sum_{\lambda,m_\lambda}\sum_{\mu}\sum_{l,m}(-1)^{m_e}\, i^{l-l_e}e^{i\delta_{l_e}}Y_{l_e,m_e}(\hat{k}_e)Y^*_{l,m}(\hat{k})\mathscr{R}^{\lambda}_{\mu,m_\lambda}(\alpha\beta\gamma)\mathcal{R}^{i}_{l_e,l,\lambda,m_\lambda}\mathcal{A}^{\lambda,\mu}_{l_e,m_e,l}\\ &\sum_{\lambda',m'_\lambda}\sum_{\mu'}\sum_{l',m'}\sum_{l'_e,m'_e}(-1)^{m'_e}i^{-l'+l'_e}e^{-i\delta_{l'_e}}Y^*_{l'_e,m'_e}(\hat{k}_e)Y_{l',m'}(\hat{k})\mathscr{R}^{\lambda'*}_{\mu',m'_\lambda}(\alpha\beta\gamma)\mathcal{R}^{i}_{l_{e'},l',\lambda',m'_\lambda}\mathcal{A}^{\lambda',\mu'}_{l'_e,m'_e,l'} .\end{aligned} \quad (3.55)$$

In order to have a TDCS that is independent of the molecule's orientation, we must average the TDCS expression over all possible orientations. In experiments, it is very difficult to determine the molecular orientation before collision. Hence, most experimental data are provided for an unknown molecular orientation and for a proper comparison of theoretical data with these measurements, it is essential to calculate TDCSs for an average molecular orientation. This can be done by integrating the TDCSs dependent on Euler angles, given in equation (3.55), over all possible orientations:

$$\sigma^{(3)} = \frac{1}{8\pi^2}\int \sigma^{(3)}_{\alpha,\beta,\gamma}\mathrm{d}\Omega_{\alpha\beta\gamma} . \quad (3.56)$$

This method is known as the Proper Average (PA) method and consists in determining the TDCSs for all molecular orientations to calculate an average TDCS. When sophisticated models are used and complex molecules are studied, such calculations become very time consuming and pose many analytical difficulties. To make such studies possible, *Gao et al.* [3] proposed performing the orientation averaging on the molecular wave function (OAMO) and calculating a single TDCS. However, the validity of this method was put into question because of the discrepancies that were observed for some molecules [4–10]. The PA method on the other hand proved to give a better agreement with experimental data [11, 12]. Since our methodology allows us to overcome most of the difficulties that are encountered when studying complex molecules, we can calculate the TDCSs for an average molecular orientation without having to compromise the validity of the results.

As already noted, the rotation operator $\mathscr{R}^{\lambda}_{\mu,m_\lambda}(\alpha\beta\gamma)$ is represented by a rotation matrix $D^{\lambda}_{\mu,m_\lambda}(\alpha\beta\gamma)$ according to equation (3.45). The product of $\mathscr{R}^{\lambda}_{\mu,m_\lambda}(\alpha\beta\gamma)$ by its complex conjugate $\mathscr{R}^{\lambda*}_{\mu,m_\lambda}(\alpha\beta\gamma)$ can therefore be simply written as:

$$\mathscr{R}^{\lambda}_{\mu,m_\lambda}(\alpha\beta\gamma)\mathscr{R}^{\lambda'*}_{\mu',m'_\lambda}(\alpha\beta\gamma) = D^{\lambda}_{\mu,m_\lambda}(\alpha\beta\gamma)D^{\lambda'*}_{\mu',m'_\lambda}(\alpha\beta\gamma) . \quad (3.57)$$

The elements of the rotation matrix $D^{\lambda}_{\mu,m_\lambda}(\alpha\beta\gamma)$ form a complete set of orthogonal functions of the Euler angles. Hence:

$$\int_0^{2\pi} d\alpha \int_0^{\pi} sin(\beta) d\beta \int_0^{2\pi} D^{\lambda}_{\mu,m_\lambda}(\alpha\beta\gamma) D^{\lambda'^*}_{\mu',m'_\lambda}(\alpha\beta\gamma) d\gamma = 8\pi^2 \frac{1}{\hat{\lambda}} \delta_{\lambda\lambda'} \delta_{\mu\mu'} \delta_{m_\lambda m'_\lambda} , \tag{3.58}$$

with $\delta_{\lambda\lambda'}, \delta_{\mu\mu'}, \delta_{m_\lambda m'_\lambda} \neq 0$ for $\lambda = \lambda', \mu = \mu', m_\lambda = m'_\lambda$.

Therefore, integrating (3.55) over Euler angles leads to the following:

$$\begin{aligned}
\sigma^{(3)} &= \frac{2^6}{q^4} \frac{k_f}{k_i k_e} \sum_{\lambda,m_\lambda} \sum_{\mu} \frac{1}{\hat{\lambda}} \sum_{l_e,m_e} \sum_{l,m} (-1)^{m_e} \, i^{l-l_e} e^{i\delta_{l_e}} Y_{l_e,m_e}(\hat{k}_e) Y^*_{l,m}(\hat{k}) \mathcal{R}^i_{l_e,l,\lambda,m_\lambda} \mathcal{A}^{\lambda,\mu}_{l_e,m_e,l} \\
&\qquad \sum_{l',m'} \sum_{l'_e,m'_e} (-1)^{m'_e} i^{-l'+l'_e} e^{-i\delta_{l'_e}} Y^*_{l'_e,m'_e}(\hat{k}_e) Y_{l',m'}(\hat{k}) \mathcal{R}^i_{l_{e'},l',\lambda,m_\lambda} \mathcal{A}^{\lambda,\mu}_{l'_e,m'_e,l'} \\
&= \frac{64}{q^4} \frac{k_f}{k_i k_e} \sum_{\lambda,m_\lambda} \sum_{\mu} \frac{1}{\hat{\lambda}} \left| \sum_{l_e,m_e} \sum_{l,m} (-1)^{m_e} \, i^{l-l_e} e^{i\delta_{l_e}} Y_{l_e,m_e}(\hat{k}_e) Y^*_{l,m}(\hat{k}) \mathcal{R}^i_{l_e,l,\lambda,m_\lambda} \mathcal{A}^{\lambda,\mu}_{l_e,m_e,l} \right|^2 .
\end{aligned} \tag{3.59}$$

Denoting the term inside the squared norm as $\mathcal{S}^i_{\lambda,m_\lambda,\mu}$, the TDCS can be written as:

$$\sigma^{(3)} = \frac{64}{q^4} \frac{k_f k_e}{k_i} \sum_{\lambda,m_\lambda} \sum_{\mu} \frac{1}{\hat{\lambda}} \left| \mathcal{S}^i_{\lambda,m_\lambda,\mu} \right|^2 , \tag{3.60}$$

with:

$$\mathcal{S}^i_{\lambda,m_\lambda,\mu} = \sum_{l_e,m_e} \sum_{l,m} (-1)^{m_e} \, i^{l-l_e} e^{i\delta_{l_e}} Y_{l_e,m_e}(\hat{k}_e) Y^*_{l,m}(\hat{k}) \mathcal{R}^i_{l_e,l,\lambda,m_\lambda} \mathcal{A}^{\lambda,\mu}_{l_e,m_e,l} . \tag{3.61}$$

To evaluate the TDCS in function of the ejected electron angle θ_e, we need to provide the radial components of the molecular wave functions. All other terms can be determined knowing the collision conditions.

3.5 The molecular target wave function

To develop the molecular orbital wave functions we consider two approaches. In the two approaches the wave function of a particular molecular orbital is written as a linear combination of atomic orbitals. These atomic orbitals are expressed in terms of Slater-type functions in the first approach, in a treatment proposed by Moccia [13, 14] for many targets including H_2O and NH_3 which we present results for. Slater-type functions can be calculated analytically for atomic and small molecular targets and therefore allow the comparison of numerical results obtained with our program with analytical data in order to validate the collision description. Slater-type orbitals on distinct atoms of bigger molecules are however difficult to express. The use of Gaussian-type orbitals is therefore preferable to describe the molecular wave functions. In the second approach, we express these atomic orbitals in terms of Gaussian-type functions using a quantum chemistry software Gaussian 09 [15].

3.5.1 Slater-type wave functions

In the approach proposed by Moccia, each molecular wave function is developed in terms of Slater-type functions centered at a common origin, the heaviest atom, according to the following:

$$\phi_i(\overrightarrow{r}) = \sum_{k=1}^{N_i} a_{ik}\ \Phi^{\zeta_{ik}}_{n_{ik},\lambda_{ik},m_{\lambda_{ik}}}(\overrightarrow{r})\ , \tag{3.62}$$

where N_i is the number of Slater-type functions used to develop the i^{th} molecular wave function, a_{ik} and ζ_{ik} are coefficients characteristic of the considered target, and $\Phi^{\zeta_{ik}}_{n_{ik},\lambda_{ik},m_{\lambda_{ik}}}(\overrightarrow{r})$ are Slater-type functions that can be written as:

$$\Phi^{\zeta_{ik}}_{n_{ik},\lambda_{ik},m_{\lambda_{ik}}}(\overrightarrow{r}) = R^{\zeta_{ik}}_{n_{ik}}(r)\ H_{\lambda_{ik},m_{\lambda_{ik}}}(\hat{r})\ . \tag{3.63}$$

$R^{\zeta_{ik}}_{n_{ik}}(r)$ is the radial component given by:

$$R^{\zeta_{ik}}_{n_{ik}}(r) = \frac{2\ \zeta_{ik}^{n_{ik}+\frac{1}{2}}}{\sqrt{(2n_{ik})!}}\ r^{n_{ik}-1}\ e^{-i\zeta_{ik}r}\ , \tag{3.64}$$

and $H_{\lambda_{ik},m_{\lambda_{ik}}}$ are real spherical harmonics that can be written in terms of the complex spherical harmonics Y_{λ,m_λ} as follows:

$$H_{\lambda_{ik},m_{\lambda_{ik}}} = \begin{cases} \frac{i}{\sqrt{2}}\ \left(\ Y_{\lambda_{ik},m_{\lambda_{ik}}} - (-1)^{m_{\lambda_{ik}}}\ Y_{\lambda_{ik},-m_{\lambda_{ik}}}\ \right)\ , \ if\ m_{\lambda_{ik}} < 0 \\ Y_{\lambda_{ik},0} \qquad\qquad\qquad\qquad\qquad\qquad\quad , if\ m_{\lambda_{ik}} = 0 \\ \frac{1}{\sqrt{2}}\ \left(\ Y_{\lambda_{ik},-m_{\lambda_{ik}}} + (-1)^{m_{\lambda_{ik}}}\ Y_{\lambda_{ik},m_{\lambda_{ik}}}\ \right)\ , \ if\ m_{\lambda_{ik}} > 0\ . \end{cases} \tag{3.65}$$

In the development proposed by Moccia, the same couple (λ, m_λ) is sometimes repeated for two different Slater-type functions. Writing the real spherical harmonic $H_{\lambda m_\lambda}$ in terms of complex spherical harmonics leads to two new Slater-type radial components corresponding to (λ, m_λ) and $(\lambda, -m_\lambda)$. These same complex harmonics are also included in the development of the couple $(\lambda, -m_\lambda)$. Regrouping the complex spherical harmonics of the same couple (λ, m_λ) so that for each (λ, m_λ) corresponds only one Y_{λ,m_λ} and one $R^{\zeta}_{n}(r)$ leads to new radial parts $\Re_i^{\lambda_{ik},m_{\lambda_{ik}}}$ that are linear combinations of the original Slater-type functions defined in equation (3.64), and to a new expression of the molecular orbital where a different number $N_i^{'}$ of Slater-type functions is used to develop $\phi_i(\overrightarrow{r})$ in terms of complex spherical harmonics:

$$\phi_i(\overrightarrow{r}) = \sum_{k=1}^{N_i^{'}} \Re_i^{\lambda_{ik},m_{\lambda_{ik}}}(r)\ Y_{\lambda_{ik},m_{\lambda_{ik}}}(\hat{r})\ . \tag{3.66}$$

The molecular wave function is therefore written in the required form presented in equation (3.43) for a particular orbital i since, in the equation above, each couple (λ, m_λ) corresponds to one k value:

$$\phi_i(\overrightarrow{r}) = \sum_{\lambda_{ik}} \sum_{m_{\lambda_{ik}}} \Re_i^{\lambda_{ik}, m_{\lambda_{ik}}}(r)\, Y_{\lambda_{ik}, m_{\lambda_{ik}}}(\hat{r}) \ . \tag{3.67}$$

Although this approach provides an accurate description of the atomic orbitals, it presents many difficulties in studies of complex molecules and Gaussian-type function have been widely used for such studies. On the other hand, a much larger number of Gaussian functions is required to express the atomic orbitals than the required number of Slater functions. However, this is not really a problem when appropriate tools that allow to accelerate the computing are used.

3.5.2 Gaussian-type wave functions

In this approach, we also aim at writing the molecular wave function developed from Gaussian-type functions under the form presented in equation (3.43). To derive these wave functions, we link our program to Gaussian 09 [15]; a quantum chemistry software that allows us to generate the molecular wave functions of any molecule directly from an output file it provides and hence makes our program easily usable for any molecule.

Development of a molecular wave function from Gaussian:

The molecular orbitals developed from Gaussian are linear combinations of basis functions chosen according to a basis set specified in the input file. The molecular orbital is developed on this basis set which is a set of atomic orbitals that are Gaussian-type orbitals. Each orbital's wave function is given as a linear combination of multicenter contracted Cartesian Gaussian Type Orbitals (cGTOs). The wave function of the i^{th} molecular orbital is:

$$\phi_i(x, y, z) = \sum_{\kappa=1}^{n_c} a_{ik}\ \varphi_\kappa(x, y, z) \ , \tag{3.68}$$

where n_c is the number of contracted Gaussian-type orbitals φ_κ used in the development of the molecular wave function of the i^{th} orbital and a_{ik} is the molecular orbital coefficient for each cGTO.

Each one of these cGTOs is calculated as a linear combination of primitive Gaussian-type orbitals (pGTOs):

$$\varphi_\kappa(x, y, z) = \sum_{j=1}^{n_p} d_{\kappa j}\ X_j(x, y, z) \ , \tag{3.69}$$

where n_p is the number of primitive Gaussian-type orbitals X_j used in the development of each cGTO and $d_{\kappa j}$ are contraction coefficients for each pGTO.

The primitive Gaussian-type orbitals are given by:

$$X_j(x,y,z) = N_{\alpha,a,b,c}\ (x-x_A)^a (y-y_A)^b (z-z_A)^c\ e^{-\alpha|\vec{r}-\vec{R}_A|^2}\ , \tag{3.70}$$

where $N_{\alpha,a,b,c}$ is a normalization constant, α is an exponent that controls the width of the orbital and is given by Gaussian for each primitive orbital, a, b, c control the angular momentum $L = a + b + c$ (we will only consider s, p, d and f-type orbitals i.e. $L \leq 4$) , $\vec{R}_A = (x_A, y_A, z_A)$ is the position vector of the origin A, and $\vec{r} = (x, y, z)$ that of the bound electron with respect to this origin.

Let's consider the H_2O molecule with a Pople basis set $6-31G$. The choice of this basis set means that we want 6 primitive Gaussians for the development of the core orbital, which is the s orbital of the Oxygen atom, and 2 basis functions for the valence orbitals: the first basis function is composed of a linear combination of 3 primitive Gaussian functions and the other one is composed of 1 primitive Gaussian function. A description of basis sets is provided in details on the Gaussian website [16]. Although Slater basis sets describe more accurately the atomic orbitals, Gaussian basis sets are more commonly used because computing multiple GTOs and combining them to approximate the shape of the orbital is much easier than computing one STO.

The input file provided to Gaussian for the water molecule in the 6-31G basis set is given in figure 3.2.

```
#RHF 6-31G SP Pop=Full gfinput

H2O Fixed Geometry, 6-31G

0 1
O
H1 O 0.9583
H2 O 0.9583 H1 105.
```

Figure 3.2: Gaussian 09 input file for the water molecule in the 6-31G basis set.

The first line specifies the method (Restricted Hartree Fock (RHF) single point (SP) energy calculation) and the basis set (6-31G). The next line is the title. The one that follows provides the overall charge (0) and multiplicity (1). Most molecules have a multiplicity of 1 meaning that there are no unpaired electrons in the molecule. The three remaining lines specify the geometry of the H_2O molecule. The geometry can be given in cartesian coordinates, (x,y,z) for each atom written in Angstrom, or in a Z-matrix form as in the example above. In this representation the length and angle between the atoms are given: the H1-O and H2-O lengths are 0.9583 A^o and the H1-O-H2 angle is 105^o.

The output file given by Gaussian gives the corresponding molecular orientation as shown in the figure below.

Input orientation:

Center Number	Atomic Number	Atomic Type	Coordinates (Angstroms) X	Y	Z
1	8	0	0.000000	0.000000	0.000000
2	1	0	0.000000	0.000000	0.958300
3	1	0	0.925647	0.000000	-0.248026

Figure 3.3: Orientation of the H_2O molecule given in Gaussian 09 defined by the coordinates of each atom of the molecule.

The Oxygen atom is considered the center of the molecular reference frame. The atoms' coordinates are given in Angstrom and therefore must be converted to atomic units while calculating the molecular orbital wave functions.

The molecular orbital coefficients a_{ik} for each orbital i are also given in the Gaussian file. In figure 3.4, the part of the output file giving these coefficients for the 5 occupied orbitals of H_2O is presented. The eigenvalues represent the ionization energies in atomic units.

Molecular Orbital Coefficients:

				1 (A1)--O	2 (A1)--O	3 (B2)--O	4 (A1)--O	5 (B1)--O
Eigenvalues --				-20.56024	-1.35526	-0.71046	-0.55953	-0.50108
1	1	O	1S	0.99578	-0.21252	0.00000	-0.07551	0.00000
2			2S	0.02196	0.46919	0.00000	0.18010	0.00000
3			2PX	0.00000	0.00000	0.00000	0.00000	0.64171
4			2PY	0.00000	0.00000	0.50548	0.00000	0.00000
5			2PZ	-0.00209	-0.11087	0.00000	0.55116	0.00000
6			3S	-0.00804	0.47991	0.00000	0.30519	0.00000
7			3PX	0.00000	0.00000	0.00000	0.00000	0.50991
8			3PY	0.00000	0.00000	0.26932	0.00000	0.00000
9			3PZ	0.00194	-0.06028	0.00000	0.40396	0.00000
10	2	H	1S	0.00012	0.13984	0.26319	-0.14331	0.00000
11			2S	0.00198	-0.00827	0.12334	-0.08039	0.00000
12	3	H	1S	0.00012	0.13984	-0.26319	-0.14331	0.00000
13			2S	0.00198	-0.00827	-0.12334	-0.08039	0.00000

Figure 3.4: Molecular orbital coefficients of the 5 occupied orbitals of water given by Gaussian 09.

The molecular orbital wave function is therefore written as a linear combination of 13 cGTOs ($n_c = 13$) with the molecular coefficients given in figure 3.4. The contraction coefficients d_{kj} for the development of each cGTO in terms of primitive GTOs are also given along with the α coefficients used to develop the single-center spherical Gaussian-type orbitals, as will be explained later, in figure 3.5.

In figure 3.5, three parts are shown each corresponding to one atom. The first part starts with a line with the index 1 corresponding to the Oxygen atom as indicated in the orientation description in Figure 3.3. Five atomic orbitals expressed as contracted Gaussian-type orbitals are considered for the Oxygen atom as already seen in Figure 3.4: 1s, 2s, 2p, 3s, 3p. In the atomic orbital basis description in Figure 3.5, the two orbitals 2s and 2p as well as the two orbitals 3s and 3p are mixed into two hybrid sp orbitals. Hence 3 cGTOs are considered for the Oxygen atom. The s orbital is written in terms of 6 primitives, the first sp orbital is written in terms of 3 primitives and the second sp orbital

```
AO basis set in the form of general basis input (Overlap normalization):
     1 0
S   6 1.00       0.000000000000
     0.5484671660D+04  0.1831074430D-02
     0.8252349460D+03  0.1395017220D-01
     0.1880469580D+03  0.6844507810D-01
     0.5296450000D+02  0.2327143360D+00
     0.1689757040D+02  0.4701928980D+00
     0.5799635340D+01  0.3585208530D+00
SP   3 1.00       0.000000000000
     0.1553961625D+02 -0.1107775495D+00  0.7087426823D-01
     0.3599933586D+01 -0.1480262627D+00  0.3397528391D+00
     0.1013761750D+01  0.1130767015D+01  0.7271585773D+00
SP   1 1.00       0.000000000000
     0.2700058226D+00  0.1000000000D+01  0.1000000000D+01
****
     2 0
S   3 1.00       0.000000000000
     0.1873113696D+02  0.3349460434D-01
     0.2825394365D+01  0.2347269535D+00
     0.6401216923D+00  0.8137573261D+00
S   1 1.00       0.000000000000
     0.1612777588D+00  0.1000000000D+01
****
     3 0
S   3 1.00       0.000000000000
     0.1873113696D+02  0.3349460434D-01
     0.2825394365D+01  0.2347269535D+00
     0.6401216923D+00  0.8137573261D+00
S   1 1.00       0.000000000000
     0.1612777588D+00  0.1000000000D+01
****
```

Figure 3.5: Part of the Gaussian 09 output file for water using the 6-31G basis set giving the contraction coefficients and the α coefficients needed to develop the cGTOs in terms of pGTOs.

is written in terms of 1 primitive as defined by the choice of the 6-31G basis set. The α and d_{kj} coefficients are given in two columns: the first column indicates the α coefficients and the second column indicates the d_{kj} coefficients. In the case of the sp orbitals, the d_{kj} coefficients are given in two columns the first one for the s-type orbitals and the second for the p-type orbitals. The coefficients are given the same way for the two hydrogen atoms.

Further detail about how the information given by Gaussian are used to write the primitive, contracted and molecular orbital functions is provided in [17] for the hydrogen molecule. The same steps are followed for any other molecule.

Development of a single centered molecular wave function

The single-center formulation of the molecular wave functions [18] is often used along with the partial wave expansion method. This technique is yet another tool that simplifies the calculations and reduces computing time by overcoming the analytical difficulties of having many diffusing centers in the case of complex molecules. This methodology was used in many previous studies, for example to study the simple ionization of liquid and vapor water by electron impact [19], of cytosine by protons [20], of thymine by electrons and positrons [21, 22] and to study the double ionization of DNA bases by electron impact [23]. We now explain how single-center molecular orbital wave functions can be developed from Gaussian.

Using the information provided by Gaussian, the molecular wave function of an orbital i can now be written as:

$$\phi_i(x,y,z) = \sum_{\kappa=1}^{n_c} \sum_{j=1}^{n_p} a_{ik}\; d_{\kappa j}\; X_j(x,y,z)\;, \tag{3.71}$$

where a_{ik} and $d_{\kappa j}$ are directly provided by Gaussian.

In order to write the molecular wave functions as in equation (3.43), we first write the primitive cartesian GTOs $X_j(x,y,z)$ in terms of spherical GTOs $\phi_{\text{sph}}(\overrightarrow{r})$: instead of using the definition in equation (3.70), we develop the pGTOs as follows:

$$X_j(x,y,z) = \sum_{n,l,m} A(abc,nlm)\;\phi_{\text{sph}}(\overrightarrow{r})\;, \tag{3.72}$$

where $A(abc,nlm)$ are calculated matrix elements for each orbital type (s,p,d,f) given in detail in [17], (n,l,m) are the quantum numbers of the state described by the spherical GTOs with $2n+l=i+j+k$, $n \geq 0$, $0 \leq l \leq n-1$ and $-l \leq m \leq l$.

The molecular wave function of the i^{th} orbital reads:

$$\phi_i(x,y,z) = \sum_{\kappa=1}^{n_c} \sum_{j=1}^{n_p} \sum_{n,l,m} a_{ik}\; d_{\kappa j}\; A(abc,nlm)\;\phi_{\text{sph}}(\overrightarrow{r})\;. \tag{3.73}$$

By separating the radial and angular components of the spherical GTOs, we get a molecular orbital wave function in the form of equation (3.43). This separation has already been presented in details in [18] which gives the final expression of the spherical GTOs as follows:

$$\phi_{\text{sph}}(\overrightarrow{r}) = 4\pi N_{\alpha,n,l}\; R_A^{2n} e^{(-\alpha(r^2+R_A^2))} \sum_{l_1,l_2=0}^{l} \sum_{\tilde{l}=0}^{\infty} \sum_{l',l''} \sum_{m',m''} C(l_1,l_2,\tilde{l},l',m',l'',m'',l,m) r^{l_1} R_A^{l_2} \zeta_l^{2n}(\alpha,r,R_A) Y_{l'',m''}(\hat{R}_A) Y_{l',m'}(\hat{r})\;. \tag{3.74}$$

The α coefficients are given by Gaussian as explained in the previous paragraph and:

$$N_{\alpha,n,l} = \left[2\,\frac{(2\alpha)^{2n+l+\frac{3}{2}}}{\Gamma(2n+l+\frac{3}{2})} \right]^{2}, \tag{3.75}$$

$$C(l_1,l_2,\tilde{l},l',m',l'',m'',l,m) = (-1)^{l+m+\tilde{l}}\;\delta_{l_1+l_2,l}\;G(l_1,l_2,l)\;H(l',l'',l) \begin{pmatrix} l' & l'' & l \\ m' & m'' & -m \end{pmatrix} \begin{Bmatrix} l' & l'' & l \\ l_2 & l_1 & \tilde{l} \end{Bmatrix}\;. \tag{3.76}$$

The last two matrices in the equation above are respectively the 3-j and 6-j Wigner symbols, G and H are given by:

$$G(l_1, l_2, l) = (-1)^{l_2} \left(\frac{4\pi\ (2l+1)!}{(2l_1+1)!(2l_2+1)!} \right)^{\frac{1}{2}}, \tag{3.77}$$

$$H(l', l'', l) = \left(\frac{(2l'+1)(2l''+1)}{4\pi\ (2l+1)} \right)^{\frac{1}{2}} \langle l'\,0\,l''\,0 \mid l\,0 \rangle\ , \tag{3.78}$$

where $\langle l'\,0\,l''\,0 \mid l\,0\rangle$ is the Clebsch gordon coefficient which is calculated in terms of the 3-j Wigner symbol as follows:

$$< l'\,m'\,l''\,m'' \mid l\,m > = \ (-1)^{l'-l''+m} \sqrt{2l+1} \begin{pmatrix} l' & l'' & l \\ m' & m'' & -m \end{pmatrix}. \tag{3.79}$$

The ζ_l^{2n} function is given by:

$$\zeta_l^{2n}(\alpha, r, R_A) = 4\pi \sum_{l''=0}^{n/2} \sum_{l'=|l-l''|}^{l+l''} H^2(l', l'', l)\ R_{l''}^m(r, R_A)\ J_{l'}(2\alpha r R_A)\ . \tag{3.80}$$

H is given in equation (3.78), $R_{l''}^m(r, R_A)$ is given by:

$$R_{l''}^m(r, R_A) = \sum_{t=l''}^{m-l''} T_{l'',t}^{(m)} \left(\frac{r}{R_A} \right)^t, \tag{3.81}$$

with:

$$T_{l'',t}^{(m)} = (-1)^{l''} \frac{(m+1)!}{(m-t+l'')!!\ (m-t+l''+1)!!\ (t-l'')!!\ (t+l''+1)!!}, \tag{3.82}$$

and $J_{l'}(2\alpha r R_A)$ are the modified spherical Bessel functions given by the following equation where $I_{l'+1/2}(2\alpha r R_A)$ are calculated with the BesselI fortran 90 function in our program:

$$J_{l'}(2\alpha r R_A) = \sqrt{\frac{\pi}{2(2\alpha r R_A)}}\ I_{l'+1/2}(2\alpha r R_A)\ . \tag{3.83}$$

Calculating all the components of equation (3.74) leads to an expression of the molecular orbital wave function with separated radial and angular components, and the final form of the wave function reads:

$$\phi_i(x, y, z) = \sum_{\lambda, m_\lambda} \tilde{R}^i_{\lambda, m_\lambda}(r) Y_{\lambda, m_\lambda}(\hat{r}), \tag{3.84}$$

where $Y_{\lambda,m_\lambda}(\hat{r})$ is $Y_{l',m'}(\hat{r})$ in (3.74).

The calculations are much simpler when an atomic target is considered. In the next section, we present the analytical formalism to calculate TDCS for the ionization of the simplest atomic case: hydrogen.

3.6 The hydrogen atom

The hydrogen atom's wave functions are well known and can be found in many references. By simply adding their analytical expressions to the collision code, the collision description can be tested and the functions and subroutines that are used can be validated by comparing the code results to analytical results.

As illustrated in the figure below, the only two interactions to account for are the interaction of the incident electron with the nucleus and its interaction with the bound electron in a state i:

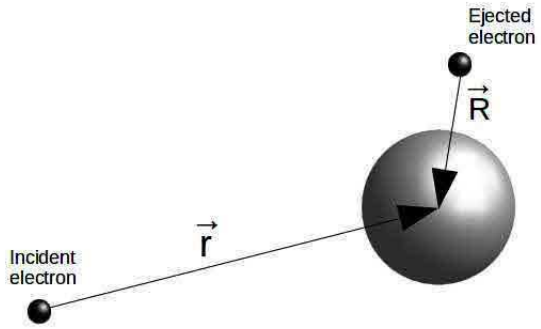

Figure 3.6: The position vectors used in the description of the interactions between the incident electron and the hydrogen atom.

The interaction potential is therefore written as:

$$V = \frac{1}{\left|\vec{r} - \vec{R}\right|} - \frac{1}{\left|\vec{R}\right|} \,. \tag{3.85}$$

The initial and final state wave functions are:

$$\Psi_i = e^{i\vec{k}_i\cdot\vec{R}}\phi_i(\vec{r}) \quad , \quad \Psi_f = e^{i\vec{k}_f\cdot\vec{R}}\mathscr{F}^{(-)}_{\vec{k}_e}(\vec{r}) \,. \tag{3.86}$$

Replacing in (3.2), the transition amplitude can be written as:

$$\begin{aligned} f_{\mathrm{B}_1} &= \left\langle e^{i\vec{k}_f\cdot\vec{R}}\mathscr{F}^{(-)}_{\vec{k}_e}(\vec{r}) \;\middle|\; \frac{1}{\left|\vec{r} - \vec{R}\right|} - \frac{1}{\left|\vec{R}\right|} \;\middle|\; e^{i\vec{k}_i\cdot\vec{R}}\phi_i(\vec{r})\right\rangle \\ &= \left[\left\langle e^{i\vec{k}_f\cdot\vec{R}}\mathscr{F}^{(-)}_{\vec{k}_e}(\vec{r}) \left|\frac{1}{\left|\vec{r}-\vec{R}\right|}\right| e^{i\vec{k}_i\cdot\vec{R}}\phi_i(\vec{r})\right\rangle - \left\langle e^{i\vec{k}_f\cdot\vec{R}}\mathscr{F}^{(-)}_{\vec{k}_e}(\vec{r}) \left|\frac{1}{\left|\vec{R}\right|}\right| e^{i\vec{k}_i\cdot\vec{R}}\phi_i(\vec{r})\right\rangle\right] \,. \end{aligned} \tag{3.87}$$

As in the molecular case, two contributions can be identified in the transition amplitude: a direct contribution D due to the interaction of the incident electron with the molecular electron and a nuclear contribution N due to its interaction with the nucleus:

$$D = \left\langle e^{i\vec{k}_f\cdot\vec{R}}\mathscr{F}^{(-)}_{\vec{k}_e}(\vec{r}) \;\middle|\; \frac{1}{\left|\vec{r}-\vec{R}\right|} \;\middle|\; e^{i\vec{k}_i\cdot\vec{R}}\phi_i(\vec{r})\right\rangle , \tag{3.88}$$

$$N = \left\langle e^{i\vec{k}_f\cdot\vec{R}}\mathscr{F}^{(-)}_{\vec{k}_e}(\vec{r}) \;\middle|\; \frac{1}{\left|\vec{R}\right|} \;\middle|\; e^{i\vec{k}_i\cdot\vec{R}}\phi_i(\vec{r})\right\rangle . \tag{3.89}$$

Considering only the direct contribution is enough to verify the functions and subroutines used in our program. So we will only present the analytical formulas for the direct contribution to the TDCS of the hydrogen states.

The direct contribution is:

$$\begin{aligned} D &= \left\langle e^{i\vec{k}_f\cdot\vec{R}}\mathscr{F}^{(-)}_{\vec{k}_e}(\vec{r}) \;\middle|\; \frac{1}{\left|\vec{r}-\vec{R}\right|} \;\middle|\; e^{i\vec{k}_i\cdot\vec{R}}\phi_i(\vec{r})\right\rangle \\ &= \int d\vec{r} \int \mathrm{d}\vec{R}\; e^{-i\vec{k}_f\cdot\vec{R}}\mathscr{F}^{(-)*}_{\vec{k}_e}(\vec{r})\frac{1}{\left|\vec{r}-\vec{R}\right|} e^{i\vec{k}_i\cdot\vec{R}}\,\phi_i(\vec{r}) \\ &= \int \mathscr{F}^{(-)*}_{\vec{k}_e}(\vec{r})\,\phi_i(\vec{r})\,d\vec{r}\int \frac{e^{i(\vec{k}_i-\vec{k}_f)\cdot\vec{R}}}{\left|\vec{r}-\vec{R}\right|}\,d\vec{R} \\ &= \int \mathscr{F}^{(-)*}_{\vec{k}_e}(\vec{r})\,\phi_i(\vec{r})\,d\vec{r}\int \frac{e^{i\vec{k}\cdot\vec{R}}}{\left|\vec{r}-\vec{R}\right|}\,d\vec{R}\;;\;\; \vec{k} = \vec{k}_i - \vec{k}_f\;. \end{aligned} \tag{3.90}$$

Using Bethe equality we get:

$$D = \frac{4\pi}{q^2}\int \mathscr{F}^{(-)*}_{\vec{k}_e}(\vec{r})\,\phi_i(\vec{r})\;e^{i\vec{k}\cdot\vec{r}}\;d\vec{r}\;. \tag{3.91}$$

We also use the partial wave expansion for the projectile, ejected and bound electron's wave functions given in equations (3.20), (3.23), (3.23), and (3.43).

Let's consider a state $(n_i, \lambda_i, m_{\lambda_i})$, the wave function of the bound electron can be written as follows:

$$\phi_i(\vec{r}) = \tilde{R}^{(i)}_{n_i,\lambda_i}(r)Y_{\lambda_i,m_{\lambda_i}}(\hat{r})\;. \tag{3.92}$$

Replacing in (3.91) :

$$D = \frac{4\pi}{q^2}(4\pi)(4\pi)\sum_{l,m}\sum_{l_e,m_e} i^l(-i)^{l_e}e^{i\delta_{l_e}}Y^*_{l,m}(\hat{k})Y_{l_e,m_e}(\hat{k}_e)\int_0^\infty r^2\tilde{R}_{n_i,\lambda}(r)\frac{F^*_{l_e}(k_e r)}{k_e r}j_l(kr)\,dr \int Y^*_{l_e,m_e}(\hat{r})Y_{l,m}(\hat{r})Y_{\lambda,m_\lambda}(\hat{r})\,d\hat{r}\ . \tag{3.93}$$

We also use the property in equation (3.51) for $\int Y^*_{l_e,m_e}(\hat{r})Y_{l,m}(\hat{r})Y_{\lambda,m_\lambda}(\hat{r})\,d\hat{r}$ and the following:

$$\mathcal{R}^i_{l_e,l,\lambda} = \int_0^\infty r^2\ \tilde{R}_{n_i,\lambda}(r)\frac{F^*_{l_e}(k_e r)}{r}j_l(kr)\,dr\ , \tag{3.94}$$

$$\mathcal{A}^{\lambda,m_\lambda}_{l_e,m_e,l} = \left(\hat{l}_e\hat{l}\hat{\lambda}\right)^{\frac{1}{2}}\begin{pmatrix} l_e & l & \lambda \\ 0 & 0 & 0\end{pmatrix}\begin{pmatrix} l_e & l & \lambda \\ -m_e & m_e-m_\lambda & m_\lambda\end{pmatrix}\ . \tag{3.95}$$

The direct contribution can therefore be written as:

$$\begin{aligned} D &= \frac{2^6\pi^3}{q^2}\frac{1}{\sqrt{4\pi}}\sum_{l,m}\sum_{l_e,m_e}(-1)^{m_e}i^{l-l_e}e^{i\delta_{l_e}}Y^*_{l,m}(\hat{k})Y_{l_e,m_e}(\hat{k}_e)\mathcal{R}^i_{l_e,l,\lambda}\mathcal{A}^{\lambda,m_\lambda}_{l_e,m_e,l} \\ &= \frac{2^5\pi^{\frac{5}{2}}}{q^2}\sum_{l,m}\sum_{l_e,m_e}(-1)^{m_e}i^{l-l_e}e^{i\delta_{l_e}}Y^*_{l,m}(\hat{k})Y_{l_e,m_e}(\hat{k}_e)\mathcal{R}^i_{l_e,l,\lambda}\mathcal{A}^{\lambda,m_\lambda}_{l_e,m_e,l}\ . \end{aligned} \tag{3.96}$$

Considering only this contribution ($f_{\mathrm{B}_1} = D$) and replacing in (3.1), leads to the following TDCS for a state $n_i, \lambda_i, m_{\lambda_i}$ of the hydrogen atom:

$$\begin{aligned} \sigma^{(3)} &= \frac{k_f}{k_i k_e}\left|\frac{-2^{\frac{5}{2}}}{q^2}\sum_{l,m}\sum_{l_e,m_e}(-1)^{m_e}i^{l-l_e}e^{i\delta_{l_e}}Y^*_{l,m}(\hat{k})Y_{l_e,m_e}(\hat{k}_e)\mathcal{R}^i_{l_e,l,\lambda}\mathcal{A}^{\lambda,m_\lambda}_{l_e,m_e,l}\right|^2 \\ &= \frac{2^5}{q^4}\frac{k_f}{k_i k_e}\left|\sum_{l,m}\sum_{l_e,m_e}(-1)^{m_e}i^{l-l_e}e^{i\delta_{l_e}}Y^*_{l,m}(\hat{k})Y_{l_e,m_e}(\hat{k}_e)\mathcal{R}^i_{l_e,l,\lambda}\mathcal{A}^{\lambda,m_\lambda}_{l_e,m_e,l}\right|^2\ . \end{aligned} \tag{3.97}$$

In order to have the TDCS for a state n_i, λ, we sum all the contributions from individual m_λ values:

$$\sigma^{(3)} = \frac{k_f}{k_i k_e}\frac{2^5}{q^4}\sum_{m_\lambda=-\lambda}^{\lambda}\left|\sum_{l,m}\sum_{l_e,m_e}(-1)^{m_e}i^{l-l_e}e^{i\delta_{l_e}}Y^*_{l,m}(\hat{k})Y_{l_e,m_e}(\hat{k}_e)\mathcal{R}^i_{l_e,l,\lambda}\mathcal{A}^{\lambda,m_\lambda}_{l_e,m_e,l}\right|^2\ . \tag{3.98}$$

This is equivalent to making the average over all possible orientations in the molecular case. To further simplify the calculations, we consider the ionization of hydrogen in an s state.

hydrogen s state

If we consider an s state ($n, \lambda = 0, m_\lambda = 0$), the angular component of the bound electron's wave function is independent of the angle:

$$\phi_i(\overrightarrow{r}) = \tilde{R}^{(i)}_{n_i,\lambda_i}(r) Y_{\lambda_i,m_{\lambda_i}}(\hat{r}) = \tilde{R}^{(i)}_{n_i,0}(r) Y_{0,0}(\hat{r}) = \tilde{R}^{(i)}_{n_i,0}(r) \frac{1}{\sqrt{4\pi}} \ . \tag{3.99}$$

Replacing in (3.91) gives the direct contribution as follows:

$$D = \tfrac{4\pi}{q^2}(4\pi)(4\pi) \sum_{l,m} \sum_{l_e,m_e} i^{l-l_e} e^{i\delta_{l_e}} Y^*_{l,m}(\hat{k}) Y_{l_e,m_e}(\hat{k}_e) Y_{0,0}(\hat{r}) \int_0^\infty r^2 \, \tilde{R}_{n_i,0}(r) \frac{F^*_{l_e}(k_e r)}{k_e r} j_l(kr) \, dr \int Y^*_{l_e,m_e}(\hat{r}) Y_{l,m}(\hat{r}) \, d\hat{r} \ . \tag{3.100}$$

Using the orthonormalization relation:

$$\int Y^*_{l_e,m_e}(\hat{r}) Y_{l,m}(\hat{r}) \, d\hat{r} = \delta_{l_e,l} \, \delta_{m_e,m} \ , \tag{3.101}$$

the direct contribution becomes:

$$\begin{aligned} D &= \frac{2^6\pi^3}{q^2} \sum_{l,m} e^{i\delta_l} Y^*_{l,m}(\hat{k}) Y_{l,m}(\hat{k}_e) Y_{0,0}(\hat{r}) \int_0^\infty r^2 \, \tilde{R}_{n_i,0}(r) \frac{F^*_l(k_e r)}{k_e r} j_l(kr) \, dr \\ &= \frac{2^6\pi^3}{q^2} \frac{1}{k_e} \sum_{l,m} e^{i\delta_l} Y^*_{l,m}(\hat{k}) Y_{l,m}(\hat{k}_e) Y_{0,0}(\hat{r}) \mathcal{R}^i_{l,0}(r) \ , \end{aligned} \tag{3.102}$$

with:

$$\mathcal{R}^i_{l,0}(r) = \int r^2 \, \tilde{R}_{n_i,0}(r) \frac{F^*_l(k_e r)}{r} j_l(kr) \, dr \ . \tag{3.103}$$

Assuming $f_{\mathrm{B}_1} = D$ and replacing in (3.1), the TDCS for an s-state of the hydrogen atom:

$$\begin{aligned} \sigma^{(3)} &= \frac{2}{(2\pi)^5} \frac{k_f}{k_i k_e} \left| \frac{2^6\pi^3}{q^2} \sum_{l,m} e^{i\delta_l} Y^*_{l,m}(\hat{k}) Y_{l,m}(\hat{k}_e) Y_{0,0}(\hat{r}) \mathcal{R}^i_{l,0}(r) \right|^2 \\ &= \frac{2^8\pi}{q^4} \frac{k_f}{k_i k_e} \left| \sum_{l,m} e^{i\delta_l} Y^*_{l,m}(\hat{k}) Y_{l,m}(\hat{k}_e) Y_{0,0}(\hat{r}) \mathcal{R}^i_{l,0}(r) \right|^2 . \end{aligned} \tag{3.104}$$

These expressions of the TDCS are programmed using the same functions and subroutines as the ones used for the molecular target case. Comparing the TDCS given by our program to published TDCSs allows us to validate these functions hence to validate the collision description in our molecular target program.

References

[1] A. R. Barnett, D. H. Feng, J. W. Steed, and L. J. B. Goldfarb, "Coulomb wave functions for all real n and q," *Computer Physics Communications*, vol. 8, no. 5, pp. 377 – 395, 1974.

[2] E. W. Schmid, G. Spitz, and W. Lösch, "Solution of the Radial Schrödinger Equation by the Fox-Goodwin Method," in *Theoretical Physics on the Personal Computer*, pp. 136–148, Springer, 1990.

[3] J. Gao, J. L. Peacher, and D. H. Madison, "An elementary method for calculating orientation-averaged fully differential electron-impact ionization cross sections for molecules," *Journal of Chemical Physics*, vol. 123, no. 20, p. 204302, 2005.

[4] K. L. Nixon, A. J. Murray, H. Chaluvadi, C. Ning, J. Colgan, and D. H. Madison, "Low energy (e, 2 e) coincidence studies of NH_3: Results from experiment and theory," *Journal of Chemical Physics*, vol. 138, no. 17, p. 174304, 2013.

[5] K. L. Nixon, A. J. Murray, H. Chaluvadi, C. G. Ning, and D. H. Madison, "Low energy (e, 2e) studies from CH_4: Results from symmetric coplanar experiments and molecular three-body distorted wave theory," *Journal of Chemical Physics*, vol. 134, no. 17, p. 174304, 2011.

[6] K. L. Nixon, A. J. Murray, H. Chaluvadi, S. Amami, D. H. Madison, and C. G. Ning, "Low energy (e, 2e) measurements of CH_4 and neon in the perpendicular plane," *Journal of Chemical Physics*, vol. 136, no. 9, p. 094302, 2012.

[7] G. B. Da Silva, R. F. C. Neves, L. Chiari, D. B. Jones, E. Ali, D. H. Madison, C. G. Ning, K. L. Nixon, M. C. A. Lopes, and M. J. Brunger, "Triply differential (e, 2e) studies of phenol," *Journal of Chemical Physics*, vol. 141, no. 12, p. 124307, 2014.

[8] D. B. Jones, E. Ali, K. L. Nixon, P. Limão-Vieira, M. J. Hubin-Franskin, J. Delwiche, C. G. Ning, J. Colgan, A. J. Murray, D. H. Madison, *et al.*, "Electron-and photon-impact ionization of furfural," *Journal of Chemical Physics*, vol. 143, no. 18, p. 184310, 2015.

[9] C. J. Colyer, S. M. Bellm, B. Lohmann, G. F. Hanne, O. Al-Hagan, D. H. Madison, and C. G. Ning, "Dynamical (e,2e) studies using tetrahydrofuran as a DNA analog," *Journal of Chemical Physics*, vol. 133, no. 12, p. 124302, 2010.

[10] D. B. Jones, E. Ali, C. G. Ning, J. Colgan, O. Ingólfsson, D. H. Madison, and M. J. Brunger, "Electron impact ionization dynamics of para-benzoquinone," *Journal of Chemical Physics*, vol. 145, no. 16, p. 164306, 2016.

[11] H. Chaluvadi, C. G. Ning, and D. H. Madison, "Theoretical triple-differential cross sections of a methane molecule by a proper-average method," *Physical Review A*, vol. 89, no. 6, p. 062712, 2014.

[12] E. Ali, K. Nixon, A. Murray, C. G. Ning, J. Colgan, and D. H. Madison, "Comparison of experimental and theoretical electron-impact-ionization triple-differential cross sections for ethane," *Physical Review A*, vol. 92, p. 042711, Oct 2015.

[13] R. Moccia, "One-Center Basis Set SCF MO's. II. NH_3, NH_4^+, PH_3, PH_4^+," *The Journal of Chemical Physics*, vol. 40, no. 8, pp. 2176–2185, 1964.

[14] R. Moccia, "One-Center Basis Set SCF MO's. III. H_2O, H_2S, and HCl," *The Journal of Chemical Physics*, vol. 40, no. 8, pp. 2186–2192, 1964.

[15] M. J. Frisch, G. W. Trucks, H. B. Schlegel, G. E. Scuseria, M. A. Robb, J. R. Cheeseman, G. Scalmani, V. Barone, G. A. Petersson, H. Nakatsuji, *et al.*, "Gaussian 09, Revision A. 02. Wallingford, CT: Gaussian," *Inc.*, 2016.

[16] "MS Windows NT kernel description." `http://gaussian.com/basissets/`.

[17] H. D. Hafied, *Etude théorique de l'ionisation par impact électronique des molécules d'eau en phase gazeuse et liquide*. PhD thesis, Metz, 2007.

[18] K. Kaufmann and W. Baumeister, "Single-centre expansion of Gaussian basis functions and the angular decomposition of their overlap integrals," *Journal of Physics B: Atomic, Molecular and Optical Physics*, vol. 22, no. 1, p. 1, 1989.

[19] H. D. Hafied, A. Eschenbrenner, C. Champion, M. F. Ruiz-Lopez, C. Dal Cappello, I. Charpentier, and P. A. Hervieux, "Electron momentum spectroscopy of the valence orbitals of the water molecule in gas and liquid phase: A comparative study," *Chemical Physics Letters*, vol. 439, no. 1, pp. 55–59, 2007.

[20] C. Dal Cappello, P. A. Hervieux, I. Charpentier, and M. F. Ruiz-Lopez, "Ionization of the cytosine molecule by protons: ab initio calculation of differential and total cross sections," *Physical Review A*, vol. 78, no. 4, p. 042702, 2008.

[21] C. Dal Cappello, I. Charpentier, S. Houamer, P. A. Hervieux, M. F. Ruiz-Lopez, A. Mansouri, and A. C. Roy, "Triple-differential cross sections for the ionization of thymine by electrons and positrons," *Journal of Physics B: Atomic, Molecular and Optical Physics*, vol. 45, no. 17, p. 175205, 2012.

[22] C. Dal Cappello, Z. Rezkallah, S. Houamer, I. Charpentier, A. C. Roy, P. A. Hervieux, and M. F. Ruiz-Lopez, "Ionization of thymine by electron impact: investigation of inner shell orbitals," *The European Physical Journal D*, vol. 67, no. 6, p. 117, 2013.

[23] M. F. Khelladi, A. Mansouri, C. Dal Cappello, I. Charpentier, P. A. Hervieux, M. F. Ruiz-Lopez, and A. C. Roy, "Angular distributions in the double ionization of DNA bases by electron impact," *Journal of Physics B: Atomic, Molecular and Optical Physics*, vol. 49, no. 22, p. 225201, 2016.

Chapter 4

Triple differential cross sections for the ionization by single electron impact of simple targets

As seen in the previous chapters, determining accurate cross sections for particle interactions with bio-molecules is an essential requirement especially in radiotherapy studies to ensure truthful modeling of the damage induced by ionizing radiation. It is however a difficult task that faces many challenges both theoretically and experimentally. Experiments have been carried out to determine these cross sections in particular kinematics, and theoretical studies aimed at testing the ability of different models to reproduce these experimental data. This is usually done numerically by developing computer programs and generating theoretical cross sections. The triple differential cross sections are of particular interest because they provide more information about the interaction. In this work, we consider a particular interaction: the ionization by single electron impact. As the ionizing particles travel through the living body, they produce a large number of secondary electrons that themselves collide with biological molecules releasing low energy electrons that have been proven to be greatly responsible for DNA damage [1–3]. Extensive research was done in the previous past years to evaluate the TDCSs for the ionization of many molecules by electron impact. In this work, we aim at developing a program that can calculate these cross sections for any molecule. The program is built in a way that the user can easily choose the required parameters, with an automatic transition from the Gaussian software output which should be provided before running the program. To do that, the user only has to provide Gaussian with the geometry file for the chosen molecule. As a result, the program will give the calculated TDCSs for the 0-360 degrees range of ejected electron angles under the chosen kinematics. The theoretical framework described in the previous chapter is used hence providing two options that the user can choose from: considering or neglecting the short range interaction between the ejected electron and the ionized target.

In this chapter, we provide examples of the calculated TDCSs for simple targets in order to validate the program. We begin by investigating the collision description without having to deal with the calculation of the single-center molecular wave functions and the automatic transition from Gaussian to the program, and that by considering the simplest

atom: hydrogen. Then we move on to simple molecules to validate the entire structure of the code. We present the recent theoretical and experimental studies for each molecular target. We consider the water molecule which has been greatly studied due to its wide use as an approximate entity of biological structures, and the ammonia molecule for which TDCSs were provided within the same theoretical model that we use in our program. The available experimental and theoretical data for these two molecules provide us with a reference to reflect on our results.

4.1 Atomic hydrogen

In a first step towards validating our program, we compute the TDCSs of the ionization of atomic hydrogen by single electron impact with the same formalism and the same functions that are used in our program. The molecular wave function is directly written in the program replacing the part where these functions are calculated from the Gaussian output file. As explained in the previous chapter, the wave function of a state (n,λ, m$_\lambda$) is given in the form:

$$\phi_i(\overrightarrow{r}) = \tilde{R}^{(i)}_{n_i,\lambda_i}(r) Y_{\lambda_i,m_{\lambda_i}}(\hat{r}) \ . \tag{4.1}$$

We consider the hydrogen states 1s, 2s, 2p, 3s, 3p and 3d. The radial components of the wave functions of these states are given as follows:

$$\tilde{R}^{(1s)}_{1,0}(r) = 2e^{-r} \ , \ \tilde{R}^{(2s)}_{2,0}(r) = \frac{1}{2\sqrt{2}} (2-r)\, e^{-\frac{r}{2}} \ , \ \tilde{R}^{(1s)}_{2,1}(r) = \frac{1}{2\sqrt{6}} r e^{-\frac{r}{2}} \ , \tag{4.2}$$

$$\tilde{R}^{(3s)}_{3,0}(r) = \frac{2}{81\sqrt{3}} \left(27 - 18r + 2r^2\right) e^{-\frac{r}{3}} \ , \ \tilde{R}^{(3p)}_{3,1}(r) = \frac{4}{81\sqrt{6}} (6-r)\, r e^{-\frac{r}{3}} \ . \tag{4.3}$$

$$\tilde{R}^{(3d)}_{3,2}(r) = \frac{4}{81\sqrt{30}} r^2 e^{-\frac{r}{3}} \ . \tag{4.4}$$

And the angular components are:

$$Y_{0,0}(\hat{r}) = \frac{1}{\sqrt{4\pi}} \ , \ Y_{1,0}(\hat{r}) = \frac{1}{2}\sqrt{\frac{3}{\pi}} cos\theta \ , \ Y_{1,\pm1}(\hat{r}) = \frac{1}{2}\sqrt{\frac{3}{2\pi}} sin\theta \ e^{\pm i\phi} \ , \tag{4.5}$$

$$Y_{2,0}(\hat{r}) = \frac{1}{4}\sqrt{\frac{5}{\pi}} \left(3cos^2\theta - 1\right) \ , Y_{2,\pm1}(\hat{r}) = \frac{1}{2}\sqrt{\frac{15}{2\pi}} sin\theta cos\theta e^{\pm i\phi} \ . \tag{4.6}$$

We compare the computed TDCSs in figure 4.1 for these states with analytical TDCSs provided by Professor Claude Dal Cappello considering an incident energy of 250 eV, an ejected energy of 5 eV and a scattering angle of -5°. The analytical TDCSs are given in the stars symbols while the solid lines represent the TDCSs calculated with our program. For each state, the red lines and red stars correspond to the final TDCSs resulting from the sum

over all possible values of m_λ, while the blue, green and orange lines and stars correspond to m_λ =0, ±1, ±2 respectively. These TDCSs were calculated in the 1CW model where the ejected electron is described by a Coulomb wave and the projectile electron is described by plane waves. The nuclear contribution to the transition amplitude was not taken into account and only the direct contribution was considered. The resultant TDCSs reproduce the analytical calculations and we conclude the validity of the 1CW collision description using the functions integrated in the program. We note here that we have performed tests on each used function separately and verified its validity and that our goal now is to investigate the overall program validity.

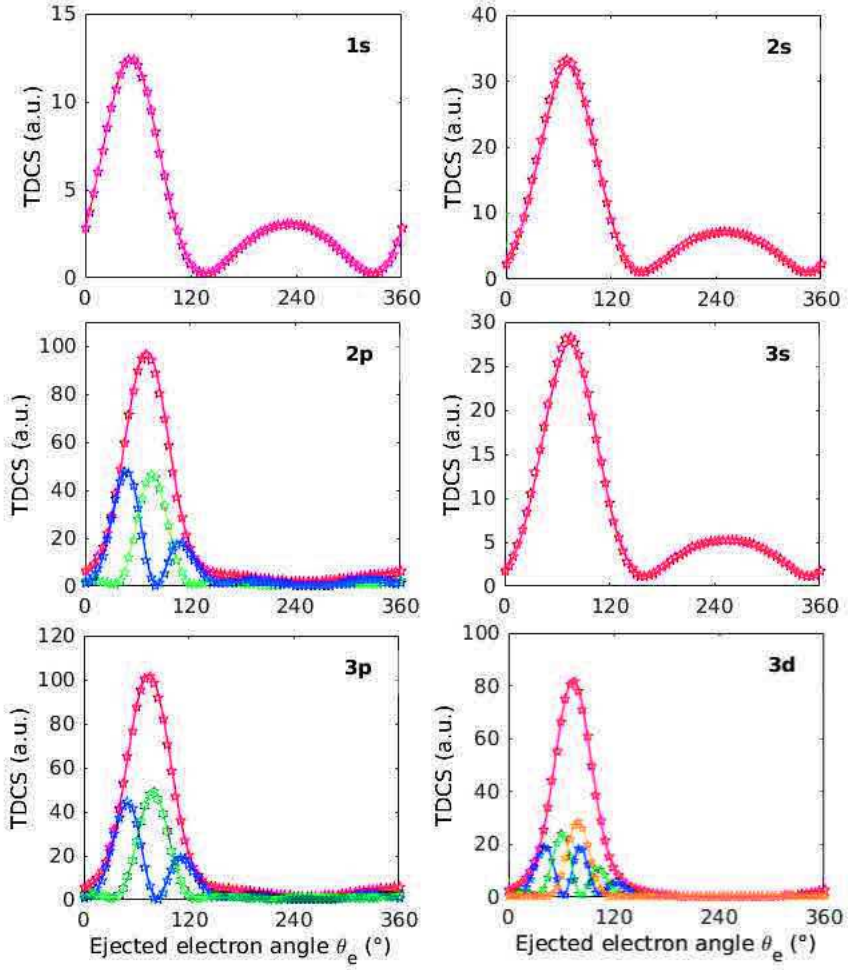

Figure 4.1: Triple differential cross sections for the ionization of hydrogen states by electron impact. The incident electron energy is 250 eV, the ejected electron energy is 5 eV and the scattered electron angle is -5°. The solid curves indicate the numerical results calculated within the approach described in this thesis while the stars represent analytical results provided by professor Claude Dal Cappello.

After these simple tests, we now move on to molecular targets and we begin with the water molecule which has gained particular interest in the past years.

4.2 Water

Water is the main component of biological material and the latter is approximated by water in studies of particle interactions with living matter. The interaction cross sections with water are also usually used to simulate interactions with DNA. Recent studies showed that the cross sections for interactions with DNA differ clearly from water cross sections in the low energy regime; for energies less than 250 eV [4]. These findings lead to abundant research aiming at developing theoretical models to provide the cross sections of particle interactions with DNA for low incident energies. As already discussed previously, providing these cross sections is very challenging because much more complex mechanisms take place between the electrons and the target and cannot be neglected when these electrons have a low energy. These are post collision interactions (PCI) and are usually modeled by non first order approaches. At higher incident energies, the approximation of DNA interaction cross sections with water cross sections remains valid and hence a lot of research groups focused on measuring and developing theoretical models to evaluate water cross sections. These studies were performed at intermediate and high energies and low energy studies are, on the other hand, not as abundant. Although the doubly differential cross sections as well as the singly differential and total cross sections have been explored extensively, it wasn't until very recently that triply differential cross section data were provided for the water molecule.

4.2.1 Structure and properties

The water molecule is a small symmetric molecule belonging to the point group C_{2v} with a bent geometry (V-shape). This means that it has two mirror reflection symmetry planes (σ_v and $\sigma_{v'}$) and a 2-fold rotation symmetry axis (C_2) as represented in figure 4.2. It consists of two light Hydrogen atoms and a 16-fold heavier Oxygen atom: the O-H length and the H-O-H angle are approximately 0.958 A^o and 105^o. The position of the Oxygen atom does not coincide with the center of mass of the molecule.

Five occupied molecular orbitals are identified by molecular orbital theory for water which has in its ground state the configuration: $1a_1^2\ 2a_1^2\ 1b_2^2\ 3a_1^2\ 1b_1^2$. The four outermost valence orbitals with their ionization energies are represented in figure 4.3.

Owing to its simple structure, a lot of experimental studies were carried out to measure the double differential cross sections for the ionization of water by electron impact since 1971 [5–8]. Many studies followed providing measurements and theoretical predictions of the singly differential and total ionization cross sections since then, but it wasn't until very recently that triple differential cross section data for water were provided.

4.2.2 Previous experimental studies

Four experimental studies have been recently published providing measurements of the triple differential cross sections of water by electron impact. The first experiment was

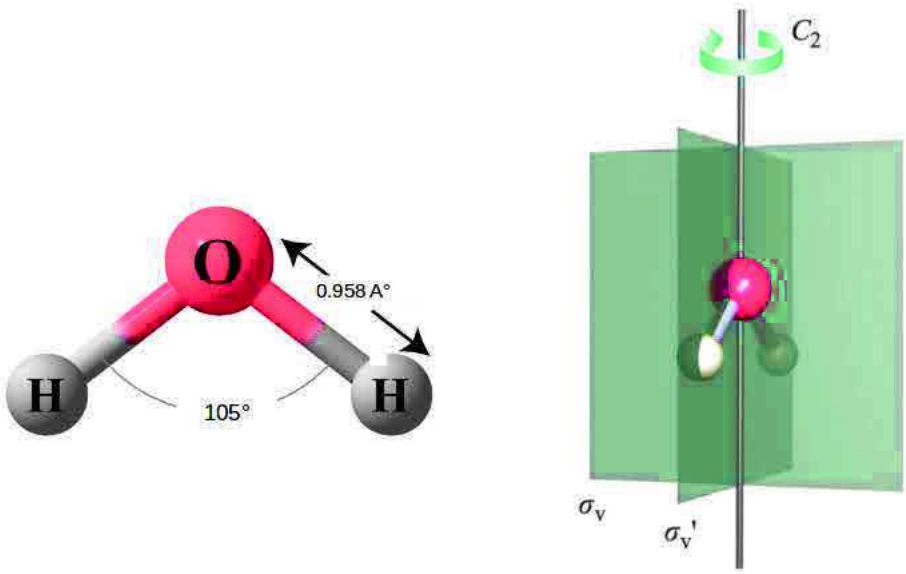

Figure 4.2: The structure of the water molecule with its two reflection symmetry planes σ_v and $\sigma_{v'}$ and its rotation symmetry axis C_2.

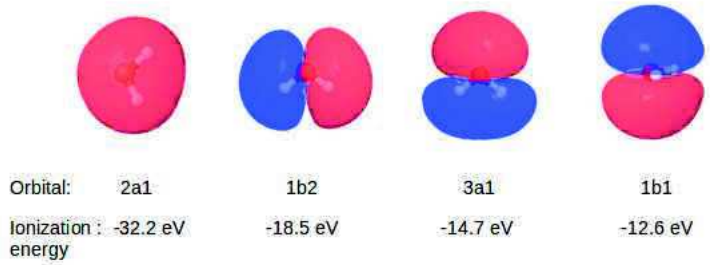

Figure 4.3: The four valence molecular orbitals of water with the corresponding ionization energies.

performed in 2004 by *Milne-Brownlie et al.* [9] with a 250 eV incident energy in an asymmetric coplanar geometry. The resolution of the experiment did not allow to resolve the contributions of the two outermost orbitals $3a_1$ and $1b_1$ and so the summed contribution from these two orbitals to the TDCSs was given. The ejected electron energy was fixed at 10 eV for all orbitals except the $3a_1$ orbital for which the ejected energy was fixed at 8 eV. This lead to the same scattered energy from the ionization of $3a_1$ and $1b_1$. The authors provided the separate contribution of each orbital by fitting the corresponding peak in the binding energy spectrum with two Gaussians. The scattered electron detection angle was fixed at 15°.

The second experiment was done in 2007 by *Kaiser et al.* [10] measuring triple differential cross sections for only the $1b_1$ orbital with lower incident electron energies in both coplanar symmetric geometry, with incident energies 32.6, 52.6 and 72.6 eV, and coplanar asymmetric geometry with incident energies 27.6, 67.6 and 107.6 eV (ejected electron energy fixed at 5 eV and scattered electron detection angle at 22°). Three years later the

same group provided measurements for the $2a_1$ orbital for 19 – 55 eV incident electron energies in three different geometries: symmetric coplanar and symmetric non-coplanar geometries with equal and unequal energy sharing kinematics [11].
Very recently, the same group published experimental data for the summed TDCSs for the unresolved $1b_1$ and $3a_1$ states also in the low energy regime (incident energy of 81 eV) [12]. As the ionization energies of these two orbitals are very close, it is difficult to distinguish them in experiments and a higher resolution of the collision apparatus is required to separate the contributions to the TDCS from each of these two orbitals.

According to the experimental data, when the scattered and ejected electrons are detected in the scattering plane, the shape of the TDCS in function of the angular distribution of the ejected electron presents in general one forward peak at the transfer momentum direction $\vec{k}$ for the s-type $2a_1$ orbital and two forward peaks for the p-type orbitals $1b_2$, $3a_1$ and $1b_1$. In the recoil region, a backward peak is identified at the transfer momentum direction $-\vec{k}$. This shape of the TDCS in function of the ejected electron angle differs when non coplanar geometries are considered. It has also been shown in the work of *Lin et al.* [13] that this shape also varies according to the considered kinematics. Although most theoretical studies were able to predict the structure of the binary region, few were able to reconstruct the recoil region.

In each of these experimental studies, theoretical calculations were also presented and compared to the measured data. Other groups proposed different theoretical approaches to evaluate these cross sections, in the same kinematics as the ones used in these experiments, in the aim of finding the model that best describes the single electron impact ionization of the water molecule.

4.2.3 Previous theoretical studies

Milne-Brownlie et al. [9] used an approach proposed by *Champion et al.* in 2002 [14] to calculate the TDCS in the kinematical conditions of their experiments; *Champion et al.* had presented calculations of double and single differential cross sections as well as total cross sections for the single electron impact ionization of water in a particular molecular orientation using the distorted wave Born approximation (DWBA) where the ejected electron's wave function is a distorted wave and the interaction potential is a spherically averaged distorted potential. The molecular orbital wave function was expressed in terms of Slater-like functions, as proposed by Moccia [15]. Using this approach, *Milne-Brownlie et al.* showed that it predicts well the experimental binary region: the angles at which the peaks were found, the minimum between the two peaks and the width of the peaks are all in acceptable agreement with the experimental data. However, the theory did not predict the relative magnitudes of the two binary peaks in the experimental data: while measurements indicate that the first peak is higher than the second one (for the $1b_1$ and $3a_1$ orbitals), the theoretical results show two peaks of equal amplitude for the three p-type orbitals. This observation is expected since a first order model is used, and as will be seen in later studies the shifts in the relative amplitudes of the two binary peaks for p-type orbitals is due to PCIs. In addition to that, the theoretical model failed at describing the recoil region. The authors suggested the use of distorted waves for all electrons for a better

estimation of recoil scattering.

Two years later, *Champion et al.* published theoretical TDCSs using the same model but this time for an average orientation of the water molecule [16]. They provided a test of the accuracy of their wave functions by comparing the TDCSs obtained using these wave functions with electron momentum spectroscopy (EMS) data published by *Bawagan et al.* [17]. They also computed the TDCSs using other descriptions for the electrons' functions: 1CW, 2CW, BBK [18] and DS3C [19]. In general, all the models were unable to describe the relative amplitudes of the binary peaks and showed underestimated predictions for small ejected angles but the recoil peak was well observed in all these models even with the DWBA model used in *Milne-Brownlie et al.* [9]. Moreover, using models that do not provide a complete description of post collision interactions (1CW, DWBA) lead to two forward peaks of equal amplitude in the binary region for p-type orbitals. On the other hand, the amplitude of the first forward peak was clearly higher than that of the second forward peak with the 2CW model that accounts for the interaction of the scattered electron with the ionized water molecule, while the contrary was observed with the BBK and DS3C models that account for the interactions of the scattered and ejected electrons after collision with each others as well as with the ionized target. Since the more sophisticated models did not lead to much improvement in the prediction of the TDCSs for these orbitals, the simpler first order models (1CW and DWBA) were considered the most convenient for the description of the water ionization process under the considered kinematics. In the case of the s-type $2a_1$ orbital, better agreement with experimental data was obtained using the 2CW model despite an underestimated recoil peak.

The next experiment's measurements for the $1b_1$ orbital were provided by *Kaiser et al.* [10] and compared to calculations done using distorted waves to describe the projectile and ejected electron (M3DW) [20] with an orientation averaged molecular wave function (OAMO) that they derived using a computational chemistry software: GAMESS [21]. They tested these wave functions by computing the elastic differential cross sections for electron scattering from the H_2O molecule and compared the results for different incident electron energies to published data by *Danjo and Nishimura* [22] and found that their wave functions are more accurate at lower incident energies. To account for post collision interactions they used an interaction potential which includes two contributions: the Coulomb interaction of the incident electron and the neutral molecule before collision in addition to a spherically averaged distorted potential. The distorted potential was calculated using three different methods that were labeled 3DW, 3DW-CPE and 3DW-APE. Different interactions were considered in each method. Details about how the potential is calculated in these methods are given in [10, 23–25]. In general, all three methods did not imitate the trend of the experimental data and many structures not appearing in the experimental profile were predicted by theory.

In their next work [11] they suggested that the molecular averaging of the wave function might have been a reason for the obtained discrepancies between theory and experiment in their previous work [10]. They explained that the method they used for orientation averaging is not convenient for the atom-like and symmetrical orbital $1b_1$ and presented calculated TDCSs for the $3a_1$ orbital which charge density distribution is not symmetric. The wave functions they used were calculated using the Amsterdam Density Functional program (ADF) [26] with a Slater-type basis set. They presented experimental and calculated TDCSs in the ejected electron range 0-160 degrees and used lower incident

energies than the ones used in their precious work [10]. They also used the Molecular 3-body Distorted Wave (M3DW) model [20] in addition to the Molecular Distorted Wave (MDW) Born approximation which does not include the post collision interaction factor representing the Coulomb interaction between the scattered and ejected electrons. Their MDW results were in better agreement with experimental data than the M3DW results which overestimated the post collision interaction. They concluded that the shift in the peaks towards 90° is due to post collision interactions between the outgoing electrons since it becomes more pronounced as the outgoing energies decrease leading to a stronger repulsion between the ejected and scattered electrons.

In 2007 *Hafied* [27] presented a detailed approach to develop single center molecular wave functions using Gaussian 03 [28] in the framework of the First Born approximation (FBA) using the partial wave expansions of the wave functions. Calculated TDCSs were presented for the four orbitals of water in the kinematic conditions of the experiment performed by *Milne-Brownlie et al.*, using different basis sets in Gaussian 03 to describe the molecular wave function. Orientation averaging in the laboratory frame was performed by integrating the TDCSs over Euler angles according to the proper average method. The results were also compared to TDCSs calculated with Moccia wave functions. Good overall agreement with experimental data was observed: the general shape of the TDCS was well predicted by the proposed theory, the peak angles and widths were in agreement with the experimental data. Indeed, the relative amplitudes of the two binary peaks in the case of p-type orbitals as well as the binary to recoil amplitude ratio were however not accurately described by this model that does not provide a good description of PCI. On the other hand, the use of Gaussian-type wave functions developed with the proposed approach was shown to provide better agreement with the experimental data than the use of the Slater-type wave functions as proposed by Moccia.

The same methodology was later used by *Champion* [29] to calculate the TDCSs in the same kinematics for both liquid and vapor phases of water in the FBA-1CW framework. The results showed little difference between the two phases of water for the two outer valence orbitals ($1b_1$ and $3a_1$) while almost no difference was observed for the other two orbitals. Good overall agreement with the experimental results was found with no drawbacks compared to the DWBA approach used previously by the same group.

In the same scope, *Hafied et al.* [30] had presented a comparison of the TDCSs of vapor and liquid water in the EMS geometry and compared the results to experimental data published by *Bawagan et al.* [31]. They presented the TDCS calculated with three approaches to describe the molecular wave function in the plane wave impulse approximation (PWIA): a high level Hartree Fock calculation of single-centered Gaussian wave functions which they used in their previous work, using Dyson orbitals instead of these Gaussian wave functions [32], and using Moccia wave functions [15]. In these conditions too, almost no difference was found in the calculated TDCSs between the two phases of water.

Sahlaoui and Bouamoud [33] later compared the TDCSs calculated with Gaussian-type molecular wave functions in the 1CW model by *Champion* [29] with TDCSs calculated using Slater-type molecular wave functions as proposed by Moccia using the 1CW, 2CW, BBK and DS3C models in *Champion et al.* [16] to their own data calculated analytically in the 1CW model using Moccia wave functions. By comparing their results with the 1CW results of *Champion* [29] obtained using partial wave expansion, they found that

their results better estimated the recoil region of the $2a_1$ orbital. They also noted that the use of higher order effects as in the case of the DS3C model could yield to better results in the recoil region as seen in the case of the $1b_1$ orbital. This work concluded that the use of Moccia wave functions in the 1CW framework without using partial wave expansion leads to better agreement with experimental data than using partial wave expansion as was done in *Champion et al.* [16].

In 2012, *Toth et al.* [34] published theoretical TDCSs of water and also compared their results to the DS3C data of *Champion et al.* [16]. They used the DWBA with multicenter Gaussian-type molecular wave functions. Partial wave expansions of the wave functions were used to calculate the TDCSs which were obtained by integration over Euler angles in order to average the molecular orientation. Two descriptions of the potential were used and the two corresponding approaches were denoted by TS and TS*. In the total screening approach (TS), the ejected electron was considered to be moving in the spherically averaged potential of the ionized target while the scattered electron was considered to be moving in both this same potential field as well as an averaged potential due to the target's electrons. In the modified total screening approach (TS*), both electrons were considered to be moving in the same potential field: the spherically averaged potential of the ion. They also studied the effect of the nuclear charge distribution on the resulting TDCSs by proposing to place all the nuclear charge at the center of the molecule in a model denoted by (TS,0) or (TS*,0) and comparing the results to the TDCSs resulting from the spherical averaging of the potential and obtained in the usual case according to which the nuclear charge is distributed along a sphere with the molecular center as the sphere's center and the radius being the distance between this center and the considered nucleus. Placing the nuclear charge in a single center in the models (TS,0) or (TS*,0) lead to enhanced recoil peaks due to the stronger nuclear potential than the one obtained when the charge is distributed along a sphere. The influence of the projectile's charge was also studied by presenting TDCSs for the ionization by electron and positron impact. They concluded that the ionization of water by positron impact is more probable than by electron impact in the binary region for small ejection angles. Little agreement was found between their results and the DS3C results of *Champion et al.* [16] as well as the experimental results of *Milne-Brownlie et al.* [9]. A better agreement was found for the $2a_1$ orbital which is almost spherical. They attributed these discrepancies to the description of the molecular wave functions obtained with the simple STO-3G basis set and proposed the use of a larger basis set for better results.

Also in 2012, *Sahlaoui and Bouamoud* [35] proposed the use of the Second Born approximation (SBA) with the closure approximation to describe the ionization by single electron impact of water and molecules of the form XH_n emphasizing the importance of including PCI particularly between the outgoing electrons in the Born approximation. They noted that PCI can be included in the SBA framework by simply multiplying the TDCS by the Gamow factor, which was previously proven to contain the greatest effects of PCI [36]. This factor is the normalization factor of the wave function describing the PCI between the scattered and ejected electrons. They first calculated TDCSs for the Hydrogen atom to test the accuracy of their model and investigate the importance of this factor for a simple target. Comparing their results using both the FBA and the SBA with and without this factor to experimental data from three studies [37–39] and to theoretical data from *Dal Cappello et al.* [40] and *Brauner et al.* [41] obtained with the 3CW model which requires

more complicated analytical calculations, they found that adding the Gamow factor into the FBA and the SBA clearly improves the agreement with experimental data. In the experimental settings of *Ehrhardt et al.* [37, 38], the SBA with the Gamow factor lead to TDCSs very close to the ones predicted by the 3CW model [41] which confirms that the Gamow factor is mostly responsible for the inclusion of PCI effects in the theoretical model. For the other measurements at higher ejection angles, the inclusion of the Gamow factor shifted the theoretical data towards experimental results but they were still overestimated by both the FBA and the SBA which supports the findings of other studies that show that, under these kinematics, the SBA with the closure approximation fails to describe the experimental data [40, 42, 43]. Following these tests, they presented TDCSs for the water molecule using both FBA and SBA models also with and without the Gamow factor using the closure approximation and the representation given by Moccia to describe the molecular wave function developed on a Slater-type basis set. They first considered four different values of the average excitation energy $\overline{w}$ without using the Gamow factor to investigate the influence of this parameter on the TDCSs and they found that no apparent difference is observed by taking this parameter to be equal to the ionization energy of each orbital or any of the other values they considered. Hence they justified assigning the ionization energy values to the average excitation energy in their later comparison to the experimental data of *Milne-Brownlie et al.* [9] and the DS3C and 3CW data of *Champion et al.* [16]. They found improved agreement with experimental data when the Gamow factor is considered in the theoretical framework of both the FBA and SBA models. Without this factor, good agreement for the 3CW model, the DS3C model and the SBA was found in the second binary lobe of the TDCS for $1b_2$, $1b_1$ and the sum $1b_1$+$3a_1$ but the recoil peak was underestimated for these orbitals by their FBA and SBA models even after adding the Gamow factor. Better description of the TDCSs in the case of the atomic-like $2a_1$ orbital with their FBA and SBA models was obtained than with the other models. The main particularity observed with their SBA model using the closure approximation is the double recoil peak observed for $1b_2$, $1b_1$ and $1b_1$+$3a_1$. After adding the Gamow factor, they found that the SBA gives results that are very close to the 3CW results in the binary region, except for $2a_1$, but that the recoil region is still underestimated for $1b_2$, $1b_1$ and $1b_1$+$3a_1$. They concluded that their SBA model needs some corrections but is more suitable than the FBA to describe the dynamics of the single ionization of water.

In 2014, *Lin et al.* [13] calculated TDCSs of water numerically as an application to a theoretical framework that is based on the complex Kohn variational method [44] in the FBA-1CW framework. Self-Consistent field (SCF) wave functions developed in terms of contracted Gaussian functions were used for the molecular wave functions which orientation was averaged in the laboratory frame numerically by means of numerical quadrature. The final state wave function was written in partial wave expansion with up to 4 partial waves for the continuum functions. Unlike most studies using partial wave expansion, they did not use the partial wave series of projectile wave function. Instead, they calculated its matrix elements as bound-bound elements which they determined analytically in a previous work [45] and bound-free elements calculated numerically using three-dimensional adaptive quadrature. Another distinctive aspect of their work is that they used their formalism to calculate the TDCSs according to approximations considered in previous studies for the electron-nuclear attraction term $(e^{i\overrightarrow{k.r}} - B)$ which in most studies was taken as $(e^{i\overrightarrow{k.r}} - 1)$ or simply $(e^{i\overrightarrow{k.r}})$. In the previous chapter, we showed that according to the approximations we use, this term reduces to $(e^{i\overrightarrow{k.r}} - 1)$, but it could vary with the

considerations of other models. The B factor is considered zero when the attraction between the electron and the nucleus is neglected. Their method proved to be efficient in predicting the TDCSs for all four orbitals as well as for the summed $3a_1$+$1b_1$ TDCSs. In the binary region, two binary peaks of the same amplitude were found for p-type orbitals unlike experimental data which is predictable since the FBA was used. However the peak angles as well as the relative amplitudes between the second binary peak and the minimum between the two peaks were well predicted by their theory. The recoil region showed particular tendencies in the case of the $3a_1$, $1b_2$ orbitals, where a split recoil peak was found, and in the case of the $2a_1$ orbital where minor peaks appeared from either sides of a tighter recoil peak. These findings are in agreement with the experimental data that show a split peak structure in the recoil region of the $1b_2$ orbital at ejected electron angles of $225degree$ and $270degree$ and a minor peak at $140degree$ for the $2a_1$ orbital. The proposed model described very well the shape of the TDCS for the ionization of the $2a_1$ orbital in both the binary and recoil regions. They also computed the TDCSs over a wide range of the transfer momentum by varying the scattered electron angle which was fixed at $15degree$ in the previous kinematics. This lead to interesting findings about the shape of the TDCS which clearly depends on the transfer momentum. For the $1b_1$ orbital, they showed that the two binary peaks merge into a single binary peak as the transfer momentum exceeds 0.7 a.u., and that the binary to recoil peak ratio decreases to half its value as the transfer momentum increases from 0.7 a.u. to 1.8 a.u.. For the other three orbitals $3a_1$,$1b_2$ and $2a_1$, the shape of the binary region is the same for all k values: two peaks for $3a_1$ and $1b_2$ and one binary peak for $2a_1$. However, the recoil regions for $3a_1$ and $1b_2$ showed a split peak disappearing in the case of $1b_2$ for a transfer of momentum less than 0.8 a.u., and minor peaks on both sides of the $2a_1$ recoil peak.

In the same year, *Zhang et al.* [46] found similar results using a distorted wave for the ejected electron. They proposed a new methodology to calculate the distorted wave of the free electrons and also explored the influence of the different considerations of the nuclear term in the transition amplitude. The proposed model is denoted as MCDW with Coulomb tail for multicenter distorted wave when the second term in the transition amplitude is approximated by a Coulomb tail. When this nuclear term is eliminated, the corresponding model is denoted MCDW without Coulomb tail. In distorted wave models, the distorted wave is usually calculated by solving Schrödinger equation using a spherically averaged potential which only depends on the radial distance. This potential is obtained after simplifying the original anisotropic potential and the multicenter nature of the molecule is reduced to a single-center atom-like case. In their work, *Zhang et al.* [46] argue that it is important to keep the anisotropic potential to prevent losing important information and to correctly describe the state of the ejected electron which is influenced by this anisotropic multicenter nature especially when it is slow. The distorted potential in Schrödinger equation is written as the sum of three components that are all anisotropic and have angular distributions: a static potential, a correlation polarization potential [47, 48] and a model exchange potential [48–50]. Instead of using the spherical averaging approximation to simplify the anisotropic potential to an isotropic potential as is usually done, they directly solved the three dimensional potentials using single center expansion techniques [48, 51, 52]. The calculated TDCSs were compared to the experimental data and DWBA data of *Milne-Brownlie et al.* [9] and to the DWBA of *Champion et al.* [16]. They also found that their results are similar to those obtained in the previous work [13] where the complex Kohn approach was used and stated that this

similarity is probably due to the fact that these two methods use a single configuration SCF target. The computed TDCSs are in better agreement with the experimental data than the previously published DW data in the binary region : the width of the binary peaks as well as the relative intensity of the peaks and the minimum between them for the p-type orbitals were well predicted by the MCDW models. Very good agreement with experimental data was found for the $2a_1$ orbital where a second binary peak and a second recoil peak of small amplitudes were predicted by the MCDW models just as in the previous work. The few experimental statistics and large uncertainties do not however allow to justify the existence of these peaks. The recoil region for the p-like orbitals consists of a two shoulder structure consisting of two minor peaks at the same amplitude for the $1b_1$ orbital and a slightly higher amplitude second peak for the $3a_1$ and $1b_2$ states. The authors concluded that a more precise experiment with more experimental data are required to better understand the theoretical outcomes.

Recently in 2017 *Houamer et al.* [53] calculated analytically the TDCS for the $2a_1$ orbital of water in a study where other atomic and molecular targets were considered (argon, methane and ammonia). The molecular wave function was developed according to the approach proposed by Moccia and its orientation was averaged in the laboratory frame by integration over Euler angles. They used non first order models which take into account the interaction between the diffused and ejected electrons to describe the collision dynamics and that are variations of the Brauner-Briggs-Klar model: BBK [18], BBKDW [54] and BBKSR [53]. The presented data for water were calculated with BBK and BBKSR and showed that the recoil peak is better predicted by the BBKSR model than the BBK model which highlights the importance of the short range potential term that is included in BBKSR and not in BBK to describe the recoil region. They suggested that a combination of the BBKDW and BBKSR models could lead to improved results but pointed out to the computational difficulties of such an approach.

The most recent experimental TDCSs were published also in 2017 by *Ren et al.* who presented summed TDCSs for the $1b_1$ and $3a_1$ orbitals in three planes: the scattering plane, the half perpendicular plane and the full perpendicular plane which are all orthogonal in three dimensions [12]. Low incident energy of 81 eV was considered and the TDCSs were measured over the full range of ejected electron angles owing to the used reaction microscope that covers the entire 4π solid angle of the ejected electron. They compared the measured summed TDCSs for the two states in each plane to calculated TDCSs using two approaches within the M3DW model. The two approaches differ in the way they treat the orientation averaging over the spatial molecular alignment. In the first approach, the molecular wave function is averaged over all orientations before calculating the TDCS. In the proper average approach [55], the TDCS is evaluated at each orientation and then an average TDCS over all orientations is calculated. The resultant TDCSs from each approach were presented for each orbital as well as the sum of the two orbital TDCSs in four conditions: two values of the scattered electron angle (-6° and -10°) and two ejected electron energies (5 eV and 10 eV) were considered in each of the three planes. There was an apparent difference in the TDCS trends obtained using the two orientation averaging methods and the proper averaging method lead to better agreement with experimental data.

4.2.4 Summary

To summarize, we present the theoretical TDCSs for the ionization of the four valence orbitals of water in the conditions of *Milne-Brownlie et al.* [9] compared to the experimental data. In figures 4.4 and 4.5, the TDCSs from 9 theoretical studies as well as the experimental TDCSs were all normalized to unity at the first binary peak position. The data from all the previously discussed studies that were performed in the kinematics of *Milne-Brownlie et al.* are represented in these figures. In brief, the DWBA of *Milne-Brownlie et al.* [9] denoted as DWBA$^{(1)}$ was applied to a single molecular orientation without considering the second term in the transition amplitude to calculate the TDCS. In contrast, this term was included in the 2CW$^{(2)}$, DWBA$^{(2)}$, BBK$^{(2)}$ and DS3C$^{(2)}$ models of *Champion et al.* [16] and an average molecular orientation was considered according to the PA method. Moccia molecular wave functions and partial waves were used. The same approach was adopted in [27] (1CW$^{(3,M)}$) and the same results are obtained by the two 1CW models in [16] and [27]; they are given by the same symbol in the figure: the empty light blue stars. *Hafied* [27] also proposed the 1CW$^{(3,G)}$ model where Gaussian 03 [28] was used to develop single-center Gaussian-type molecular wave functions in the 6-31G basis set (cf. Setion 3.5.2). In both 1CW$^{(3,M)}$ and 1CW$^{(3,G)}$ partial waves were used. The same approach as in 1CW$^{(3,G)}$ was used in [29] (1CW$^{(4)}$) but with a different basis set in Gaussian 03: the aug-cc-pVQZ basis set. In the TS 0$^{(6)}$, TS* 0$^{(6)}$, TS 1$^{(6)}$ and TS* 1 $^{(6)}$ models of *Toth et al.* [34] multicenter Gaussian molecular wave functions and partial wave series were used. The FBA$^{(5,7)}$ model denotes the 1CW model of *Sahlaoui and Bouamoud* [33, 35] and the SBA$^{(7)}$ corresponds to their Second Born Approximation model where analytical TDCSs were calculated without the use of partial waves and Moccia molecular wave functions were considered. The Gamow factor was included in the FBA, Gamow factor$^{(7)}$ and the SBA, Gamow factor$^{(7)}$ models [35]. The 1CW$^{(8)}$ model refers to the study of *Lin et al.* [13] where SCF Gaussian molecular functions were developed, partial waves and the complex Kohn approach were used. The MCDW, without Coulomb tail$^{(9)}$ and the MCDW$^{(9)}$ models are those of *Zhang et al.* [46] where the anisotropic potential was used to calculate the distorted waves in the partial wave expansion method, and the molecular wave functions were calculated with Gaussian 03. Within the BBK$^{(10)}$ and BBKSR$^{(10)}$ of *Houamer et al.* [53] the molecular wave functions were developed according to Moccia and partial waves were not used.

Unfortunately, this experiment does not allow to investigate the accuracy of the theoretical models in describing the recoil region for the outer orbitals $1b_1$ and $3a_1$.

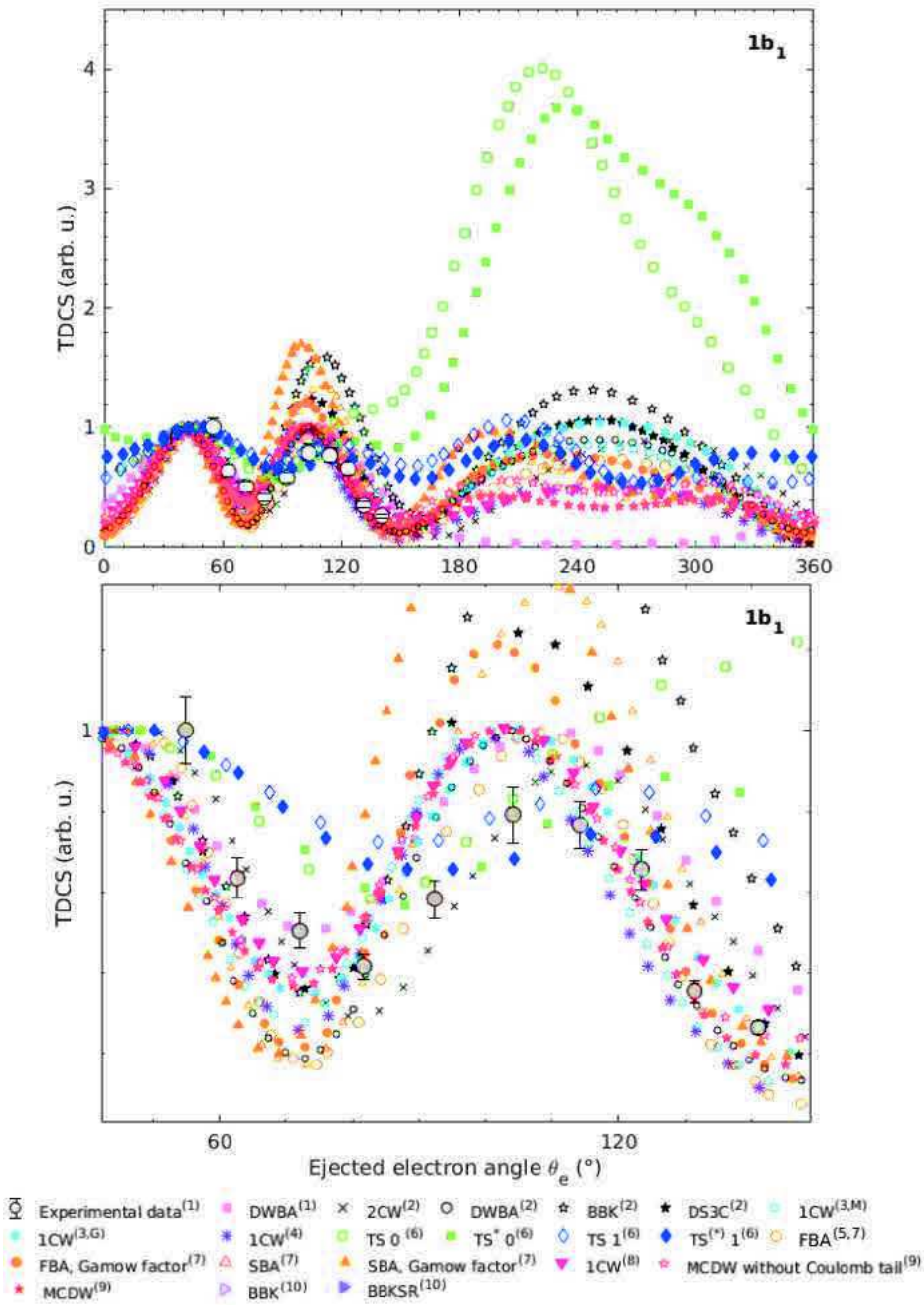

Figure 4.4: Theoretical TDCSs from recent studies for the ionization by single electron impact of the outer valence orbital of water $1b_1$ compared to the experimental data of *Milne-Brownlie et al.* [9]. The kinematical conditions are: E_i=250 eV, E_e=10 eV, θ_f=15°. All the presented data are normalized to unity at the first binary peak position. In the upper graph, we show these TDCSs over the entire ejected eletron range. Since the experimental data are only given in the binary region, we focus on this region in the lower graph. The theories corresponding to the different symbols are given in the figure legend and explained in the text.

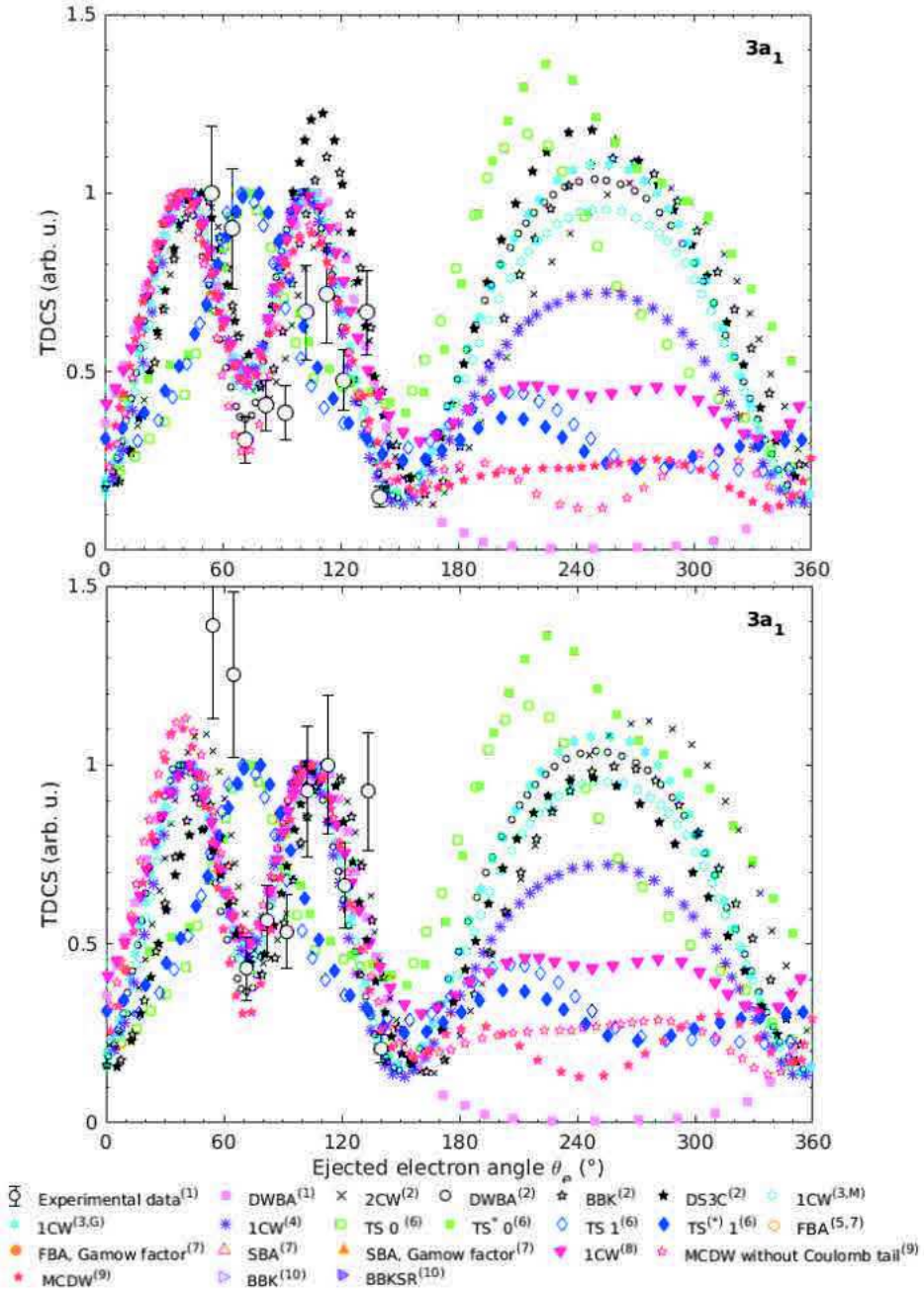

Figure 4.5: Same as figure 4.4 but for the $3a_1$ orbital. The theoretical TDCSs were calculated for an ejected electron energy of 8 eV. All the presented data are normalized to unity at the first binary peak position in the upper figure while in the lower figure they are normalized at the second binary peak to one.

Despite the multitude of theoretical models that were proposed, it is clear from figures 4.4 and 4.5 that none of these models accurately describes the experimental data for the two outermost orbitals.

For the $3a_1$ orbital two comparisons are presented. In the first one, the TDCSs were normalized to unity at the first peak amplitude and at the second binary peak amplitude in the lower graph to investigate the ability of the theoretical approaches to describe

the relative amplitude of the two binary peaks as well as the relative amplitude of the minimum between them. The lower intensity of the second binary peak in comparison to the first binary peak was only predicted by the TS and TS* models of *Toth et al.* [34] that best describe the relative amplitude of the two binary peaks for the ionization of the $1b_1$ orbital and the 2CW model of *Champion et al.* [16] as well as the MCDW models (with and without Coulomb tail) of *Zhang et al.* [46] that show a lower second binary peak for the $3a_1$ orbital. The binary peak obtained for the $3a_1$ orbital with the TS and TS* models obstructs this advantage; a broad binary peak in the summed contributions from the two orbitals completely disagrees with the experimental profile. On the other hand, the two binary peaks are approximately at the same amplitude with the $2CW^{(2)}$ [16] and MCDW models [46] and so the sum of the two contributions is also characterized by a higher amplitude for the first binary peak although still lower than the uncertainty limits of the first experimental point. The summed TDCSs from the two orbitals are given in [16, 34, 46] and show that the recoil region amplitude is in better agreement with the experimental data with the $2CW^{(2)}$ [16] model and that the MCDW models [46] underestimate the recoil amplitude. Hence, we can conclude that the $2CW^{(2)}$ [16] model best describes the summed contributions from the $1b_1$ and $3a_1$ orbitals. In some studies the $DWBA^{(2)}$ [16] is thought to give the best description of the experimental data despite the equal binary peak amplitudes that it predicts because it seems to better determine the peak angles. However, with the lack of experimental data for almost half of the first binary peak and with the large uncertainties on the provided measurements, it remains impossible to conclude which model is better.

By examining the $1b_2$ orbital's TDCSs in figure 4.6, we can see that the model that provides a good description of both the binary and recoil region is mainly the 1CW model in [27] using single centered Gaussian wave functions with the 6-31G basis set in Gaussian (filled light blue stars). The 1CW model in this same work using Moccia wave functions also provides an overall good description of the binary and recoil peaks, so do the 1CW model used in [29] with Gaussian molecular functions but with another basis set, a quadruple zeta correlation consistent polarized basis set aug-cc-pvQZ (empty black circles), and the FBA-1CW in [33, 35] (empty orange circles).

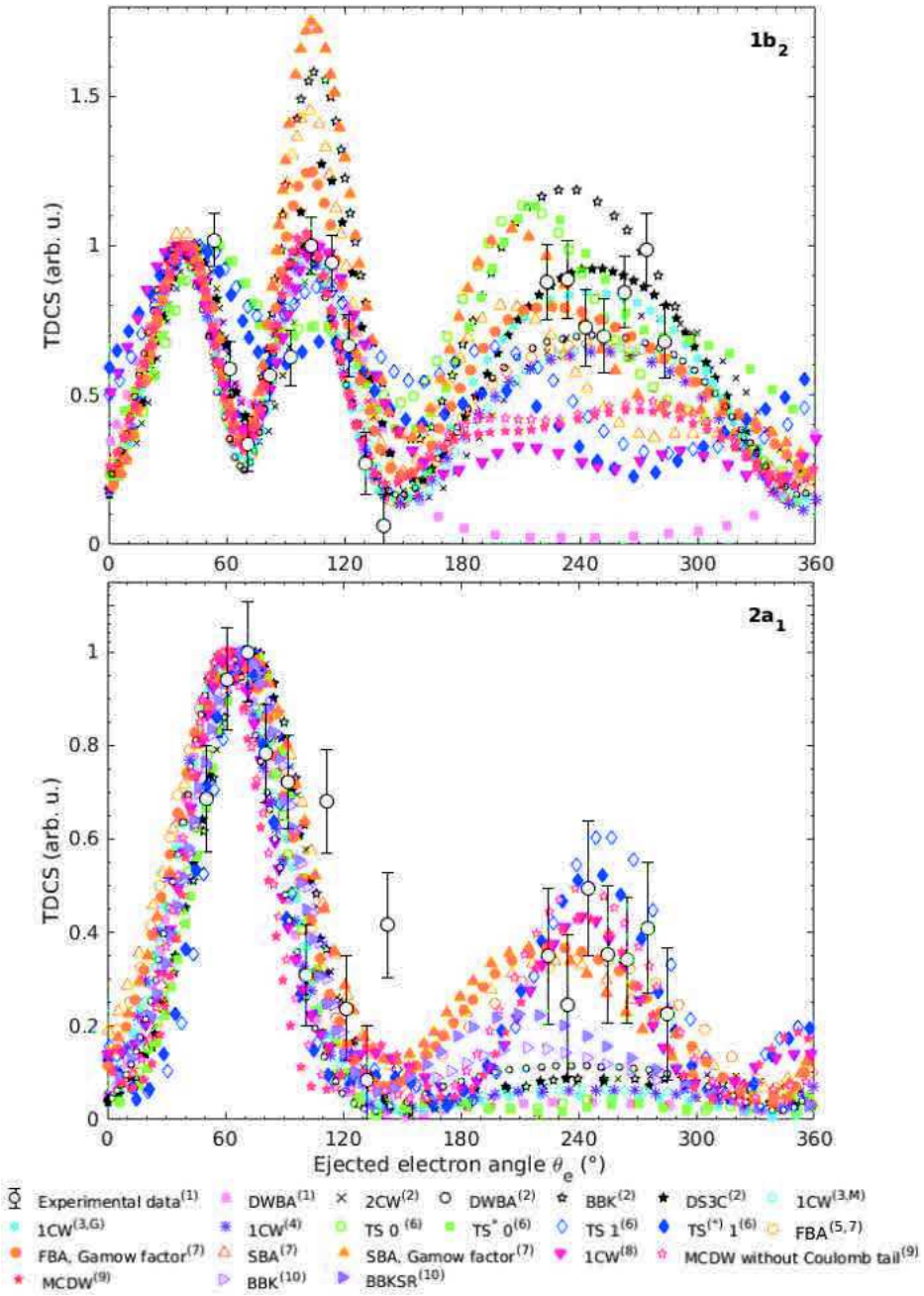

Figure 4.6: Same as figure 4.4 for the $1b_2$ (upper figure) and $2a_1$ (lower figure) orbitals. The data were normalized to unity at the first binary peak in the upper figure.

The models that best describe the binary region of the $2a_1$ orbital are the 2CW, BBK, BBKSR, DS3C models of *Champion et al.* [16] and *Houamer et al.* [53] (the black x symbols, black empty and filled stars and the pink empty and filled triangles) as well as the TS and TS* models (blue empty and filled diamonds and green empty and filled squares) of *Toth et al.* [34]. In general, most of the TDCSs are within the uncertainties of the experimental data in the binary region of $2a_1$ but these latter data agree the most with the peak position and the binary peak width. In the recoil region, the models that best describe the recoil peak's relative amplitude are the FBA and SBA in [35] with and without the Gamow factor (orange empty and filled circles and triangles), the 1CW model

of *Lin et al.* [13] (red triangles), the TS1 and TS*1 models of *Toth et al.* [34] as well as the MCDW in [46] with and without the Coulomb tail. Interestingly, all these models predict a minor second binary peak at around 140°. A single measurement is provided in this region at 142° and indicates a higher amplitude in this region but more data are required to verify the presence of a second binary peak.

These previous studies show the validity of the 1CW and 1DW approaches in describing the dynamics of this experiment, especially the $1CW^{(3,G)}$, $1CW^{(3,M)}$ that are similar to our approach, since they provide good agreement with the experimental data even more than other sophisticated models. The $1CW^{(3,G)}$ and $1CW^{(3,M)}$ models only fail to correctly estimate the recoil amplitude of the $2a_1$ TDCSs. We expect to have similar results with our 1CW model using Gaussian and Slater-type wave functions and hope to have improved agreement for the $2a_1$ orbital with our 1DW model.

4.2.5 Results

As in the case of atomic hydrogen, we begin by comparing our results with TDCSs calculated by Professor Dal Cappello for the ionization of the four valence orbitals in the conditions of the experiment of *Milne-Brownlie et al.* [9]. As presented earlier, the 1CW approach used in [27] is very similar to our 1CW model. In fact, different approaches were considered in [27] to develop the molecular wave functions: Moccia Slater-type wave functions [15] and single center Gaussian-type wave functions generated with Gaussian 03 [28] using the 6-31G basis set and the aug-cc-pvQZ basis set. We first calculate these wave functions according to the approach proposed by Moccia with our 1CW model. To investigate the validity of this 1CW model, we compare the resultant TDCSs to the analytical data provided by Professor Dal Cappello. Figure 4.7 shows that our 1CW TDCSs (purple lines) are similar to the 1CW analytical data (yellow stars). The use of Gaussian-type functions with the 6-31G basis set in Gaussian 09 also leads to similar results. Figure 4.8 shows that the same shape of the TDCS distributions is obtained with a slight shift in the amplitudes of the peaks and minima. The computed 1CW data with both the Slater-type and the Gaussian-type molecular wave functions are compared in figure 4.9 to the published 1CW TDCSs. The studies corresponding to the symbols in the figure are given in the legend and are the same as in 4.4. As expected, the TDCSs given in [27] using the same 1CW approach with Moccia wave functions, presented with the open light blue stars, are similar to our 1CW results with the same approach (purple line).

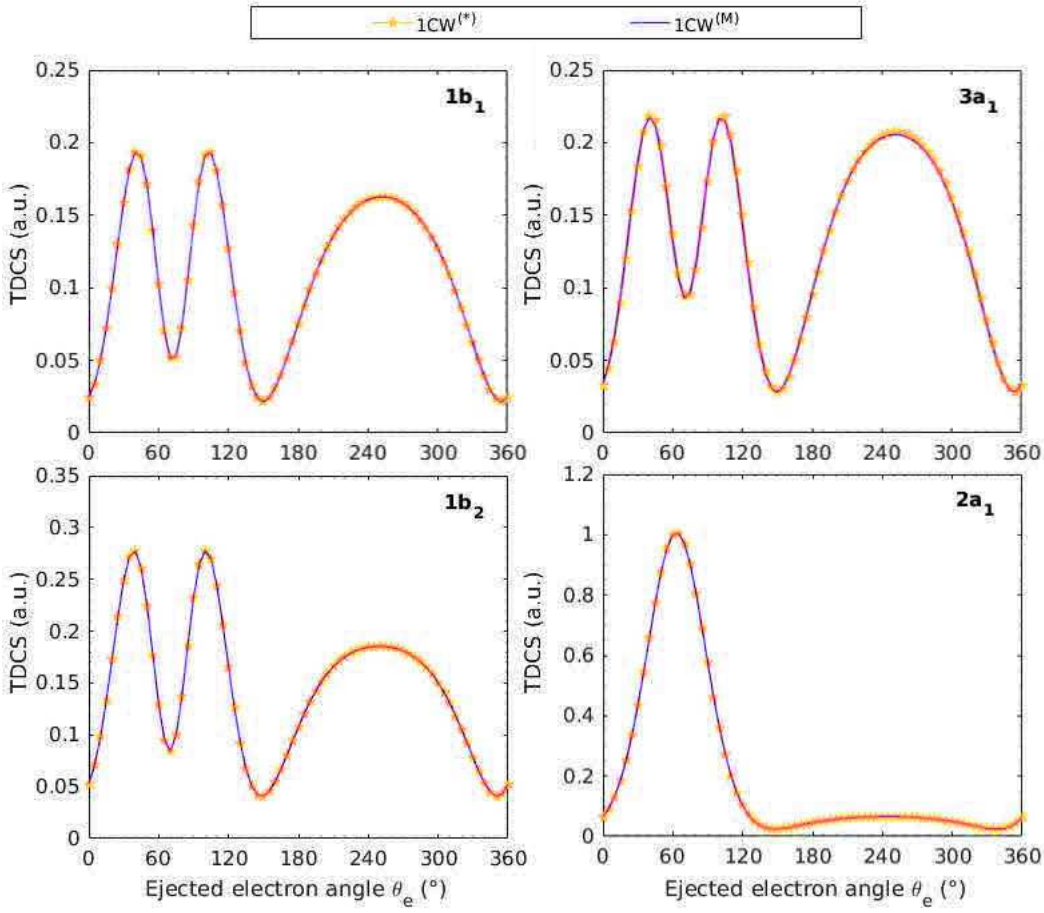

Figure 4.7: Triple differential cross sections for the ionization by single electron impact of the four outer valence orbitals of water calculated in the 1CW model. The considered kinematics are: E_i=250 eV, θ_f=15°, E_e= 10 eV for $1b_1$, $1b_2$, $2a_1$ and E_e= 8 eV for $3a_1$. The calculated TDCSs are given in the purple lines while the yellow stars represent calculations performed by Professor Claude Dal Cappello. Moccia wave functions were used in the two approaches.

The TDCSs calculated with the Gaussian 09 program with the 6-31G basis set are also similar to the TDCSs given in [27] and using Gaussian-type wave functions with the 6-31G basis set in Gaussian 03, with a slightly higher recoil peak amplitude obtained with our approach. In comparison with the experimental data, the lower intensity of the second binary peak for the two outer orbitals is not predicted by our CW models which is expected. For the two other orbitals, the binary region is in good agreement with the experimental data. The recoil region amplitude is also in good agreement with the experimental recoil amplitude for the $1b_2$ orbital. However, the $2a_1$ orbital's recoil amplitude clearly underestimates the recoil amplitude. Among these 1CW models, the approach of *Sahlaoui and Bouamoud* [33, 35] which uses Moccia molecular wave functions to analytically calculate the TDCSs without using partial waves, gives a good description of the recoil region for this orbital. The approach of *Lin et al.* [13] also provides a good prediction of the $2a_1$ TDCSs in both the binary and recoil regions.

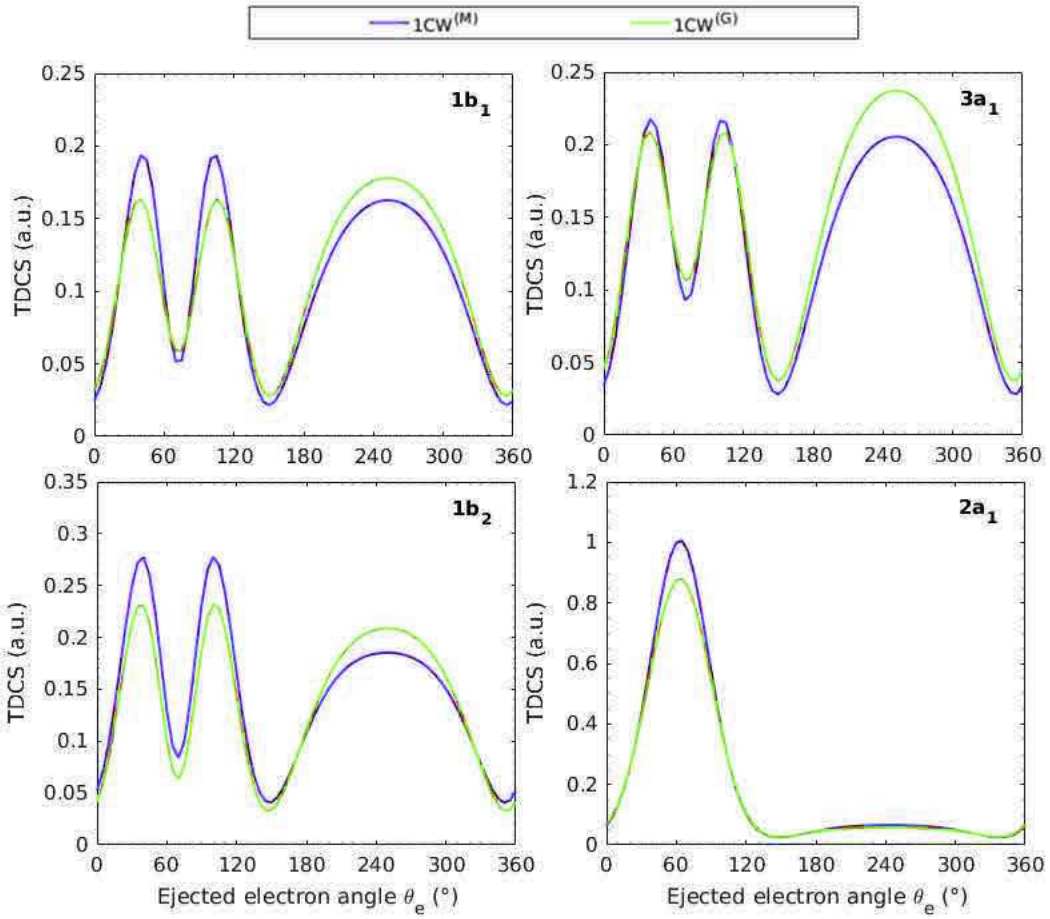

Figure 4.8: Triple differential cross sections for the ionization by single electron impact of the four outer valence orbitals of water calculated in the CW model. The considered kinematics are: E_i=250 eV, θ_f=15°, E_e= 10 eV for $1b_1$, $1b_2$, $2a_1$ and E_e= 8 eV for $3a_1$. The calculated TDCSs using Moccia wave functions with our 1CW approach are represented by the purple lines while the green lines correspond to TDCS calculated with single center Gaussian type wave functions using Gaussian 09 with the 6-31G basis set.

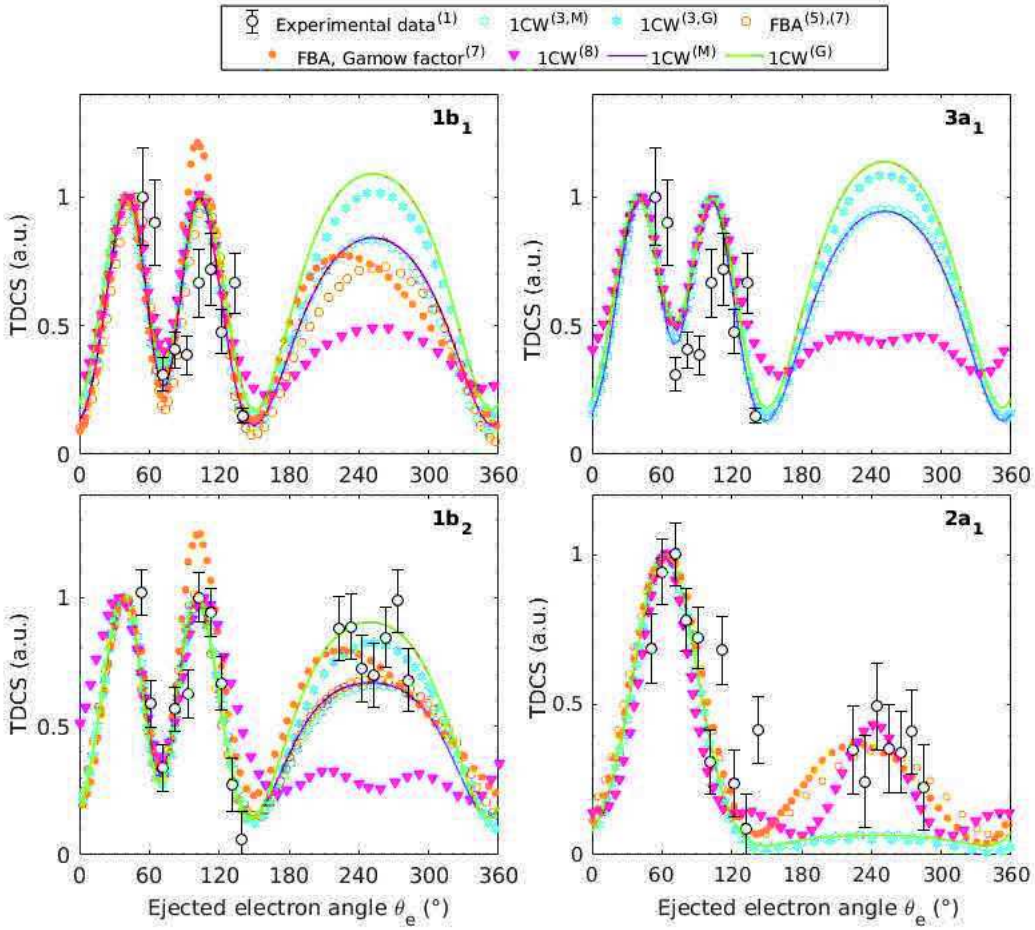

Figure 4.9: Triple differential cross sections for the ionization by single electron impact of the four outer valence orbitals of water calculated within the 1CW model. Our results using both Moccia and Gaussian wave functions are given in the purple and green lines respectively and compared to previous studies. The studies corresponding to the symbols, indicated in the legend, are the same as detailed in the text before figure 4.4. All the data are normalized to unity at the binary peak for the $2a_1$ orbital and the first binary peak for the other orbitals. The experimental kinematics are: E_i=250 eV, θ_f=15°, E_e= 10 eV (E_e= 8 eV for $3a_1$).

As presented in figure 4.10 with the 1DW model, the TDCS presents a higher relative recoil amplitude for the $2a_1$ orbital with a shape that resembles the 1CW results of [13]. For the other orbitals a split recoil peak is obtained with a lower amplitude relatively to the binary amplitude than the 1CW data. This double peak structure of the recoil region was also found in [13] in the case of the $3a_1$ and $1b_2$ orbitals but with a lower recoil intensity.

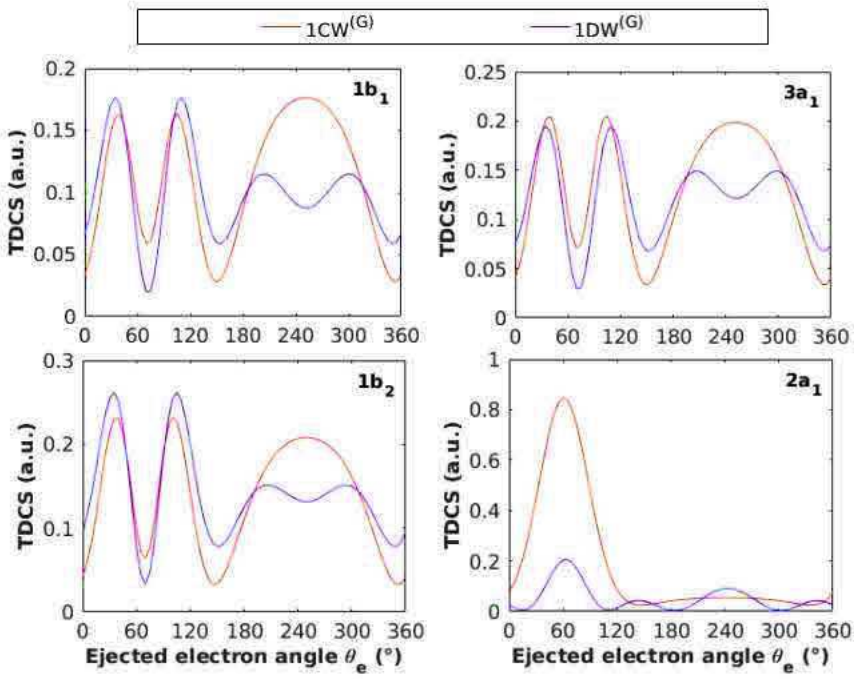

Figure 4.10: Triple differential cross sections for the ionization by single electron impact of the four outer valence orbitals of water. The considered kinematics are: E_i=250 eV, θ_f=15°, E_e= 10 eV for $1b_1$, $1b_2$, $2a_1$ and E_e=8 eV for $3a_1$. Single center molecular wave functions were developed using Gaussian 09 with the 6-31G basis set. The TDCSs calculated with the 1CW approach (orange line) are compared to TDCSs calculated with the 1DW approach (purple line).

In figure 4.11, the computed TDCSs with the 1DW model are compared to the experimental data of [9] and the previous theoretical TDCSs calculated within the DWBA. The DWBA data given in [16] are represented by the black dashed lines, the other symbols correspond to the studies as explained in the caption of figure 4.4.

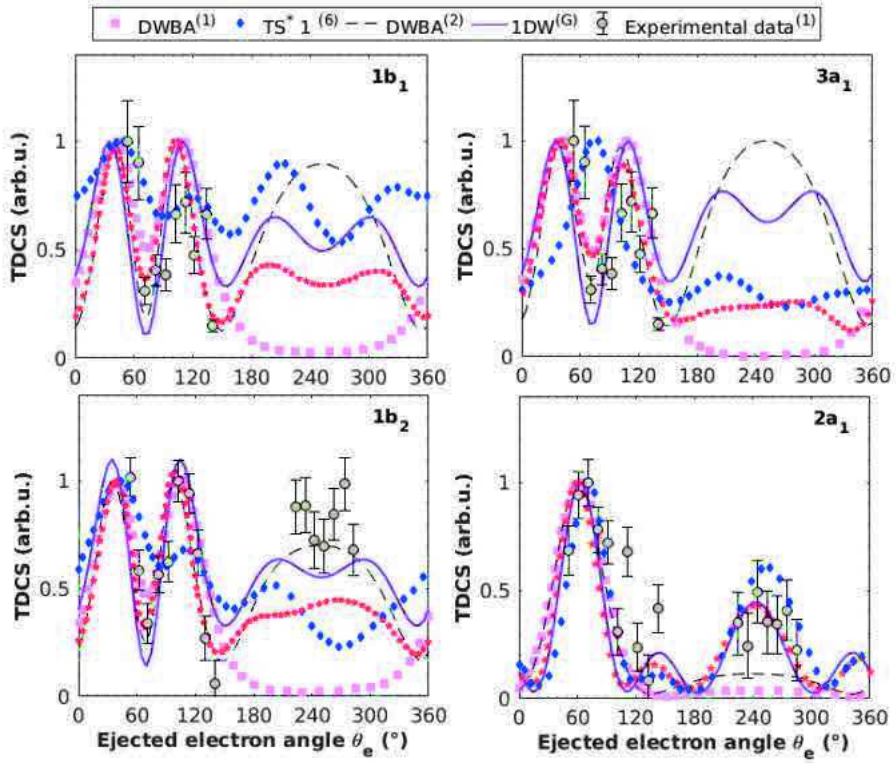

Figure 4.11: Triple differential cross sections for the ionization by single electron impact of the four outer valence orbitals of water calculated within the 1DW model. Our results using Gaussian wave functions are given in the purple lines and compared to previous DWBA studies. The studies corresponding to the symbols and superscripts in the legend are the same as detailed in the caption of figure 4.4 except for the DWBA of [16] given by the black dashed curves here. All the data are normalized to unity at the binary peak for the $2a_1$ orbital and the first binary peak for the other orbitals. The experimental kinematics are: E_i=250 eV, θ_f=15°, E_e= 10 eV (E_e= 8 eV for $3a_1$).

As previously noted, the binary regions of the $1b_1$ and $3a_1$ orbitals are not accurately described by any of the theoretical models presented in figure 4.11 including our 1DW models (purple lines). Acceptable agreement is found for the $1b_2$ orbital between our 1DW TDCSs and the experimental data with a slightly underestimated recoil region. For the $2a_1$ orbital however, our 1DW results are in very good agreement with the experimental data in both binary and recoil regions. These results provide a better approximation of the experimental $2a_1$ data than the DW models in [9] and [16]. We conclude that our 1DW model provides the best agreement with experimental data since it presents only a slightly lower recoil amplitude compared to the DWBA$^{(2)}$ model and gives a much better description of the $2a_1$ TDCSs in both the binary and recoil regions.

For better comparison with the experimental data and further validation of our program, we now consider a target which orbitals are well separated and for which an experiment was performed in the intermediate energy regime and theoretical 1CW and 1DW data have been recently published.

4.3 Ammonia

4.3.1 Structure and properties

The ammonia molecule has the same number of electrons as H_2O, with a simple geometry containing one Nitrogen atom bounded to three Hydrogen atoms, hence allowing the measurement of TDCSs and the testing of theoretical models describing the simple ionization process without having to confront many difficulties. NH_3 has a trigonal pyramidal geometry and belongs to the C_{3v} point group as illustrated in figure 4.12. It has a 120° rotation symmetry axis (C_{3v}) that passes through the Nitrogen atom and is perpendicular to the plane of the three Hydrogen atoms, and three reflection symmetry planes (σ_v) that each contain one N-H bond and bisect the opposite H-N-H angle.

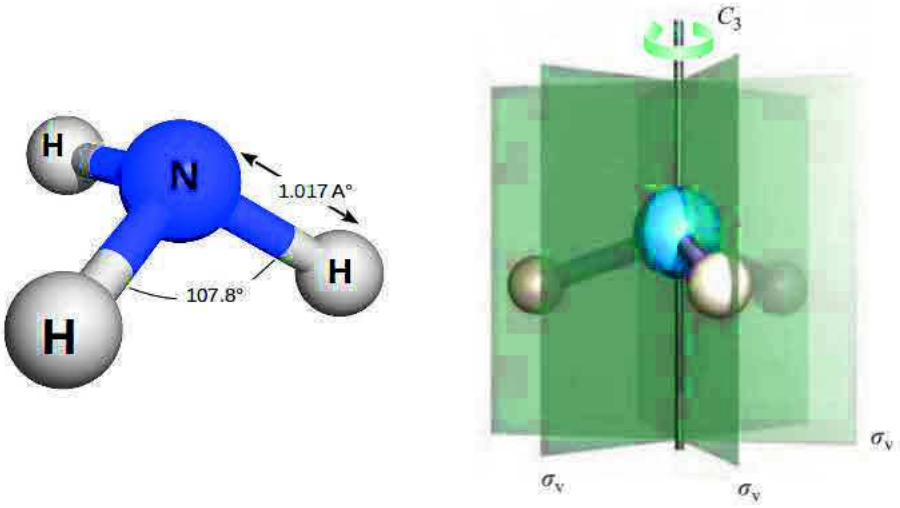

Figure 4.12: Geometry and symmetries of the ammonia molecule.

The three outermost molecular orbitals of ammonia are shown in figure 4.13: the highest occupied molecular orbital ($3a_1$) is due to the lone pair of Nitrogen atom electrons and is of p-character, the second highest occupied orbital $1e_1$ is also of p-character, while the third, $2a_1$, is of s-character. A detailed description of the molecular structure of ammonia is given in [56]. The ionization energies given in figure 4.13 are the values considered in the studies of the simple ionization of ammonia by electron impact that are presented next.

The well separated energy levels of ammonia make it easier to study this molecule since its orbitals are easily discerned in experiments. Nevertheless, only four recent studies have been published providing TDCSs for ionization by electron impact of the ammonia molecule.

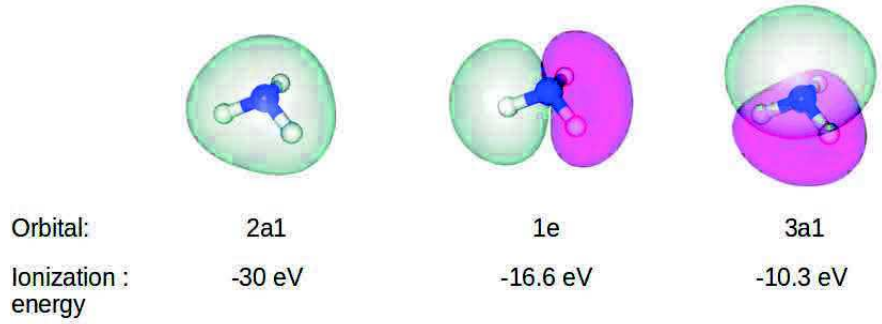

Figure 4.13: The three outer valence molecular orbitals of ammonia with their corresponding ionization energies [57].

4.3.2 Previous studies

Experimental data in the low energy regime for the TDCSs of ionization of ammonia by single electron impact were provided by *Nixon et al.* [56] in doubly symmetric coplanar and perpendicular geometries. In the coplanar geometry, TDCSs were provided for ejected electron angles between 0° and 180° for ejected electron energies ranging from 2.5 eV to 20 eV for the $3a_1$ and $1e_1$ orbitals and from 5 eV to 20 eV for the $2a_1$ orbital. In the perpendicular geometry, TDCSs for only the $3a_1$ and $1e_1$ orbitals were given for ejected electron energies in the range 1.5 - 20 eV. As in their previously presented work on water, they compared the measured data for NH_3 to TDCSs calculated in the M3DW approximation using the ADF program [26] to develop Slater-type wave functions for the molecular orbitals. They also presented measured and theoretical TDCSs for the ionization of other isoelectronic targets: Methane and Neon. The molecular structure of the target did not seem to influence the shape of the calculated and measured cross sections for all the considered molecular targets but differences were found when the atomic target's cross sections were compared to the cross sections of the isoelectronic molecules. In the coplanar geometry only the binary region was given. For the p-type orbitals, experimental data showed that the TDCS consists of two peaks: a shoulder structure appeared in the first peak which was of higher amplitude at the highest outgoing energy (20 eV), this peak was shifted towards a higher angle and the second peak increased in amplitude as the outgoing energy decreased. A different behavior of the TDCS was observed for the inner $2a_1$ orbital: a minor peak increasing in intensity with the decrease in outgoing energy, until it became the main peak at the lowest energy (5 eV), was identified between the two binary peaks. The shoulder-like structure was not found for this s-type orbital. This structure was previously observed in studies of other molecules and was attributed to nuclear interactions and not orbital-type. Hence its presence only for p-type orbitals in this experiment is problematic and demonstrates the complexity of theoretically describing the ionization process in the low energy regime. In general, M3DW predicted a double peak structure of the TDCS for all three orbitals although it does not provide a good description of the peak positions as well as the relative amplitude between the peaks and the minimum between them for p-type orbitals nor the minor peak structure that is clearly found in experimental data for the $2a_1$ orbital. They attributed the dissimilarities between theoretical and experimental data to the molecular orientation averaging method they used

(OAMO) which does not provide accurate description of the electron charge distribution leading to the loss of important information for states of odd parity.

Two years later, *Toth et al.* [58] compared the experimental and theoretical data of this study in the coplanar geometry to theoretical data calculated within the Distorted Wave Born Approximation (DWBA) with the TS and TS* models that they proposed in their previous work for the water molecule [34]. They used Gaussian 09 [59] to develop multi-center molecular wave functions which orientation they averaged by integrating the cross sections over Euler angles. All wave functions were written in partial wave series. They investigated the importance of considering PCI in the low energy regime by comparing their results with and without including a Coulomb distortion factor in their theoretical model. Predictably, more agreement with the experimental data was found with their model including the Coulomb distortion factor than without it. The peak positions were better predicted by their model than by the M3DW model of the previous study. They were also able to reproduce the shoulder structure in the forward peak but the relative amplitudes of the peaks were better predicted by M3DW. In the DWBA with the distortion factor, the backward peak showed a double structure that increased in amplitude as the energy decreased to become more like the experimental data for lower energies. In the case of the $2a_1$ orbital better agreement was found for the backward peak especially as the energy decreased, but the forward peak was not well predicted at lower energies.

At higher incident energies, the study of the ionization process becomes less complicated as the nuclear interactions become less important. Experimental data provided later in 2015 by *El Mir et al.* [60] in the intermediate energy regime in asymmetric coplanar geometry showed a much simpler trend of the TDCS for the three orbitals: a binary peak at the transfer momentum direction $\vec{k}$ and a recoil peak at -$\vec{k}$. If a shoulder structure was to be identified in the presented experimental data, it would surprisingly be more apparent for the s-type orbital $2a_1$ where a small dip is observed around 70°. The experimental data were compared to calculated TDCSs using the 1CW, 1DW and BBK models. Slater-type molecular wave functions calculated according to the approach proposed by Moccia [61] were used and the wave functions were not written in partial wave expansion. Molecular orientation averaging in the laboratory frame was considered by integrating the cross section over Euler angles. Overall good agreement with experimental data was found for the three valence orbitals in these conditions in the binary region, with an underestimated recoil region in comparison with experimental data.

Very recently, *Houamer et al.* [53] attempted to reconstruct the recoil region in the previous kinematics using non first order approaches that are variations of the Brauner-Briggs-Klar model: BBK [18], BBKDW [54] and BBKSR [53]. As previously presented in the section of water, they used Moccia functions to describe the molecular wave functions and also presented theoretical results for argon, methane and water. The presented results for NH_3 highlight the importance of considering an interaction potential that takes into account the short-range interaction between the ejected electron and the ion in order to better model the ionization dynamics in the recoil region. The BBKSR model which uses such a potential was shown to reproduce the TDCS in the recoil region at best. However, the peak angles in the binary region where slightly shifted towards 90° due to non first order effects. They concluded their study by proposing to merge the BBKDW and BBKSR models and highlighting the computational challenges that this approach poses.

Summary

The previous outcomes of the different theoretical models that were applied for ammonia, in the kinematical conditions of *El Mir et al.* [60], are presented in figure 4.14. Since 1CW and 1DW data were provided under these kinematics [60], the comparison of our results with these data can be useful to comment on the collision description in our program.

It is clear from figure 4.14 that the binary peak's width is not well predicted by all the theoretical models. The BBK and BBKSR TDCSs present a shift of the binary peak towards 90° since they include PCI. The 1CW and 1DW models present similar behavior in the binary region. In the recoil region, the enhanced amplitude with respect to the binary region is only reproduced by the BBKSR model which differs from the BBK model only in the way the interaction potential is treated. In the BBKSR model, the interaction between the projectile electron and the target is described by a potential that is the sum of a short range potential and the Coulomb potential. The better agreement with experimental data obtained using the BBKSR model in comparison with the BBK results shows the importance of considering this short range interaction to understand the interaction in the backwards direction. However, the inner valence $2a_1$ orbital does not show such behavior and it is the BBK model used in [60] that seems to give the best approximation of the recoil region's relative amplitude. Clearly, the two BBK models do not provide the same TDCS tendencies: the second BBK model used by *Houamer et al.* [53] predicts a wider binary peak and a higher recoil relative amplitude for the two outermost orbitals. In the case of the inner $2a_1$ orbital, the first BBK used in *El Mir et al.* [60] shows a much different behavior in the backward region as the relative amplitude of the recoil peak is much higher than that obtained with the second BBK model.

In fact, different methodologies have been used to calculate TDCSs with the BBK model. The first approach was initially proposed by Brauner, Briggs and Klar [18] for the ionization of atomic hydrogen by electron and positron impact. It consists in describing the incident, scattered and ejected electrons by Coulomb wave functions to take into account the interaction between the outgoing electrons as well as their interaction with the residual ion. However, this model requires heavy calculations and immense computing time because of the three confluent hypergeometric functions that lead to a six-dimensional integral in the transition amplitude. In order to apply this model to other targets, different approaches were used to simplify the calculations. Professor Dal Cappello developed this model for other atomic and molecular targets reducing the six-dimensional integral to a two-dimensional numerical integral [16, 60, 62]. However, it still requires the calculation of hypergeometric functions which poses many difficulties and limits its application for more complex molecules. Another approach, proposed by *Kornberg and Miraglia* [63], makes use of Fourier transforms to reduce the six-dimensional integral to a three-dimensional numerical one. This method was used by *Houamer et al.* [53] and also requires challenging calculations especially regarding the choice of the integration points in the non linear grid.

4.3.3 Results

Since our program uses both 1CW and 1DW models, we consider the 1CW and 1DW results of *El Mir et al.* [60] calculated in the kinematical conditions of their experiment:

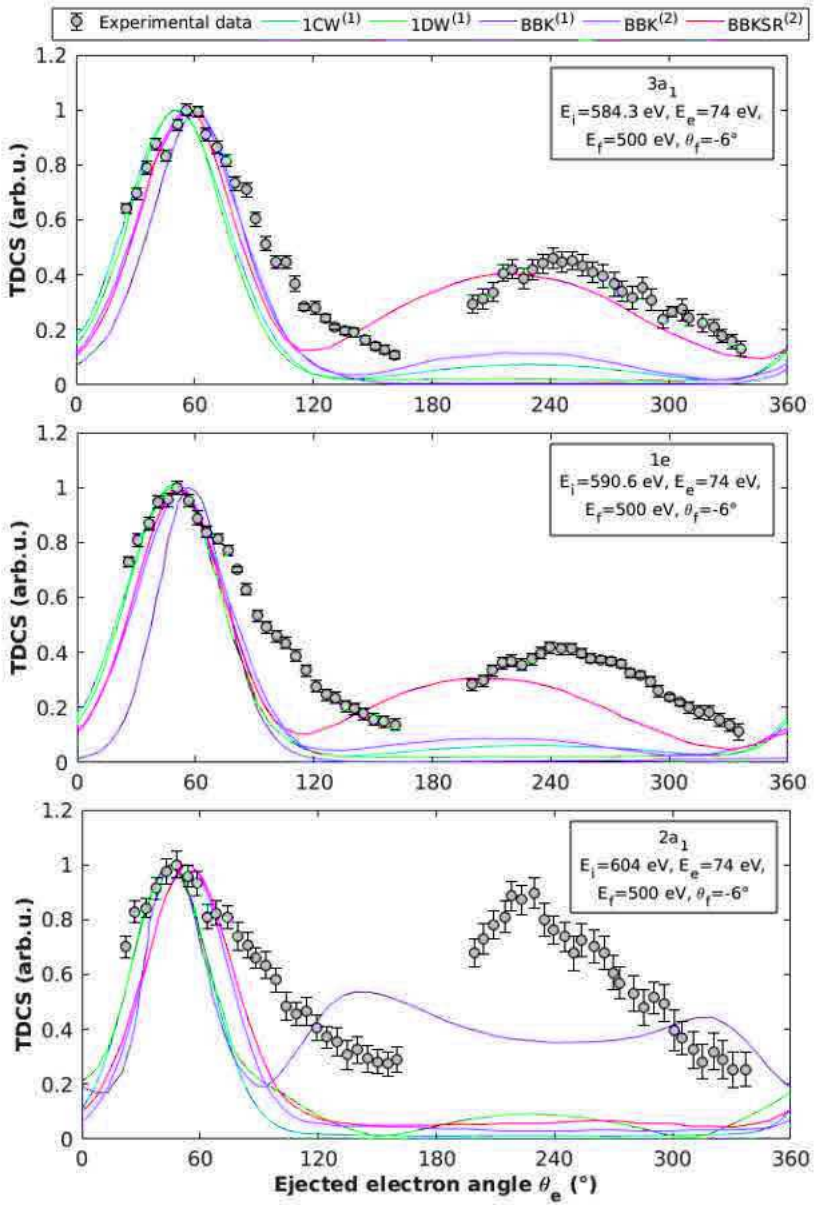

Figure 4.14: Theoretical TDCSs for the ionization by single electron impact of the three outermost valence orbitals of ammonia: $3a_1$, 1e and $2a_1$, compared to the experimental data from *El Mir et al.* [60]. The legend indicates the corresponding theory for every TDCS curve; the superscript (1) refers to TDCSs taken from [60] while (2) refers to the results of *Houamer et al.* [53]. All the TDCSs are normalized to unity at the binary peak.

scattered electron energy of 500 eV, ejected electron energy of 74 eV and scattered electron angle of -6°, in a coplanar asymmetric geometry. Before examining the obtained TDCSs in these conditions with our program, we investigate the quality of the used molecular wave functions.

Testing the molecular wave functions

Since *El Mir et al.* [60] use Moccia wave functions to calculate the TDCSs, we also develop these wave functions and integrate them in our code to better explore the validity of the collision description. To do that, we follow the methodology described in the previous chapter by using the coefficients given in table 4.1.

The orthonormalization of the wave functions developed with the two approaches is verified by calculating the scalar products of the orbitals' wave functions. For two states i and j this scalar product is calculated as follows:

$$\begin{aligned}\left\langle \psi_i | \psi_j \right\rangle &= \int \psi_i^*(\overrightarrow{r})\psi_j(\overrightarrow{r})\mathrm{d}\overrightarrow{r} \\ &= \sum_{\lambda,m_\lambda} \int_0^{+\infty} \tilde{R}^{i*}_{\lambda m\lambda}(r)\ \tilde{R}^{j}_{\lambda m\lambda}(r)\ r^2\ \mathrm{d}r\ .\end{aligned} \tag{4.7}$$

To calculate these products, we consider a linear radial grid of 1333 points with 0.03 a.u. increment. Using 12 partial waves for the molecular wave function ($\lambda_{max} = 12$), the precision obtained for the normalization condition $\left\langle \psi_i | \psi_j \right\rangle = \delta_{i,i} = 1$ is of the order of 10^{-4} for the Slater wave functions and 10^{-3} for the Gaussian wave functions. The calculated values for Slater-type and Gaussian-type orbitals are given in tables 4.2 and 4.3 respectively.

Orbital	$2a_1$	$1e_x$	$1e_y$	$3a_1$
$2a_1$	0.999695	0	0	-6.17E-05
$1e_x$	0	0.999987	0	0
$1e_y$	0	0	0.999987	0
$3a_1$	-6.17E-05	0	0	0.999989

Table 4.2: The scalar product of the ammonia molecular wave functions of the three valence orbitals $2a_1$, $1e$ and $3a_1$ calculated according to the approach proposed by Moccia using Slater-type functions.

Orbital	$2a_1$	$1e_x$	$1e_y$	$3a_1$
$2a_1$	0.999802	8.43E-08	-1.37E-17	8.55E-06
$1e_x$	8.43E-08	0.999724	-5.32E-17	-2.60E-09
$1e_y$	-1.37E-17	-5.32E-17	0.999726	5.89E-18
$3a_1$	8.55E-06	-2.60E-09	5.89E-18	0.999951

Table 4.3: The scalar product of the ammonia molecular wave functions of the three valence orbitals $2a_1$, $1e$ and $3a_1$ calculated from Gaussian 03 using the 6-31G basis set with 12 partial waves.

n_{ik}	λ_{ik}	$m_{\lambda_{ik}}$	ζ_{ik}	a_{ik}				
				$1a_1$	$2a_1$	$3a_1$	$1e_x$	$1e_y$
1	0	0	11	0.06572	0.01157	0.00605	-	-
1	0	0	6.4	0.93704	-0.23268	-0.06461	-	-
2	0	0	1.75	-0.01261	0.75114	0.24313	-	-
2	0	0	1.28	0.00524	0.12576	-0.14177	-	-
2	0	0	2.56	0.01545	0.14793	0.0751	-	-
2	1	-1	1.34	-	-	-	-	1.00304
2	1	-1	1.99	-	-	-	-	-0.28579
2	1	-1	2.9	-	-	-	-	0.31169
2	1	0	1.34	-0.00164	-0.14357	0.95405	-	-
2	1	0	1.99	0.00393	-0.01826	-0.29504	-	-
2	1	0	2.9	-0.00355	-0.00938	0.40188	-	-
2	1	1	1.34	-	-	-	1.00304	-
2	1	1	1.99	-	-	-	-0.28579	-
2	1	1	2.9	-	-	-	0.31169	-
3	2	-2	1.6	-	-	-	-0.22929	-
3	2	-2	2.35	-	-	-	0.05282	-
3	2	-1	1.6	-	-	-	-	-0.18794
3	2	-1	2.35	-	-	-	-	0.03710
3	2	0	1.6	0.00002	-0.0783	-0.0144	-	-
3	2	0	2.35	-0.00006	0.00659	-0.00699	-	-
3	2	1	1.6	-	-	-	-0.18794	-
3	2	1	2.35	-	-	-	0.03710	-
3	2	2	1.6	-	-	-	-	-0.22929
3	2	2	2.35	-	-	-	-	0.05282
4	3	-3	2	-0.0002	-0.08013	0.0242	-	-
4	3	-2	2	-	-	-	0.06080	-
4	3	-1	2	-	-	-	-	-0.04008
4	3	0	2	0.00011	0.04992	-0.04098	-	-
4	3	1	2	-	-	-	-0.04008	-
4	3	2	2	-	-	-	-	0.06080
4	3	3	2	-	-	-	-	-

Table 4.1: List of the coefficients ζ_{ik} and a_{ik} with the corresponding quantum numbers $n_{ik}, \lambda_{ik}, m_{\lambda_{ik}}$ that contribute to the development of the molecular wave function of each of the ammonia orbitals $1a_1$ ($i = 1$), $2a_1$ ($i = 2$), $3a_1$ ($i = 3$), $1e_x$ ($i = 4$) and $1e_y$ ($i = 5$), as a linear combination of N_i Slater-type functions $\Phi^{\zeta_{ik}}_{n_{ik}\lambda_{ik}m_{\lambda_{ik}}}$.

We also calculate the electronic spatial extent of NH_3 from the wave functions of the 5 occupied orbitals of ammonia developed using Gaussian, according to the following formula:

$$\left\langle r^2 \right\rangle = 2 \sum_{i=1}^{5} \left\langle \psi_i \mid r^2 \mid \psi_i \right\rangle \ . \tag{4.8}$$

The calculated wave functions give a good approximation of the electronic spatial extent of ammonia $\left\langle r^2 \right\rangle = 26.0285$ a.u. compared to the value given in Gaussian $\left\langle r^2_{Gaussian} \right\rangle = 26.0342$ a.u..

To further explore the validity of the wave functions before moving on to the collision description, we present calculated TDCSs from the Gaussian single-centered wave functions in non coplanar symmetric EMS conditions: both outgoing electrons have the same energy $E_f = E_e = 600$ eV and the same angle $\theta_f = \theta_e = 45$ °. Figure 4.15 depicts the momentum profiles for the three orbitals in these EMS conditions, calculated with the single-centered molecular wave functions used in our program, and the Moccia Slater-type wave functions also using our program, in comparison with the experimental data provided by *Bawagan et al.* [17].

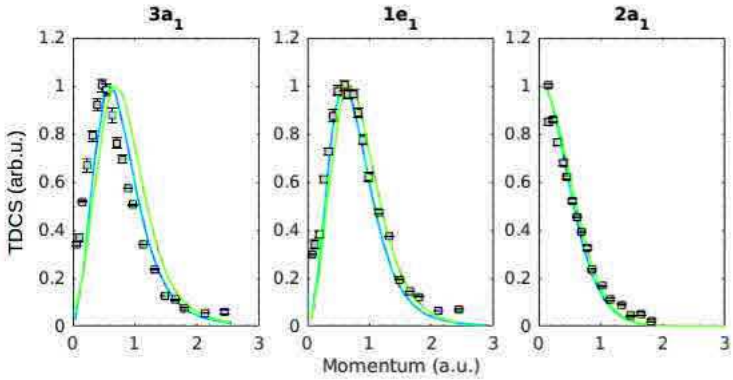

Figure 4.15: Absolute momentum distributions of the three outermost valence orbitals of NH_3 calculated using Moccia wave functions (Blue lines) and from single-center Gaussian-type wave functions generated using restricted Hartree-Fock theory in Gaussian 09 with the 6-31G basis set (Green lines), compared to experimental data provided by *Bawagan et al.* [17] (Solid squares)

As can be seen in figure 4.15, the general shape of the momentum distributions obtained with the single-centered wave functions developed with the simple 6-31G basis set is similar to that obtained with Moccia wave functions and in good agreement with the experimental EMS data.

All these tests allow us to conclude on the good quality of the single-center Gaussian and Slater molecular wave functions. We can now use these wave functions to study the collision description in our program. Since in the work of *El Mir et al.* the TDCSs are calculated with Moccia wave functions, we first compute the TDCSs with these same wave functions to explore the effect of the differences in the collision description within the same model (1CW or 1DW). We then present the calculated TDCSs with the Gaussian wave functions.

TDCSs in the 1CW model

The 1CW approach used in *El Mir et al.* [60] consists in calculating the TDCSs with a Coulomb wave for the ejected electron while the projectile electron is described by a plane wave, just like our 1CW approach. However, these TDCSs are calculated using the analytic form of the Coulomb wave function while we do so numerically using partial wave series. The analytical form of the Coulomb wave function reads:

$$\mathscr{F}^{(-)*}_{\vec{k}_e}(\vec{r}_1) = (4\pi)e^{-i\vec{k}_e.\vec{r}_1}\Gamma(1-i\eta_e)e^{(-\frac{\pi}{2}\eta_e)}\ {}_1F_1(-i\eta_e, 1, i(\vec{k}_e.\vec{r}_1 + k_e r_1))\,, \tag{4.9}$$

while the partial wave development of this function (cf. Section 3.3.2) is calculated as follows:

$$\mathscr{F}^{(-)*}_{\vec{k}_e}(\vec{r}_1) = \sum_{l_e=0}^{\infty}\sum_{m_e=-l_e}^{l_e}(4\pi)(-i)^{l_e}e^{i\delta_{l_e}}\frac{F^*_{l_e}(k_e r_1)}{k_e r_1}Y_{l_e,m_e}(\hat{k}_e)Y^*_{l_e,m_e}(\hat{r}_1)\,, \tag{4.10}$$

with:

$$F_{l_e}(k_e r_1) = \frac{2^{l_e}e^{-\frac{\pi}{2}\eta_e}\,|\Gamma(l_e+1+i\eta_e)|}{(2l_e+1)!}\,(k_e r_1)^{l_e+1}\ e_1^{-ik_e r_1}\ {}_1F_1(l_e+1-i\eta_e, 2l_e+2, 2ik_e r_1)\,. \tag{4.11}$$

Moreover, Slater-type wave functions developed according to the approach proposed by Moccia [61] are used in *El Mir et al.* [60] while our program calculates these wave functions from the output of the Gaussian software [59] as linear combinations of Gaussian-type orbitals.

We begin by using Moccia wave functions in our program and calculating the TDCSs with our partial wave series numerical formalism. Figure 4.16 shows that the same result is obtained with the two approaches. This further validates our 1CW collision description. The superscript (1) in the legend indicates the 1CW model used in [60] and the (M) indicates the 1CW model used in our work with Moccia molecular wave functions. These results are obtained with 10 partial waves for the projectile electron, associated to the development of $e^{i\vec{k}.\vec{r}}$, and 14 partial waves for the ejected electron. Hence, numerically calculating the TDCSs in the 1CW model using Moccia wave functions for the target, numerically with our program using partial wave series leads to the same results as the analytical approach.

Similar results are also obtained with the Gaussian wave functions. As shown in figure 4.17, the order of magnitude of the TDCSs calculated with the Gaussian wave functions is the same as that of the TDCSs calculated with the Moccia wave functions, the shape of the TDCSs is also the same for the three orbitals, with a slight difference in the amplitudes that is expected since two completely different descriptions of the bound electron's wave function are considered in each approach. The superscript (G) in the legend of figure 4.17 refers to the TDCSs calculated with Gaussian wave functions. In the partial wave

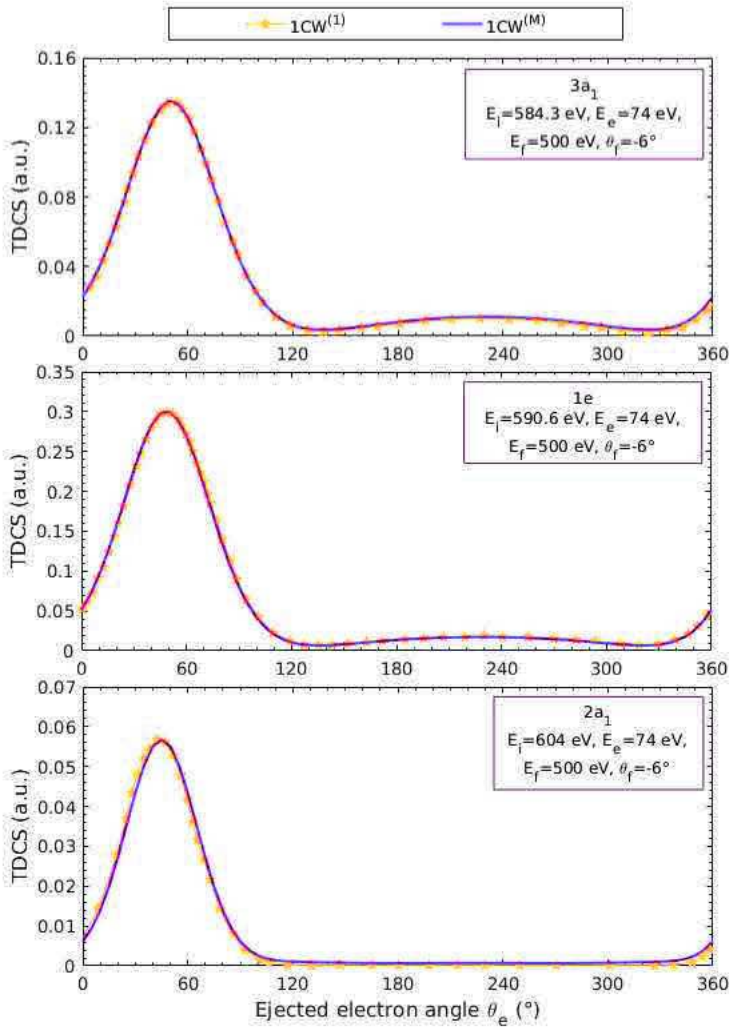

Figure 4.16: Numerical TDCSs calculated within the 1CW model using partial wave expansion (Purple line) compared to the analytical TDCSs presented in [60] (Orange stars). Moccia wave functions [61] are used for the wave functions of the three outermost valence orbitals of NH_3.

development of these wave functions, 12 partial waves were used while 10 and 22 partial waves were used for the development of the projectile wave function $e^{i\vec{k}.\vec{r}}$ and the ejected electron respectively.

TDCSs in the 1DW model

As pointed out to for the 1CW model, a different approach is used in *El Mir et al.* [60] to calculate the TDCSs within the 1DW model; the distorted wave is calculated analytically without using its partial wave development. To calculate this distorted wave, an average distorted potential is used, as explained in the previous chapter. To make sure this potential is properly calculated, we compute the effective charge seen by the electron as it travels away from the target. As shown in [60], the charge seen by the ejected electron from the three orbitals is very similar. This justifies considering an average potential from all the

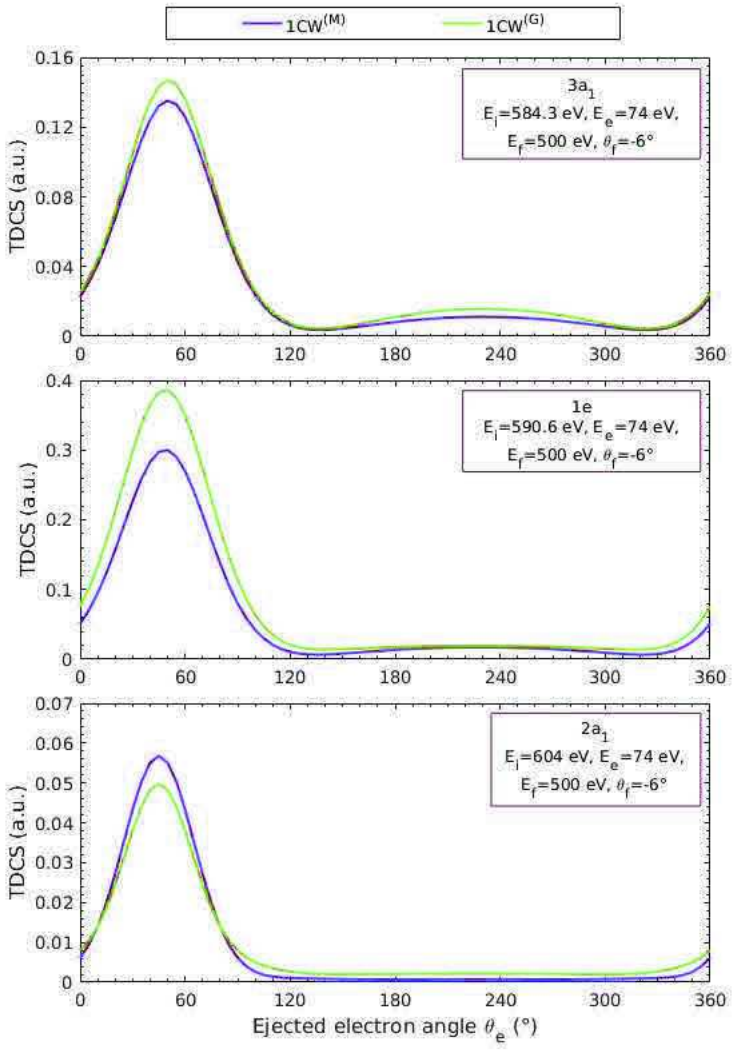

Figure 4.17: Numerical TDCSs calculated within the 1CW model using partial wave expansion, with both Moccia (Purple lines) and Gaussian-type (Green lines) molecular wave functions.

orbitals, which provides a good approximation of the potential for each orbital. In figure 4.18, we present the effective charge seen by the electron that is ejected from the each of the three outermost valence orbitals of ammonia as well as the average charge from all orbitals, in function of the distance that the electron travels away from the origin of the reference frame.

In figure 4.19, we compare this average potential from all the valence orbitals of ammonia using Gaussian wave functions to that obtained with the Moccia functions.

In the description of the molecular orbital wave functions proposed by Moccia, these wave functions are developed considering the heaviest atom as the center of the reference frame. On the other hand, in the single-centered Gaussian description, we consider the geometrical origin that is (0,0,0) and that is not necessary an atom of the considered molecule. Just as the electron leaves the molecule, the charge it experiences is the charge of the atom from which it is ejected ($Z_N = 7$). It results that when the origin is this atom,

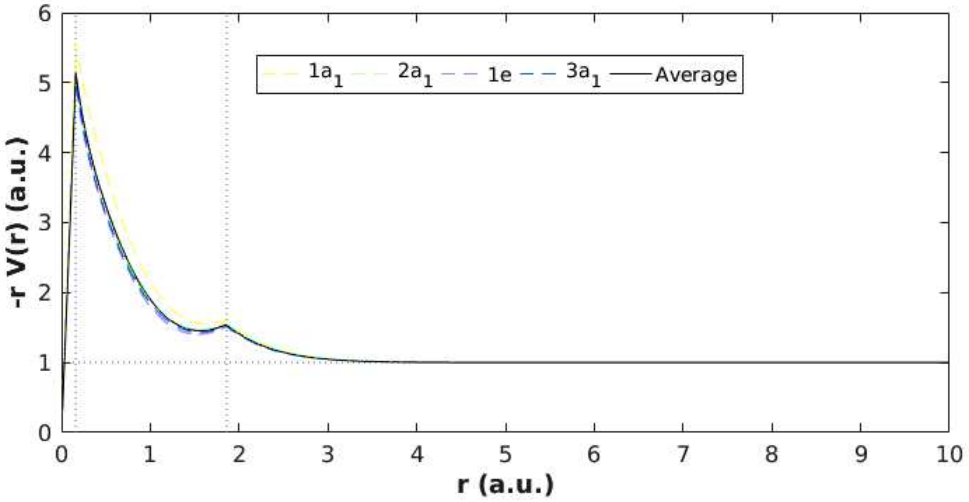

Figure 4.18: Effective charge seen by the ejected electron from the $3a_1$, 1e, $2a_1$ and $1a_1$ orbitals of ammonia. The average potential for all valence orbitals is also presented. Single center Gaussian wave functions are used to describe the molecular orbitals with the Gaussian 09 using the 6-31G basis set. A linear radial grid of 3000 points from 0.01 a.u. with 0.01 increment is considered.

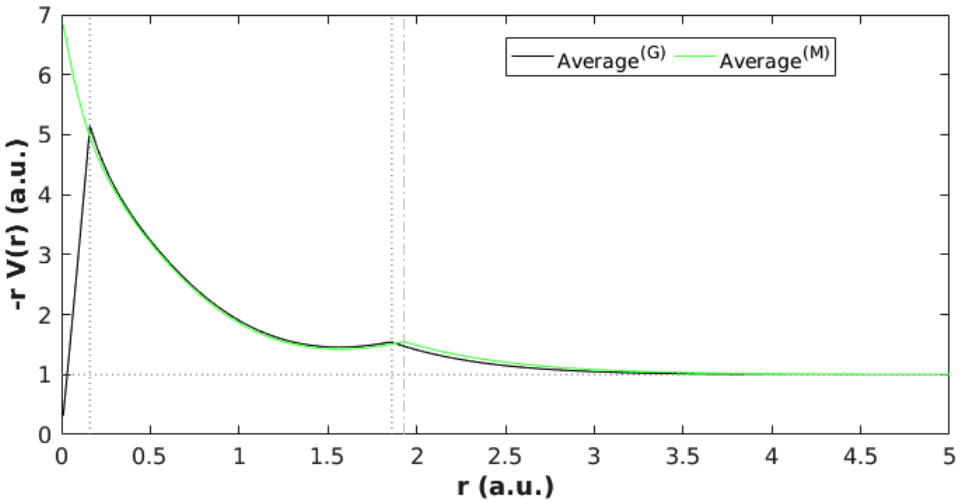

Figure 4.19: Effective charge seen by the ejected electron averaged over all the valence orbitals of ammonia. Single center Gaussian wave functions (Average$^{(G)}$) and Moccia wave functions (Average$^{(M)}$) are used to describe the molecular orbitals.

as in the description proposed by Moccia, the charge seen by the ejected electron at the origin is 7. This charge decreases as the electron moves away from the nucleus. It exhibits a minor maximum at $r = r_{NH} = 1.928$ a.u. which is equivalent to the distance between the Nitrogen and Hydrogen atoms. This maximum is slightly shifted when Gaussian wave functions are used, since according to the used geometry in Gaussian the $N - H$ length is $r_{NH} = 1.89$ a.u. which is the peak position in this case. Another difference is that at the origin the charge seen by the electron is zero in the description using Gaussian since the origin does not coincide with the nitrogen atom. The latter is at 0.16 a.u. from the origin

and it is at this distance that the ejected electron experiences a charge of 7. As the electron moves further away from the target, the effective charge tends asymptotically to 1.

We now go on to investigate the computed TDCSs after calculating the distorted wave by numerically integrating Schrödinger's equation using this potential. In figure 4.20, we present the TDCSs obtained with Moccia wave functions compared to the analytical data in [60] as well as those obtained using the Gaussian molecular wave functions.

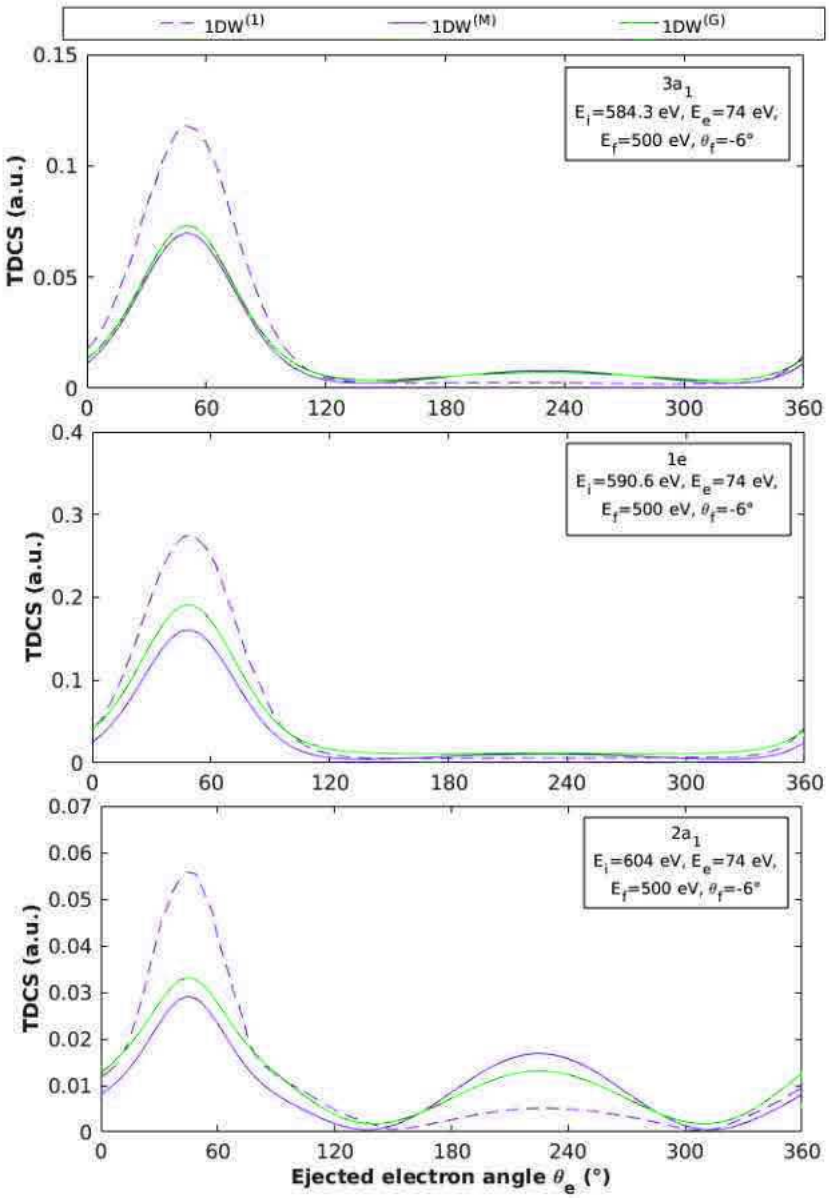

Figure 4.20: Triple differential cross sections for the ionization of the three outer valence orbitals of ammonia calculated within the 1DW model compared to the analytical TDCSs presented in [60] ($1DW^{(1)}$). The TDCSs are computed using Moccia functions [61] ($1DW^{(M)}$) and Gaussian functions ($1DW^{(G)}$) with the 6-31G basis set in Gaussian 09.

Unlike the 1CW case, the TDCSs from the two approaches, the one used in [60] and the one used in our program, are clearly different. Even with Moccia wave functions to describe the target, a reduced binary peak amplitude is found when the distorted wave

is numerically calculated with the use of partial waves and a slightly increased recoil peak amplitude, more pronounced for the inner $2a_1$ orbital, decreasing the amplitude ratio between the two regions. When these data are normalized to one at the binary peak, little difference is visible between the different approaches for the two outer orbitals. As seen in figure 4.21, our 1DW model clearly provides a wider binary peak and a more intense recoil peak for the $2a_1$ orbital than the 1DW model in [60] and the 1CW approaches. The binary peak is still not as wide as the experimental binary peak and the recoil peak still not as intense, but in comparison to the other models, our 1DW TDCSs for this orbital are closer to the experimental data especially in the recoil region where a more intense peak is found than with models using a more sophisticated description of the interaction such as BBKSR and BBK where a high recoil amplitude is obtained as well but the shape of the recoil region is not compatible with the experimental profile.

To conclude, none of the previously proposed theoretical models succeeds in reproducing the experimental TDCSs of ammonia in the kinematical conditions of *El Mir et al.* [60] neither do our 1CW and 1DW approaches. The theoretical binary peaks are all not as wide as the experimental peak, but it appears as though this experimental width is the result of a shoulder structure adding up to the side of the peak towards 90° since the experimental peak does not seem to be symmetric especially for the 1e and $2a_1$ orbitals. This is further noted with our 1DW results that describe well the lower angles side of the peak but underestimate all the TDCSs of the other side. The peak position is also shifted towards 90° in the case of the $3a_1$ orbital and that is only identified with the BBK and BBKSR models [53, 60]. The recoil peak also presents a shift towards higher angles for the $3a_1$ and the 1e orbitals and that is not predicted by any of the theoretical models. The amplitude of this region is only well described in the BBKSR model [53] for the $3a_1$ and 1e orbitals. For the inner $2a_1$ orbital, the BBK model in [60] as well as our 1DW model both predict a higher amplitude than the other models but still underestimate the experimental recoil region. Further work is required in order to understand the physical meanings of these discrepancies by using more sophisticated models that are a mixture of these proposed models. For example, as suggested in [53], the BBK, BBKDW and BBKSR models could all be combined in one model where the two outgoing electrons are described by distorted waves and both electrons are influenced by the short range potential. The potential experienced by each of the two electrons remains another problematic that needs more investigation in order to understand if, in the considered kinematics, the scattered and ejected electrons experience the same potential as they travel away from the target. In the kinematics of the water experiment [9], a similar investigation of the charge seen by the outgoing electron was considered in [34] where it seemed that not much difference is observed when the scattered electron is considered to be moving in the same potential as the ejected electron or in both this same potential field as well as an averaged potential due to the target's electrons. However, since the contributions of the two outer orbitals of water were not clearly separated in the experiment, no clear conclusions were drawn from the extensive theoretical work that was done in these kinematics. Since approaches very similar to our 1CW and 1DW models [16, 27] were used in these theoretical studies, we were able to validate our program by comparing our results to these data. In the next chapter, we apply these models for more complex molecules for which less studies were performed because of the difficulties of experiments and the heavy computing required for such targets.

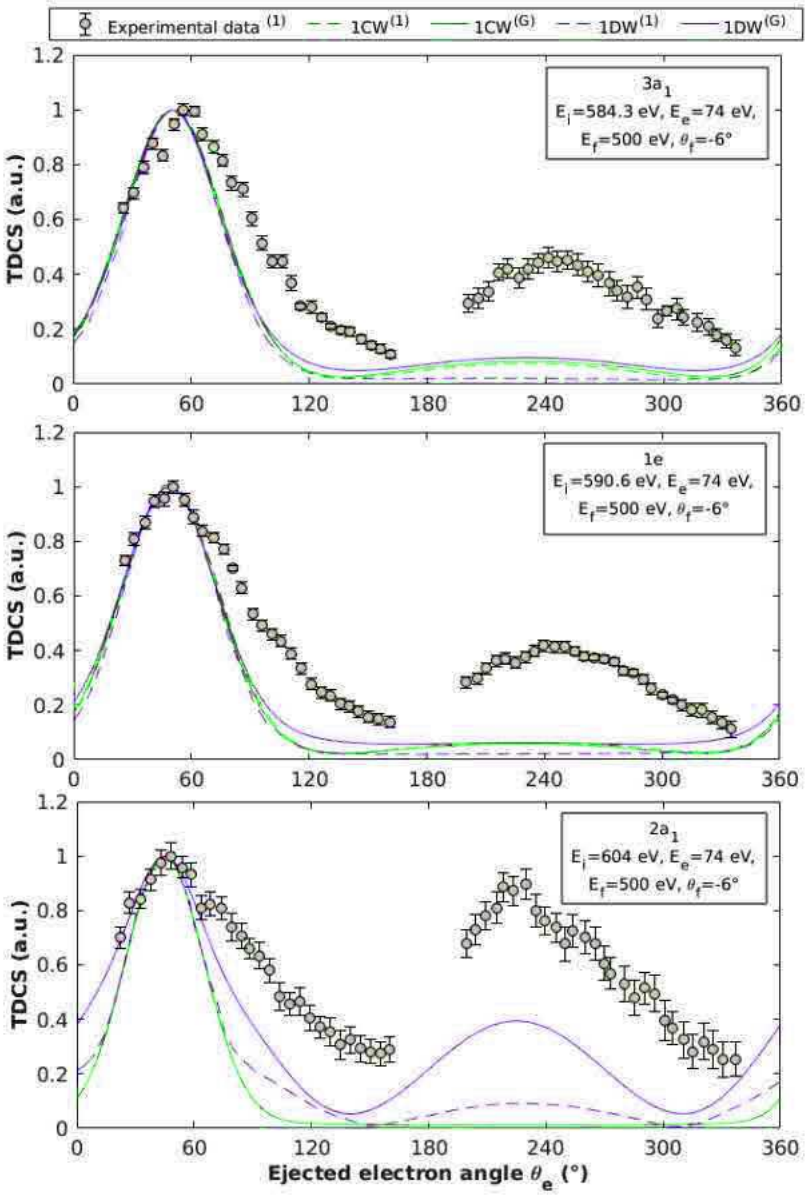

Figure 4.21: Triple differential cross sections for the ionization of the three outer valence orbitals of ammonia calculated within the 1CW and 1DW model (green and purple solid lines), using the single centered Gaussian wave functions, compared to the TDCSs given in [60] calculated within the 1CW (1CW(1)) and 1DW ($1DW^{(1)}$) models and to the experimental data of the same study.

References

[1] L. Sanche, "Biological chemistry: Beyond radical thinking," *Nature*, vol. 461, no. 7262, pp. 358–359, 2009.

[2] X. Pan and L. Sanche, "Mechanism and site of attack for direct damage to DNA by low-energy electrons," *Physical review letters*, vol. 94, no. 19, p. 198104, 2005.

[3] J. Berdys, I. Anusiewicz, P. Skurski, and J. Simons, "Theoretical study of damage to DNA by 0.2- 1.5 eV electrons attached to cytosine," *The Journal of Physical Chemistry A*, vol. 108, no. 15, pp. 2999–3005, 2004.

[4] P. Bernhardt and H. G. Paretzke, "Calculation of electron impact ionization cross sections of DNA using the Deutsch–Märk and Binary-Encounter-Bethe formalisms," *International Journal of Mass Spectrometry*, vol. 223, pp. 599–611, 2003.

[5] C. B. Opal, W. K. Peterson, and E. C. Beaty, "Measurements of secondary-electron spectra produced by electron impact ionization of a number of simple gases," *The Journal of Chemical Physics*, vol. 55, no. 8, pp. 4100–4106, 1971.

[6] R. F. Mathis and D. A. Vroom, "The energy distributions of secondary electrons from Ar, N_2, H_2O, and H_2O with clusters present," *The Journal of Chemical Physics*, vol. 64, no. 3, pp. 1146–1149, 1976.

[7] D. A. Vroom and R. L. Palmer, "Measurement of energy distributions of secondary electrons ejected from water vapor by fast electrons," *The Journal of Chemical Physics*, vol. 66, no. 8, pp. 3720–3723, 1977.

[8] M. A. Bolorizadeh and M. E. Rudd, "Angular and energy dependence of cross sections for ejection of electrons from water vapor. I. 50-2000 ev electron impact," *Physical review A*, vol. 33, no. 2, p. 882, 1986.

[9] D. S. Milne-Brownlie, S. J. Cavanagh, B. Lohmann, C. Champion, P. A. Hervieux, and J. Hanssen, "Dynamics in electron-impact ionization of H_2o," *Physical Review A*, vol. 69, no. 3, p. 032701, 2004.

[10] C. Kaiser, D. Spieker, J. Gao, M. Hussey, A. Murray, and D. H. Madison, "Coplanar symmetric and asymmetric electron impact ionization studies from the $1b_1$ state of H_2o at low to intermediate impact energies," *Journal of Physics B: Atomic, Molecular and Optical Physics*, vol. 40, no. 13, p. 2563, 2007.

[11] K. L. Nixon, A. J. Murray, O. Al-Hagan, D. H. Madison, and C. G. Ning, "Low-energy symmetric coplanar and symmetric non-coplanar (e, 2e) studies from the $3a_1$ state of H_2o," *Journal of Physics B: Atomic, Molecular and Optical Physics*, vol. 43, no. 3, p. 035201, 2010.

[12] X. Ren, S. Amami, K. Hossen, E. Ali, C. G. Ning, J. Colgan, D. H. Madison, and A. Dorn, "Electron-impact ionization of H_2o at low projectile energy: Internormalized triple-differential cross sections in three-dimensional kinematics," *Physical Review A*, vol. 95, no. 2, p. 022701, 2017.

[13] C.-Y. Lin, C. W. McCurdy, and T. N. Rescigno, "Complex kohn approach to molecular ionization by high-energy electrons: Application to h_2o," *Phys. Rev. A*, vol. 89, p. 012703, Jan 2014.

[14] C. Champion, J. Hanssen, and P. A. Hervieux, "Theoretical differential and total cross sections of water-molecule ionization by electron impact," *Physical Review A*, vol. 65, no. 2, p. 022710, 2002.

[15] R. Moccia, "One-Center Basis Set SCF MO's. III. H_2O, H_2S, and HCl," *The Journal of Chemical Physics*, vol. 40, no. 8, pp. 2186–2192, 1964.

[16] C. Champion, C. Dal Cappello, S. Houamer, and A. Mansouri, "Single ionization of the water molecule by electron impact: Angular distributions at low incident energy," *Physical Review A*, vol. 73, no. 1, p. 012717, 2006.

[17] A. O. Bawagan, C. E. Brion, E. R. Davidson, and D. Feller, "Electron momentum spectroscopy of the valence orbitals of H_2o and D_2O: Quantitative comparisons using Hartree—Fock limit and correlated wavefunctions," *Chemical physics*, vol. 113, no. 1, pp. 19–42, 1987.

[18] M. Brauner, J. S. Briggs, and H. Klar, "Triply-differential cross sections for ionisation of hydrogen atoms by electrons and positrons," *Journal of Physics B: Atomic, Molecular and Optical Physics*, vol. 22, no. 14, p. 2265, 1989.

[19] S. Zhang, "Momentum correlation in the three-body Coulomb continuum problem," *Journal of Physics B: Atomic, Molecular and Optical Physics*, vol. 33, no. 18, p. 3545, 2000.

[20] J. Gao, D. H. Madison, and J. L. Peacher, "Distorted wave Born and three-body distorted wave Born approximation calculations of the fully differential cross section for electron-impact ionization of nitrogen molecules," *The Journal of Chemical Physics*, vol. 123, no. 20, p. 204314, 2005.

[21] M. W. Schmidt, K. K. Baldridge, J. A. Boatz, S. T. Elbert, M. S. Gordon, J. H. Jensen, S. Koseki, N. Matsunaga, K. A. Nguyen, S. Su, T. L. Windus, M. Dupuis, and J. A. Montgomery, "General atomic and molecular electronic structure system," *Journal of Computational Chemistry*, vol. 14, no. 11, pp. 1347–1363, 1993.

[22] A. Danjo and H. Nishimura, "Elastic scattering of electrons from h2o molecule," *Journal of the Physical Society of Japan*, vol. 54, no. 4, pp. 1224–1227, 1985.

[23] J. P. Perdew and A. Zunger, "Self-interaction correction to density-functional approximations for many-electron systems," *Physical Review B*, vol. 23, pp. 5048–5079, May 1981.

[24] J. B. Furness and I. E. McCarthy, "Semiphenomenological optical model for electron scattering on atoms," *Journal of Physics B: Atomic and Molecular Physics*, vol. 6, no. 11, p. 2280, 1973.

[25] N. T. Padial and D. W. Norcross, "Parameter-free model of the correlation-polarization potential for electron-molecule collisions," *Physical Review A*, vol. 29, pp. 1742–1748, Apr 1984.

[26] C. F. Guerra, J. G. Snijders, G. Te Velde, and E. J. Baerends, "Towards an order-N DFT method," *Theoretical Chemistry Accounts*, vol. 99, no. 6, pp. 391–403, 1998.

[27] H. D. Hafied, *Etude théorique de l'ionisation par impact électronique des molécules d'eau en phase gazeuse et liquide*. PhD thesis, Metz, 2007.

[28] M. J. Frisch, G. W. Trucks, H. B. Schlegel, G. E. Scuseria, M. A. Robb, J. R. Cheeseman, G. Scalmani, V. Barone, B. Mennucci, G. A. Petersson, *et al.*, "Gaussian 09, revision b. 01. wallingford, ct: Gaussian," *Inc.,(2*, 2004.

[29] C. Champion, "Electron impact ionization of liquid and gaseous water: a single-center partial-wave approach," *Physics in medicine and biology*, vol. 55, no. 1, p. 11, 2009.

[30] H. D. Hafied, A. Eschenbrenner, C. Champion, M. F. Ruiz-Lopez, C. Dal Cappello, I. Charpentier, and P. A. Hervieux, "Electron momentum spectroscopy of the valence orbitals of the water molecule in gas and liquid phase: A comparative study," *Chemical Physics Letters*, vol. 439, no. 1, pp. 55–59, 2007.

[31] A. O. Bawagan, C. E. Brion, E. R. Davidson, and D. Feller, "Electron momentum spectroscopy of the valence orbitals of H_2O and D_2O: Quantitative comparisons using Hartree—Fock limit and correlated wavefunctions," *Chemical physics*, vol. 113, no. 1, pp. 19–42, 1987.

[32] C. Brion, G. Cooper, Y. Zheng, I. Litvinyuk, and I. McCarthy, "Imaging of orbital electron densities by electron momentum spectroscopy – a chemical interpretation of the binary (e,2e) reaction," *Chemical Physics*, vol. 270, no. 1, pp. 13 – 30, 2001.

[33] M. Sahlaoui and M. Bouamoud, "Cross sections for electron-impact ionization of water molecules," *Canadian Journal of Physics*, vol. 89, no. 6, pp. 723–727, 2011.

[34] I. Tóth, R. I. Campeanu, and L. Nagy, "Triple differential cross sections for the ionization of water by electron and positron impact," *The European Physical Journal D-Atomic, Molecular, Optical and Plasma Physics*, vol. 66, no. 1, pp. 1–6, 2012.

[35] M. Sahlaoui and M. Bouamoud, "Electron impact single ionization of the water molecule in the second Born approximation," *Journal of Physics B: Atomic, Molecular and Optical Physics*, vol. 45, no. 8, p. 085201, 2012.

[36] A. S. Kheifets, A. Naja, E. M. Staicu Casagrande, and A. Lahmam-Bennani, "DWBA-G calculations of electron impact ionization of noble gas atoms," *Journal of Physics B: Atomic, Molecular and Optical Physics*, vol. 41, no. 14, p. 145201, 2008.

[37] H. Ehrhardt, G. Knoth, P. Schlemmer, and K. Jung, "Absolute H(e, 2e)p cross section measurements: Comparison with first and second order theory," *Physics Letters A*, vol. 110, no. 2, pp. 92 – 94, 1985.

[38] H. Ehrhardt, K. Jung, G. Knoth, and P. Schlemmer, "Differential cross sections of direct single electron impact ionization," *Zeitschrift für Physik D Atoms, Molecules and Clusters*, vol. 1, no. 1, pp. 3–32, 1986.

[39] E. Weigold, C. J. Noble, S. T. Hood, and I. Fuss, "Electron impact ionisation of atomic hydrogen: experimental and theoretical (e, 2e) differential cross sections," *Journal of Physics B: Atomic and Molecular Physics*, vol. 12, no. 2, p. 291, 1979.

[40] C. Dal Cappello, A. Haddadou, F. Menas, and A. C. Roy, "The second born approximation for the single and double ionization of atoms by electrons and positrons," *Journal of Physics B: Atomic, Molecular and Optical Physics*, vol. 44, no. 1, p. 015204, 2010.

[41] M. Brauner, J. S. Briggs, and H. Klar, "Triply-differential cross sections for ionisation of hydrogen atoms by electrons and positrons," *Journal of Physics B: Atomic, Molecular and Optical Physics*, vol. 22, no. 14, p. 2265, 1989.

[42] A. Pathak and M. K. Srivastava, "Comments on the triple differential ionisation cross sections in the second Born approximation," *Journal of Physics B: Atomic and Molecular Physics*, vol. 14, no. 23, p. L773, 1981.

[43] F. W. Byron Jr, C. J. Joachain, and B. Piraux, "On the second born approximation for the ionisation of atomic hydrogen and helium by fast electrons," *Journal of Physics B: Atomic and Molecular Physics*, vol. 15, no. 8, p. L293, 1982.

[44] T. N. Rescigno, C. W. McCurdy, A. E. Orel, and B. H. Lengsfield III, "The complex Kohn variational method," in *Computational Methods for Electron—Molecule Collisions*, pp. 1–44, Springer, 1995.

[45] C. W. J. McCurdy and V. McKoy, "Equations of motion method: Inelastic electron scattering for helium and CO_2 in the Born approximation," *The Journal of Chemical Physics*, vol. 61, no. 7, pp. 2820–2826, 1974.

[46] S. b. Zhang, X. Y. Li, J. G. Wang, Y. Z. Qu, and X. Chen, "Multicenter distorted-wave method for fast-electron-impact single ionization of molecules," *Physical Review A*, vol. 89, p. 052711, May 2014.

[47] F. A. Gianturco, A. Jain, and J. A. Rodriguez-Ruiz, "Test of local model potentials for positron scattering from rare gases," *Physical Review A*, vol. 48, no. 6, p. 4321, 1993.

[48] N. Sanna and F. A. Gianturco, "SCELib: A parallel computational library of molecular properties in the single center approach," *Computer physics communications*, vol. 128, no. 1-2, pp. 139–169, 2000.

[49] F. A. Gianturco and S. Scialla, "Local approximations of exchange interaction in electron-molecule collisions: the methane molecule," *Journal of Physics B: Atomic and Molecular Physics*, vol. 20, no. 13, p. 3171, 1987.

[50] F. A. Gianturco, L. C. Pantano, and S. Scialla, "Low-energy structure in electron-silane scattering," *Physical Review A*, vol. 36, no. 2, p. 557, 1987.

[51] N. Sanna, I. Baccarelli, and G. Morelli, "The VOLSCAT package for electron and positron scattering of molecular targets: A new high throughput approach to cross-section and resonances computation," *Computer Physics Communications*, vol. 180, no. 12, pp. 2550–2562, 2009.

[52] N. Sanna, I. Baccarelli, and G. Morelli, "SCELib3. 0: The new revision of SCELib, the parallel computational library of molecular properties in the Single Center Approach," *Computer Physics Communications*, vol. 180, no. 12, pp. 2544–2549, 2009.

[53] S. Houamer, M. Chinoune, and C. Dal Cappello, "Theoretical study of (e, 2e) process of atomic and molecular targets," *The European Physical Journal D*, vol. 71, no. 1, p. 17, 2017.

[54] M. Chinoune, S. Houamer, C. Dal Cappello, and A. Galstyan, "Application of a post-collisional-interaction distorted-wave model for (e, 2e) of some atomic targets and methane," *Journal of Physics B: Atomic, Molecular and Optical Physics*, vol. 49, no. 20, p. 205201, 2016.

[55] E. Ali, K. Nixon, A. Murray, C. g. Ning, J. Colgan, and D. H. Madison, "Comparison of experimental and theoretical electron-impact-ionization triple-differential cross sections for ethane," *Physical Review A*, vol. 92, p. 042711, Oct 2015.

[56] K. L. Nixon, A. J. Murray, H. Chaluvadi, C. G. Ning, J. Colgan, and D. H. Madison, "Low energy (e, 2e) coincidence studies of NH_3: Results from experiment and theory," *The Journal of chemical physics*, vol. 138, no. 17, p. 174304, 2013.

[57] S. G. Sayres, M. W. Ross, and A. W. Castleman, "Influence of clustering and molecular orbital shapes on the ionization enhancement in ammonia," *Physical Chemistry Chemical Physics*, vol. 13, pp. 12231–12239, 2011.

[58] I. Tóth, R. I. Campeanu, and L. Nagy, "Ionization of NH_3 and CH_4 by electron impact," *The European Physical Journal D*, vol. 69, no. 1, p. 2, 2015.

[59] M. J. Frisch, G. W. Trucks, H. B. Schlegel, G. E. Scuseria, M. A. Robb, J. R. Cheeseman, G. Scalmani, V. Barone, G. A. Petersson, H. Nakatsuji, *et al.*, "Gaussian 09, Revision A. 02. Wallingford, CT: Gaussian," *Inc.*, 2016.

[60] R. El Mir, E. M. Staicu Casagrande, A. Naja, C. Dal Cappello, S. Houamer, and F. El Omar, "Triple differential cross sections for the ionization of the valence states of NH_3 by electron impact," *Journal of Physics B: Atomic, Molecular and Optical Physics*, vol. 48, no. 17, p. 175202, 2015.

[61] R. Moccia, "One-Center Basis Set SCF MO's. II. NH_3, NH_4^+, PH_3, PH_4^+," *The Journal of Chemical Physics*, vol. 40, no. 8, pp. 2176–2185, 1964.

[62] A. Lahmam-Bennani, A. Naja, E. M. Staicu Casagrande, N. Okumus, C. Dal Cappello, I. Charpentier, and S. Houamer, "Dynamics of electron impact ionization of the outer and inner valence ($1t_2$ and $2a_1$) molecular orbitals of CH_4 at intermediate and large ion recoil momentum," *Journal of Physics B: Atomic, Molecular and Optical Physics*, vol. 42, no. 16, p. 165201, 2009.

[63] M. A. Kornberg and J. E. Miraglia, "Double photoionization of helium: Use of a correlated two-electron continuum wave function," *Physical Review A*, vol. 48, no. 5, p. 3714, 1993.

Chapter 5

Application to more complex biomolecules

The advancements in computing and technology in the past recent years allowed to overcome some of the experimental and computing difficulties and provide triple differential cross sections (TDCSs) for many molecular targets. Experiments were carried out to measure the TDCSs of complex molecules such as tetrahydrofuran (C_4H_8O) [1–4], tetrahydropyran ($C_5H_{10}O$) [3, 5], 1,4-dioxane ($C_4H_8O_2$) [3, 5], furfural ($C_5H_4O_2$) [6], tetrahydrofurfuryl ($C_5H_{10}O_2$) [2], para-benzoquinone ($C_6H_4O_2$) [7], pyrimidine ($C_4H_4N_2$) [8] and the DNA base thymine ($C_5H_6N_2O_2$) [9]. Despite the theoretical difficulties for such complex targets, theoretical studies were performed attempting to reproduce the experimental data. However, precise experimental data that are relevant for comparison with theoretical TDCSs for the ionization of complex targets are very difficult to acquire. We have seen in the previous chapter that investigating the theoretical approaches validity becomes a difficult task when the contributions of the two outer orbitals of water were included in the measured TDCSs. For more complex molecules, this becomes even harder as the outer valence region of such molecules includes more orbitals that are not clearly separated. In an experiment to measure TDCSs for thymine, contributions from eight inner orbitals were included in the TDCSs. Despite the great importance of such an experiment, the experimental constraints limited its usefulness for theoretical studies that could not clearly relate the experimental data to the theoretical results. In this chapter we present the recent experimental and theoretical studies that were done to provide TDCSs for the ionization by single electron impact of relatively complex targets: formic acid, tetrahydrofuran, and thymine. We also provide the TDCSs calculated with our 1CW model for formic acid and tetrahydrofuran.

5.1 Formic acid

5.1.1 Structure and properties

Formic acid is the simplest organic acid commonly used as a model of larger biomolecules such as amino acids and proteins. It is also considered the main catalyzer for enzymatic activity [10]. Formic acid exists under the form of hydrogen-bonded dimers or cyclic structures. The dimer of formic acid is often used as a model to study the molecular hydrogen bonding which governs most of the intermolecular interactions of complex biomolecules such as DNA [11, 12]. Formic acid vapor consists of hydrogen-bonded dimers which cannot easily be broken up into formic acid monomers and the first Electron Momentum Spectroscopy (EMS) study containing contributions from only the monomer was performed in 2009 [13]. The formic acid monomer (CH_2O_2) has 12 occupied orbitals. The outer valence region includes seven orbitals five of which are in the molecular plane (10a′, 9a′, 8a′, 7a′ and 6a′) and two are out of the molecular plane (2a″ and 1a″). The ionization energies of the seven outermost orbitals of formic acid are given in table 5.1.

Molecular orbital	Ionization energy (eV)				
	Gaussian fit of BES[1]	EMS[2]	PES[3]	B3LYP/TZVP[4],	RHF/6-31G
10a′	11.6	11.48	11.5	8.37	12.91
2a″	12.5	12.55	12.6	9.48	13.23
9a′	14.6	14.7	14.8	11.51	16.11
1a″	15.8	15.8	15.8	12.63	17.43
8a′	17.3	17.15	17.1	13.7	19.10
7a′	19.0	17.95	17.8	14.58	20.16
6a′	21.5	21.9	22	-	24.79

[1] *Colyer et al.* [14]
[2] *Nixon et al.* [13]
[3] *Vizcaino et al.* [15]
[4] *Nixon et al.* [16]

Table 5.1: Ionization energies of the seven outer valence orbitals of formic acid. The first set of data are taken from *Colyer et al.* [14] where the binding energy spectrum (BES) was fitted with a sum of Gaussian functions. The EMS data of *Nixon et al.* [13] are given next; similar results were obtained in another EMS study [17]. Photoelectron spectroscopy results [15] are also given. In the last two columns, theoretical binding energies obtained with Becke 3-parameter Lee-Yang-Parr (B3LYP) calculations using the Triple Zeta Valence Polarization (TZVP) basis set and with Restricted Hartree Fock (RHF) calculations in Gaussian 09 with the 6-31G basis set are given.

The theoretical methods given in table 5.1 do not accurately determine the experimental energies which are very close with the different experimental techniques. The Becke 3-parameter Lee-Yang-Parr (B3LYP) [18] method with the Triple Zeta Valence Polarization (TZVP) [19] basis set clearly underestimates the experimental binding energies while the Restricted Hartree Fock (RHF) calculations with Gaussian 09 using the 6-31G basis set

overestimate these energies. Other theoretical models, not presented in the table, better describe the ionization energies of these orbitals [16]. The energy separation between the highest occupied moleclar orbital (HOMO) 10a′ and the next highest occupied moleclar orbital ($HOMO^{-1}$) 2a″ is about 1.1 eV. Hence a high resolution coincidence apparatus is essential to separate the contributions of these two orbitals to the TDCS. These two orbitals are represented in figure 5.1.

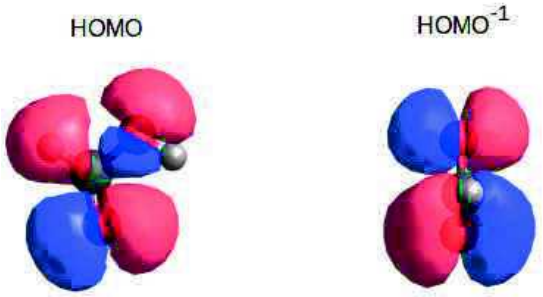

Figure 5.1: The highest occupied molecular orbital 10a′ and the next highest occupied molecular orbital 2a″ of formic acid monomer given by Gaussian 09 [20]. The large oval shapes are the electron wave functions of positive and negative sign. The smaller balls represent the carbon atom, the two hydrogen atoms and the two oxygen atoms.

5.1.2 Previous studies

A single set of experimental data for the TDCSs of the ionization of formic acid by electron impact was provided by *Colyer et al.* [14]. In fact, most of the experimental studies for this molecule were concerned with dissociative electron attachment [21–23] and electron scattering [15, 24]. EMS studies were also carried out to investigate the structure of formic acid [13, 16, 17]. Since formic acid exists as a monomer and as a dimer, the measured data often included contributions from the formic acid dimer. In the experiment of *Colyer et al.* [14], formic acid vapor was heated at 135°C in order to eliminate the dimer contribution by making sure most of the dimers break up into monomers [16]. In this study, experimental and theoretical TDCSs were provided at two incident energy kinematics: E_i=250 and 100 eV. Three scattered angles were considered in the E_i=250 eV case: θ_f=-5°, -10°, -15° and two scattered angles in the E_i=100 eV case: θ_f=-10° and -15°. In both cases, the ejected electron energy was fixed at 10 eV. The experimental resolution of 1.2 eV did not allow to separate the contributions from the two outermost valence orbitals 10a′ and 2a″ and hence the experimental TDCSs contained summed contributions from the two orbitals. Theoretical TDCSs were also calculated within the Molecular 3-body Distorted Wave (M3DW) model where the incoming and outgoing electrons are described by distorted waves. The Amsterdam Density Functional program [25] was used to calculate the molecular wave functions in Density Functional Theory (DFT) with the standard hybrid B3LYP functional [18] with the triple-zeta with two polarization functions Slater-type basis set (TZ2P). The orientation averaged molecular orbital (OAMO) approximation was applied thereby averaging the molecular wave functions over all possible orientations before calculating the TDCSs. Since the average of the molecular wave function of the 2a″ orbital yields zero due to its symmetry, TDCSs for the ionization of only the 10a′ orbital

were compared to the summed experimental TDCSs from the two orbitals. The initial and final state distorted waves were calculated using a spherically symmetric distorted potential which is the sum of a spherically symmetric static potential, an exchange-distortion potential [26], and a correlation-polarization potential [27]. The initial and final state static potentials were calculated from the charge density obtained from averaging the orbitals over all orientations, removing the active electron from the charge distribution to calculate the final state distorted static potential. Calculated TDCSs within this model were given considering these three components of the potential as well as with only the static potential. The corresponding models were labeled M3DW-CPE and M3DW respectively.

Colyer et al. [14] first presented calculated TDCSs with their M3DW-CPE model for the 10a′ orbital in the EMS settings of an experiment performed by *Nixon et al.* [13]. This experiment [13] provided the experimental momentum profiles of the 7 outermost valence orbitals of formic acid in a coplanar asymmetric geometry with ejected and scattered energies of 105 and 715 eV respectively and a scattered electron angle of 20.5°. They also presented theoretical TDCSs calculated with a code developed by *McCarthy and Weigold* [28] using plane waves for the incoming and outgoing electrons. Since this code was initially developed to calculate the TDCSs in the usual EMS symmetric non-coplanar kinematics, it only provided qualitative information about the shape of the distributions and not the real intensities of the TDCSs. *Nixon et al.* [13] used the sophisticated B3LYP/TZVP basis set [18, 19, 29, 30] to develop the molecular wave functions. *Colyer et al.* [14] found better agreement with their M3DW-CPE model with experimental TDCSs for the 10a′ orbital than with the Plane Wave Impulse Approximation (PWIA) of *Nixon et al.* [13] which is predictable in the experiment's kinematics. They stated that they performed the calculations using the basis used in [13] to generate the molecular wave functions (B3LYP/TZVP) and found similar results with the (B3LYP/TZ2P) that they use in their work. They also concluded that the OAMO approximation works for the 10a′ state. In the other kinematical conditions (E_i=250 eV and 100 eV), the theoretical M3DW and M3DW-CPE TDCSs did not agree with the experimental data especially in the binary region where a narrow peak was predicted by theory as opposed to the broad binary experimental peak. The relative amplitude between the binary and recoil peaks was also in disagreement with the experiment. The best agreement with the experimental data was found for the E_i=250 eV, θ_f=-15° case where the relative amplitudes of the binary and recoil peaks was better predicted by the M3DW-CPE model. In the E_i=100 eV, θ_f=-10° case, the relative amplitudes were also in acceptable agreement with the experimental data using the M3DW-CPE model. In the other conditions, the shape of the experimental data was not reproduced by both models. The recoil region obtained using the M3DW model was surprisingly in better agreement with the experimental recoil profile than the M3DW-CPE model. The authors suggested that these differences are probably due to the fact that the contribution of the 2a″ orbital is missing from the theoretical TDCSs and highlighted the need for experimental data for individual orbitals. Indeed, it was not possible to compute the TDCSs in these frameworks for the 2a″ orbital since the OAMO approximation did not work for this state. Despite the need for such approximations to make the study of complex molecules possible and overcome the computing difficulties that are encountered as the target becomes more complex, the OAMO does not allow to always have reliable results and a methodology based on the proper average method (PA) is essential to have accurate results.

The OAMO approximation was proposed by *Gao et al.* [31] to simplify the heavy calculations required in studies of complex molecules and that by averaging the molecular wave functions and calculating a single TDCS instead of calculating the TDCSs for all possible molecular orientations and then an average TDCS. Although this method worked for particular kinematics and molecular states [31–34], it failed in other studies while the PA method provided good agreement with experimental data [35, 36]. However, due to the heaviness of the calculations required for complex molecules, the OAMO method was used for many targets other than formic acid such as phenol [37], furfural [6], tetrahydrofuran [1–4], tetrahydrofurfuryl [2], tetrahydropyran [3, 5], 1,4-dioxane [3, 5], pyrimidine [8] and para-benzoquinone [7].

Using the PA approach, *Xingyu et al.* [38] computed the TDCSs of formic acid in the kinematics of the experiment of *Colyer et al.* [14] with a distorted wave to describe the ejected electron in a model that they labeled as MCDW for MultiCenter Distorted Wave. They previously used this approach to calculate the TDCSs for water as presented in the previous chapter. In the MCDW method, an anisotropic distorted potential is used to determine the distorted wave of the ejected electron within the distorted wave model, as opposed to calculating a spherically averaged isotropic potential as done in most distorted wave methods including our 1DW approach, arguing that the latter method could cancel important information about the anisotropic nature of the multicenter molecule. The molecular wave functions were calculated using DFT in Gaussian 03 [39] with the B3LYP hybrid functional [29, 40] and the TZVP basis set [19]. They also studied the effect of considering the nuclear term in the transition amplitude on the results by computing the TDCSs with and without it denoting the corresponding models by MCDW-NT and MCDW respectively. Since the proper average method does not pose the limitations of the OAMO method for the 2a″ orbital, they presented TDCSs for both the 10a′ and 2a″ orbitals as well as the summed contributions from the two states and compared them to the M3DW, M3DW-CPE and experimental data of *Colyer et al.* [14] in the 100 eV and 250 eV incident energy conditions. Better agreement with experimental data was obtained; the relative amplitude of the binary and recoil regions as well as the width of the binary peak were better predicted by the MCDW and MCDW-NT models of *Xingyu et al.* [38] than by the M3DW and M3DW-CPE models of *Colyer et al.* [14]. In the 100 eV incident energy conditions, the MCDW model better predicted the recoil region which amplitude was underestimated by the MCDW-NT. This was also the case for the 250 eV incident energy at the lowest scattering angle (-5°). The authors stated that the better accordance with experimental data with the MCDW model is probably by chance and attributed the inability of the MCDW-NT model to describe the recoil region in these conditions to the use of the First Born Approximation (FBA) and other approximations that were used. The obtained TDCSs for the 10a′ state also presented a wide binary peak and an acceptable relative amplitude of the recoil region with respect to the binary region which could mean that either the multicenter anisotropic nature of the target has to be taken into account to have a good description of the ionization dynamics and that the MCDW model is more suitable than the M3DW model in the considered kinematics or that the OAMO method used in [14] is the reason for the great disagreement with experimental data.

Applying our 1DW models to determine the summed TDCSs of the 10a′ and 2a″ orbitals within the PA approach, using an isotropic potential to calculate the distorted wave would lead to a better understanding of the importance of using the PA method and the anisotropic

potential. We intend to do that in a future work and only provide here the 1CW results which were the subject of a paper published in Journal of Physics B: Atomic, Molecular and Optical Physics [41].

5.1.3 Results

We begin by investigating the quality of the developed wave functions by presenting the momentum distributions of the 7 outer valence orbitals of formic acid. We consider the EMS experiment performed by *Nixon et al.* [13] in a coplanar asymmetric geometry where the ejected and scattered electrons were detected with energies 105 and 715 eV respectively, the scattered electron angle was fixed at 20.5° and the TDCSs were measured for the seven highest occupied orbitals of formic acid. In these kinematics, the contributions of the dimer of formic acid was eliminated by heating formic acid vapor to 120°C [42]. We present the calculated TDCSs in both our 1CW approach and in the plane wave approximation (PW) where all electrons are described by plane waves. In figure 5.2, the experimental data of *Nixon et al.* [13] are given by the gray squares while our theoretical PW and 1CW results are given by the red and blue lines respectively. The presented results were calculated considering the following ionization energies: 11.5, 12.65, 14.7, 15.8, 17.15, 17.9 and 22 eV from the highest occupied orbital $10a'$ to the $6a'$ orbital respectively.

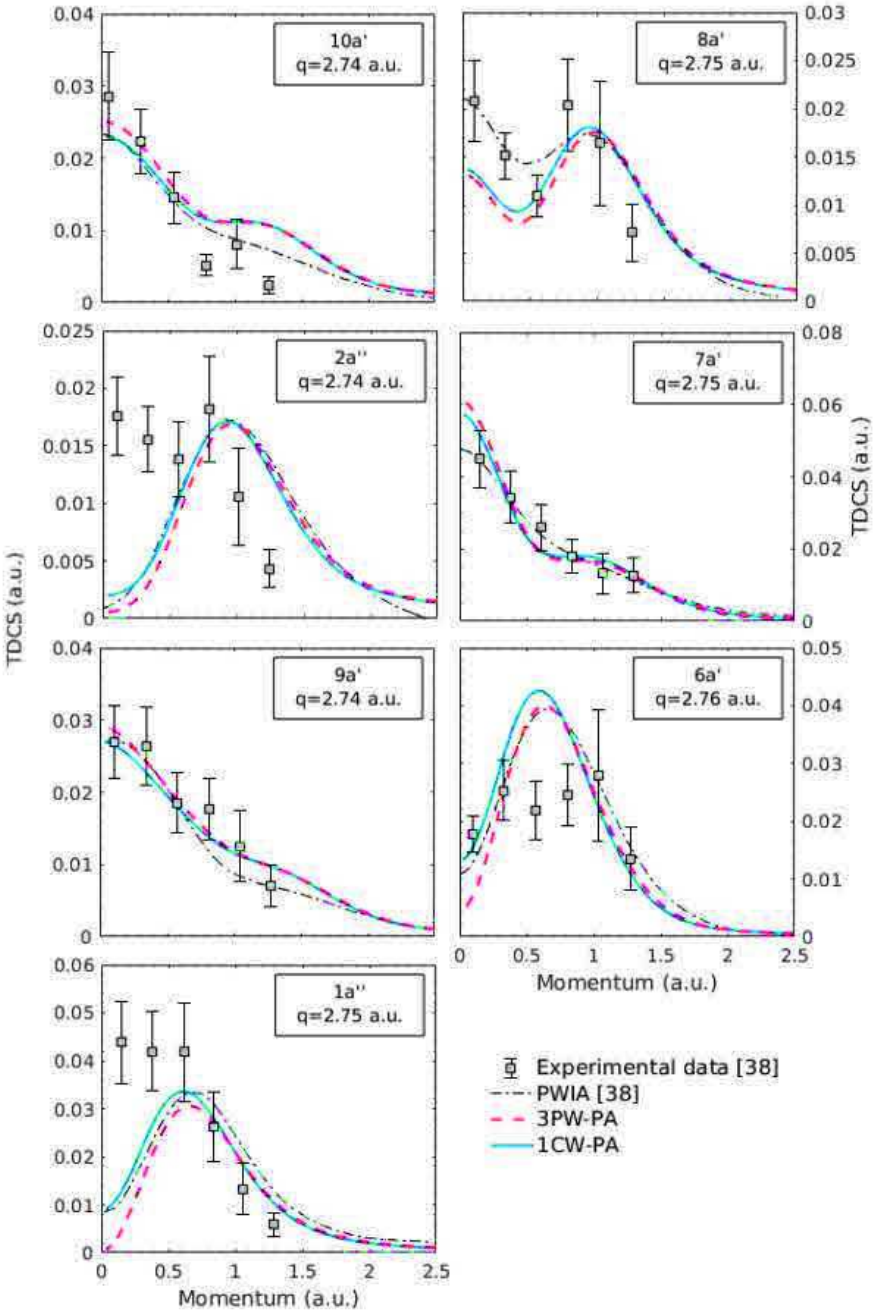

Figure 5.2: Triple differential cross sections of the seven highest occupied molecular orbitals of formic acid as a function of the momentum transferred from the projectile electron to the ejected electron. The solid squares represent the experimental data of *Nixon et al.* [13] measured in coplanar asymmetric kinematics with E_i = 820 eV plus the ionization energy of the corresponding orbital, E_f = 715 eV, E_e = 105 eV and the scattered electron angle is $\theta_f = -20.5°$. These experimental data as well as the theoretical data also given in [13], calculated in the PWIA and given by the dash-dotted black curves, were scaled to the the TDCSs computed within the theoretical framework detailed in this work. A plane wave (PW) and a coulomb wave (1CW) were considered for the ejected electron and are given in the dashed red curves and solid blue curves respectively.

The momentum transferred to the target is indicated in figure 5.2 for each orbital. The momentum transferred to the ejected electron, being equal to 2.78 a.u., is very close to these values therefore confirming the bethe-ridge kinematics of EMS where the main interaction is that of the projectile electron with the ejected electron. The obtained PW

TDCSs show that even with the simple 6-31G basis set our single centered Gaussian wave functions still provide acceptable agreement with the experimental EMS data [13]. Clearly for the $2a''$ and the $1a''$ orbitals, the theoretical TDCSs are not so much in agreement with the experimental TDCSs. This difference is also observed with the plane wave impulse approximation (PWIA) of *Nixon et al.* [13] and it was suggested that it is due to the symmetry of these two p-type orbitals. The use of the plane wave approximation in such kinematics is also problematic since it has been shown to provide better results as the incident energy increases beyond 1 keV [28]. Similar results are obtained with the 1CW model. In the considered kinematics, the use of a coulomb wave for the ejected electron does not provide a significant difference in the resultant TDCS profiles. Since the ejected electron has a somewhat low energy ($105eV$) compared to the usual EMS kinematics where the ejected electron energy is equal to $600eV$, describing the outgoing electrons with plane and coulomb waves is probably insufficient to have a truthful description of the ionization dynamics. However, since no experimental EMS data for the pure monomer of formic acid in higher energy kinematics are available, we can conclude on the good quality of the developed molecular wave functions as they provide an overall good agreement between the TDCSs and the experimental data in [13] and since similar results were obtained by *Nixon et al.* [13] using the more sophisticated B3LYP/TZVP basis set.

We now calculate the 1CW TDCSs for the two outermost valence orbitals $10a'$ and $2a''$ in the kinematics of the experiment of *Colyer et al.* [14]. We first consider the 250 eV incident energy kinematics and calculate the TDCSs for the three scattered angle values: $-5°$, $-10°$ and $-15°$. In these conditions, the 1CW model can provide a good description of the interaction with little drawbacks in comparison with more sophisticated models [43, 44]. The 1CW and 1DW TDCSs are shown in figure 5.3 where the individual contributions of the two orbitals as well as the summed contribution are given.

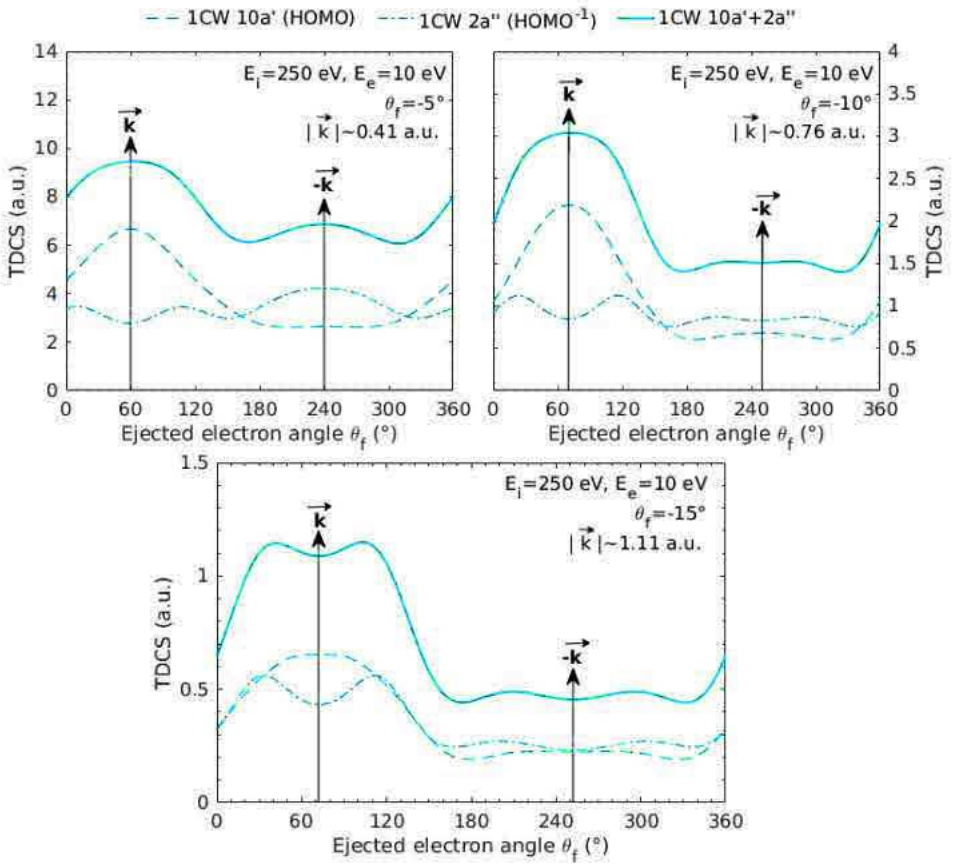

Figure 5.3: Triple differential cross sections of the ionization of the two outermost orbitals of formic acid, 10a′ and 2a′′, in function of the ejected electron angle θ_e. The considered kinematics are: E_i=250 eV, E_e=10 eV and three values of the scattered angle are considered: θ_f= -5°, -10° and -15°. The 1CW model presented in this work is used. The dashed curves correspond to the 10a′ orbital, the HOMO of formic acid monomer, while the dash-dotted curves correspond to the 2a′′ orbital, the HOMO^{-1}, and the summed TDCSs are given in the solid lines. The vertical arrows indicate the momentum transfer directions $\vec{k}$ and $-\vec{k}$.

The calculated TDCSs within the 1CW model are also given in the lower incident energy conditions, E_i=100 eV, in figure 5.4.

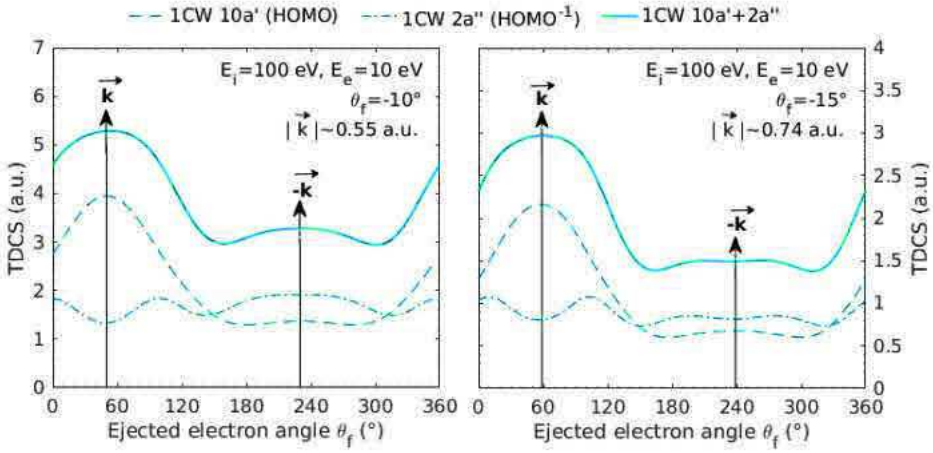

Figure 5.4: Same as figure 5.3 but for E_i=100 eV, E_e=10 eV and θ_f=-10°, -15°.

After examining the TDCS distributions in figures 5.3 and 5.4 we can clearly see that the two orbitals have different characters; the single broad peak structure of the TDCSs for the 10a′ orbital indicates a dominant s-character while the double peak structure for the 2a″ reveals a 2p-character. In the binary region, the ionization of the HOMO (10a′) is dominant while it becomes less prominent than the ionization of the 2a″ orbital in the recoil region. As the scattering angle increases, the binary peak becomes more narrow, the relative intensity of the recoil region decreases and the single peak structure of the binary and recoil regions breaks into a double peak structure. The momentum transferred from the projectile electron the the residual ion is about 0.42 a.u. and the considered conditions correspond to below (E_i=250 eV, θ_f=-5°, and E_i=100 eV, θ_f=-10°), on (E_i=250 eV, θ_f=-10° and E_i=100 eV, θ_f=-15°) and above (E_i=250 eV, θ_f=-15°) the Bethe ridge region. Although the 1CW TDCS profile for the 10a′ presents broad binary peaks, it is evident that the 2a″ contributions greatly influence the resultant summed TDCS especially in the split binary structure and the enhanced recoil region. Hence, eliminating the 2a″ contributions from the summed TDCS and comparing the 10a′ TDCSs directly to the experimental summed 10a′ and 2a″ TDCS, as was done in [14], omits a lot of information from the real theoretical summed contribution and does not provide a truthful comparison between the M3DW theory and the experimental data. In figure 5.5 we compare our 1CW TDCSs calculated in the 250 eV kinematics of *Colyer et al.* [14] to the M3DW, M3DW-CPE and experimental data in [14] and to the MCDW and MCDW-NT theoretical data in [38].

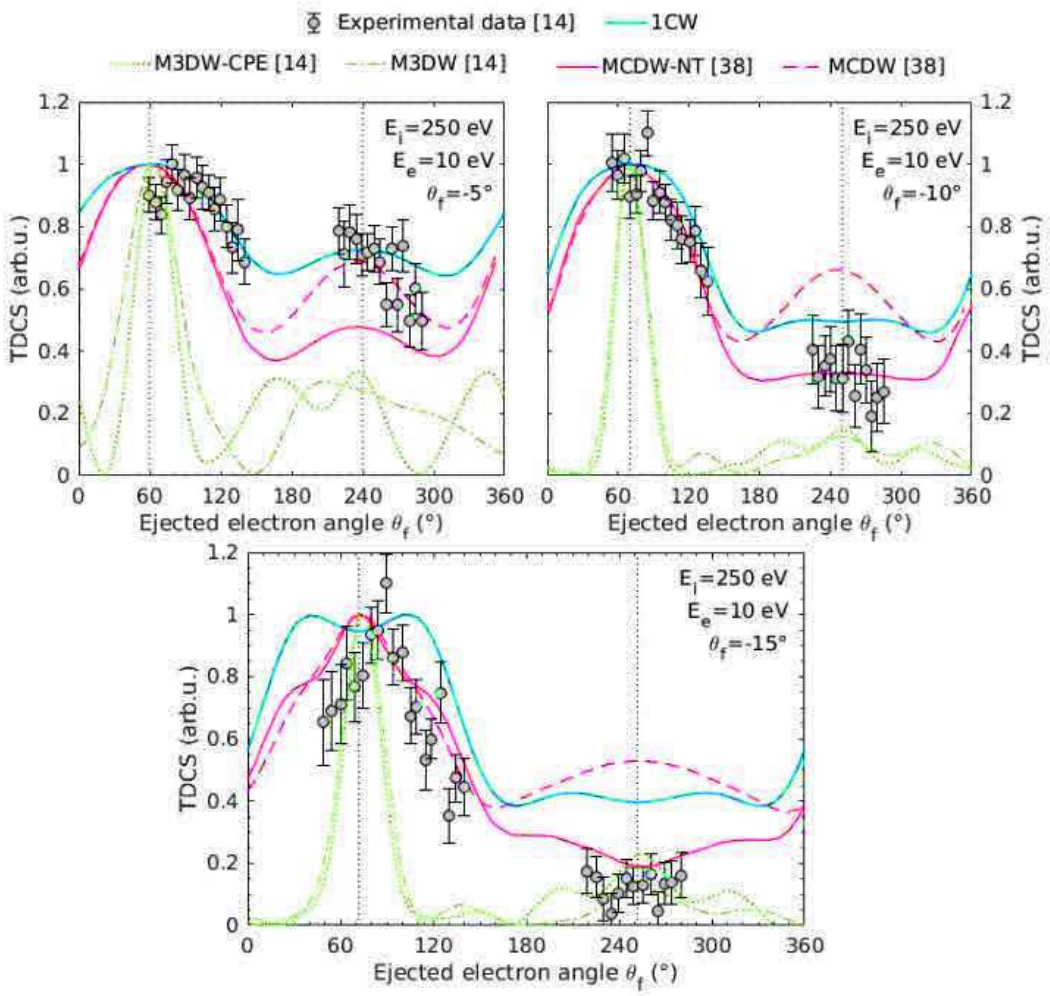

Figure 5.5: Triple differential cross sections for the ionization by single electron impact of the $10a'$ and $2a''$ orbitals of formic acid. The summed TDCSs from the two orbitals are presented and compared to the experimental TDCSs also containing contributions from the two orbitals. Our theoretical TDCSs calculated within the 1CW model are given in the blue curves. The experimental data are given in the solid squares, the M3DW and M3DW-CPE TDCSs provided by *Colyer et al.* [14] are given in the dash-dotted and dotted green curves, the MCDW TDCSs provided by *Li et al.* [38] are represented by the solid red curves and the dashed red curves with two considerations for the nuclear term: MCDW-NT and MCDW respectively. The experiment was performed in coplanar asymmetric geometry with $E_i = 250$ eV, $E_e = 10$ eV and the scattered electron angle was fixed at three values $\theta_f = -5°$, $-10°$ and $-15°$.

As explained in chapter 3, the transition amplitude can be written as the sum of two terms that correspond to a direct contribution and a nuclear contribution. In the considered theoretical framework, this leads to a $(e^{i\vec{q}\cdot\vec{r}} - 1)$ term in the transition amplitude. However, this is not always the case when other approximations are used. According to other proposed approaches, the nuclear term is sometimes omitted owing to the orthogonality of the initial and final state bound wave functions while in some studies it is calculated and is different from 1. In our theoretical framework, the molecular wave function is calculated from the potential of the target while the ejected electron wave function is calculated using a potential describing the continuum states of the hydrogen atom. Therefore, the orthogonality condition between the initial and final states is not fulfilled in our model and we cannot really eliminate the " – 1". In the previous chapter, we presented the

work of *Lin et al.* [45] on the water molecule in the 1CW framework where they used the complex Kohn variational method [46] to describe the interaction of the ejected electron with the ionized target. They focused on the different considerations used to describe this interaction and concluded that the use of the $(e^{i\vec{q}\cdot\vec{r}} - 1)$ term leads to better agreement with experimental data in the case of the $1b_2$ orbital and the summed $1b_1 + 3a_1$ TDCSs especially regarding the relative intensities of the binary and recoil peaks. Hence we only present the resultant 1CW TDCS distributions with this term in figure 5.5. Our results are given in the blue curves and are in acceptable agreement with the experimental data especially in the lowest scattered angle case.

As the scattering angle and consequently the momentum transfer increase, the agreement with the experimental data becomes more evident with the MCDW model in [38]. Among the presented theoretical models, it is indeed the MCDW-NT model of *Li et al.* [38] that provides the best description of the experimental data. The experimental data reveals a shift of the binary peak towards 90° which could be due to post collision interactions (PCI). This shift is only seen with the M3DW model of *Colyer et al.* [14]. The use of distorted waves for the projectile and ejected electrons could be expected to improve the agreement with the experimental binary peak position. As for the other features of the experimental TDCS profiles, the M3DW and M3DW-CPE models completely fail at reproducing them. It is interesting to see that the first order models (our 1CW model and the MCDW and MCDW-NT models in [38]), both based on the proper average method, agree much better with the experimental data. This proves the importance of the orientation averaging technique used in the theoretical approach and shows that the OAMO approximation alters the validity of even a very detailed model such as M3DW. Although the MCDW results better reproduce the relative amplitude of the recoil peak in the lowest scattering angle case, the decrease of this amplitude as the scattered angle increases is very well predicted by the MCDW-NT model. This shows that fully including the nuclear term in the MCDW model [38] leads to a better description of the ionization dynamics in the recoil region. Hence, the inability of our model to describe the recoil intensity as the scattering angle increases is probably due to the description of the nuclear term which is approximated by a Coulomb tail in our 1CW approach. Comparing our 1DW TDCSs to the MCDW data could allow us to better understand whether the shape of the binary peak is due to the distortion on the ejected electron or to the multicenter anisotropic nature of the target.

5.2 Tetrahydrofuran

5.2.1 Structure and properties

Tetrahydrofuran, C_4H_8O (THF), is similar to structural units of the sugar phosphate backbone of DNA and the latter is usually modeled as a series of THF and other cyclic ethers bonded to DNA bases and phosphate units. Determining the cross sections for particle interactions with THF is therefore an important step to understand the damage induced by ionizing radiation to DNA. Figure 5.6 shows the similarity between THF and a structure of the phosphate deoxyribose backbone in DNA.

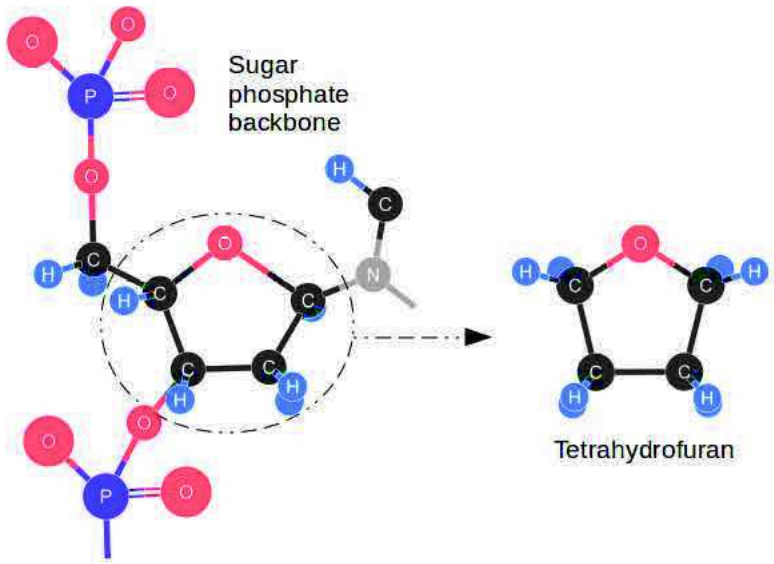

Figure 5.6: Tetrahydrofuran as a structural analog of a repetitive unit of the sugar phosphate backbone of DNA linked to a cytosine base.

THF has a five-member ring structure that exists in three different geometries. These isomers belong to point groups C_1, C_2 and C_s, which means that their symmetry is characterized by a center of symmetry, a two-fold symmetry axis and a mirror plane respectively. These isomers are presented in figure 5.7.

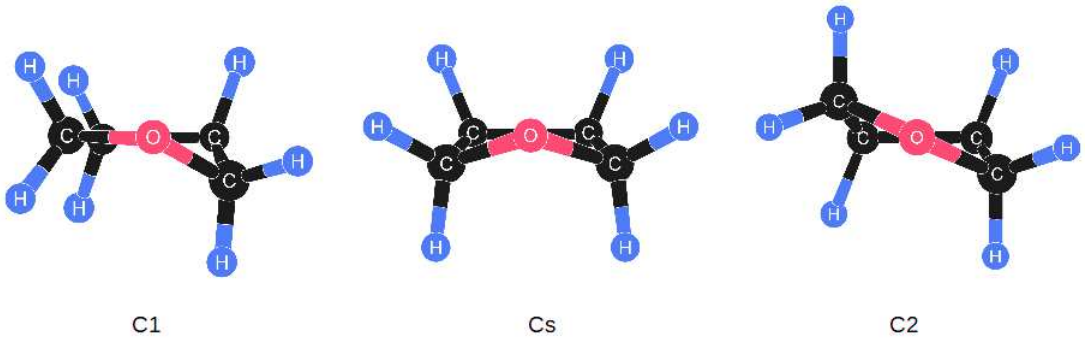

Figure 5.7: The three tetrahydrofuran isomers: C_1 (to the right), C_s (in the middle) and C_2 (to the right).

Many experiments and theoretical studies were done to determine which isomer has the lowest energy and is the most populated. The C_1 isomer was identified as the most populated of the three isomers in some studies [47, 48]. In other studies, it is the C_2 isomer that was found to be the most populated [49–52]. And in some studies, the equilibrium geometry was attributed to the C_s geometry [53–56]. Nevertheless, it was concluded that the C_1 isomer is the least stable of the three since it was identified as a transition state with an imaginary frequency in studies of high experimental resolution and high level calculation [53, 57]. On the other hand, the C_2 and C_s isomers were considered almost equally populated and they coexist at room temperature [58].

In most (e,2e) studies of THF, the TDCSs were presented for a set of combined two by two orbitals, each from one of these two isomers and having almost the same binding energy, using weights for each isomer based on the percentages provided by the previously mentioned studies.

In table 5.2, the ionization energies of the occupied orbitals of the two isomers are given as predicted by theory [59, 60], as measured in electron momentum spectroscopy [61] and photoelectron spectroscopy experiments [62], and as deduced from fitting the binding energy spectrum with Gaussian functions [1] in previous studies. It is clear that the highest occupied molecular orbitals of THF are 9b and 12a'. Most TDCSs were provided for the combined contributions of these two states which present both p and s character owing to the O(2p) and H(1s) atomic orbitals.

Molecular orbital		Ionization energy (eV)				
C_2	C_s	Theory[1] C_2	Theory[1] C_s	EMS[2]	PES[3]	Gaussian fit of BES[4]
9b	12a′	9.94	9.91	9.70	9.67	9.70
11a	11a′	11.65	11.65	12.14	11.41	11.80
10a	8a″	12.20	11.89	-	11.99	-
8b	10a′	12.43	12.26	-	12.48	12.80
9a	7a″	12.62	12.30	-	12.90	-
7b	6a″	14.21	13.74	14.54	14.00	14.30
6b	9a′	14.82	14.49	-	14.45	-
8a	5a″	14.95	15.29	-	15.29	-
7a	8a′	16.57	16.29	16.74	16.70	16.60
5b	7a′	16.93	16.83	-	-	17.70
6a	6a′	18.64	18.67	19.74	19.42	19.60

[1] *Giuliani et al.* [60] and *Yang et al.* [59]
[2] *Ning et al.* [61]
[3] *Yamauchi et al.* [62]
[4] *Colyer et al.* [1]

Table 5.2: Ionization energies of the valence orbitals of the two isomers C_2 and C_s of Tetrahydrofuran. The theoretical results are taken from *Giuliani et al.* [60] for all orbitals except the 6a and 6a′ orbitals, the ionization energies of which are taken from *Yang et al.* [59]. The EMS data and the PES data are taken from respectively *Ning et al.* [61] and *Yamauchi et al.* [62]. The ionization energies measured using the binding energy spectrum (BES) through the experiment of *Colyer et al.* performed in the aim of measuring the TDCSs of the single ionization of THF are given next [1].

As can be seen in the table, the binding energies of the orbitals are very close adding to the difficulty of performing (e,2e) experiments for this relatively complex molecule. For these reasons, identifying the contributions from separate orbitals is a very difficult task and contributions from many orbitals are often included in the measured TDCSs.

5.2.2 Previous studies

The first experiment providing TDCSs for the ionization of THF by single electron impact was done in 2010 by *Colyer et al.* [1] with an incident energy of 250 eV and an ejected energy of 10 eV in the coplanar asymmetric geometry at three scattering detection angles: -5°, -10° and -15° corresponding to three kinematic cases: below, on and above the bound Bethe ridge condition. Measurements were given for the combined 9b and 12a′ orbitals of THF which are the outermost orbitals of the two isomers C_2 and C_s. They first presented the binding energy spectrum (BES) of the outer valence region of THF which they fitted to a sum of seven Gaussian functions. The BES is usually measured and fitted with known functions in studies of complex molecules having orbitals with close binding energies that are hard to experimentally differentiate. This spectrum gives an idea about whether the TDCS of the considered orbital is well resolved or includes contributions from neighboring orbitals. In the kinematics of this study, the first peak was measured at a binding energy of 9.7 eV and was therefore attributed to the combined 9b and 12a′ orbitals of the C_2 and C_s isomers with respective binding energies of 9.94 and 9.91 eV. The spectrum also showed that this peak includes contributions from eight other orbitals since it is not completely resolved from the following broader peak. The apparatus that was used to measure the coincidence has a resolution of 1.5 eV and hence does not allow to separate the contributions of the two isomers. However, these two isomers were proven to be indistinguishable in previous measurements even with a higher resolution apparatus. The presented measurements were relative, with large error bars owing to the small magnitude of the coincidence cross section and the experimental difficulties for such a complex molecule. The experimental data for the three cases (three scattered electron angles) were fitted with a function that is a linear combination of Legendre polynomial functions of the ejected electron angle. In general, a double binary peak structure was observed with a local minimum between the peaks near the transfer momentum direction $\overrightarrow{q}$ in the two lowest scattered angle cases, while a broad binary peak was obtained for the -15° scattered angle case. A low intensity recoil peak in the three cases was found also having a minimum at the inverse momentum direction -$\overrightarrow{q}$ for $\theta_f = -5°$. The binary to recoil ratio was higher as the absolute value of θ_f increased. The low intensity of the recoil peak with respect to the binary peak is an interesting observation that many studies investigated. This was previously found in the same group's study for formic acid where it was suggested that the charge distribution is responsible for this low binary lobe. They suspected that the low charge in the center of mass of both formic acid and THF was responsible for this low scattering in the backward direction [63]. The experimental data were then compared to theoretical data calculated within the M3DW model. The molecular wave function of THF was calculated using the ADF program using density functional theory on a Slater-type basis set. The orientation averaged molecular orbital approximation was used to obtain an averaged orientation molecular orbital. Since the 9b and 12a′ orbitals are non symmetrical states, the OAMO gives an average of the wave function that is equal to zero, so the average of the absolute value of the wave function was considered instead of the direct average of the wave function. As in most previous M3DW studies, the potential consists of three parts: a static part, an exchange potential and a correlation-polarization potential. In this model, PCI are included to all orders of perturbation theory. The nuclear charge is placed on thin spherical shells centered on the molecule's center of mass, thereby averaging the nuclei over all possible orientations. M3DW did not predict the double binary peak structure that was found in experimental

data at lower angles but this was justified by the averaging process in M3DW which automatically produces s-type angular dependence and therefore leads to a single binary peak at the transfer momentum direction in the considered kinematics. The recoil peak was in agreement with experimental data except for the -5° case in which the M3DW results greatly underestimated the experimental recoil peak which was much higher than in the other two cases. In their interpretation of the theoretical data, the authors also hinted that the charge distribution was responsible for the low recoil peak recalling a previous study performed by *Toth and Nagy* [64] where they held the weak nuclear term in the static potential, that is due to the spreading of the nuclear charge over a spherical shell, responsible for the underestimated recoil peak found for methane. Since the recoil peak's relative amplitude with respect to the binary peak was well predicted by M3DW for the other two kinematic conditions, it was concluded that further investigation is required to explain the influence of kinematics on the scattering dynamics.

In this respect, they considered in their next work [2] different kinematical conditions with an ejected electron energy of 20 eV instead of 10 eV and presented measured TDCSs of the combined 9b and 12a′ states of THF, with a scattered electron angle of -5°. They found that the recoil peak has a much lower intensity under these kinematical conditions than under the previous ones. In order to explain this difference, they presented the momentum distributions (MD) of each of the two orbitals as well as the conformational average of the two. Less agreement was found between the M3DW data in these conditions than was obtained in the previous work and the recoil peak was still underestimated by the theory. In this study, they also presented the TDCSs of the ionization of the 28a orbital of THFA, another cyclic ether, and found a higher recoil amplitude for this target than for THF.

Furthermore, they explored the influence of the target structure on the TDCSs and particularly on the relative amplitude of the binary and recoil amplitude by considering two other cyclic ethers and comparing the results with the THF data of the previous study [3]. A higher relative intensity of the recoil peak was measured for the two other targets and the same TDCS tendency was found for these two targets in general in both theory and experiment. They also presented momentum profiles for the three targets and found that a similar profile for the two other molecules in the range of momentum corresponding to the transition from the binary peak to the recoil peak which is in harmony with the similar recoil to binary ratio and TDCS shape in general for these targets. The THF momentum showed a faster decrease from a higher intensity in this range of momentum which is in agreement with the higher binary to recoil amplitude ratio with a much lower recoil peak than was found for the other ethers. These findings confirm that the structure of the target influences the TDCSs. Moreover, they affirm the link between the momentum profile and the observed binary and recoil relative amplitude in the TDCSs and the importance of considering electron momentum profiles to explain the experimental recoil peak amplitude that was not predicted by theory.

Another recent experiment was performed by the same group [4] for lower energies, an incident energy of 26.5 eV and ejected energy of 3.5 eV, also in a coplanar asymmetric geometry with three scattered electron angles: 15°, 25° and 35°. Three cases were considered each corresponding to a different product of the ionization interaction. Naturally, each case corresponds to the ionization of different orbitals of THF. The ionization of the outermost 9b orbital leading to the formation of $C_4H_8O^+$, the ionization of the 9b and 11a orbitals leading to the formation of $C_4H_7O^+$ and the ionization of the 11a, 10b, 8b and

9a orbitals leading to the formation of $C_3H_6^+$ were treated. In each of the three cases they presented experimental TDCSs and compared them to theoretical data performed with M3DW using two approaches. The standard M3DW model, which consists in describing the incoming and outgoing electrons by distorted waves with a PCI term in the final state wave function for the Coulomb interaction between the outgoing electrons, was denoted by M3DW. In a second approach, the PCI term was written according to the Ward-Macek (WM) approximation [65] where the electron-electron separation is replaced by an average value leading to a PCI term that is independent of the electron coordinates and hence can be removed from the transition amplitude. This approach was denoted by WM. Before providing the data for each of the three ionization product cases with the two approaches, they presented TDCSs of the two main isomers of THF separately and for all scattered electron angles and found very little difference between them. Hence the weights normally used for each isomer to determine the TDCS of the combined isomers theoretically do not seem to have an important influence on the results. The same shape of the TDCS was found for all three interactions: instead of the usual general binary lobe-recoil lobe structure, the highest TDCS was obtained in the middle region, near 180° for the ejected electron angle. The same general trend was also found for the theoretical data. This is consistent with the fact that the PCI is strongest in this ejected electron angle range under the considered kinematics. They also justified the similar outcomes of the TDCSs for the ionization from all the considered orbitals by referring to electron momentum distributions presented in a previous study [66] showing that these distributions are similar for the considered orbitals despite their different structure and despite belonging to different symmetries. They also noted that the charge distribution of the orbitals over the whole molecule leads to the outgoing electron experiencing the same multicenter potential regardless of the orbital from which it is ejected, which also supports the similarity in the general shape of the TDCS for all the interactions concerning the ionization of different orbitals. In general, M3DW gave better agreement with experimental data than WM, both leading to the best agreement for a scattered angle of 25°.

Although acceptable agreement of the M3DW TDCSs with experimental data was observed under low energy kinematics, little agreement was found in the higher energy kinematics. As argued in the previous section on formic acid, the THF studies using the M3DW model show that the reliability of the M3DW approach is not always certain. The OAMO approximation might be the reason for the failure of this approach since in many studies the PA approach, which we use in this work, was proven to give more reliable results. We now present the computed TDCSs for the 12a′ and 9b HOMOs of the two isomers C_s and C_2 of THF using our 1CW approach in the 250 eV incident energy kinematics.

5.2.3 Results

We calculate the 1CW TDCSs for the ionization of the HOMOs 9b and 12a′, of the two THF isomers C_2 and C_s, within the experimental kinematics in [1, 2]: E_i =250 eV, E_e =10 eV and θ_f =-5°, -10°, -15° [1], and E_e =20 eV with θ_f =-5° [2]. In figure 5.8, we give the individual contributions from each isomer C_2 and C_s as well as the summed contribution to the TDCS assuming that the two isomers are equally populated. The ionization energies that we consider for 9b and 12a′ are respectively 9.94 and 9.91 eV [60].

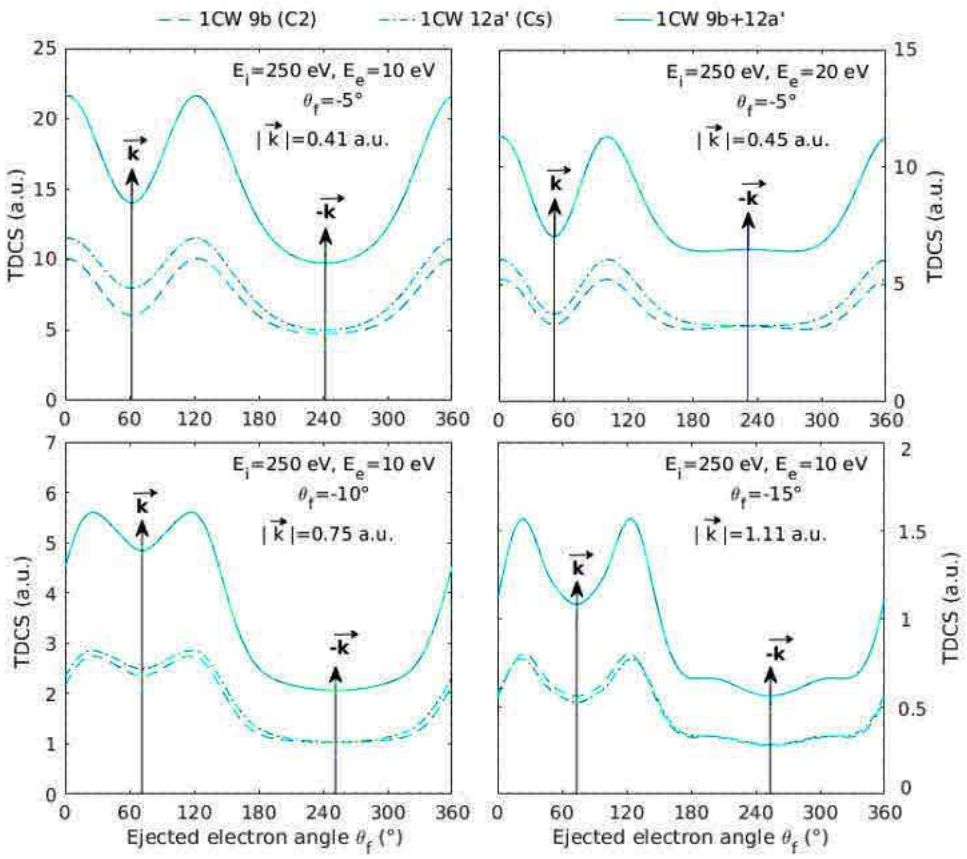

Figure 5.8: Triple differential cross sections for the ionization of the HOMOs 9b (dashed curves) and 12a′ (dash-dotted curves) of the C_2 and C_s isomers of tetrahydrofuran. The summed contribution is given in the solid curves. The considered kinematics are those of experiments [1] and [2]. The vertical arrows indicate the momentum transfer directions $\vec{k}$ and $-\vec{k}$.

With the 1CW model, the general shape of the TDCS in all the considered conditions consists of a double binary peak structure that is symmetrical with respect to the momentum transfer direction and a recoil region where no peaks are observed except for a small bump in the higher ejected energy case and a shoulder-like structure beyond the Bethe ridge region. The three conditions at the ejected electron energy of 10 eV correspond to below, on and beyond the Bethe ridge conditions. From the Legendre polynomial fit of the experimental data in [1], it was concluded that the split binary peak structure becomes less apparent as the momentum transfer increases. At the Bethe ridge condition (E_e=10 eV, θ_f=-10°), the minimum between the two binary 1CW peaks is less sharp than in the lower momentum case (E_e=10 eV, θ_f=-5°) but then this descent is steeper in the higher momentum condition (E_e=10 eV, θ_f=-15°) where two distinct binary peaks with a wide separation between them are observed. At the lowest momentum transfer case ($|\vec{k}|$=0.41 a.u.), the recoil lobe is not observed in the recoil region. The relative intensity of this region with respect to the binary region increases as the momentum value increases to 0.45 a.u. then it is at its lowest at the Bethe ridge condition ($|\vec{k}|$=0.75 a.u.) and above this region ($|\vec{k}|$=1.11 a.u.). The recoil region is also wider in the higher momentum conditions. The minimum relative amplitude of this region at the Bethe ridge region is expected since in these conditions, all the momentum is transferred to the ejected electron

and the residual ion does not participate in the backscattering of this electron. Beyond this region, two minor recoil peaks are observed making up a shoulder-like structure. This trend, not observed in the other conditions, can be explained by the higher momentum transferred to the target leading to a more important role of the residual ion in the post collision behavior of the ejected electron. The dominance of the 12a′ ionization over the 9b ionization in the binary region, seen with the M3DW model [1, 2], is also found with the 1CW model. It is more pronounced in the lower momentum transfer cases (E_e=10 eV, θ_f=-5° and E_e=20 eV, θ_f=-5°). In the other two cases the two seem to be equally probable with a slightly higher intensity of the 9b TDCSs in the binary region in the θ_f=-15° case.

These 1CW TDCSs are normalized to unity at the binary peaks' amplitude and compared to the experimental and M3DW data from [1] and [2] in figure 5.9.

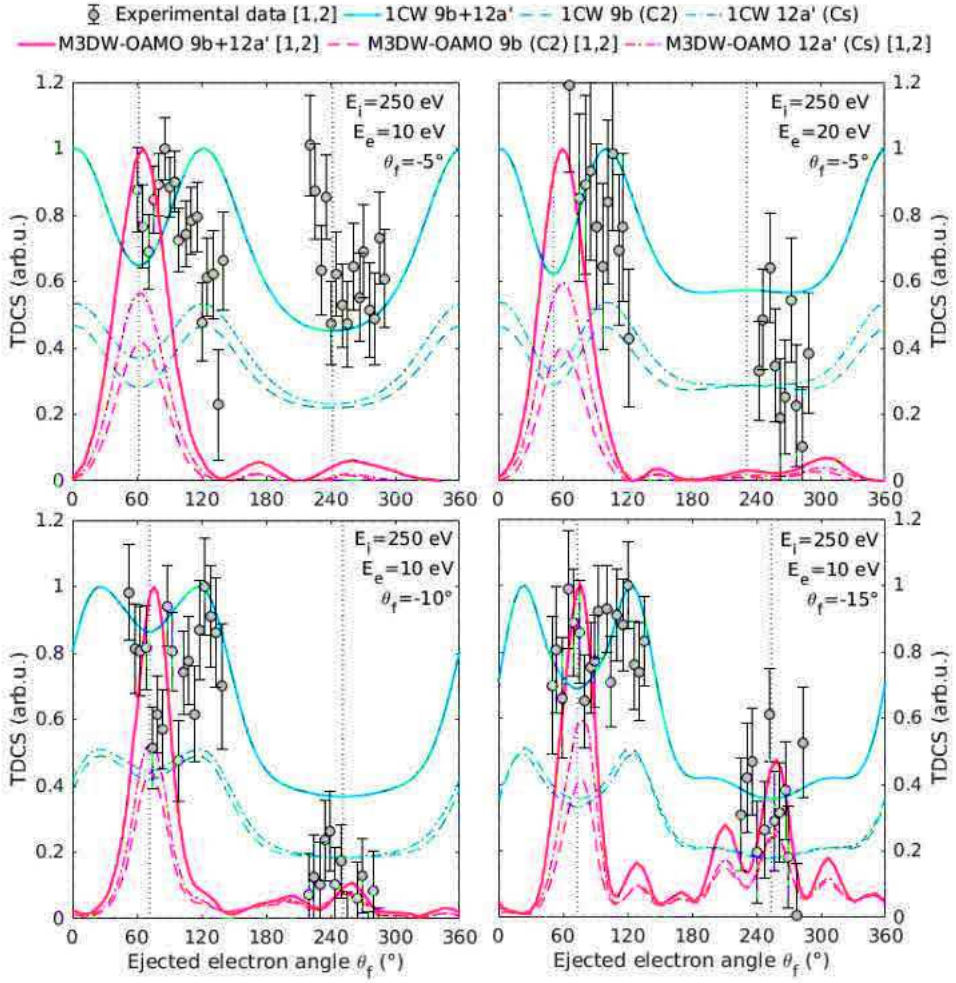

Figure 5.9: Triple differential cross sections of the ionization of the HOMOs of the C_2 and C_s isomers of tetrahydrofuran. The 1CW TDCSs are given in the blue curves and compared to the M3DW TDCSs from [1] (E_e=10 eV) and [2] (E_e=20 eV) given in the red curves. The 9b (C_2 HOMO) and 12a′ (C_s HOMO) TDCSs are given in the dashed and dash-dotted curves respectively while the summed TDCSs are given in the solid curves. The experimental data are taken from [1, 2] and given in the solid gray circles. The vertical dotted lines indicate the transfer momentum directions $\vec{k}$ and $-\vec{k}$.

The simple 1CW model better predicts the width of the binary region and its double

peak structure. The averaging process used in the M3DW method cancels the imprint of the 2p-state on the structure of the TDCS reducing it to an s-state single binary peak structure regardless of the molecular state. The disagreement of the M3DW TDCSs with the experimental data highlights the impact of the information contained in the individual molecular orbital wave functions on the TDCS trends and the importance of keeping this information in order to have a truthful understanding of the ionization dynamics. The relative intensity of the recoil region is also in acceptable agreement with the experimental data with the 1CW model. The best agreement is obtained in the highest momentum transfer case where the double peak structure of the recoil region is also reproduced in the 1CW TDCS. The use of a distorted wave for the ejected electron within the PA averaging method might lead to a better agreement with the experimental data in the other conditions. The large uncertainties of the experiment however prevent us from precisely concluding on the adequacy of the 1CW model in these kinematics. Nevertheless, it clearly shows the importance of performing a proper average on the TDCSs and the potential loss of important information with the OAMO approximation.

5.3 Thymine

5.3.1 Structure and properties

thymine, a pyrimidine derivative, is one of the nucleobases of DNA. Being a DNA component, providing particle interaction cross sections with thymine is a crucial step towards correctly modeling interactions with DNA. The single 6-member ring structure with two Nitrogen atoms is found in thymine $C_5H_6N_2O_2$ which exists in two isomers that only differ by the rotational orientation of the methyl group attached to the ring structure. The two isomers are illustrated in figure 5.10. In the cis isomer, a Hydrogen atom lies in the ring plane in a cis position with respect to the Carbon atom labeled C* while in the trans isomer this atom is oriented towards the other side of the ring.

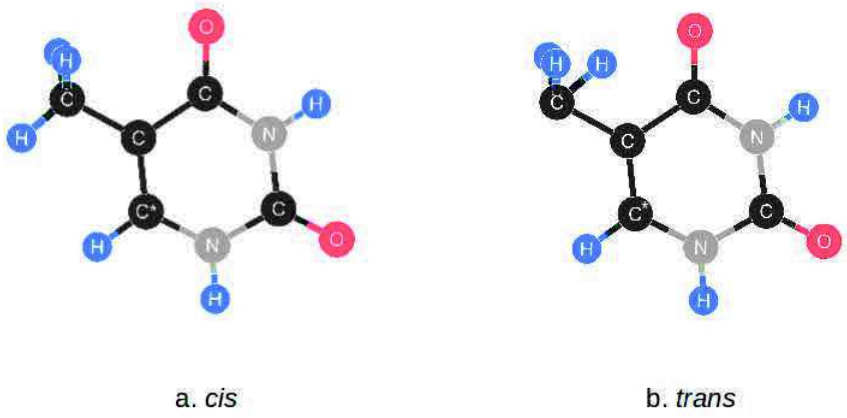

Figure 5.10: Structure of thymine in the two conformers *cis* and *trans* [67]. In the *cis* conformer (a), the in-plane Hydrogen of the methyl group is oriented towards the C*-H bond while in the *trans* conformer (b) it is oriented in the opposite direction.

Unlike the case of THF isomers, orbital assignment does not differ in the two isomers of thymine and very little differences in ionization energies are found. *Dolgounitcheva et al.* [67] found a difference of 0.14 eV in the ionization energy of the 18a′ orbital which is linked to the lone-pair of the oxygen atom in the two isomers. They used the P3 electron propagator method [68–70] to interpret the photoelectron spectrum measured by *Pavda et al.* [71] and optimized the molecular geometry of thymine using the many body perturbation theory (MBP2) [72] with the 6-311G** basis set in Gaussian 98 [73]. However, a later study [74] did not find this difference for the 18a′ orbital and argued that it was related to the MBP2 method. Using density functional theory with the B3LYP potential [18] under the same basis set, they found a shift of 0.3 eV between the two isomers for the 16a′ orbital that is located on the methyl group which orientation is not the same for the two conformers.

The main occupied molecular orbitals of thymine and their corresponding ionization energies are reported in table 5.3.

Molecular orbital	Ionization energy (eV)			
	HF[1]	PES[2]	Gaussian fit of BES[3]	RHF/6-31G
6a″	9.66	9.19	9.4	9.5742
5a″	11.88	10.45	11.4	11.5454
18a′	12.24	10.14	-	12.0228
17a′	13.12	10.89	-	12.9164
4a″	13.98	12.27	12.9	13.8292
16a′	15.09	13.32	14.4	14.9962
3a″	15.29	-	-	15.2834
15a′	15.55	-	-	15.6641
2a″	16.13	14.87	-	16.1703
14a′	16.91	-	-	16.8283
13a′	17.57	15.58	15.2	17.1252
1a″	18.14	-	-	17.9832
12a′	18.48	-	-	18.3698
11a′	19.34	17.93	17.8	19.6112
10a′	-	-	18.8	20.9081
9a′	-	20.85	20.7	21.1218
8a′	-	22.09	23.8	24.082
7a′	-	-	-	25.0217
6a′	-	-	-	26.3582
5a′	-	-	-	30.3925
4a′	-	-	-	33.7008
3a′	-	-	-	35.3574
2a′	-	-	-	38.693
1a′	-	-	-	39.2834

[1,2] *Trofimov et al.* [74]
[3] *Bellm et al.* [9]

Table 5.3: Ionization energies of the outer valence orbitals of thymine. The Hartree Fock (HF) and PES results are taken from *Trofimov et al.* [74]. The ionization energies measured through the experiment of *Bellm et al.* [9] discussed later are then presented. These values were obtained by fitting the measured binding energy spectrum with a sum of 9 Gaussians and they have been assigned to orbitals by comparison with the PES data of *Trofimov et al.* [74]. The error in the Gaussian peak position is 0.6 eV for the 9 peaks.

5.3.2 Previous studies

The closeness of the energy levels of thymine renders the experimental measurements as well as their interpretation a difficult task. Consequently, only one experiment was performed to determine TDCSs of thymine for a combination of valence shells and the

comparison with theoretical models has been very difficult because it is hard to interpret the measured TDCSs and separate the contributions of the different orbitals.

This experiment was performed in 2012 by *Bellm et al.* [9] for an incident energy of 250 eV, an ejected energy of 20 eV, and for a scattered electron detection angle of 15° and 10° in a coplanar asymmetric geometry. Due to the difficulty of separating the thymine orbitals which ionization energies are very close, the measured TDCSs in this experiment correspond to contributions from multiple inner valence orbitals. Although this difficult experiment provided very important data that incited other studies following very shortly after to test which theoretical model is best to describe the ionization by single electron impact of this very essential biomolecule, these data being relative and representing TDCSs of a combination of 8 inner orbitals, make it very hard for theoretical studies to reflect on their own results for individual orbitals. To simplify this translation from experimental data into theory, the authors tried to identify the contributions of orbitals to the measured data. They assumed that the greater contributors are the 2a″ and the 14a′ orbitals based on a previous study providing photoelectron spectra of the valence shells of nucleobases including thymine [75]. Hence they presented summed TDCSs of these two orbitals calculated in the FBA, using partial wave expansions of the wave functions and the frozen core approximation. To determine the initial state molecular wave function, they used the completely neglected differential overlap (CNDO) approximation. According to this approximation, the TDCS for the ionization of a thymine molecular orbital is expressed as the sum of cross sections corresponding to atomic contributions to the molecular subshell that are written in terms of spherical harmonics with Slater-type radial parts. This approximation was previously used to determine doubly differential cross sections of the ionization of molecules by protons and proved to be in good accordance with experimental measurements [76]. However, in their study *Bellm et al.* [9] used information provided by Gaussian 09 to develop the wave functions in the CNDO approximation which had not been done previously. They stated that their calculations were in very good agreement with the measured data while pointing out to the need for absolute measurements for a more truthful critique of the theoretical model. Summed TDCSs of the 2a″ and the 14a′ orbitals were given for a scattered electron angle of 15 degrees, corresponding to a transfer of momentum of magnitude 1.12 a.u., as well as 10°, corresponding to a transfer of momentum of magnitude 0.78 a.u.. The theoretical TDCSs of the 14a′ orbital underestimated the width of the experimental binary peak as well as the recoil to binary ratio at both scattering angles. A shift in the binary peak at a scattering angle of 10° was observed for both orbitals and was attributed to post collisional effects. A split binary peak was obtained with the FBA for the 2a″ orbital at 15° scattering detection angle and was not found in experimental data. This difference between theory and experimental data was justified by the missing contributions of other orbitals to the measured TDCSs.

Shortly after this work was published, *Houamer et al.* [77] published a comment on the previous paper questioning the validity of the presented results by presenting three tests. First, they tested the simple description of the molecular wave function that was given in *Bellm et al.* and which uses a weighted sum of atomic components instead of directly using a molecular wave function as in the description given by Moccia. They computed TDCSs for water in the same kinematical conditions using this method and compared the results to the experimental data of *Milne-Brownlie et al.* [78]. They found that this approach fails at describing the TDCS of the $1b_2$ and $3a_1$ orbitals where one binary peak is observed

instead of the two binary peaks predicted by the experiment. Then, they computed the TDCSs of methane in EMS conditions at high energies, where the FBA is certainly valid, with the same method used by *Bellm et al.* [9] to describe the TDCS as a sum of atomic contributions, and compared the results to TDCSs calculated in the FBA with Moccia wave functions. The two theoretical data were compared to the experimental data of *Clark et al.* [79]. The comparison showed clearly that the CNDO method used by *Bellm et al.* [9] leads to complete disagreement with experimental data for the $1t_2$ methane orbital. In the final test, they calculated the TDCSs of additional orbitals using the same approach as *Bellm et al.* [9] but for a scattering angle of 10° and showed that the shape of the TDCSs is similar for all these orbitals despite the differences between them which is very surprising. They also stated that they computed the TDCSs at the 15° scattering angle and found only two similar possible shapes for all the orbitals. Hence, it can be concluded from the work presented in *Bellm et al.* [9] are questionable. *Houamer et al.* [77] also suggested that the FBA does not include sufficient considerations of the interactions to accurately describe the ionization of thymine and that a more sophisticated model should be used.

In a consequent work, they calculated the TDCSs for the ionization of the $2a''$ and $14a'$ of thymine with the dynamic screening of three two-body Coulomb interaction (DS3C) model, which uses the Brauner-Briggs-Klar (BBK) method with effective charges, and considering the CNDO approximation for a scattered angle of 10° [80]. They compared the DS3C results to FBA results also using CNDO and to the experimental data of *Bellm et al.* [9] and found that the DS3C does indeed give better agreement with the experimental data than the FBA. They also investigated the similar shape of the TDCS for all the orbitals obtained in the work of *Bellm et al.* [9] with the FBA and calculated themselves the TDCSs using the FBA and the CNDO approximation with the same coefficients used by *Bellm et al.* [9]: they too found a similar shape of all the orbitals which they judged as surprising since the differences between the orbitals should lead to differences in the shape of the TDCS as shown in previous studies [81]. So they checked the CNDO approximation again, for the water molecule too just as in their previous work, but this time they compared the summmed TDCSs for the $3a_1$ and $1b_1$ orbitals of water calculated using the FBA with the CNDO approximation to TDCSs calculated with the FBA using single centered Gaussian wave functions developed from the Gaussian software. They found that using the CNDO leads to complete disagreement with the experimental data of *Milne-Brownlie et al.* while the FBA with single centered initial state molecular wave functions calculated from Gaussian gives good agreement with the experimental data. Hence it can be concluded that the CNDO method used by *Bellm et al.* [9] does not work for simple molecules such as the water and methane molecules, as shown in their previous work, and should not be used for a complex molecule such as thymine and that the results it leads to are, most probably, by chance close to the experimental data but don't mean that the theoretical framework proposed by *Bellm et al.* [9], based on the FBA with the CNDO approximation, is an accurate model that can be used for any molecule. In their work, *Dal Cappello et al.* proposed the use of second order models such as the Second Born Approximation (SBA) or the BBK model to determine the TDCSs for thymine. They also proposed to calculate the molecular wave functions as single-centered Gaussian wave functions written in partial wave expansion. They tested the convergence of their results by presenting TDCSs using different numbers of partial waves and concluded that it is reached for a sum up to $L = 7$. They also provided a test to choose the appropriate value of the average excitation energy of the intermediate states which is considered in the SBA

and concluded that its choice does not have a great influence on the calculated TDCS for ionization by electron impact. Throughout their work, they highlighted the complexity and heaviness of calculations required to perform both the SBA and the BBK methods and showed TDCSs for all eight inner valence orbitals only with the SBA, which calculations are less complex than BBK. The obtained TDCSs with the SBA for a scattered angle of 10° were compared to TDCSs obtained with the FBA and to the experimental data of *Bellm et al.* [9]. They found that, unlike the FBA, the SBA was capable of predicting the shift in the binary peak for the 2a″ orbital, and that the binary to recoil ratio is much better described with the SBA than the FBA. However, the complex structure of the recoil peak was not well predicted by neither of the two approximations. In conclusion, all these studies support the fact that the FBA with the CNDO approximation is not the best model to describe the ionization of such a complex molecule in the considered kinematics as conveyed by *Bellm et al.* [9] and other models should be explored to improve the compatibility of theory with the experimental data. Nevertheless, it is to note that the complexity of the experiment, and the fact that the experimental data presented in *Bellm et al.* [9] include contributions from eight inner orbitals make the task of judging on the agreement between experimental data and theoretical predictions also a complex task.

The TDCSs obtained with our 1CW and 1DW models for the ionization of thymine will not be presented here. The 1CW results are in fact very similar to the FBA results of *Houamer et al.* [77]. We intend to test our 1DW model within the kinematics of the thymine experiment but we don't expect to have much information from the comparison with the experimental data. Although it is very difficult to perform such measurements, a more precise experiment providing the TDCSs for the outer valence orbitals of thymine is necessary if the experimental data are to be compared with theoretical results.

Throughout this chapter, we highlight the importance of performing the orientation averaging on the cross section, within the proper average method, and not on the molecular wave functions as suggested in the OAMO approximation. The problem of orientation averaging is indeed one of the challenges that impose heavy computing and render determining the cross sections for the ionization of complex molecules somewhat impossible especially with sophisticated models. As seen in the presented studies on formic acid and tetrahydrifuran, the use of a complex model was possible only by using the OAMO approximation to overcome the orientation averaging problem. However, we show that this method is not reliable. It not only weakens the detailed model that is being used, but also omits important information about the state that is being studies and its relevance is questioned when it only works for particular states. Despite the complexity introduced in the calculations with the reliable proper average method, we propose a theoretical formalism that allows its use, therefore making the study of complex molecules possible, within a reduced time as the program is parallelised and can be run on multiple processors or computing grids, and also without compromising the accuracy of neither the theoretical model and the obtained TDCSs nor the developed molecular wave functions. Good agreement with experimental data was found with our approach even with the simple FBA model for simple molecules and also for complex molecules. The kinematics in which the results are presented were chosen because they are convenient for the FBA model. Indeed, this model might not work for lower energy kinematics, and more detailed approaches need to be considered. The structure of the developed program allows us to easily implement other models and this can be very useful to cover the entire energy range. Other assets

of the program is that it is user friendly and can be applied to any molecular target which makes it interesting for different applications.

References

[1] C. J. Colyer, S. M. Bellm, B. Lohmann, G. F. Hanne, O. Al-Hagan, D. H. Madison, and C. G. Ning, "Dynamical (e, 2e) studies using tetrahydrofuran as a DNA analog," *The Journal of chemical physics*, vol. 133, no. 12, p. 124302, 2010.

[2] D. B. Jones, J. D. Builth-Williams, S. M. Bellm, L. Chiari, H. Chaluvadi, D. H. Madison, C. G. Ning, B. Lohmann, O. Ingólfsson, and M. J. Brunger, "Dynamical (e, 2e) investigations of tetrahydrofuran and tetrahydrofurfuryl alcohol as DNA analogues," *Chemical Physics Letters*, vol. 572, pp. 32–37, 2013.

[3] J. D. Builth-Williams, S. M. Bellm, L. Chiari, P. A. Thorn, D. B. Jones, H. Chaluvadi, D. H. Madison, C. G. Ning, B. Lohmann, G. B. Da Silva, *et al.*, "A dynamical (e, 2e) investigation of the structurally related cyclic ethers tetrahydrofuran, tetrahydropyran, and 1,4-dioxane," *The Journal of chemical physics*, vol. 139, no. 3, p. 034306, 2013.

[4] E. Ali, X. Ren, A. Dorn, C. G. Ning, J. Colgan, and D. H. Madison, "Experimental and theoretical triple-differential cross sections for tetrahydrofuran ionized by low-energy 26-eV-electron impact," *Physical Review A*, vol. 93, p. 062705, Jun 2016.

[5] J. D. Builth-Williams, G. B. Da Silva, L. Chiari, D. B. Jones, H. Chaluvadi, D. H. Madison, and M. J. Brunger, "Dynamical (e, 2e) studies of tetrahydropyran and 1,4-dioxane," *The Journal of chemical physics*, vol. 140, no. 21, p. 214312, 2014.

[6] D. B. Jones, E. Ali, K. L. Nixon, P. Limão-Vieira, M. J. Hubin-Franskin, J. Delwiche, C. G. Ning, J. Colgan, A. J. Murray, D. H. Madison, *et al.*, "Electron-and photon-impact ionization of furfural," *The Journal of chemical physics*, vol. 143, no. 18, p. 184310, 2015.

[7] D. B. Jones, E. Ali, C. G. Ning, J. Colgan, O. Ingólfsson, D. H. Madison, and M. J. Brunger, "Electron impact ionization dynamics of para-benzoquinone," *The Journal of chemical physics*, vol. 145, no. 16, p. 164306, 2016.

[8] J. D. Builth-Williams, S. M. Bellm, D. B. Jones, H. Chaluvadi, D. H. Madison, C. G. Ning, B. Lohmann, and M. J. Brunger, "Experimental and theoretical investigation of the triple differential cross section for electron impact ionization of pyrimidine molecules," *The Journal of chemical physics*, vol. 136, no. 2, p. 024304, 2012.

[9] S. M. Bellm, C. J. Colyer, B. Lohmann, and C. Champion, "Experimental and theoretical study of the triple-differential cross section for electron-impact ionization of thymine molecules," *Physical Review A*, vol. 85, no. 2, p. 022710, 2012.

[10] J. F. Beck and Y. Mo, "How resonance assists hydrogen bonding interactions: An energy decomposition analysis," *Journal of computational chemistry*, vol. 28, no. 1, pp. 455–466, 2007.

[11] N. Huang and A. D. MacKerell, "An ab initio quantum mechanical study of hydrogen-bonded complexes of biological interest," *The Journal of Physical Chemistry A*, vol. 106, no. 34, pp. 7820–7827, 2002.

[12] W. Qian and S. Krimm, "C- H...O and O- H...O Hydrogen Bonding in Formic Acid Dimer Structures: A QM/MM Study Confirms the Common Origin of Their Different Spectroscopic Behavior," *The Journal of Physical Chemistry A*, vol. 106, no. 47, pp. 11663–11671, 2002.

[13] K. Nixon, W. Lawrance, and M. Brunger, "Electron momentum spectroscopy of formic acid," *Chemical Physics Letters*, vol. 474, no. 1, pp. 23 – 27, 2009.

[14] C. J. Colyer, M. A. Stevenson, O. Al-Hagan, D. H. Madison, C. G. Ning, and B. Lohmann, "Dynamical (e, 2e) studies of formic acid," *Journal of Physics B: Atomic, Molecular and Optical Physics*, vol. 42, no. 23, p. 235207, 2009.

[15] V. Vizcaino, M. Jelisavcic, J. P. Sullivan, and S. J. Buckman, "Elastic electron scattering from formic acid (HCOOH): absolute differential cross-sections," *New Journal of Physics*, vol. 8, no. 6, p. 85, 2006.

[16] K. L. Nixon, W. D. Lawrance, D. B. Jones, P. Euripidies, S. Saha, F. Wang, and M. J. Brunger, "An (e, 2e) coincidence study of formic acid monomer and dimer," *Chemical Physics Letters*, vol. 451, no. 1, pp. 18–24, 2008.

[17] S. M. Bharathi, S. K. Datta, A. M. Grisogono, R. Pascual, E. Weigold, and W. von Niessen, "Investigation of the complete valence shell of formic acid by electron momentum spectroscopy and Green's function methods," *Journal of electron spectroscopy and related phenomena*, vol. 53, no. 1-2, pp. 51–78, 1990.

[18] A. D. Becke, "Density-functional thermochemistry. III. the role of exact exchange," *The Journal of chemical physics*, vol. 98, no. 7, pp. 5648–5652, 1993.

[19] N. Godbout, D. R. Salahub, J. Andzelm, and E. Wimmer, "Optimization of Gaussian-type basis sets for local spin density functional calculations. Part I. Boron through neon, optimization technique and validation," *Canadian Journal of Chemistry*, vol. 70, no. 2, pp. 560–571, 1992.

[20] M. J. Frisch, G. W. Trucks, H. B. Schlegel, G. E. Scuseria, M. A. Robb, J. R. Cheeseman, G. Scalmani, V. Barone, G. A. Petersson, H. Nakatsuji, *et al.*, "Gaussian 09, Revision A. 02. Wallingford, CT: Gaussian," *Inc.*, 2016.

[21] A. Pelc, W. Sailer, P. Scheier, M. Probst, N. J. Mason, E. Illenberger, and T. D. Märk, "Dissociative electron attachment to formic acid (HCOOH)," *Chemical physics letters*, vol. 361, no. 3, pp. 277–284, 2002.

[22] A. Pelc, W. Sailer, P. Scheier, N. J. Mason, E. Illenberger, and T. D. Märk, "Electron attachment to simple organic acids," *Vacuum*, vol. 70, no. 2, pp. 429–433, 2003.

[23] V. S. Prabhudesai, D. Nandi, A. H. Kelkar, R. Parajuli, and E. Krishnakumar, "Dissociative electron attachment to formic acid," *Chemical physics letters*, vol. 405, no. 1, pp. 172–176, 2005.

[24] M. Allan, "Study of resonances in formic acid by means of vibrational excitation by slow electrons," *Journal of Physics B: Atomic, Molecular and Optical Physics*, vol. 39, no. 14, p. 2939, 2006.

[25] C. F. Guerra, J. G. Snijders, G. Te Velde, and E. J. Baerends, "Towards an order-N DFT method," *Theoretical Chemistry Accounts*, vol. 99, no. 6, pp. 391–403, 1998.

[26] J. B. Furness and I. E. McCarthy, "Semiphenomenological optical model for electron scattering on atoms," *Journal of Physics B: Atomic and Molecular Physics*, vol. 6, no. 11, p. 2280, 1973.

[27] J. P. Perdew and A. Zunger, "Self-interaction correction to density-functional approximations for many-electron systems," *Physical Review B*, vol. 23, pp. 5048–5079, May 1981.

[28] I. E. McCarthy and E. Weigold, "Electron momentum spectroscopy of atoms and molecules," *Reports on Progress in Physics*, vol. 54, no. 6, p. 789, 1991.

[29] A.-D. Becke, "Density functional thermochemistry. The role of exact exchange," *The Journal of Chemical Physics*, vol. 98, no. 7, pp. 5648–5652, 1993.

[30] M. J. Brunger and W. Adcock, "High-resolution electron momentum spectroscopy of molecules," *Journal of the Chemical Society, Perkin Transactions 2*, no. 1, pp. 1–22, 2002.

[31] J. Gao, J. L. Peacher, and D. H. Madison, "An elementary method for calculating orientation-averaged fully differential electron-impact ionization cross sections for molecules," *The Journal of chemical physics*, vol. 123, no. 20, p. 204302, 2005.

[32] J. Gao, D. H. Madison, and J. L. Peacher, "Fully differential cross sections for low-energy electron-impact ionization of nitrogen molecules," *Physical Review A*, vol. 72, no. 2, p. 020701, 2005.

[33] J. Gao, D. H. Madison, and J. L. Peacher, "Distorted wave Born and three-body distorted wave Born approximation calculations of the fully differential cross section for electron-impact ionization of nitrogen molecules," *The Journal of chemical physics*, vol. 123, no. 20, p. 204314, 2005.

[34] C. Kaiser, D. Spieker, J. Gao, M. Hussey, A. Murray, and D. H. Madison, "Coplanar symmetric and asymmetric electron impact ionization studies from the 1b1 state of H_2O at low to intermediate impact energies," *Journal of Physics B: Atomic, Molecular and Optical Physics*, vol. 40, no. 13, p. 2563, 2007.

[35] H. Chaluvadi, C. G. Ning, and D. H. Madison, "Theoretical triple-differential cross sections of a methane molecule by a proper-average method," *Physical Review A*, vol. 89, no. 6, p. 062712, 2014.

[36] E. Ali, K. Nixon, A. Murray, C. G. Ning, J. Colgan, and D. H. Madison, "Comparison of experimental and theoretical electron-impact-ionization triple-differential cross sections for ethane," *Physical Review A*, vol. 92, p. 042711, Oct 2015.

[37] G. B. Da Silva, R. F. C. Neves, L. Chiari, D. B. Jones, E. Ali, D. H. Madison, C. G. Ning, K. L. Nixon, M. C. A. Lopes, and M. J. Brunger, "Triply differential (e, 2e) studies of phenol," *The Journal of chemical physics*, vol. 141, no. 12, p. 124307, 2014.

[38] X. Li, M. Gong, L. Liu, Y. Wu, J. Wang, Y. Qu, and X. Chen, "Calculation of (e, 2e) triple-differential cross sections of formic acid: An application of the multicenter distorted-wave method," *Phys. Rev. A*, vol. 95, p. 012703, Jan 2017.

[39] M. J. Frisch, G. W. Trucks, H. B. Schlegel, G. E. Scuseria, M. A. Robb, J. R. Cheeseman, J. A. Montgomery Jr, T. Vreven, K. N. Kudin, J. C. Burant, *et al.*, "Gaussian 09, Revision C. 02. Wallingford, CT: Gaussian," *Inc.*, 2004.

[40] C. Lee, W. Yang, and R. G. Parr, "Development of the Colle-Salvetti correlation-energy formula into a functional of the electron density," *Physical review B*, vol. 37, no. 2, p. 785, 1988.

[41] L. Mouawad, P. A. Hervieux, C. Dal Cappello, J. Pansanel, A. Osman, M. Khalil, and Z. El Bitar, "Triple differential cross sections for the ionization of formic acid by electron impact," *Journal of Physics B: Atomic, Molecular and Optical Physics*, 2017.

[42] M. D. Taylor and J. Bruton, "The Vapor Phase Dissociation of Some Carboxylic Acids. II. Formic and Propionic Acids1, 2," *Journal of the American Chemical Society*, vol. 74, no. 16, pp. 4151–4152, 1952.

[43] C. Champion, C. Dal Cappello, S. Houamer, and A. Mansouri, "Single ionization of the water molecule by electron impact: Angular distributions at low incident energy," *Physical Review A*, vol. 73, no. 1, p. 012717, 2006.

[44] M. Sahlaoui and M. Bouamoud, "Cross sections for electron-impact ionization of water molecules," *Canadian Journal of Physics*, vol. 89, no. 6, pp. 723–727, 2011.

[45] C. Y. Lin, C. W. McCurdy, and T. N. Rescigno, "Complex Kohn approach to molecular ionization by high-energy electrons: Application to H_2O," *Physical Review A*, vol. 89, no. 1, p. 012703, 2014.

[46] T. N. Rescigno, C. W. McCurdy, A. E. Orel, and B. H. Lengsfield III, "The complex Kohn variational method," in *Computational Methods for Electron—Molecule Collisions*, pp. 1–44, Springer, 1995.

[47] G. G. Engerholm, A. C. Luntz, W. D. Gwinn, and D. O. Harris, "Ring Puckering in Five-Membered Rings. II. The Microwave Spectrum, Dipole Moment, and Barrier to Pseudorotation in Tetrahydrofuran," *The Journal of Chemical Physics*, vol. 50, no. 6, pp. 2446–2457, 1969.

[48] R. Meyer, J. C. López, J. L. Alonso, S. Melandri, P. G. Favero, and W. Caminati, "Pseudorotation pathway and equilibrium structure from the rotational spectrum of jet-cooled tetrahydrofuran," *The Journal of chemical physics*, vol. 111, no. 17, pp. 7871–7880, 1999.

[49] B. Cadioli, E. Gallinella, C. Coulombeau, H. Jobic, and G. Berthier, "Geometric structure and vibrational spectrum of tetrahydrofuran," *The Journal of physical chemistry*, vol. 97, no. 30, pp. 7844–7856, 1993.

[50] S. J. Han and Y. K. Kang, "Pseudorotation in heterocyclic five-membered rings: tetrahydrofuran and pyrrolidine," *Journal of Molecular Structure: THEOCHEM*, vol. 369, no. 1-3, pp. 157–165, 1996.

[51] A. H. Mamleev, L. N. Gunderova, and R. V. Galeev, "Microwave spectrum and hindered pseudorotation of tetrahydrofuran," *Journal of Structural Chemistry*, vol. 42, no. 3, pp. 365–370, 2001.

[52] D. G. Melnik, S. Gopalakrishnan, T. A. Miller, and F. C. De Lucia, "The absorption spectroscopy of the lowest pseudorotational states of tetrahydrofuran," *The Journal of chemical physics*, vol. 118, no. 8, pp. 3589–3599, 2003.

[53] V. M. Rayón and J. A. Sordo, "Pseudorotation motion in tetrahydrofuran: An ab initio study," *The Journal of chemical physics*, vol. 122, no. 20, p. 204303, 2005.

[54] T. Yang, G. Su, C. G. Ning, J. Deng, F. Wang, S. Zhang, X. Ren, and Y. Huang, "New diagnostic of the most populated conformer of tetrahydrofuran in the gas phase," *The Journal of Physical Chemistry A*, vol. 111, no. 23, pp. 4927–4933, 2007.

[55] C. G. Ning, Y. R. Huang, S. F. Zhang, J. K. Deng, K. Liu, Z. H. Luo, and F. Wang, "Experimental and theoretical electron momentum spectroscopic study of the valence electronic structure of tetrahydrofuran under pseudorotation," *The Journal of Physical Chemistry A*, vol. 112, no. 44, pp. 11078–11087, 2008.

[56] M. Dampc, B. Mielewska, M. R. F. Siggel-King, G. C. King, and M. Zubek, "Threshold photoelectron spectra of tetrahydrofuran over the energy range 9–29 eV," *Chemical Physics*, vol. 359, no. 1, pp. 77 – 81, 2009.

[57] A. Giuliani, P. Limão-Vieira, D. Duflot, A. R. Milosavljevic, B. P. Marinkovic, S. V. Hoffmann, N. Mason, J. Delwiche, and M. J. Hubin-Franskin, "Electronic states of neutral and ionized tetrahydrofuran studied by VUV spectroscopy and ab initio calculations," *The European Physical Journal D-Atomic, Molecular, Optical and Plasma Physics*, vol. 51, no. 1, pp. 97–108, 2009.

[58] M. Dampc, B. Mielewska, M. R. F. Siggel-King, G. C. King, and M. Zubek, "Threshold photoelectron spectra of tetrahydrofuran over the energy range 9–29 eV," *Chemical Physics*, vol. 359, no. 1–3, pp. 77 – 81, 2009.

[59] T. Yang, G. Su, C. G. Ning, J. Deng, F. Wang, S. Zhang, X. Ren, and Y. Huang, "New Diagnostic of the Most Populated Conformer of Tetrahydrofuran in the Gas Phase," *The Journal of Physical Chemistry A*, vol. 111, no. 23, pp. 4927–4933, 2007. PMID: 17511427.

[60] A. Giuliani, P. Limão-Vieira, D. Duflot, A. R. Milosavljevic, B. P. Marinkovic, S. V. Hoffmann, N. Mason, J. Delwiche, and M. J. Hubin-Franskin, "Electronic states of neutral and ionized tetrahydrofuran studied by VUV spectroscopy and ab initio calculations," *The European Physical Journal D*, vol. 51, no. 1, pp. 97–108, 2009.

[61] C. G. Ning, Y. R. Huang, S. F. Zhang, J. K. Deng, K. Liu, Z. H. Luo, and F. Wang, "Experimental and Theoretical Electron Momentum Spectroscopic Study of the Valence Electronic Structure of Tetrahydrofuran under Pseudorotation," *The Journal of Physical Chemistry A*, vol. 112, no. 44, pp. 11078–11087, 2008. PMID: 18842033.

[62] M. Yamauchi, H. Yamakado, and K. Ohno, "Penning Ionization of Cyclic Ethers by Collision with He*(23S) Metastable Atoms," *The Journal of Physical Chemistry A*, vol. 101, no. 35, pp. 6184–6194, 1997.

[63] C. J. Colyer, M. A. Stevenson, O. Al-Hagan, D. H. Madison, C. G. Ning, and B. Lohmann, "Dynamical (e, 2e) studies of formic acid," *Journal of Physics B: Atomic, Molecular and Optical Physics*, vol. 42, no. 23, p. 235207, 2009.

[64] I. Tóth and L. Nagy, "Triple-differential cross-section calculations for the ionization of CH_4 by electron impact," *Journal of Physics B: Atomic, Molecular and Optical Physics*, vol. 43, no. 13, p. 135204, 2010.

[65] S. J. Ward and J. H. Macek, "Wave functions for continuum states of charged fragments," *Phyical Review A*, vol. 49, pp. 1049–1056, Feb 1994.

[66] C. G. Ning, Y. R. Huang, S. F. Zhang, J. K. Deng, K. Liu, Z. H. Luo, and F. Wang, "Experimental and theoretical electron momentum spectroscopic study of the valence electronic structure of tetrahydrofuran under pseudorotation," *The Journal of Physical Chemistry A*, vol. 112, no. 44, pp. 11078–11087, 2008.

[67] O. Dolgounitcheva, V. G. Zakrzewski, and J. V. Ortiz, "Ionization energies and Dyson orbitals of thymine and other methylated uracils," *The Journal of Physical Chemistry A*, vol. 106, no. 36, pp. 8411–8416, 2002.

[68] J. V. Ortiz, "Partial third-order quasiparticle theory: Comparisons for closed-shell ionization energies and an application to the Borazine photoelectron spectrum," *The Journal of chemical physics*, vol. 104, no. 19, pp. 7599–7605, 1996.

[69] A. M. Ferreira, G. Seabra, O. Dolgounitcheva, V. G. Zakrzewski, and J. V. Ortiz, "Application and testing of diagonal, partial third-order electron propagator approximations," in *Quantum-mechanical prediction of thermochemical data*, pp. 131–160, Springer, 2001.

[70] E. S. Kryachko and J. L. Calais, *Conceptual trends in quantum chemistry*. Springer Science & Business Media, 2012.

[71] A. Padva, T. J. O'Donnell, and P. R. LeBreton, "UV photoelectron studies of biological pyrimidines: the valence electronic structure of methyl substituted uracils," *Chemical Physics Letters*, vol. 41, no. 2, pp. 278–282, 1976.

[72] R. J. Bartlett, "Many-body perturbation theory and coupled cluster theory for electron correlation in molecules," *Annual Review of Physical Chemistry*, vol. 32, no. 1, pp. 359–401, 1981.

[73] M. J. Frisch, G. W. Trucks, H. B. Schlegel, G. E. Scuseria, M. A. Robb, J. R. Cheeseman, V. G. Zakrzewski, J. A. Montgomery Jr, R. E. Stratmann, J. C. Burant, *et al.*, "Gaussian 98, Revision a. 7, Gaussian," *Inc., Pittsburgh, PA*, vol. 12, 1998.

[74] A. B. Trofimov, J. Schirmer, V. B. Kobychev, A. W. Potts, D. M. P. Holland, and L. Karlsson, "Photoelectron spectra of the nucleobases cytosine, thymine and adenine," *Journal of Physics B: Atomic, Molecular and Optical Physics*, vol. 39, no. 2, p. 305, 2005.

[75] A. B. Trofimov, J. Schirmer, V. B. Kobychev, A. W. Potts, D. M. P. Holland, and L. Karlsson, "Photoelectron spectra of the nucleobases cytosine, thymine and adenine," *Journal of Physics B: Atomic, Molecular and Optical Physics*, vol. 39, no. 2, p. 305, 2006.

[76] B. Senger, "Calculated molecular double-differential cross-sections for ionisation under proton impact," *Zeitschrift für Physik D Atoms, Molecules and Clusters*, vol. 9, no. 1, pp. 79–89, 1988.

[77] S. Houamer, C. Dal Cappello, I. Charpentier, P. A. Hervieux, and A. C. Roy, "Comment on "Experimental and theoretical study of the triple-differential cross section for electron-impact ionization of thymine molecules"," *Physical Review A*, vol. 86, no. 2, p. 026701, 2012.

[78] D. S. Milne-Brownlie, S. J. Cavanagh, B. Lohmann, C. Champion, P. A. Hervieux, and J. Hanssen, "Dynamics in electron-impact ionization of H_2o," *Physical Review A*, vol. 69, no. 3, p. 032701, 2004.

[79] S. A. C. Clark, T. J. Reddish, C. E. Brion, E. R. Davidson, and R. F. Frey, "The valence orbital momentum distributions and binding energy spectra of methane by electron momentum spectroscopy: Quantitative comparisons using near Hartree-Fock limit and correlated wavefunctions," *Chemical Physics*, vol. 143, no. 1, pp. 1 – 10, 1990.

[80] C. Dal Cappello, I. Charpentier, S. Houamer, P. A. Hervieux, M. F. Ruiz-Lopez, A. Mansouri, and A. C. Roy, "Triple-differential cross sections for the ionization of thymine by electrons and positrons," *Journal of Physics B: Atomic, Molecular and Optical Physics*, vol. 45, no. 17, p. 175205, 2012.

[81] C. Dal Cappello, Z. Rezkallah, S. Houamer, I. Charpentier, P. A. Hervieux, M. F. Ruiz-Lopez, R. Dey, and A. C. Roy, "Second-order Born approximation for the ionization of molecules by electron and positron impact," *Physical Review A*, vol. 84, p. 032711, Sep 2011.

Conclusion

The work presented in this thesis was performed in a collective work within the scope of a project that was started in the past [1, 2] and is now being revived for further developments. It was conducted with the combined efforts and expertise of the individuals that are involved in this project. This work was made possible because of Ziad El Bitar who closely supervised it with important insight and guidance and parallelized the program allowing its use possible for big molecules. The developed program is based on a code written by Professor Paul-Antoine Hervieux who very kindly put so much effort and time into teaching me all that I need to know about the theoretical aspect of this work so that I can develop a similar program adapted for the considered theoretical framework. In the first stages of this work, multiple tests had to be done in order to verify the accuracy of the different components and that they were correctly implemented in the developed program. The hard work that was done in this prospect, although not provided in this thesis, was a long process of validating functions and subroutines, testing and tracking potential errors in the program and it wouldn't have lead to a valid program if it weren't for the valuable guidance and experience of professor Claude Dal Cappello. My individual role in this work was mainly to absorb the different expertises and translate them into a program that is structured in a way that makes its use the simplest possible despite the complex calculations on which it is based.

The results presented in this thesis were performed on an Intel Xenon (2.10 GHz) E5-2620 v4 processor on 8 cores. We intend to provide in the future more details about the computing time in function of the studied molecules, the kinematic conditions, the employed method and the precision that is required. It will be more relevant to provide these information once the new version of the program is ready, including the distorted wave method option and the automatic optimization of the required number of partial waves. It is important to note that the computing time is tightly related to the number of partial waves that is used, and the optimization of this number in the program does indeed increase the computing time. As the number of atoms and electrons in the molecule increases, more partial waves are needed to achieve convergence for the molecular orbital wave functions. This convergence is tested by calculating the scalar product of the wave functions of all the molecule's orbitals and verifying that they are well orthonormalized, and then verifying that the value of the dipole moment calculated using these wave functions is similar to that given in Gaussian. As an example, in the case of the water molecule, using 7 partial waves for the molecular orbital wave function is enough to achieve convergence with a precision of 10^{-4}. For the more complex THF molecule, 20 partial waves are necessary to achieve convergence with a precision of 10^{-3}. In the considered kinematics of intermediate energy, 10 partial waves for the ejected electron are enough to achieve a good precision on the TDCS (10^{-5}) using the FBA model with a Coulomb wave for the ejected electron. In

EMS conditions, 70 partial waves are needed to have the same precision. More partial waves are required when the distorted wave model is used. In the considered conditions of intermediate energy, 25 partial waves are needed to achieve a convergence of the TDCSs with a precision of 10^{-5}. The computing time also depends on the number of processors that are used. In figure 5.11, we give the computing time in function of the number of processors for two molecules: water and THF.

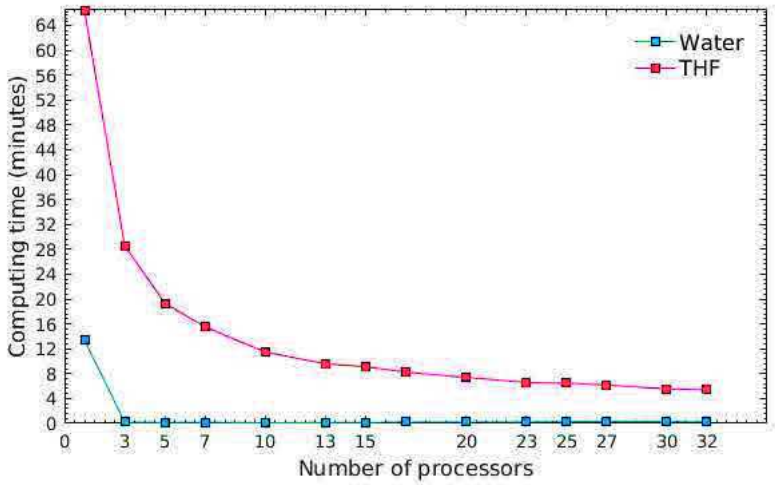

Figure 5.11: The time taken by the program to determine the molecular wave functions of the $2a_1$ orbital of water and the 9b orbital of THF, in function of the number of processors that are used with an Intel Xenon (2.10 GHz) E5-2620 v4 processor on 8 cores. These calculations were done with 7 partial waves for the water molecular wave function and 20 partial waves for the THF molecular wave function.

It is clear that the computing time is greatly reduced by using the parallel version of the program; it decreases from 13 minutes to a couple of seconds even with only 3 processors for water. The required time for the more complex molecule THF is obviously greater but is still acceptable with the parallel version of the program. It can be reduced from an hour and 6 minutes down to only 5 minutes and 40 seconds using 32 processors.

Unfortunately, the computing time is usually not provided in publications where numerical programs are used to generate cross sections. Hence the comparison of computing time between our program and existing programs is not possible. We however stress on the fact that the tools used in our program allow to greatly economize in terms of computing time without compromising the quality of the results. This is rarely achieved and in contrast, existing approaches that were applied to complex molecules often relied on approximations that are not always reliable [3, 4]. Calculating the cross sections numerically saves a lot of effort in comparison with analytical approaches. Using the partial wave series form of the wave functions simplifies the translation of the theoretical framework into a parallel program in which the cross sections are determined numerically, bypassing difficult analytical calculations. Developing single center molecular wave functions reduces the multi-center problem to an atom-like case. This approach was used in many studies [5–9] and is considered as an asset that allows to overcome the problem of having multiple centers making the study of complex molecules possible. Using Gaussian wave functions also accelerates the calculations and is complementary to the single center approach. Linking

the program to Gaussian 09 [10] is also particularly important because it makes it usable for any molecular target. The theoretical formalism was successfully applied to simple molecules, like water [1], and to thymine [7], a more complex molecule, in past studies. The originality of the work presented in this thesis resides especially in the structure of the program that is 'user friendly' giving the user the only task of changing simple parameters like the kinematics, the precision and the method used (a Coulomb wave or a distorted wave for the ejected electron). It also reads the output file of Gaussian automatically and independently configures parameters like the number of partial waves for the molecular and ejected electron wave functions saving the user the time to try different values to adjust these parameters. With such a structure and with the used tools, it is easy to add more considerations into the theoretical approach and develop it into a more sophisticated framework. As seen throughout this thesis, extensive research is being conducted using various methods that are more sophisticated than the theoretical approach our program relies on [11–14]. The simplicity of the theoretical model that is proposed here was chosen as a starting point to ensure that the different used tools are correctly interlaced together and implemented in the program.

As shown in chapter 5, we are currently working on adding the option of using a distorted wave for the ejected electron instead of a Coulomb wave. This model will be then applied to formic acid and THF and other more complex molecules. The comparison with the multi-center distorted wave (MCDW) results for formic acid [13] would elucidate the effect of not taking into account the multi-center anisotropic nature of the molecule on the resultant TDCSs. The DWBA model might also yield improved agreement with the experimental data for THF. Now that the overall structure of the program has been validated throughout this work, improving the theoretical framework becomes a less difficult task. For example, in order to add the DWBA option, we had to add a function that determines distorted wave functions and use it for the ejected electron instead of the Coulomb-wave function, and program the distorted potential that is used to determine this wave function using information read from the Gaussian output file. Indeed, many tests were carried out to verify that these additions were correctly programmed. But all the other functions and subroutines were already tested within the FBA model. The molecular wave functions could also be improved by adding correlation factors using density functional theory (DFT) [15]. For some molecules it might be necessary to go beyond the Hartree-Fock level of calculations to describe the molecular properties more accurately within Gaussian calculations. Another perspective is to extend the calculations to determining double differential, single differential and total cross sections which can be derived from the TDCSs as explained in chapter 2.

Many applications could benefit from this work since the developed program can be applied to any molecular target. For example, providing the cross sections of bio-molecules could be of interest for molecular biodosimetry where these molecules are used to measure the dose received by a person at risk [16]. Another application that has been discussed in this thesis is the use of the developed cross sections to improve simulations of biological damage. The calculated cross sections for biological molecules could be implemented in Geant4-DNA [17], for example, and used instead of water cross sections. The consequent influence of using more accurate cross sections on the predicted damage can hence be identified. Even at the macroscopic scale, correct modeling of the biological medium and the interaction of particles within it is essential for efficient treatment planning. This would

no longer be a difficult task if specific cross sections for the DNA and other biological species were made available. In the same goal, a very recent study provided the total ionization cross sections of DNA bases by proton impact [18]. These cross sections were implemented in Geant4-DNA and the resultant lineal energies calculated in micrometric volumes filled with water and the DNA bases material were found to be significantly different.

More broadly, this project aims at creating an open access cross section database for the electron impact ionization of molecules. The fundamental work that is presented in this thesis, once complete, will enable the generation of the cross sections of any molecule in any kinematial conditions. Creating a website where these cross sections can be accessed and used for any desired purpose would help fill the gaps in the many studies relying on these cross sections for various applications. The NIST platform [19] currently provides the total electron impact ionization cross sections of some atomic and molecular targets. The cross section is given for any incident energy determined by the user. The choice of the target is however limited to the proposed molecules and only the total cross sections are given. We could create an open access database for the TDCSs of electron ionization of a large number of molecules especially of interest in the biomedical field. The Plasma Data Exchange project serves the same goal of providing the urgently needed cross section database and is particularly dedicated to low temperature plasma applications [20]. The developed LXCat website [21] is an open access website where the electron scattering cross sections are given for some kinematic conditions as a function of the scattered electron angle, for various targets including water, ammonia, formic acid and THF. Giving the electron impact ionization cross sections would be complementary to this work for a more complete description of particle interactions.

To summarize, the need for accurate interaction cross sections is growing and has become pressing in the biomedical field where the interaction cross sections of ionizing particles with complex biological molecules are required. Determining these cross sections is a challenging process and becomes more difficult both theoretically and experimentally as the considered target becomes more complex. The underlying fundamental research that has been going on in the past recent years attempts at proposing models based on particular approximations that allow to provide these cross sections. In this thesis, we present a theoretical framework that allows to overcome the analytical difficulties and heavy computing without compromising the quality of the derived triple differential cross sections. The work presented here is only the starting point of a project that is much needed for many domains.

References

[1] H. D. Hafied, *Etude théorique de l'ionisation par impact électronique des molécules d'eau en phase gazeuse et liquide*. PhD thesis, Université de Metz, 2007.

[2] C. Champion, "Electron impact ionization of liquid and gaseous water: a single-center partial-wave approach," *Physics in medicine and biology*, vol. 55, no. 1, p. 11, 2009.

[3] J. Gao, J. L. Peacher, and D. H. Madison, "An elementary method for calculating orientation-averaged fully differential electron-impact ionization cross sections for molecules," *The Journal of chemical physics*, vol. 123, no. 20, p. 204302, 2005.

[4] E. Ali, K. Nixon, A. Murray, C. G. Ning, J. Colgan, and D. H. Madison, "Comparison of experimental and theoretical electron-impact-ionization triple-differential cross sections for ethane," *Physical Review A*, vol. 92, p. 042711, Oct 2015.

[5] H. D. Hafied, A. Eschenbrenner, C. Champion, M. F. Ruiz-Lopez, C. Dal Cappello, I. Charpentier, and P. A. Hervieux, "Electron momentum spectroscopy of the valence orbitals of the water molecule in gas and liquid phase: A comparative study," *Chemical physics letters*, vol. 439, no. 1, pp. 55–59, 2007.

[6] C. Dal Cappello, P. A. Hervieux, I. Charpentier, and M. F. Ruiz-Lopez, "Ionization of the cytosine molecule by protons: Ab initio calculation of differential and total cross sections," *Physical Review A*, vol. 78, no. 4, p. 042702, 2008.

[7] C. Dal Cappello, I. Charpentier, S. Houamer, P. A. Hervieux, M. F. Ruiz-Lopez, A. Mansouri, and A. C. Roy, "Triple-differential cross sections for the ionization of thymine by electrons and positrons," *Journal of Physics B: Atomic, Molecular and Optical Physics*, vol. 45, no. 17, p. 175205, 2012.

[8] C. Dal Cappello, Z. Rezkallah, S. Houamer, I. Charpentier, A. C. Roy, P. A. Hervieux, and M. F. Ruiz-Lopez, "Ionization of thymine by electron impact: investigation of inner shell orbitals," *European Physics Journal D*, vol. 67, no. 6, p. 117, 2013.

[9] M. F. Khelladi, A. Mansouri, C. Dal Cappello, I. Charpentier, P. A. Hervieux, M. F. Ruiz-Lopez, and A. C. Roy, "Angular distributions in the double ionization of DNA bases by electron impact," *Journal of Physics B: Atomic, Molecular and Optical Physics*, vol. 49, no. 22, p. 225201, 2016.

[10] M. J. Frisch, G. W. Trucks, H. B. Schlegel, G. E. Scuseria, M. A. Robb, J. R. Cheeseman, G. Scalmani, V. Barone, G. A. Petersson, H. Nakatsuji, *et al.*, "Gaussian 09, revision a. 02. wallingford, ct: Gaussian," *Inc.*, 2016.

[11] C. Y. Lin, C. W. McCurdy, and T. N. Rescigno, "Complex kohn approach to molecular ionization by high-energy electrons: Application to H_2O," *Physical Review A*, vol. 89, p. 012703, Jan 2014.

[12] J. Gao, D. H. Madison, and J. L. Peacher, "Distorted wave Born and three-body distorted wave Born approximation calculations of the fully differential cross section for electron-impact ionization of nitrogen molecules," *The Journal of Chemical Physics*, vol. 123, no. 20, p. 204314, 2005.

[13] X. Li, M. Gong, L. Liu, Y. Wu, J. Wang, Y. Qu, and X. Chen, "Calculation of (e, 2e) triple-differential cross sections of formic acid: An application of the multicenter distorted-wave method," *Physical Review A*, vol. 95, p. 012703, Jan 2017.

[14] I. Tóth, R. I. Campeanu, and L. Nagy, "Triple differential cross sections for the ionization of water by electron and positron impact," *The European Physical Journal D-Atomic, Molecular, Optical and Plasma Physics*, vol. 66, no. 1, pp. 1–6, 2012.

[15] E. K. U. Gross and R. M. Dreizler, *Density functional theory*, vol. 337. Springer Science & Business Media, 2013.

[16] F. Marchetti, M. A. Coleman, I. M. Jones, and A. J. Wyrobek, "Candidate protein biodosimeters of human exposure to ionizing radiation," *International journal of radiation biology*, vol. 82, no. 9, pp. 605–639, 2006.

[17] S. Incerti, G. Baldacchino, M. Bernal, R. Capra, C. Champion, Z. Francis, P. Guèye, A. Mantero, B. Mascialino, P. Moretto, *et al.*, "The geant4-DNA project," *International Journal of Modeling, Simulation, and Scientific Computing*, vol. 1, no. 02, pp. 157–178, 2010.

[18] Z. Francis, Z. El Bitar, S. Incerti, M. A. Bernal, M. Karamitros, and H. N. Tran, "Calculation of lineal energies for water and DNA bases using the Rudd model cross sections integrated within the Geant4-DNA processes," *Journal of Applied Physics*, vol. 122, no. 1, p. 014701, 2017.

[19] K. K. Irikura, M. E. Rudd, *et al.*, "Electron-Impact Cross Sections for Ionization and Excitation Database," 2005.

[20] L. C. Pitchford, L. L. Alves, K. Bartschat, S. F. Biagi, M. C. Bordage, I. Bray, C. E. Brion, M. J. Brunger, L. Campbell, A. Chachereau, *et al.*, "LXCat: an Open-Access, Web-Based Platform for Data Needed for Modeling Low Temperature Plasmas," *Plasma Processes and Polymers*, vol. 14, no. 1-2, 2017.

[21] LXCat. `https://fr.lxcat.net/home/`.

List of abbreviations

ADN	Acide désoxyribonucléique
ADF	Amsterdam Density Functional
aug-cc-pVQZ	Quadruple Zeta Correlation Consistent Polarized basis set
BBK	Brauner-Briggs-Klar
BBKDW	Brauner-Briggs-Klar Distorted Wave
BBKSR	Brauner-Briggs-Klar Short Range
BES	Binding Energy Spectrum
B3LYP	Becke 3-Parameter, Lee, Yang and Parr
cGTO	Contracted Gaussian Type Orbital
CNDO	Completely Neglected Differential Overlap
CW	Coulomb Wave
1CW	One Coulomb Wave
2CW	Two Coulomb Waves
DeSIs	Dosimétrie, Simulation, Instrumentation
DBSCAN	Density Based Spatial Clustering for Applications with Noise
DDCS	Double Differential Cross Section
DFT	Density Functional Theory
DNA	Deoxyribonucleic acid
DSB	Double Strand Break
DS3C	Dynamic Screening of three two-body Coulomb interaction
DW	Distorted Wave
DWBA	Distorted Wave Born Approximation
1DW	One Distorted Wave
3DW	Three Distorted Waves
3DW-CPE	Three Distorted Waves calculated using the Perdew–Zunger correlation potential and the Furness–McCarthy exchange distortion potential
3DW-APE	Three Distorted Waves calculated including the adjustable polarization potential and Furness– McCarthy exchange distortion potential
EMS	Electron Momentum Spectroscopy
FBA	First Born Approximation
FLUKA	FLUktuierende KAskade

GATE	Geant4 Application for Tomographic Emission
GAMESS	General Atomic and Molecular Electronic Structure System
Geant4	GEometry ANd Tracking 4
Geant4-DNA	GEometry ANd Tracking 4-DNA
GTO	Gaussian Type Orbital
HOMO	Highest Occupied Molecular Orbital
HOMO^{-1}	Next Highest Occupied Molecular Orbital
IPHC	Institut Pluridisciplinaire Hubert Curien
LET	Linear Energy Transfer
MBP2	Many Body Perturbation theory
MCDS	Monte Carlo Damage Simulation
MCDW	MultiCenter Distorted Wave
MCDW-NT	MultiCenter Distorted Wave with Nuclear Term
MD	Momentum Distribution
MDW	Molecular Distorted Wave Born approximation
mpi	Multiple Passing Interface
M3DW	Molecular 3-body Distorted Waves
M3DW-CPE	Molecular 3-body Distorted Waves calculated with a static potential, an exchange- distortion potential, and a correlation-polarization potential
NIST	National Institute of Standards and Technology
OAMO	Orientation Averaged Molecular Orbital
PA	Proper Average
PARTRAC	PARticles TRACks
PCI	Post Collision Interaction
PENELOPE	Penetration and ENErgy LOss of Positrons and Electrons
PES	PhotoElectron Spectroscopy
pGTO	Primitive Gaussian Type Orbital
PW	Plane Wave
PWIA	Plane Wave Impulse Approximation
RaMsEs	Radioprotection et Mesures Environnementales
RBE	Relative Biological Effectiveness
RHF	Restricted Hartree Fock
SBA	Second Born Approximation
SCF	Self Consistent Field
SDCS	Simple Differential Cross Section
SOBP	Spread Out Bragg Peak
SP	Single Point
SSB	Simple Strand Break
STO	Slater Type Orbital

TDCS	Triple Differential Cross Section
THF	Tetrahydrofuran
TS	Total Screening
TS*	Modified Total Screening
TZVP	Triple Zeta Valence Polarization
TZ2P	Triple Zeta with 2 Polarization functions
WM	Ward-Macek

Acknowledgments

I know that the three years that I spent so focused on this work will probably not change the world. I didn't after all invent a cure for cancer, discover a new planet, or a way to make the world a better place. And there are so many people who continue to live the same way completely untouched by the results of this thesis. To me, this thesis was not only an academic journey. It was much more enriching than that. And it changed my world. I am very lucky to say that there was not one time I felt unhappy working on this thesis. Indeed, it was very difficult to get disconnected from a way of life and from people I loved, every six months, and have to live in a completely different country within a completely different society. But despite all the complications that come with a co-tutelle thesis, I got to spend three years working with so much passion and motivation and happiness because of the incredible support and love of the people I had to leave in both countries and because of the unending kindness and commitment of the people who were guiding me all along the way. Because of how great human beings you all are, I got to enjoy every second. You have not only changed my life, but also changed me. And I am part of this world. In some way, you have changed the world.

So I want to thank you not only for helping me with my thesis, but for inspiring me in so many ways. And for changing the world.

I want to begin by thanking *my mother* who is the reason for all the good things in my life. I do not know how you are who you are despite everything you've been through and how you continue to be as brave and loving and supporting as you are. You grew up in a time of war, a time of fear and loss and disappointment and helplessness. Yet you had big dreams and you went after them, you read more books than I ever will, you even learned a language all by yourself, and you raised us with so much wisdom and love. Thank you for being the special person you are. For being a role model. For working in a time and place where a working mother was considered a bad mother. You were and you are beyond everything that a mother should be. You taught me what commitment is and what discipline is. You taught me that a woman can love both her career and her family. That a woman can be brilliant in both. That a woman doesn't have to sacrifice who she is and what she wants to do with her life, to love others and take care of her family. I watched you excell at your job and get promoted year after year and you were always there at home waiting for us to come back from school with lunch ready, many great stories about how much you enjoyed your day at work and still had the energy to tutor us patiently and lovingly although you must have been very tired. I could write a million pages about how much I love you and how much of a great person you are. Thank you for encouraging me to do this, for supporting me, for getting me a desk where I can work at home on my thesis, for not letting me help you with the housework although you needed help, so that I

can keep working or just take a break when I'm not and do whatever I want. Thank you for teaching me to be independent and never making me feel guilty for wanting to go. Thank you for not telling me what I should do with my life, that I should learn how to cook, and clean the house, and be the perfect wife. When this was the way all the other girls I knew were raised. Instead, you taught me to be the best of me, to go after opportunities and push the limits. And when I graduated from highschool, you didn't tell me that I have to be either a doctor, a lawyer or an engineer just because I'm the first of my class. You told me I can be an actress if I wanted to. You told me I can do anything I want. I hope you know, everytime I accomplish something, or finally grasp something I've wished for, or just feel happy, I think of you, and I imagine you in my place. And I wish you could feel as though it is you who have gotten everything you wanted. I love you so much.

It was also you who introduced me to *Prof. Mohammad Khalil*, who changed my life too. I want to thank you Professor Khalil for being the very kind, caring and brilliant person that you are. You have changed the lives of so many students allowing us to go after our ambitions despite the situation of our country and the very limited research opportunities there. Thank you for believing in me and for accepting to be my thesis surpervisor. I will never forget the day you called me into your office and we signed the "convention de cotutelle" and how you were encouraging me and telling me not to worry about a thing and that it will all be good. You were always looking out for me, even from a distance, and despite all your occupations, you always made time for me to help me whenever I needed help. Thank you for this opportunity. And thank you for introducing me to Dr. Ziad El Bitar.

I can never thank you enough, *Dr. Ziad El Bitar*, for all the ways you have changed my life. You are the best supervisor I could've had. And you are much more than just a supervisor. You are a friend, a mentor and a role model. Your good sense of humour, your patience, understanding, the trust that you have given me, your openness and wisdom, your kindness and endless help have allowed me to work with so much motivation and not give up. Even when I was far away in Lebanon, you still did everything you can to help and support me. You opened up so many opportunities for me. When I started this thesis it was something else and now it is something much bigger because of you. I learned how to deal with the change watching you so fearlessly start from zero when we first got to RaMsEs. You inspire me so much and you're a role model for all young researchers. And I am only one of the many people who look up to you and whose lives you've changed. I cannot forget to thank you for helping me with my luggage everytime I came to Strasbourg and for rewriting the long "acte de caution" and being my "garant" every time. I also thank your wife, Dalia, for her friendship and kindness and for treating me like a member of your family.

My co-supervisor, *Dr. Ahmad Osman*, you have also made this journey more beautiful by being the supportive and very kind person that you are. I will never forget our meetings at centre AZM discussing progress and suggesting new approaches. Despite having stopped research from a long time, you still had the motivation and passion to begin again. And you put so much effort into this project even though it is not within your area of expertise and despite your busy schedule. Thank you for always wanting to be part of it even after the subject had changed and even while I was in France. For always checking up on me making sure I was okay, for all your help. Thank you!

My thesis reporters *Dr. Marie-Claude Bordage*, and *Dr. Mohamad Roumie*, thank you for taking the time to read my thesis, for helping me provide the best version of this work and for your questions and remarks that I'm sure will have a great impact on the future work that will be done within this project. *Prof. Adnan Naja* and *Dr. Ziad Francis*, thank you for accepting to be in my thesis jury too, and for your kindness, support and help throughout my thesis. You are role models to me and I am very honored to have you in my jury.

This thesis was funded by an "ARTS" grant co-financed by Institut de Recherche pour le Dévelopement (IRD) and Institut National de Physique Nucléaire et de Physique des Particules (in2p3), in the aim of encouraging research in nuclear physics for medical applications, in southern countries. I want to thank IRD and in2p3 for their kindness and their valuable help. *Gaelle Brulé*, in charge of the follow up of the ARTS program at IRD, *Coline Rendu-Douce* from Campus France, and *Pierre Vicente*, the international officer for researchers in Strasbourg, without your kindness and readiness for help many things could've been much harder. Thank you so much for your professional assistance and for your heart warming kindness. I also want to thank *Nabil El Kente*, in charge of the animation and training of the southern scientific community within the IRD, for his incredible help and kindness. Your passion to make a difference in the world is inspiring.

I am very grateful to the director of Institut Pluridisciplinaire Hubert Curien (IPHC) *Christelle Roy* and the Imabio group director *David Brasse* for allowing me to join the IPHC and for this opportunity. A special gratitude to *Prof. Abdel-Mjid Nourreddine* for welcoming me into the RaMsEs team, for being so caring and thoughtful, and for creating such a beautiful group that I am very honored to have had the privilege to be part of. I also thank each member of RaMsEs (and DeSIs). Thank you for being extraordinary, brilliant and very kind. You have taught me so much about the beauty and power of team work. *Nicolas Arbor*, you are a role model to me, I want to thank you particularly for your very constructive comments and remarks especially during our group reunions, that have been a great source of motivation and guidance to me throughout my thesis. *Emilien Wilhelm*, thank you for your wise words when they were not needed. And when they were, thank you for your sarcastic jokes. And for all the paper airplanes (that don't fly) especially *l'avion de bonne chance*. Thank you for being such a great friend. Always. *Youbba-Ould Salem*, thank you for being so kind and goodhearted and for protecting us all from *Le chat maudit de Maryse*. *Addil Sellam*, thank you for always being so kind to me, for never getting angry at me, for teaching me to always finish everything on my plate. I will never forget all the jokes you told us especially the ones I understood. *Nicolas Spanier*, you make RaMsEs, and the world, a happier place. Being around such a caring person is very heart warming. *Severine Chefson*, your kindness, poise and conscientiousness are very inspiring. *Abdou Bensaida*, thank you for treating me like family. *Eric Schaeffer*, thank you for being the great person you are and for always having my back. *Rodolphe Combe*, thank you for being the best *co-bureau* one can have! For being the genius you are, and for teaching me so many things, like french expressions, that are true, unlike *other people* who taught me wrong words. *Abbas Nasreddine*, thank you for your friendship and for being so kind and always being there to help whenever I needed help. For the boats that don't sink and for being always such a gentleman. *Quentin Ricard*, I'm so happy I got the chance to meet you and so sad that you're not with us anymore. I hope you're doing well and that you're not saying as many insults to your new PC as you used to. But thanks for

teaching me all those words. *Matthias Clusan*, thank you for not stealing my bags and for being the very very kind and very very caring person that you are. *Halima El Azhar*, you are like a sister to me. Thank you for always telling me what I needed to hear and for being so kind! *Pierre Gillet*, thank you for the best weird conversations, for being such a good dream analyst, and for the few visits you have honored us with. If it weren't for you and Halima, I would still not know the difference between *un temps de chien méchant* and *un temps de chien gentil*. *Thomas Deschler*, thank you for being a great friend and for being so caring and kind and always walking me home! *Daniel Husson* and *Stephane Higueret*, thank you so much for your kindness, guidance and support! *Edgard Seif*, I will never forget the interesting conversations and the laughs we've had. *Rita Abboud*, thank you for being the beautiful person you are and for all the great memories we shared! *Stella Syuzanne-ochsenbein* and *Emmanuel Medernach* thank you for your kindness and support. I also thank the *Imabio group* for their welcoming and especially *Marie Vanstalle*, *Patrice Marchand*, *Bruno Jessel*, *Lionel Thomas*, *Jean Michel Gallone* and *Ali Ouadi* for their kind words and support!

Two exceptional human beings that have particularly influenced me and taught me so much about science, physics and team work, are Professors Paul Antoine Hervieux and Claude Dal Cappello. The best memories I keep from these three years, are our meetings, *Prof. Paul Antoine Hervieux*, at the "Institut de physique". Despite your very busy schedule, you dedicated so much of your time to teach me so many things and explain to me what I need to do. You showed me great support and encouragement and trust. Your passion is very inspiring and it is because of you that I felt so motivated to keep working until we have good results. It is because I felt very priviledged to have had the opportunity to work with you and to be guided by you. I can never thank you enough for all the effort and time that you have invested to help me and for your kindness and your support. You allowed me to do something that I am very passionate about and to feel that I'm part of something very great. Thank you so much! *Prof. Claude Dal Cappello*, I can never thank you enough for all the help you have given me. I did not know that such kind people so willing to selflessly help others with so much love and humility exist. I remember finding your name in almost every publication I read and knowing that you are the expert. And then to have the chance to work with you! To talk to you and to have you help me and then to meet you in person! I am so honored to have met you and to have known you. I hope you know how grateful I am to you and how much I admire you and respect you. Your passion to help others is incredible. Thank you so much for saving my thesis, when I just couldn't find what was wrong with the program and you suggested all these tests that finally lead to us fixing all the errors. And how you always replied to my emails even on weekends, and helped me with the paper and with my thesis. None of this work would have been possible without your help. Thank you so much for everything!

I also want to thank *Pr. Ziad Herro*, *Pr. Joseph Bechara* and *Dr. Pierre Ziade* from the Lebanese University, and *Shawki Jabbour*, *Georges Inati* and *Ghada Esber* from the Lady of Balamand highscool. I will never forget how much you have influenced me and changed my life. You are inspiring teachers and the reason why I have all the skills that I needed for this thesis and why I have so much passion for physics, mathematics and programming. I hope I made you proud.

I am very grateful to my friends and family in Lebanon for their love and support throughout these three years. *Rafaat*, thank you for having such a beautiful heart and for all your

help and support without which I couldn't have done this. *Pierrette*, thank you for always being there when I needed a friend and for being the sweet and loving best friend that you are. *Yasmine*, I'm so grateful for your friendship, for having you in my life, and for all the beautiful memories with you and yassouma! *Rouba*, I'm so glad I had such a great friend by my side the entire time throughout this thesis! My brother *Georges*, thank you for helping me always and for making my stays in Lebanon so beautiful and stress-free. You are my younger brother but I look up to you in so many ways. My sister *Vana* thank you for being the best sister anyone can have. You are a role model to me and I wish you all the happiness in the world. I love you so much. *My father* thank you for always being there for me. For encouraging me to go after my ambitions and my dreams. Even when it was to become a singer. You took me to Beirut to an audition without even asking me what it was. I don't know another lebanese father who would do that. For the long midnight drives to the airport and from the airport. For your love and your trust, and your support always. For always telling me that everything will be okay, that everything can be fixed. I know that wherever I am in the world, I will be okay because I have you.

I will always be grateful to *France*, and *Strasbourg* in particular, for being so beautiful and for making this experience everything that it was. For being a place where I feel like I'm home. For allowing me to do something that I love and providing me with opportunities to be a researcher and to grow. And to all the french people I've met who inspired me with their kindness, readiness to help, their professionalism and their discipline. Thank you for changing my life.

Léna Mouawad

Monte Carlo simulations and a theoretical study of the damage induced by ionizing particles at the macroscopic scale as well as the molecular scale

Résumé

Le travail présenté dans cette thèse se place dans le contexte de la simulation de dommages biologiques. D'abord, une étude macroscopique met en question la pertinence des plans de traitement basés sur la dose absorbée et le passage à une étude de micro-dosimétrie permet l'utilisation de paramètres biologiques plus pertinents, tels que les cassures de brins d'ADN. La validité des sections efficaces d'interaction sur lesquelles se basent ces simulations est discutée en plus de détails. Suite à la complexité du milieu biologique, les sections efficaces d'interaction avec l'eau sont souvent utilisées. Nous développons un algorithme qui permet de fournir les sections efficaces d'ionisation pour n'importe quelle cible moléculaire, en utilisant des outils qui permettent de surmonter les difficultés de calcul, ce qui rend notre programme particulièrement intéressant pour les molécules complexes. Nous fournissons des résultats pour l'eau, l'ammoniac, l'acide formique et le tétrahydrofurane.

Mots clés : Plan de traitement, cassures de brins d'ADN, dégâts biologiques, simulations Monte Carlo, ionisation par impact d'un électron, section efficace triplement différentielle, molécules complexes.

Résumé en anglais

The work presented in this thesis can be placed in the context of biological damage simulation. We begin with a macroscopic study where we question the relevance of absorbed-dose-based treatment planning. Then we move on to a micro-dosimetry study where we suggest the use of more biologically relevant probes for damage, such as DNA strand breaks. More focus is given to the fundamental considerations on which the simulations are based, particularly the interaction cross sections. Due to the complexity of the biological medium, the interaction cross sections with water are often used to simulate the behavior of particles. We develop a parallel user-friendly algorithm that can provide the ionization cross sections for any molecular target, making use of particular tools that allow to overcome the computational difficulties, which makes our program particularly interesting for complex molecules. We provide preliminary results for water, ammonia, formic acid and Tetrahydrofuran.

Keywords : Treatment planning, DNA strand breaks, biological damage, Monte Carlo simulations, ionization by electron impact, triple differential cross section, complex molecules.